



**NANYANG
TECHNOLOGICAL
UNIVERSITY**

STUDY AND DEVELOPMENT OF ADVANCED
PACKAGING TECHNIQUE FOR
SEMICONDUCTOR LASERS



TEO JIN WAH RONNIE
SCHOOL OF MATERIALS SCIENCE AND ENGINEERING
2007

Study and development of advanced packaging
technique for semiconductor lasers

Teo Jin Wah Ronnie

School of Materials Science and Engineering

A thesis submitted to the Nanyang Technological University
in fulfilment of the requirement for the degree of
Doctorate of Philosophy

2007

ABSTRACT

The development of Erbium-Doped Fiber Amplifiers (EDFA) in long-haul telecommunications applications resulted in the rapid evolution of high power semiconductor lasers. In these applications, the demand for increased channel density in fiber-optic communication has pushed forward the use of single-mode ridge-waveguide laser diodes (LDs).

One of the major concerns in these single-mode LD packages is the thermal management of the module. These semiconductor lasers usually generate large heat fluxes, up to the range of MWcm^{-2} , that adversely affect their performance and reliability. Thus, the aim of packaging is to dissipate heat as efficiently as possible, in order to operate the LD at its maximum optical performance, without exceeding the permitted device temperature. As a first stage packaging, die-attachment of LDs onto a submount/heatsink is adopted and face-down bonding approach is recommended to meet the large heat generation rate. Some of the packaging-related issues faced in this bonding configuration are precision bonding alignment, low bonding yield, high bonding stress, good bonding integrity, as well as long-term reliability issues.

This thesis introduces the development of a modified bonding technique for single-mode ridge-waveguide LDs. The effects of bonding parameters on the microstructure, bonding integrity of the solder joint, and LD performances were analyzed. Reliability tests such as thermal cycling and accelerated aging tests were also performed to prove the package's long-term stability. The solder joint possessed good long-term reliability, with little intermetallic compounds (IMC) growth at the interfaces. The formation of Au-rich β and

ζ' phase Au/Sn compounds in the solder joint limit the interfacial IMC growth. Mechanical testing exhibited excellent bonding integrity, with brittle fracture occurring within the LD. No degradation of threshold current I_{th} could be observed and a 3X optical improvement over unbonded LDs was attained due to improved thermal management.

Band structure theory of semiconductor lasers was conducted to understand the temperature-dependence characteristics of LDs. Transient and steady-state thermal analysis of semiconductor lasers showed that the heat generated in the LD and its associated thermal resistance R_{th} was induced by the radiative energy transfer of free carriers. The dependence of R_{th} on different bonding configurations and its correlation with the output power was discussed. Finite Element (FE) modeling was also carried out to provide theoretical understanding on the temperature distribution and thermal dissipation for different bonding configurations. Face-down bonded LDs demonstrated improved thermal management with ~80% of heat flow towards the heatsink while face-up bonded LDs could only manage ~50%. The analytical method using electronic band structure calculations and FE modeling gave close fitting to the experimental results. This verified the performance capability of the LD under different bonding configurations.

Although this modified bonding technique focuses on long-haul telecommunications applications, where 980 nm single-mode ridge-waveguide LDs are utilized, they are also applicable to a plurality of other semiconductor lasers from short wavelength (0.6-1.1 μm) GaAs-based LDs to InP-based long wavelength (1.3-1.5 μm) semiconductor lasers. Their applications in military, industrial, commercial, and consumer products typically involves space communication systems, fiber optic transmission systems, sensors, laser printers, optical disk players, and diode-pumped solid-state lasers etc. In particular, the growth of long wavelength applications in telecommunications network has shown an

explosive rate. Development of this modified bonding technique will complement the introduction of new cutting-edge classes of high-power semiconductor lasers.

ACKNOWLEDGEMENTS

The author wishes to extend his sincerest gratitude and appreciation to the following persons, who have offered invaluable contributions towards the completion of this research project:

First of all, I would like to express my heartfelt gratitude to my ex-SIMTech supervisor, Dr. Shi Xunqing, for his meticulous nurture and guidance. His commitment and patient mentorship throughout the course of this study inspire me to exercise independent research mentality. He has shown me the way of critical, scientific thinking in electronics and optoelectronics packaging processing and simulation. Despite leaving SIMTech, he has continued to assist me in my thesis writing and give valuable advice on related issues.

I would also like to express my sincerest gratitude to my supervisors, Assoc Prof. Chen Zhong and Dr. Wang Zhenfeng, for their guidance and valuable suggestions in my project. I would also like to thank my ex-NTU supervisors, Dr. Yuan Shu and Dr. Li Guoyuan, for facilitating the initial phase of my project.

From SIMTech, I like to thank Dr. Su Fei and Mr. Sun Yaofeng, for their guidance in the numerical modeling, Mr. Lim Lay Huat and Mr. Tan Yeow Meng, for their kind assistance in accelerated temperature cycling test and Ms. Ng Fern Lan and Mr. Sim Mong Chye Wilson for their guidance in using SEM and XRD.

I would also like to thank Ms. Lai Mei Ying Doreen, Ms. Lata Vishwanath, and Prof. Chua Soo Jin from IMRE for utilizing SIMS and their pulse LD characterization system,

and Mr. Yee Kwok Chuen Michael from Denselight for technical advice on the characterization of LDs.

I would also like to thank my fellow colleagues Mr. Goi Lim Sheng Kip, Ms. Ng Boon Sing Jovice, Ms. Ngoh Shwu Lan Cassandra, Mr. Chua Beng Wah, Ms. Goh Chwee Sim and Ms. Nai Mui Ling Sharon for their discussions.

Finally, I would like to thank Heryani Binte Ahmad, Mastura Aidel Bte A Bakar, Sze Lay Peng Fiona, and Sng Jing Li for their logistic support in the NTU Microelectronics Materials Lab.

TABLE OF CONTENTS	PAGE
ABSTRACT	i
ACKNOWLEDGEMENT	iv
NOMENCLATURE	ix
LIST OF FIGURES	x
LIST OF TABLES	xix
1. INTRODUCTION	1
1.1 Background	1
1.2 Objectives	3
1.2.1 Development of Modified Face-Down Bonding Technique of Semiconductor Lasers	3
1.2.2 Multi-scale Thermal Analysis of Packaged Laser	4
1.2.3 Long-Term Reliability Investigation of Laser Diode	4
1.3 Thesis Outline	4
2. LITERATURE REVIEW	6
2.1 Semiconductor Lasers	6
2.1.1 Types of Semiconductor Lasers	7
2.1.2 Principles of Lasing Dynamics	9
2.1.3 Thermal behavior of Semiconductor Lasers	15
2.1.4 Reliability of Laser Diodes	16
2.2 Optoelectronic Packaging Methodology	19
2.2.1 Technical Considerations in LD Bonding	20
2.2.2 Existing Face-down Bonding Techniques of LDs	25
2.2.3 Bonding Process Considerations	29
2.3 Bonding Requirements	32
2.4 Classification of Material	35
2.4.1 Heatsink	35
2.4.2 Bonding Layer (Solder)	35
2.4.3 Diffusion Barrier	39
2.5 Conclusion of LD Packaging Technique	40
3. EXPERIMENTAL TECHNIQUE	42
3.1 Preparation of Cu Heatsink	42
3.2 Bonding Process	44
3.3 Characterization of Semiconductor Lasers	46
3.4 Microstructure Preparation	47

3.5 Mechanical Testing	49
3.6 Reliability Testing	50
4. DEVELOPMENT OF MODIFIED FACE-DOWN BONDING PROCESS FOR PACKAGING OF RIDGE-WAVEGUIDE LASERS	52
4.1 Introduction	52
4.2 Electroless Ni/Au Plating	52
4.3 Bonding Process	57
4.3.1 Effects of Bonding Temperature	70
4.3.2 Effects of Bonding Pressure	74
4.3.3 Optimal Bonding Window	87
4.4 Microstructure of Solder Interconnect	90
4.5 Mechanical Strength and Failure Mode	101
4.6 Summary	103
5. PERFORMANCE VERIFICATION OF BONDED LASER DIODES WITH NUMERICAL SIMULATION	106
5.1 Introduction	106
5.2 Thermal Behavior of Semiconductor Lasers	107
5.2.1 Thermal Analysis using Electronic Bandgap Calculations	107
5.2.2 Transient and Steady-state Analysis	109
5.2.3 Radiative Energy Transfer	114
5.2.4 Joules Heating due to Series Resistance	122
5.3 Influence of Bonding on the Lasing Characteristics	123
5.4 Numerical Simulation of Packaged LDs	130
5.4.1 Face-up Bonding Configuration	140
5.4.2 Face-down Bonding Configuration	144
5.5 Discussion	147
6. ASSESSMENT OF LONG-TERM RELIABILITY OF MODIFIED FACE- DOWN BONDING PROCESS	150
6.1 Introduction	150
6.2 Effect of Thermal Cycling Loading on reliability of Bonded LDs	150
6.3 Effect of Thermal Aging Loading on reliability of Bonded LDs	154
6.3.1 Analysis of LD degradation	156
6.3.2 Catastrophic Optical Damage	158
6.4 Summary	164
7. CONCLUSIONS	165

7.1 Conclusion	165
7.2 Recommendations	167
LIST OF PUBLICATIONS	169
REFERENCES	171

NOMENCLATURE

Metallurgy

δ	AuSn phase of Au-Sn solder
ζ'	Au ₅ Sn phase of Au-Sn solder
hcp	Hexagonal close packing

Photonics

λ	Emission wavelength
η_D	Differential quantum efficiency
η_i	Total internal laser-loss coefficient
α	Internal optical loss
α_i	Internal optical loss
α_m	Mirror optical loss
α_1	absorption coefficient in region 1
α_2	absorption coefficient in region 2
α_3	absorption coefficient in region 3
α_{fc}	free-carrier absorption coefficient in the active region
R	Reflective index
COD	Catastrophic optical damage
DLD	Dark line defect
QW	Quantum well in the active region
I_{th}	Threshold current
J_{th}	Threshold current density
I_{tr}	Transparency current
J_{tr}	Transparency current density
I_L	Leakage current
J_L	Leakage current density
N_{tr}	Transparency carrier density
Γ	Confinement factor
g_{th}	Optical gain at threshold
E_g	Bandgap energy
T_o	Characteristic temperature
R_S	Series resistance
F_e	Electron Fermi energy level
F_h	Hole Fermi energy level
V_f	Forward voltage
P_O	Nominal optical power
ηkT	Exponential factor
η	Ideality factor
κ	Planck's constant
q	Electronic charge
τ_C	Carrier lifetime

Numerical modeling

ρ	Density
κ	Thermal conductivity
Q	Distribution of heat source density
C_p	Specific heat

	LIST OF FIGURES	PAGE
Figure 1-1	Schematic diagram of pump laser used to amplify signal in EDFA module	1
Figure 2-1	Simplified schematic layer structure of 980 nm GRIN-SCH laser and its energy lineups at QW/Confining/Cladding regions. SiN layer suppressed current flow within the ridge.	8
Figure 2-2	Typical double-heterostructure energy levels in a single QW active region for carrier and light confinement. Carriers are injected into the QW during biasing to induce population inversion.	9
Figure 2-3	Bandgap dependence on alloy composition. Ternary compounds can be formed from binary materials by motion along the line joining the two points that represent the binary materials.	10
Figure 2-4	Fermi-Dirac distribution at a function of temperature. At 0K, $f(E)$ is unity for $E < E_f$. This indicates that all energy levels below E_f are occupied and all energy levels greater than E_f are empty. The probability of occupancy for $T > 0$ K is always $\frac{1}{2}$ at $E = E_f$, independent of temperature.	11
Figure 2-5	Schematic of the diode structure showing the waveguide effect in the junction region. Distribution of impurities and variation in the bandgap energy is defined in the three laser region.	13
Figure 2-6	Different types of degradation characteristic as a function of time. Gradual, rapid or catastrophic degradation occurs under constant driving current.	17
Figure 2-7	Failure mechanism of Catastrophic Optical Damage (COD) in the active region	18
Figure 2-8	The inside of the completed butterfly package style laser diode module showing various components. These include the laser diode chip mounted on the optical subassembly, and the saddle shaped clip which is welded to the base of the package. The metallic fiber ferrule is welded to the saddle shaped clip.	19
Figure 2-9	Comparison of different bonding configuration of ridge-waveguide laser diodes. (a) For face-up bonded LDs, the heat generated in the active region is ineffectively transferred	22

	through the 100 μm substrate; (b) For face-down bonded LDs, the heat flux is effectively resided onto the heatsink within several microns.	
Figure 2-10	Alignment considerations for bonding of LDs. (a) Underhanging of LDs onto heatsink impaired the optical signal; (b) Overhanging of LDs onto heatsink resulted in higher temperature at the facet; (c) The LD should flush along the edge of the heatsink for optimum device performance and effective fibre coupling.	24
Figure 2-11	Schematic diagram of various bonding techniques. (a) Lee et al. composite structure for Au-Sn solder joint; (b) Merritt et al. approach using In-Sn solder joint; (c) Boudreau et al. bridged bonding using In solder.	27
Figure 2-12	(a) Schematic diagram of ridge-waveguide LD and its diverging output beam profile; (b) Typical cross-sectional view of multi-layer metallization in packaged LD.	33
Figure 2-13	Gold-Tin binary phase diagram.	38
Figure 3-1	Development of electroless plating technique. a) After surface polishing, residues and oxide remains on the surface of copper; b) An acid solution removes the residues from the surface; c) Native oxide is etched off with a micro-etchant; d) Deposition of Ru metal behaves as a chemical activation for Ni plating; e) Ni is strongly absorbed on the Ru thin film accompanied by dissolution of Ru by simple immersion; f) Ion exchange between Ni and Au ion in the solution.	42
Figure 3-2	Die bonder with stage encapsulation. Ar gas is flushed into the stage to ensure good wettability.	45
Figure 3-3	Schematic diagram of LD holder in laser diode characterization system. The LD holder provides good electrical contact and stable temperature control.	47
Figure 3-4	Cross-sectional view of (a) grinded and (b) polished samples before polishing.	48
Figure 3-5	Shear Test. The shear tool was elevated from the surface to ensure consistent shearing measurement.	50
Figure 3-6	(a) Thermal cycling chamber; (b) Temperature profile using	51

Bellcore Reliability Practice - Thermal cycling Test.

Figure 4-1	Typical cross-sectional view of Ni/P layer, sandwiching between Au/Sn solder and Cu heatsink. EDX analysis showed ~10wt.% of P content in the Ni layer.	54
Figure 4-2	Surface morphology at different stages of the plating process. (a) Grinding scratches on the Cu surface; (b) Activation of Ru atoms onto the Cu surface; (c) Complete deposition of Ni layer with isolated Ni atoms on the surface; and (d) Good Au surface texture overlapping the Ni surface area.	55
Figure 4-3	Typical surface roughness measured during the plating process. Striations of peaks (red) and valleys (blue) could be observed from the surface.	56
Figure 4-4	Comparison of surface roughness at different stages of the plating process. Improved surface roughness could be obtained from the plating process.	57
Figure 4-5	Simplified cross-sectional view of ridge-waveguide edge emitting.	58
Figure 4-6	Binary phase diagram of Au-AuSn system.	59
Figure 4-7	Binary phase diagram of Ni-Sn alloy system.	60
Figure 4-8	Binary phase diagram of Au-Ni system.	61
Figure 4-9	Comparison of different bonding profile at the bonding stage. (a) The LDs were subjected to long bonding duration and large bonding pressure in the conventional approach. (b) Short bonding cycle, together with low bonding pressure, can be attained in this modified bonding process	64
Figure 4-10	Effects of bonding parameters on the optical performance of the LDs.	70
Figure 4-11	(a) Typical cross-sectional view of as-bonded LDs with insufficient wetting at the solder layer. (b) Au ₈₀ Sn ₂₀ solder was detected from the fracture surface after shear test	71
Figure 4-12	Optical performance of partially bonded LDs. Marginal optical output of 80-120 mW can be achieved, depending on the degree of bonding integrity. The differential quantum efficiency was observed to improve slightly after bonding.	72
Figure 4-13	Typical cross-sectional view of solder bridging onto facet of	73

	LDs.	
Figure 4-14	Fracture analysis of sheared LD package in face-down bonding configuration. Solder was observed to obscure the emitting facet and short-circuitry along the length of the LD was observed.	74
Figure 4-15	Typical cross-sectional view of insufficient bonding contact at the solder interface.	75
Figure 4-16	(a) Typical sheared surface of partially bonded LDs; (b) SEM/EDX analysis at region A of the fracture surface.	76
Figure 4-17	Typical cross-sectional view of well-bonded LDs in the bonding process window.	77
Figure 4-18	Fracture analysis of well-bonded LDs after shear test. LD residues was found on the fracture surface after shear test.	78
Figure 4-19	Optical performance of well-bonded LDs. Optimal optical performance, with more than 150 mW optical output can be achieved. The differential quantum efficiency showed good stability at high injection current.	80
Figure 4-20	Deformation contour of LD package after bonding process from 280 °C to 25 °C. Compressive stress would occur on the LD if face-down bonded while tensile stress would be imposed if it is face-up bonded.	81
Figure 4-21	Von mises stress induced after the bonding process. (a) face-up bonded LDs and (b) face-down bonded LDs.	82
Figure 4-22	Electrical derivative measurements of I-V characteristic of LDs. Heterojunction distortion can be observed for large bonding load.	83
Figure 4-23	Threshold current degradation due to large residual stress experienced.	84
Figure 4-24	Temperature dependence of threshold current I_{th} in these LDs. The I_{th} deteriorated at elevated temperature due to increased non-radiative processes at high operating temperature.	84
Figure 4-25	Temperature dependence of differential quantum efficiency η_D in these LDs. The η_D deteriorated at elevated temperature due to increased non-radiative processes at high operating temperature.	86

Figure 4-26	Effects of emission wavelength at different heatsink temperatures. Linear dependence of wavelength shift on operating temperature could be observed. The modified bonding approach showed reduced spectral dependence with temperature.	87
Figure 4-27	Comparison of different bonding profiles for Au ₈₀ Sn ₂₀ solder joint. Bonding pressure, temperature and time were three key bonding parameters used. (a) The heating and cooling rate of Pittroff et al. method were measured using Semiconductor Equipment Corp. Model 860 die bonder; (b) The heating and cooling rate of Lee et al. bonding process were assumed to be linear.	89
Figure 4-28	Microstructure evolution of Au ₈₀ Sn ₂₀ solder (a) before and (b) after solder reflow with Au/Ni metallization. (c) Phase diagram of binary Au-Sn system.	90
Figure 4-29	Ternary phase diagram of Au-Ni-Sn system.	93
Figure 4-30	Delaminations observed in partially bonded LDs.	95
Figure 4-31	(a) Cross-sectional view of as-solidified LD bonding interface; (b) δ phase is identified at regions A and C; (c) (Au,Ni)Sn IMC at region D; and (d) ζ' phase at region B.	96
Figure 4-32	(a) Cross-sectional view of solder/heatsink interface; (b) SEM/EDX analyses of Ni concentration at different locations of δ phase at the solder/heatsink interface.	97
Figure 4-33	Typical SEM micrograph Au ₈₀ Sn ₂₀ solder joint and its corresponding EDX mapping results.	98
Figure 4-34	EBSD diffraction patterns of intermetallics formed in the solder joint. (a) Diffraction pattern found from the Sn-rich region and (b)-(c) diffraction patterns found from the Au-rich phases. Kikuchi bands and poles of (d) δ , (e) ζ' and (f) β phases was indexed according to the lattice orientations on the specimen surface. (g) EBSD mapping of the solder joint.	100
Figure 4-35	(a) Typical planar-view of well-bonded LDs after shear test; (b) Magnified view of sheared LD at region B; (c) SEM/EDX analysis of fracture mode at region A; (d) SEM/EDX analysis	101

	of fracture initiation at region C.	
Figure 4-36	SIMS depth profile at region A of the fracture surface. Ga and Si were detected off the fracture surface.	102
Figure 4-37	SIMS depth profile on the LD epitaxial metallizations.	103
Figure 5-1	Calculated emission wavelength as a function of heatsink temperatures using electronic band structure theory	108
Figure 5-2	Transient temperature of the active region is derived from the calibrated emission properties. Temperature was observed to rise within micro-seconds and saturate in milli-seconds.	109
Figure 5-3	Influence of pulse repetition rate on the temperature characteristics of the LDs.	110
Figure 5-4	Schematic diagram of pulsed LD characterization system. Short pulse width and low duty cycle was performed to prevent parasitic heating in the LD.	112
Figure 5-5	Experimental measurement of emission wavelength as a function of various heatsink temperatures	113
Figure 5-6	Typical light output power versus injection current at a function of heatsink temperature for these LDs under cw operation.	114
Figure 5-7	(a) Typical emission spectra at different injection currents. (b) Change of emission wavelength and FWHM w around the lasing threshold.	115
Figure 5-8	(a) Current dependence of spectral emission peak and differential quantum efficiency. The differential quantum efficiency is given by the solid curve while the dotted points show the spectral measurements at different injection current. (b) Current dependence of temperature rise at the active region for different heatsink temperatures. The temperature in the active region dropped to a minimum at its lasing threshold.	117
Figure 5-9	Thermal resistance of LD at a function of current. The effective thermal resistance of the diode varies with current.	119
Figure 5-10	Temperature rise at high pulsed and cw injection currents. Joules heating due to the series resistance increased facet heating significantly.	122
Figure 5-11	Comparison of bonding configuration on the thermal behavior	123

	of LD. The temperature in the active region reduced after bonding, with improved thermal management in face- down bonding approach.	
Figure 5-12	Heating response of unbonded and bonded LDs at high pulse and cw operation. Joules heating could be observed at high cw injection current.	125
Figure 5-13	Comparison of bonding configuration on the thermal resistance of LD. The associated thermal resistance of the LDs reduced after bonding.	127
Figure 5-14	Influence of bonding on the electrical-optical characteristics of LDs. Inset: Characteristic temperature T_0 improved after bonding due to better heat dissipation means through the solder joint.	128
Figure 5-15	Comparison of emission wavelength under different bonding configurations.	129
Figure 5-16	Thermal boundary conditions for (a) face-up and (b) face-down bonding configurations.	132
Figure 5-17	Global meshing elements was conducted on both packaged LDs with higher concentration at the active region. Instances were constructed such that the ridge region and the heat source have higher biased node elements compared to the peripheral of the bonding designs.	133
Figure 5-18	(a) Schematic structure of InGaAs/GaAs/AlGaAs ridge-waveguide LD; (b) the thermal properties of each layer are represented.	134
Figure 5-19	Study of temperature rise in the active region with various heatsinking widths.	137
Figure 5-20	Study of temperature rise in the active region at various heatsinking thickness.	138
Figure 5-21	Study of heat distribution using different solder materials; (a) Comparison of temperature profile across the LD to the solder layer; (b) Comparison of temperature rise in the active region.	139
Figure 5-22	(a) Typical temperature contour at the facet of the LD for face-up bonded LDs; (b) Typical heat flux distribution across the cross-sectional laser structure for face-up bonding	142

	configuration. The bulk of the heat flux was observed to accumulate within the active region under the ridge.	
Figure 5-23	Temperature profile of face-up bonded LD onto Cu heatsink; (a) lateral profile along the active region of the LD; (b) vertical profile across from the LD to the base of the heatsink material.	144
Figure 5-24	(a) Typical temperature contour at the facet of the LD for face-down bonded LDs; (b) The bulk of the heat flux was observed to flow towards the heatsink effectively; (c) Typical heat flux distribution across the cross-sectional laser structure for face-down bonding configuration.	145
Figure 5-25	Temperature profile of face-down bonded LD onto Cu heatsink; (a) lateral profile along the active region of the LD; (b) vertical profile across from the LD to the base of the heatsink material.	146
Figure 5-26	Comparison of temperature profile across the active region to the top surface of the Cu heatsink. Face-down bonding approach demonstrates an effective heat dissipating channel compared to face-up bonding.	148
Figure 6-1	Typical temperature profile of thermal cycling conditions of -40 °C to +85 °C.	151
Figure 6-2	Electrical and optical characteristic of LDs before and after each interim cycles. (a) Comparison of series resistance before and after every 100 cycles; (b) Comparison of optical performance before and after every 100 cycles.	152
Figure 6-3	Typical cross-sectional view of bonded LD after 500 thermal cycling. SEM/EDX analysis showed no significant microstructure changes in the solder joint.	154
Figure 6-4	Characterization of optical performance during the aging process. Rapid degradation process can be observed for unbonded LDs while face-down bonded LDs exhibit gradual degradation.	156
Figure 6-5	Electrical characterization of LD as a function of time; (a) Forward voltage drops while (b) series resistance increases due to changes to the junction properties.	157
Figure 6-6	Effect of COD degradation on the optical performance.	158

	Threshold current and differential quantum efficiency deteriorated significantly.	
Figure 6-7	Schematic diagram of non-radiative recombination near the facet end. Carrier absorption towards the facet resulted in higher heat generated along the cavity length.	159
Figure 6-8	Evaluation of parametric behavior during the aging process; (a) Threshold current increases significantly while differential quantum efficiency decreases gradually in the aging process; (b) The characteristic temperature T_0 increase gradually with reduced temperature sensitivity.	160
Figure 6-9	Facet observation (a)-(b) before and (c)-(d) after aging. Evidence for this catastrophic failure can be seen from scanning electron microscope (SEM) images of post-COD laser facets. Protrusion can be observed from the outline of the laser ridge. Material at the active region has molten and pushed through the facet before resolidifying. The damage occurred at the center where optical field intensity is at maximum.	162
Figure 6-10	Facet deformation at the active region resulted from the localized melting. Progressive propagation of molten zone along the active region resulted in malfunction of the device.	163

LIST OF TABLES		PAGES
Table 1	Comparison of various bonding techniques. The bonding parameters depend largely on the bonding technique and bonding material used.	25
Table 2	Comparison of various bonding mediums used in advanced packaging.	32
Table 3	Properties of materials used in optoelectronic packaging.	34
Table 4	Comparison of various solder materials used in photonics packaging applications and its physical properties.	36
Table 5	Test program for face-down bonding of LDs using Au80Sn20 solder.	66
Table 6	Experimental results of bonded LDs at various bonding parameters.	67
Table 7	Mechanical integrity of bonded LDs.	68
Table 8	Effect of bonding parameters on the bonding yield.	69
Table 9	Optical performance comparison with different bonding area	79
Table 10	Experimental matrix for face-down bonding of 3 μm ridge-waveguide LDs using Au80Sn20 solder. The bonding window is derived from both interfacial and parametric evaluations.	88
Table 11	Comparison of packaged LD before and after accelerated aging.	161

CHAPTER 1

INTRODUCTION

1.1 Background

Laser diode (LD) is one of the key components in applications, including material processing, marking and label printing, medical applications such as skin treatment, and military/aerospace applications ranging from laser warning and targeting to “directed-energy” weapons and inter-satellite communications. LDs with an emitting wavelength of 980 nm have a key application in telecommunication networks such as pumping of solid-state lasers such as NdYAG lasers, fibre lasers and disc lasers, as well as direct applications of the LD output. However, the majority of these LDs are used in telecommunications applications as pumping source for Erbium-Doped Fiber Amplifiers (EDFA). The development of EDFA has made direct optical transmission long-haul fiber telecommunication possible.

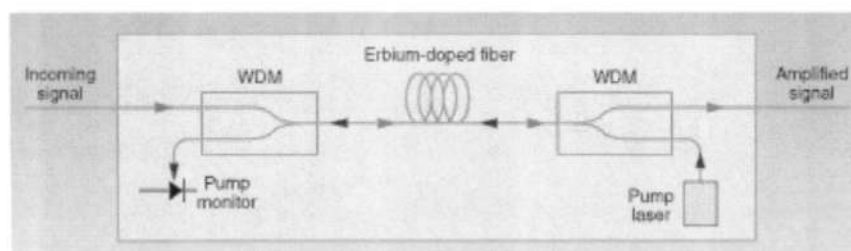


Figure 1-1 Schematic diagram of pump laser used to amplify signal in EDFA module.

These fiber-optic communication systems, which require high fiber coupling efficiency, are not inherent in broad area lasers due to their multi-mode behavior. The demand for increased channel-density in Dense Wavelength Division Multiplexing (DWDM) networks further pushed forward rapid evolution of high-power single-mode pump lasers. Development of high-power LDs has attracted a lot of attention to add new dimensions

into the photonics industries. With the continuous pursue for higher lasing power, efficient thermal management is essential in the packaging design to facilitate controlled operation. Low-cost packaging of optoelectronic devices is important with the introduction of optical telecommunication networks in metropolitan and local areas as well as in parallel optical data communication links, because packaging dominates the cost of optoelectronic modules from 60% up to more than 90% [1]. However, the development of LD packaging not only is a critical step for possible commercialization of the product, but also a technological challenge for achieving better performance. Material-oriented problems concerning electrical, mechanical and thermal issues must be resolved, while design-oriented issues strive for ease of manufacture, reworking and inspection.

Presently, the heat generated in a semiconductor laser cannot be dissipated effectively to their surrounding and require a thermo-electric cooler (TEC) module to regulate the operating temperature. To facilitate proper thermal management, the LDs must be bonded onto a submount/heatsink. A well-controlled, high yield, void-free bonding interface is required to accommodate efficient thermal management in the die attachment. In die attachment, thermo-compression bonding and ultrasonic bonding are two commonly used bonding processes and they are bonded in either face-up or face-down configuration. The face-up bonding approach has been widely adopted [2-5]. However, the heat generated is confined within the LD due to the low thermal conductivity of the device. Hence, the face-down approach using Au80Sn20 solder is recommended to effectively dissipate the heat generation. However, a number of thermal, mechanical, optical, and electrical factors complicate the development of optoelectronic packaging in single-mode ridge-waveguide laser diodes (LDs). Despite its increasing popularity of Au80Sn20 solder, the microstructure evolution of Au80Sn20 solder joint is still not clear as there is not much

documentation on the bonding process using Au80Sn20 solder for semiconductor lasers [6], [7]. A systematic study of the bonding process is also required to ease the stringent requirements faced in LD packaging.

1.2 Objectives

From the aforementioned research background, high-power semiconductor lasers employed in fiber-optic communication systems generate significant heating that affect their performance and reliability considerably. These LDs require a thermally-effective packaging technique to improve on their performance and reliability. This thesis aims to provide a systematic understanding of the bonding technique and long-term reliability investigation of the bonded LDs. The objectives of this thesis can be described with three sections as detailed below.

1.2.1 Development of Modified Face-down Bonding Technique of Semiconductor Lasers.

Au80Sn20 solder joint specimen based on the application of LD package will be designed. The soldering and packaging parameters for the fabrication of Au80Sn20 solder joint will be optimized to attain well-controlled bonding interface. Effects of bonding parameters on the integrity of the bonding interface and the principal performances of the LD will be reported. The electrical, optical, and spectral characteristics of LDs will be investigated before and after packaging. Such studies will provide guidance to the construction of a bonding window using Au80Sn20 solder.

1.2.2 Multi-scale Thermal Analysis of Semiconductor Laser

Firstly, band structure theory of semiconductor lasers will be conducted to understand the thermal behavior of LDs. Temporal and spectrally resolved measurement will be explored to understand the physics of heat generation in a LD. Then, a thermal simulation exercise will be conducted to understand the heat transfer in a packaged LD. From the experimental findings and the simulation results, the temperature profile of the LD package will be investigated under different bonding configurations. This thermal model will be used to verify the performance capability of packaged LDs.

1.2.3 Long-Term Reliability Investigation of Laser Diode Package

To ensure that these bonded LD exhibit good long-term reliability, the LD package was investigated under thermal cycling and thermal aging conditions. Effects of thermal cycling and thermal aging loadings on the reliability of the package were investigated. The degradation characteristics of LD packages were identified and an empirical life prediction model for these LDs was also developed.

1.3 Thesis Outline

This thesis is organized in the manner whereby CHAPTER 1 gives the background and motivation of this project, determines the aims and objectives of the work to be performed, and provides the scope of the work carried out. CHAPTER 2 elucidates the principles of LD operation, highlights the key technologies involved in existing optoelectronics packaging methodology, and identifies the importance of the bonding process. In CHAPTER 3, the experimental techniques will be highlighted. CHAPTER 4

introduces the development of the modified face-down bonding process. The effects of different bonding temperatures and bonding pressures on the integrity of the bonding structure and its associated electrical-optical performance of the LD will be discussed. A bonding process window using Au80Sn20 solder will then be established. CHAPTER 5 describes a thermal behavior of semiconductor laser. The heating mechanism of semiconductor laser will be explored. Band structure analytical calculation and FE modeling will be used to comprehend the temperature profile of the LD and verify the performance capability of the LD under different bonding configurations. CHAPTER 6 assesses the long-term reliability of bonded LDs. Effects of thermal cycling and thermal aging loading on the reliability of bonded LDs will be reported. A life prediction model for bonded LDs will also be developed. Lastly, CHAPTER 7 summarizes the project accomplishments and suggests future recommendations.

CHAPTER 2

LITERATURE REVIEW

Optoelectronic packaging today serves the purposes of heat dissipation, mechanical support and electrical conduction in the die bonding layer. While strong interfaces are necessary to ensure mechanical integrity of the bonded components, they are also responsible for lowering electrical and thermal conductivity of the assemblage. The heat generated by high-power laser diodes/arrays has to be transferred optimally to the semiconductor package in order to ensure efficient thermal management. Premature failure due to inadequate heat dissipation and mechanical integrity has remained a challenge to the current development.

Hence, the packaging methodology for optoelectronics devices will be carefully reviewed in this chapter. Although the LD fabrication process will not be reviewed, a typical LD epitaxial structure is studied since it is directly related to the bonding process and simulation exercise. The principles of lasing operation in semiconductor lasers will also be discussed to facilitate evaluation of key LD performances. Existing optoelectronics packaging techniques and classification of different packaging materials are then appraised. From the comprehensive appraisal, the packaging methodology and the classification of packaging material can be designed accordingly.

2.1 Semiconductor Lasers

High-power LDs have a key application in these telecommunication networks [8, 9]. Both 980 nm and 1480 nm LDs have been used as pumping sources for EDFAs [10]. However, there are more application fields for 980 nm LD such as terrestrial communication

systems, undersea use, etc. with the largest portion in communication areas. This is because 980 nm was identified as being the most efficient pump wavelength where no excited state absorption exists [11]. Amplification with an excitation wavelength of 980 nm ideally has a low-noise figure close to the 3-dB limit [12] and low-power consumption [13]. The improved noise figures permit increased separation between repeaters. Application of wavelength-division-multiplexing technology for larger transmission capacity is also a key point to meet the increasing demands of communications in the world today. Hence, 980 nm single-mode ridge-waveguide LD is an attractive candidate to increase the channel capacity in the network. A ridge waveguide structure is widely used for reasons of easy fabrication and modal control [14].

2.1.1 Types of Semiconductor Lasers

There are various types of lasers used in the industries i.e. ridge lasers, broadarea lasers, ring lasers, VCSELs (Vertical Cavity Surface Emitting Laser) etc. Generally, these lasers are categorized into edge-emitting and surface-emitting. The focus of this thesis is edge-emitting laser for fiber optics applications. Within this LD structure, there are various heterostructure designs reported for these applications; namely GaAs/AlGaAs, InGaAs/GaAs, InGaAs/Ga(In)As(P)/GaInP, and InGaAs/AlGaAs etc. Generally, these heterostructures provide optical confinement perpendicular to the junction, and the use of ridge in the laser structure allows optical confinement parallel to the active region. The stripe essentially acts as a guiding mechanism by limiting current spread over the active layer. This can be achieved by creating an area of high resistance, SiN passivation layer, over the region of the active layer in which lasing is to be suppressed underneath the ridge. As shown in Figure 2-1, 980 nm Fabry-Perot (FP) lasers consist of multiple quantum-wells (QWs) surrounded by cladding layers.

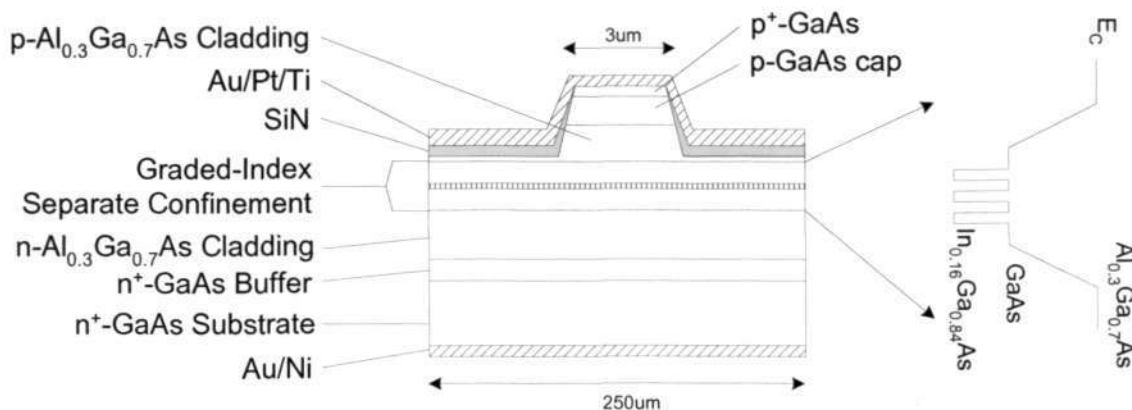


Figure 2-1 Simplified schematic layer structure of 980 nm GRIN-SCH laser and its energy lineups at QW/Confining/Cladding regions. SiN layer suppressed current flow within the ridge.

The cladding layers create potential wells for carrier confinement in the active region as shown in Figure 2-2. This double-heterostructure permits absorption and emission of radiation. To allow emission to occur, absorption of photons increases the concentrations of holes and electrons in the QWs (a condition known as population inversion) and, is then stimulated to give energy in the form of light radiation.

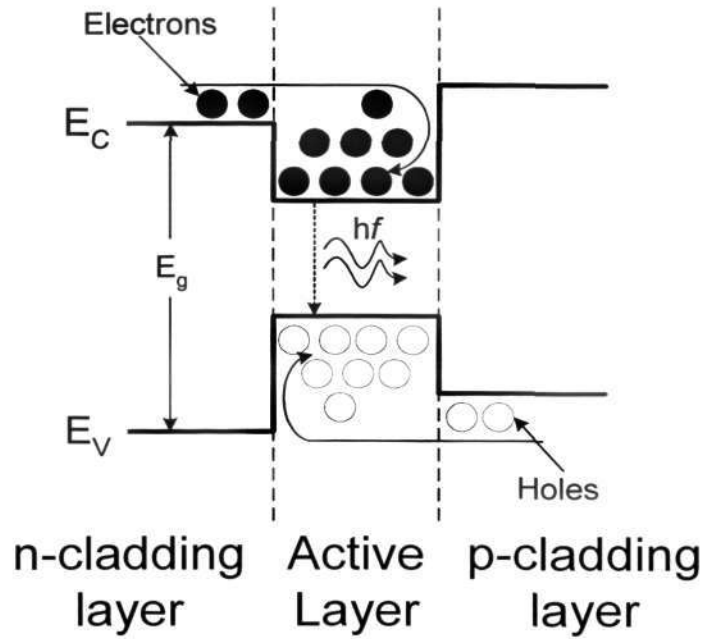


Figure 2-2 Typical double-heterostructure energy levels in a single QW active region for carrier and light confinement. Carriers are injected into the QW during biasing to induce population inversion.

2.1.2 Principles of Lasing Dynamics

Stimulated recombination of free carriers in the quantum wells generates lasing emission with energy $\sim E_g$. Typically, both direct and indirect energy gaps in semiconductor materials are dependent on alloy composition and are frequently assumed to fit a simple quadratic form [15] as shown in Figure 2-3. For these ternary InGaAs QWs, the energy bandgap can be approximated by,

$$E_g(\text{In}_x\text{Ga}_{1-x}\text{As}) = xE_g(\text{InAs}) + (1-x)E_g(\text{GaAs}) - x(1-x)b \text{ in eV} \quad (2-1)$$

where the bowing parameter b is 0.477 [16].

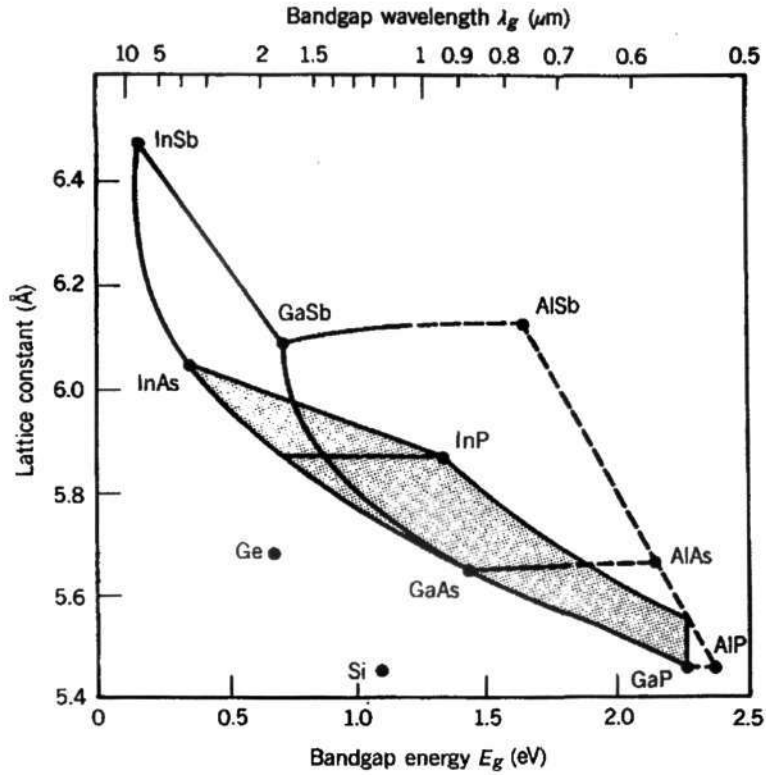


Figure 2-3 Bandgap dependence on alloy composition. Ternary compounds can be formed from binary materials by motion along the line joining the two points that represent the binary materials.

To determine the characteristic of a semiconductor, the carrier density for current conduction must first be defined. The carrier density in the confinement layer can be obtained from the distribution function $f(E)$ and density-of-states function $g_c(E)$. The probability of electrons confined in the active region follows the Fermi-Dirac distribution [17],

$$f(E) = \frac{1}{\exp\left[\frac{E - E_f}{k_B T}\right] + 1} \quad (2-2)$$

where E_f is the Fermi energy and the population of electrons [18] can be approximately expressed as,

$$N = W \int_0^\infty \frac{1}{\exp\left[\frac{E - E_{fc}}{k_B T}\right] + 1} g_c(E) dE \quad (2-3)$$

where W is the total thickness of the confinement layers, g_c the density of states in the conduction band, and E_{fc} the quasi-Fermi level of the conduction band.

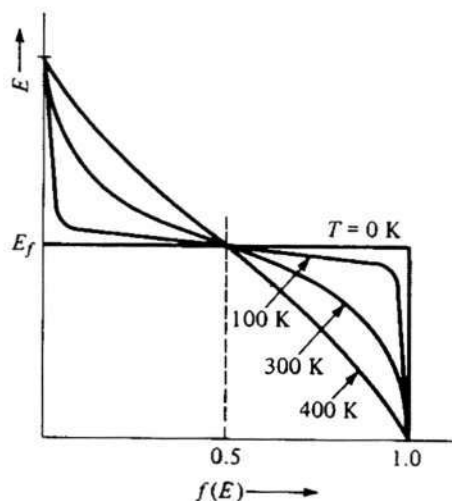


Figure 2-4 Fermi-Dirac distribution as a function of temperature. At 0 K , $f(E)$ is unity for $E < E_f$. This indicates that all energy levels below E_f are occupied and all energy levels greater than E_f are empty. The probability of occupancy for $T > 0\text{ K}$ is always $\frac{1}{2}$ at $E = E_f$, independent of temperature [19].

From equation 2-2 to 2-3, the density of carrier confinement is dependent on temperature and can be explained with Figure 2-4. The decaying function of temperature reflects the distribution of carriers in the bands and depends on the bandtail density of states distribution. As the temperature increases, the carrier density reduces. To acquire the same amount of carrier density at higher temperature, higher current must be injected. The theoretical implications of variations in key laser parameters on performance constitute the study of optical losses in p-n junction lasers. When the temperature increased, α_i was raised. This was attributed to the larger separation of quasi-Fermi levels due to band structure modification. At higher temperatures, to obtain the same threshold gain, the required separation of quasi-Fermi levels was higher (see equation 2-2). According to Fermi-Dirac statistics for injected carriers, the injected carriers not only

populate energy states of quantum wells but also energy states of confining layers [19]. This band/state filling phenomenon at the confining layers contributed to threshold current and led to poor temperature characteristics. The increase in temperature broadened the quasi-Fermi functions F_e and F_h such that the condition for inversion changes to $F_e + F_h > 1$ and, hence higher injection current density was required. The increased in temperature also caused electron and hole distributions to spread out into higher energies, contributing to leakage current incurred as a greater fraction of injected carriers moved, either by diffusion or drift, to the active region and ending up in the cladding or contact region. This electron leakage current consisted of a fraction of injected carriers with sufficient thermal energy to surmount the potential barrier between the active region's quasi-Fermi level and the conduction energy, E_C , of the cladding layer. This led to increased conversion of excitation energy into a non-radiative recombination process.

With reference to Figure 2-5, the threshold condition for a semiconductor laser is given by [19],

$$(-\alpha_2 - \alpha_{fc}) = (1/F_1)(-\alpha_3 - \alpha_1 F_2) + \alpha_m \quad (2-4)$$

where α_1 and α_3 are the absorption coefficients at the lasing wavelength in region 1 and 3, respectively; α_{fc} is the free-carrier absorption coefficient in the active region (region 2); $(\alpha_2 + \alpha_{fc})$ is the total absorption coefficient in region 2. F_1 and F_2 are functions of the waveguide geometry.

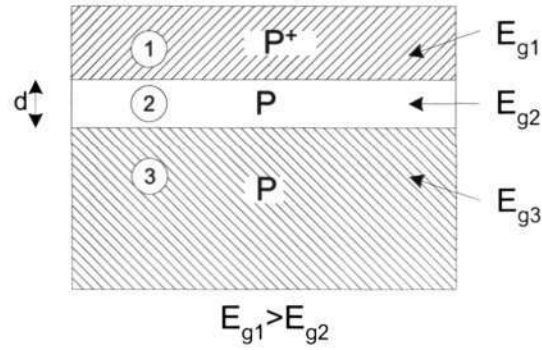


Figure 2-5 Schematic of the diode structure showing the waveguide effect in the junction region. Distribution of impurities and variation in the bandgap energy is defined in the three laser regions.

The end losses at the facets are defined by,

$$\alpha_m = \frac{1}{2L} \ln \frac{1}{R_1 R_2} \quad (2-5)$$

where $R = 0.32$ is for non facet-coating LDs, and L is the cavity length (600 μ m).

Assuming that α_2 is a linear function of the current density J ,

$$-\alpha_2 = \beta J \quad (2-6)$$

where β is the gain constant which has a decreasing function to temperature. The probability of energy occupancy is dependent on temperature as shown in Figure 2-4.

Combining equations (2-4) and (2-6), an expression for the threshold current density can be obtained. In terms of the specific expression for the loss through cavity ends with reflection coefficient R within a cavity length L ,

$$J_{th} = (1/\beta) \left[(1/F_1)(\alpha_3 + \alpha_1 F_2) + \alpha_{fc} + \frac{1}{2L} \ln \frac{1}{R_1 R_2} \right] \quad (2-7a)$$

or, more generally

$$J_{th} = (1/\beta) \left[\alpha + \frac{1}{2L} \ln \frac{1}{R_1 R_2} \right] \quad (2-7b)$$

where the total internal laser-loss coefficient α is given by,

$$\alpha = (1/F_1) (\alpha_3 + \alpha_1 F_2) + \alpha_{fc} \quad (2-8)$$

This shows that the loss consists of free carrier absorption due to carriers within the QW (region 2), free carrier absorption due to carrier in the confining layers (region 1 and 3), waveguide scattering, and impurity absorption. This absorption loss depends largely on the carrier concentration in the active region, as well as the planarity of the junction and other waveguide mechanisms [20].

Likewise, the differential quantum efficiency η_D is also dependent on the mirror and optical losses. It illustrates the ratio of photon output rate resulting from the increase in injection current and can be expressed by,

$$\eta_D = \eta_i \frac{1}{1 + 2\alpha_i L / \ln \left(\frac{1}{R_1 R_2} \right)} \quad (2-9)$$

where internal quantum efficiency η_i is a measure of the efficiency of a laser in converting electron-hole pairs into photons within the structure.

The emission power can then be expressed by,

$$P_{out} = \eta_D \frac{hf}{q} (I - I_{th} - I_L) \quad (2-10)$$

where h is Planck's constant (6.63×10^{-34} J/s); f is the frequency, I_L is the leakage current and I_{th} is the threshold current.

2.1.3 Thermal Behavior of Semiconductor Lasers

Thermal management is a critical issue in semiconductor lasers and light-emitting diodes for achieving optimum performance in cw or modulated operations. During operation, the current flowing through the device results in a localized heating at the emitting facet [21-23]. The temperature rise is a critical parameter as it strongly affects the device characteristics and reliability, including the lasing threshold current [24, 25], emitted optical power [26, 27], wavelength of longitudinal modes [28], peak of emission spectrum [24, 29, 30], terminal voltage [31], as well as the device lifetime [32, 33]. A large temperature rise during cw operation may (i) increase the threshold current, (ii) limit the maximum optical power, (iii) lead to unwanted temperature-dependent shifts in spectrum and mode, and (iv) reduce the useful lifetime of the device. In extreme case, severe heating may even lead to catastrophic failure of the facets [34].

Theoretical and experimental analyses of the thermal behavior in semiconductor lasers have been carried out extensively. The dynamics of thermal phenomena in semiconductor lasers have been considered using heat flow model [29, 35] and radiative energy transfer calculations [36, 37]. In order to study the thermal behavior in semiconductor lasers, the injection current are usually chosen close to lasing threshold so that the radiated power is minimal. However, these thermal measurements were conducted from below I_{th} (spontaneous emission) [21, 28, 30] to above I_{th} (stimulated emission) [25, 30] and at various modulating frequencies [22, 23, 26]. A large variation of thermal behavior was also observed. Hence, the thermal resistance R_{th} of the LD may not be constant and varies with current.

Feng et al. [38] gave a thermal explanation of the process of current increasing from spontaneous emission to the lasing phenomenon. At low injection current, below threshold, most of the injected power was converted to heat energy. When the injection current increased, the light production process began to increase and more of the input power transferred to light. The power input per unit area which is converted to heat due to this cause is given by

$$\text{when } I < I_{th} \quad = \eta_{LED} \cdot I \quad (2-11a)$$

$$\text{when } I \geq I_{th} \quad = \eta_{LED} \cdot I_{th} + \eta_D (I - I_{th}) \quad (2-11b)$$

where η_{LED} and η_D are the external differential efficiencies for spontaneous and stimulated emission.

2.1.4 Reliability of Laser Diodes

The reliability of 980nm semiconductor lasers is also discussed since these devices are expected to have long operational life. The reliability projection of the LDs is measured as the evolution with time of either the light output power at constant injection current or the threshold current at constant light output power. For convenience, constant current mode will be discussed. During the operation of high-power LDs, the output power under constant driving current changes. The output power tends to decrease during operation due to degradation of the device. There are several types of degradation characteristics in relation to the initial period of degradation, degradation rate, and degree of degradation [39], [40]. As shown in Figure 2-6, the degradation characteristics can be classified into three different modes: gradual, rapid and catastrophic degradation. Gradual degradation corresponds to a slow progressive decay of optical power over a long period. Non-radiative recombination at existing point defects produces new point defects, reducing the light generation efficiency [41]. Rapid degradation, which can be detected by a very fast

decrease in output power, is associated with the presence of extended defects that destroy the active region of the laser and quench the optical emission. A step-like decrease in output power is typically for catastrophic degradation.

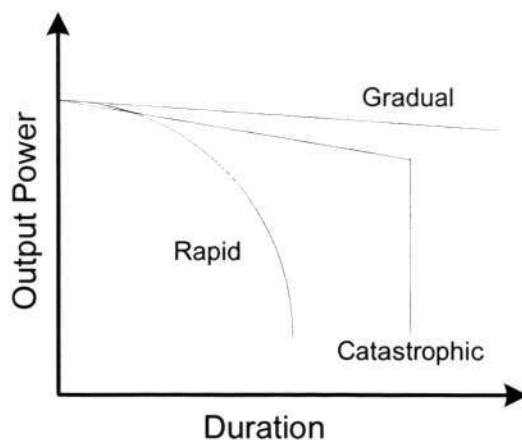


Figure 2-6 Different types of degradation characteristic as a function of time. Gradual, rapid or catastrophic degradation occurs under constant driving current.

In the aging process, different degradation modes have been reported, with Dark Line Defects (DLD) [34] and Catastrophic Optical Damage (COD) [42-44] being the dominant problems faced during long-term operation. The degradation mode is related to the generation of a dislocation network, at different magnitudes of the injected current density. At lower current density, DLDs are generally found whereas COD effect is discovered at high injection current. Reviewing the general situation of facet-related problems in semiconductor lasers is helpful to understand the complicated phenomena occurring at the facet.

In the degradation process, light absorption at the facet generates electron-hole pairs. These generated electron-hole pairs accelerate bond breaking and resultant facet oxidation. It raises the temperature near the facet due to non-radiative recombination by

way of surface states located at the facet. On the other hand, facet oxidation is enhanced by the increase in the bond breaking, which is photo-enhanced oxidation. This oxidation process can be understood as a defect injection process in the active region [45]. Consequently, DLD often takes place in the vicinity of the facet after long-term operation, showing non-radiative recombination enhanced defect motion [46]. As a result of these effects, bandgap shrinkage is enhanced and further light absorption and temperature increases occur. In the final stage, this temperature rise causes thermal runaway and the positive feedback loop reaches the melting point of the laser material. This run-away process causes COD and degradation at the facet. Based on the loop, a facet oxidation loop, a loop of dislocation growth from the facet, and some related phenomena are physically connected as shown in Figure 2-7.

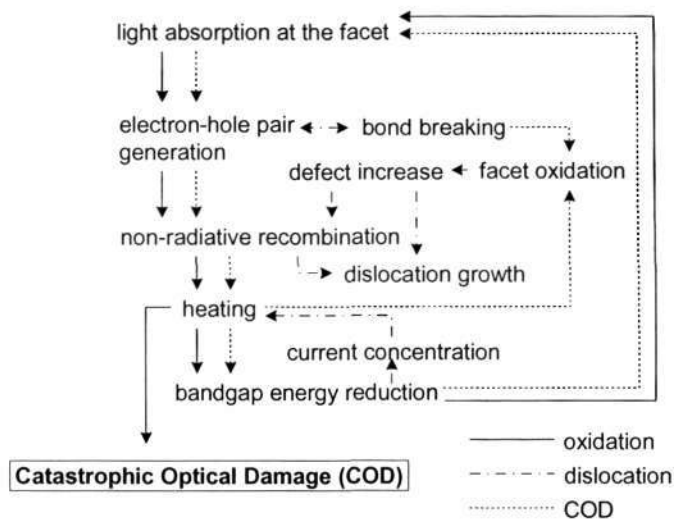


Figure 2-7 Failure mechanism of Catastrophic Optical Damage (COD) in the active region [47].

Understanding the LD structure and its lasing characteristics facilitate prominent advantages in the packaging process. The electrical and thermal characteristics of LDs can be optimized from the packaging design.

2.2 Optoelectronic Packaging Methodology [48]

High-power, single spatial-mode, 980nm LDs are critical components for EDFA in dense wavelength-division multiplex (DWDM), fiber-optic communication systems. As shown in Figure 2-8, these LDs are usually packaged into 14-pin butterfly packages, which are essentially comprised of several sub-units; Thermoelectric Cooler (TEC), optical sub-assembly (containing LD), Metallic Fiber Ferrule, and Optical Fiber. Some of these major packaging processes in this butterfly LD package include; soldering of the TEC module, attachment of the optical subassembly including LD bonding, insertion and alignment of a Metallic Fiber Ferrule, laser welding, and hermetically sealing the package. However, this thesis will focus only on the bonding process as it has an immediate thermal impact to the LD package.

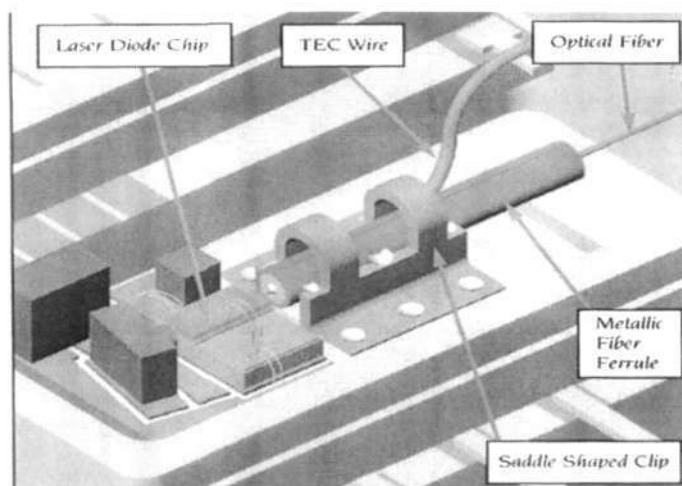


Figure 2-8 The inside of the completed butterfly package style LD module showing various components. The optical subassembly, including the bonded LD, is attached onto a TEC module to regulate the operating temperature. An optical fiber is then aligned to the LD with a Metallic Fiber Ferrule to provide the fiber with a housing necessary for rigidity and welding purposes. The metallic fiber ferrule is welded to the saddle shaped clip. Finally, the packaged assembly is completed by hermetically sealing it.

2.2.1 Technical Considerations in LD Bonding

LDs are practically applied to optical communication systems, which demand high output power and long-term reliability control. To achieve high output power, long operational life and high reliability, it is essential to improve the electrical characteristics and simultaneously release the Joule heat from the LD efficiently. The lost heat, especially in high-power LDs, must be dissipated as fast and uniformly as possible. Major temperature fluctuations during operation cause wavelength shifts, and excessive temperature increase is often associated with a drop in optical efficiency. In extreme cases, it can even cause destruction to the LD [39]. Hence, the LD is bonded onto a heatsink to ensure satisfactory thermal and electrical coupling.

This poses significant packaging challenges as a number of thermal, mechanical, optical, and electrical factors complicate the effort to package semiconductor lasers. Firstly, the performances of semiconductor lasers are temperature sensitive [49], [50]. Threshold current increases and the efficiency of electrical input into optical power decreases while the operating temperature increases. Secondly, semiconductor lasers generate large heat fluxes, which cause excessive temperature rise in the active region [23]. High power LDs can generate more than 1000 °C in the active region under high injection current. Third, these devices are sensitive to stress-induced degradation [51]. Threshold current and polarization of the optical beam change with increased stress induced. Hence, the conventional flip-chip bonding method [52] cannot be used for assembling a laser onto the heatsink because of the surface complexity in ridge-waveguide structures. Fourth, submicron positioning alignment tolerances are required to achieve high coupling

efficiencies [53]. Low-cost packaging of optoelectronic devices is also important because packaging dominates the cost of the optoelectronic modules.

Thermal Considerations

For laser die attach, there are generally two bonding configurations; face-up and face-down. Eutectic die bonding processes for face-up bonding approaches have well been established by the semiconductor packaging industry [2, 3, 5]. Due to the low thermal conductivity of ternary alloys and multiple heterostructures [54], [55], the heat generated from the active region cannot be dissipated onto the heatsink efficiently. The thermal path has to go through the entire 100 μm GaAs substrate before reaching to the heatsink. The heat generated in the active region spreads laterally over the entire width of the laser as it flows to the heatsink, leading to a two-dimensional heat flow in the LD. This two-dimensional heat flow accounts for the logarithmical dependence of ridge width [56]. For single-mode ($\leq 4 \mu\text{m}$) ridge-waveguide LDs, the bulk of the heat generation is confined to the active region. This raises concerns as significant heating in the active region influences the spectral and spatial characteristics, with longitudinal modes broadening [26]. The optical output power will also be compromised since their performance characteristics are sensitive to the LD operating temperature. As depicted in Figure 2-9, face-down bonding is recommended for effective heat transfer since the proximity of the active region is less than 2 μm from the surface [57-60]. The proximity of the active region to the top of the heatsink strongly influences the heat flow. Owing to the good conductivity of the heatsink material, the heat produced in the active region is rapidly distributed to the heatsink. Substantial improvement can be achieved as thermal resistance is inversely proportional to the ridge width for face-down approach [29]. Face-down bonding also eliminates the trade-off problem between high-frequency modulation [61]

and temperature control. In a LD package, three forms of electrical parasitics were present; intrinsic diode, external chip and package parasitics. For high-frequency applications, the external parasitics of the chip and the package prevent the module from achieving higher frequency modulation. In order to drive the LD into higher frequency modulation, a face-down bonding approach can help to reduce the external electrical parasitics significantly.

Hence, numerical modeling has been employed to perform thermal analysis of different packaging designs [29, 62, 63]. The thermal resistance for a face-down bonded LD was reported to be ~30% smaller than that of a face-up bonded. Hence, higher injection currents can be accommodated to achieve higher radiated power.

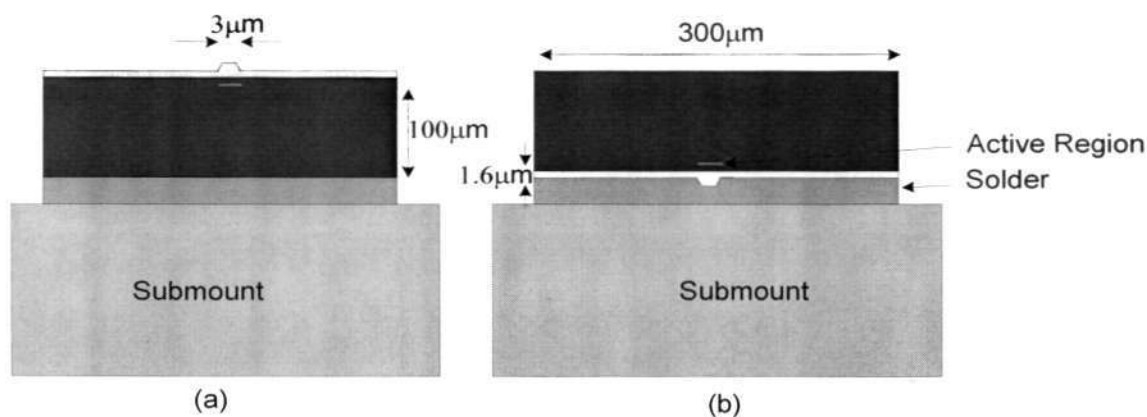


Figure 2-9 Comparison of different bonding configurations of ridge-waveguide laser diodes. (a) For face-up bonded LDs, the heat generated in the active region is ineffectively transferred through the 100 μm substrate; (b) For face-down bonded LDs, the heat flux is effectively reached the heatsink within several microns.

Stress Considerations

However, the stress associated with face-down bonding can cause mechanical distortion to the device. Due to the small distance between the active region and the contact layer, strain accumulation in the active region gets promoted. The stress experienced in the active region increases rapidly with external pressures. Hence, different bonding processes lead to different stress states. Minimizing this stress improves the operating life of the device. Various stress-mapping measurement techniques [64-68] have been proposed to study the effect of stress on its operational parameters such as spectral position and polarization [69], [70] as well as lifetime and reliability [71], [72]. Localized stress distribution in the LD can be monitored by using photoluminescence technique. The polarization ratio of transverse-magnetic to transverse-electric light has demonstrated good agreement between the wavelength and strain. From the polarization measurement, strain arising from the packaging technique and the assembling materials can be estimated. Semiconductor lasers normally operate in the TE modes (electric field parallel to the junction). However, higher-order TM modes (electric field normal to the junction) are introduced due to the presence of stress in the active region. Stress has also been implicated as one of the factors in the short-term degradation of lasers.

Alignment Considerations

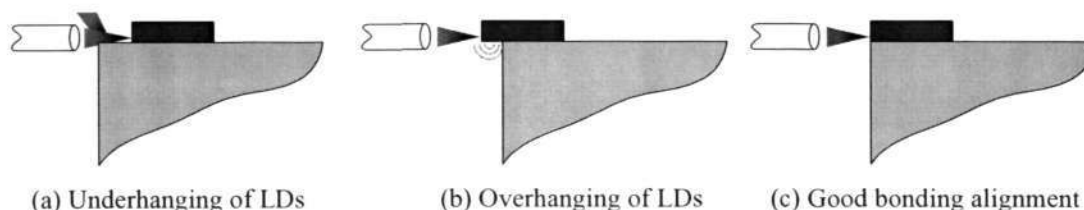


Figure 2-10 Alignment considerations for bonding of LDs. (a) Underhanging of LDs onto heatsink impaired the optical signal; (b) Overhanging of LDs onto heatsink resulted in higher temperature at the facet; (c) The LD should flush along the edge of the heatsink for optimum device performance and effective fibre coupling.

Alignment of the LD to the heatsink is absolutely critical for the face-down approach as shown in Figure 2-10. When the LD underhangs from the heatsink as depicted in Figure 2-10(a), the emission light will be interrupted. As the active region is less than $2\ \mu\text{m}$ from the surface, the laser beam diverges onto the heatsink surface easily and degrades the optical signal. On the other hand, if the LD overhangs the heatsink (see Figure 2-10(b)), the optical performance and reliability of the LD [73], [74] will be affected due to non-uniform heat transfer. Generally, the bonding alignment should observe $\pm 5\ \mu\text{m}$ accuracy as the characteristic thermal length of a LD is $5\ \mu\text{m}$ [29], [21]. As reported, the heating occurs at the emitting facet and extends inwards into the cavity length during operation. Due to the accumulation of defects at the facets, the heating was observed to occur within $5\ \mu\text{m}$ from the facets.

In addition, face-down bonding of LDs often reduces the yield significantly. Due to the proximity of the active region to the solder layer, solder bridges onto the emitting facets easily. The devices are frequently 'short-circuited' or the emitted layer beam may get obscured. These complicating issues are some of the challenges in optoelectronic packaging that deterred industries from adopting the face-down approach.

2.2.2 Existing Face-down Bonding Techniques for Semiconductor Lasers

Various face-down bonding techniques in attaching the LD onto a heatsink have been summarized in Table 1. A flip-chip interconnection technique using small solder bumps [59], [60] was introduced to resolve the alignment issues. When the solder bumps melts in the reflow process, the surface tension of the molten solder allows self-alignment and accomplishes precise chip positioning. However, thermal dissipation is compromised since heat can only be transferred through the solder bumps. Under bump metallization (UBM) must also be created on the LD and heatsink to achieve accurate alignment. To improve thermal dissipation, a vacuum-release process [75], [76] is recommended to produce a fluxless and virtually voidless solder bond. Good bonding integrity with less than 5% voids can be obtained within 1 sec. Unfortunately, this technique requires a temperature-controlled vacuum chamber, of up to 0.1 Torr, which is not available in present automated/semi-automated die-bonders.

Table 1. Comparison of various bonding techniques. The bonding parameters depend largely on the bonding technique and bonding material used.

Bonding Method	Bonding Parameters	Bonding Material	Limitations
Solder bump chip bonding [59], [60]	230 °C, 60 secs,	In-Pb	- heat transfer - additional process
Vacuum-release process [75], [76]	133.3 Pa, 1 sec	Pb37Sn63	- additional facilities
Composite solder structure [77], [78]	320 °C, 13 mins 0.276 MPa	Au-Sn	- long bonding time
Ultrasonic scrubbing [79]	310 °C, 39.2 kPa, few secs	Au80Sn20	- high stress - low yield
Bridge die bonding [56]	230 °C, 1 min	In	- heat transfer - reliability concerns
Epitaxial lift-off [80], [81]	235 °C, 30 secs, 0.345 MPa	Au80Sn20	- long bonding time
Pulsed heated thermode [82], [6]	370 °C, 5 secs, 0.375 MPa	Au80Sn20	- multi-mode lasers only - high stress
Controlled solder interdiffusion [83]	157-232 °C, 1 MPa	In-Sn	- reliance of flux - exhaustive approach - reliability concerns

Bonding of GaAs/Si chips using Au-Sn composite structures has laid a cornerstone to fluxless assembly for semiconductor lasers [77], [78]. Isothermal solidification permits good bonding integrity in the solder joint. However, the device is subjected to high bonding temperature for a long bonding duration of 13 mins. LDs are likely to experience degradation under high bonding temperature exposure for such long duration. In addition, the ridge structure does not conform to the planar bonding area and bonding homogeneity will not be attained. Ultrasonic bonding introduced by Nishiguchi et al. [79] is capable of resolving any surface irregularities in the solder joint. A good joint integrity can be achieved with significantly low bonding pressure and short bonding time. The ultrasonic energy breaks up and eliminates the oxidation layer and contamination from the connection surface. At the same time, the frictional heat generated binds the metal atoms together. Unfortunately, solder bridges onto the facet easily with this technique. In addition, the stress induced by the scrubbing process may also damage/degrade the LDs.

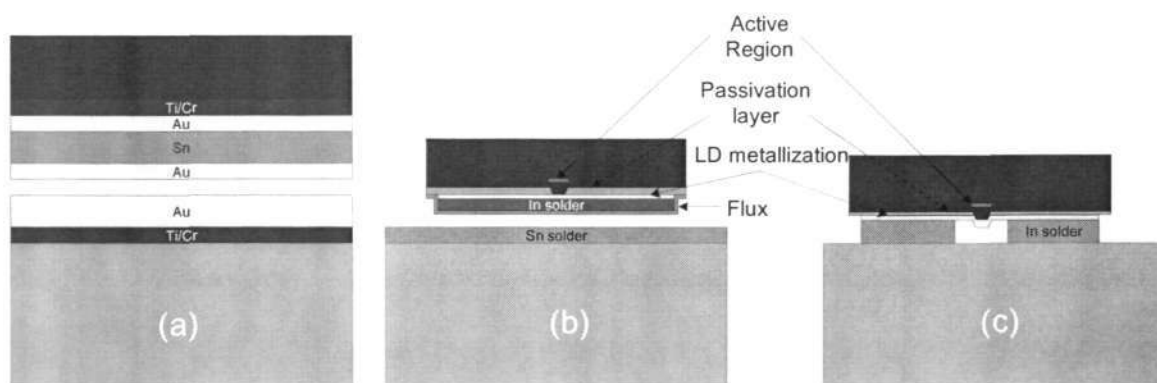


Figure 2-11 Schematic diagram of various bonding techniques. (a) Lee et al. composite structure for Au-Sn solder joint; (b) Merritt et al. approach using In-Sn solder joint; (c) Boudreau et al. bridged bonding using In solder.

Bridged die bonding [56] was introduced to reduce the associated stress, by employing a solder pattern with a gap, preventing solder from having contact with the sensitive ridge. The bridged die bond geometry is developed to exploit the advantage of face-down bonding while avoiding the stress issue. This technique does not address the thermal issues directly as the heat generated is just beneath the ridge. The heat flux generated in the active region must be re-directed to the side of the LD before traveling towards the heatsink (see Figure 2-11(c)). Mechanical integrity of the joint is also compromised. Therefore, a superior bonding metallurgical system is essential for improving the quality of the device bonding.

As such, modified bonding techniques using epitaxial lift-off [80, 81, 84] are introduced to bond devices onto substrates. A device layer structure and a solder layer are grown lattice-matched on a GaAs substrate with an intermediate sacrificial ("lift-off") layer. After lifting-off the device using a selective etching of the sacrificial layer, it can be transferred to the substrate. The solder was deposited onto the device and, hence the solder thickness can be controlled. Although the thickness of the bonding layer can be controlled to submicron accuracy, the bonding duration is evidently long. In the bonding process, a pressure cap is applied as a mechanical loading onto the device during reflow at vacuum condition. Pittroff et al. [6, 82] demonstrated face-down bonding for high-power LD arrays. Pittroff et al. uses a pulse heated thermode, controlled by Unitek Phasemaster. An AC reflow soldering can be controlled with 60 Hz of scrubbing effect. The scrubbing effect may induce distortion to the LD. For single-mode LDs, the narrow ridge width will be easily damaged or induced large mechanical stresses by the scrubbing effect. They also adopted a high bonding temperature of 370 °C, which may degrade/damage the device. In addition, their ridge widths are more than 100 µm and are

meant for multimode operation. Their bonding approach may not be applicable for single-mode LDs, which have a typical ridge width of $\leq 4\mu\text{m}$ [85].

Hitherto, a process breakthrough has been developed for face-down bonding of single-mode ridge-waveguide LDs [83]. Solder was deposited on both LD and heatsink. Flux was then applied onto the LD to prevent solder oxidation. The LDs were subsequently cleaved and bonded onto heatsink. Application of flux may leave residues that affect the optical signal. The solder joint also faces long-term reliability issues as well as misalignment after aging.

Although high quality bonds were achieved in some of the bonding techniques discussed, they may not be acceptable for real production due to cost factors. The bonding process must be modified in order to achieve good bonding integrity and obtain long-term reliability without compromising on the performance of the LDs. Hence, to maintain structural integrity within the LD, the bonding process should possess low bonding temperature and reduced bonding pressure, and shorten its bonding duration. Reducing the bonding temperature and bonding pressure lower the stress imposed on the LD and limiting the bonding duration increases the reliability of the solder joint. However, the effect of bonding parameters on the bonding integrity of the solder joint and the electrical-optical performance of the LD are not understood. Cracks and voids were observed in these solder joints [86]. Furthermore, as described by Sheen et al. [86], the microstructure evolution of Au/Sn solder joint is not fully comprehended. The solder joint was described to consist of Au-rich and Sn-rich phases. However, interdiffusion of Au and Sn can form various Au-Sn intermetallics. This will be elaborated in detail in Section 2.4.2 with the Au-Sn phase diagram.

2.2.3 Bonding Process Considerations

For bonding of optoelectronic devices, it is important to gain knowledge of the bonding process in order to improve the performance and reliability of the package. Four popular flip-chip bonding processes have been studied; Au-Sn multilayer metallization process, Anisotropic Conductive Adhesive (ACF/ACP) process, Non-Conductive Paste (NCP) process, and solder process [87]. The purpose of the bonding process is to form a joint/connection between the LD and the heatsink. Physical bonding offers contact between conductors and connection lines, while chemical bonding forms intermetallic compound (IMC). It is, therefore, necessary to form an IMC as chemical bonding between metallization and solder during reflow. This requires the soldering temperature to be higher than the melting point of the joint material. Soldering is typically initiated by the formation of an IMC, followed by diffusion and further intermetallic formation. However, the intermetallics layer can be a source of mechanical weakness in soldered joints due to its brittle cracking or delamination [88]. This can be limited by reducing the bonding temperature and bonding duration. To shorten the bonding process, the temperature must be raised rapidly as well as generate little distortion even under high temperature in order to create uniform connections. Furthermore, instantaneous bonding under high temperature raises manufacturing productivity and increases the bonding strength.

For die attachment, the key factors affecting the bonding quality are the surface quality at the bonding interface and the quality of the solder. For optoelectronics packaging, the mounting surface is required to be lapped at submicron surface flatness in order to achieve good heat transfer from the LD. In addition, the adhesion strength of a metal layer to its preceding layer is also strongly influenced by the roughness of the surface

[89]. Sufficient surface furnishing at the bonding interface is required to improve the bonding quality. As the fundamental principle of soldering is intermetallic formation, the soldering environment must also provide the condition for chemical reactions to occur. Incidentally, solders may have oxides on their surfaces. Oxidation of solders is the major difficulty in producing high quality joints. These oxide layers have very high melting temperatures ($\text{SnO} \sim 1080 \text{ }^\circ\text{C}$ and $\text{SnO}_2 \sim 1630 \text{ }^\circ\text{C}$) [90] and do not melt at the soldering temperature (typically $200 \sim 300 \text{ }^\circ\text{C}$). Thus, this forms a barrier on the solder surface and prevents the molten solder from having intimate contact with the base metal. Study of oxidation and reduction kinetics proved that with decreasing O_2 partial-pressure, good solder joint integrity can be achieved [91].

Mechanical failure may also result from thermo-mechanical stresses developed in the assembly process. During bonding, mechanical loading is applied onto the LD to create interfacial contact before solder reflow. This induces large residual stress in the ridge and active regions, especially in single-mode ($\leq 4 \mu\text{m}$) ridge-waveguide LDs with the face-down approach. Before reflow, the applied mechanical loading induces compressive stress onto the narrow ridge. This may cause structural distortion to the device, degrading the LD performance. In addition, during reflow, compressive stress is also induced onto the device due to the large CTE mismatch between the LD and the heatsink material when the bonded LD is cooled to room temperature. Hence, the mechanical pressure should be reduced to prevent permanent structural distortion to the device. The temperature profile may also affect the strain induced in the LD. During cooling, the stiff solder layer prevents relative motion between the LD and heatsink, and stresses are induced at the interface. Hence, the effect of varying cooling rates on die failure has been studied. Generally, there are three different methods to cool the device; rapid, gradual, and slow. In rapid cooling, the assembly is transferred to a cold plate immediately after

bonding with a rate of 300 °C/min. This induced large residual stress on the device as the effect of cooling rate was found to depend on the level of strain energy release rate [92]. In gradual cooling, the assembly is cooled to room temperature at 1.3-2.2 °C/min. This reduces the residual stress incurred by the device. For slow cooling, the assembly is held at elevated temperature to permit solder relaxation. High temperature creep deformation of the solder layer will further allow stress relaxation when the cooling process is controlled. The slow cooling process also shows better metallurgical effects such as diffusion and alloying [93]. However, this cooling scheme requires long bonding duration [94].

The effect of multiple furnace passes has also been investigated to improve the assembly yield [95]. The reliability of the solder joint on single die/multiple pass processing and multiple die/single pass processing have been studied to support the feasibility of multiple die devices with multiple pass processing. Localized heating at the active region also places stringent requirements on the die positioning accuracy. Bonding alignment using recognition precision is studied to enhance positioning to a submicron level [53]. Fiducial marks have been created on the surfaces of the LD chip and heatsink to correct the effects of heat expansion during the bonding stage.

2.3 Bonding Requirements

There are various types of media used for interconnections in electronic packaging i.e. metal-filled epoxy and glass, and solder [96-99]. Depending on the application and its processing environment, different bonding media will be used accordingly.

Table 2. Comparison of various bonding media used in advanced packaging.

Die Attach Classification	High Modulus (stiff)	Low Modulus (flexible)
Electrical/Thermal Conductive	Gold eutectics, silver filled glass	Silver filled polyimides, silver filled epoxies, tin-lead based solders, indium-based solders
Thermal Conductive	Tin oxide-filled glass, indium oxide filled glass, beryllia filled glass	AlN-filled epoxy, alumina-filled epoxy
Non-Conductive	Unfilled glass	Unfilled epoxies, epoxy silicone, polyimides

Both metal-filled glass and epoxies have poor thermal conductivity and thus poor heat dissipation. While metal-filled glass produces high stress on the device due to very high processing temperature and lack of plastic deformation, metal-filled epoxies do not induce high stress because they deform visco-elastic at low stress.

At present, the most widely used solder is still lead-tin (Pb-Sn) alloy, but due to the potential environmental hazards caused by lead (Pb), lead-containing solders have been banned in applications involving water and food [100]. It may eventually be banned in electronic products as well. There have been many efforts in developing alternative solders [97]. Subsequent sections will discuss two of those alternatives used in optoelectronic applications; soft indium (In) solder and hard gold-tin (Au80Sn20) alloy. The soldering process usually requires the application of flux to improve the wettability of the bonding area [56]. This has worked very well over many decades [101] until the discovery and confirmation of severe ozone depletion by Chlorofluorocarbons (CFC's). Another concern in using fluxes is attenuation/defection of the optical signal as it can leave residues on components that compromise the integrity of the optical path within the package. This further bolsters fluxless processing for optoelectronic packaging [102].

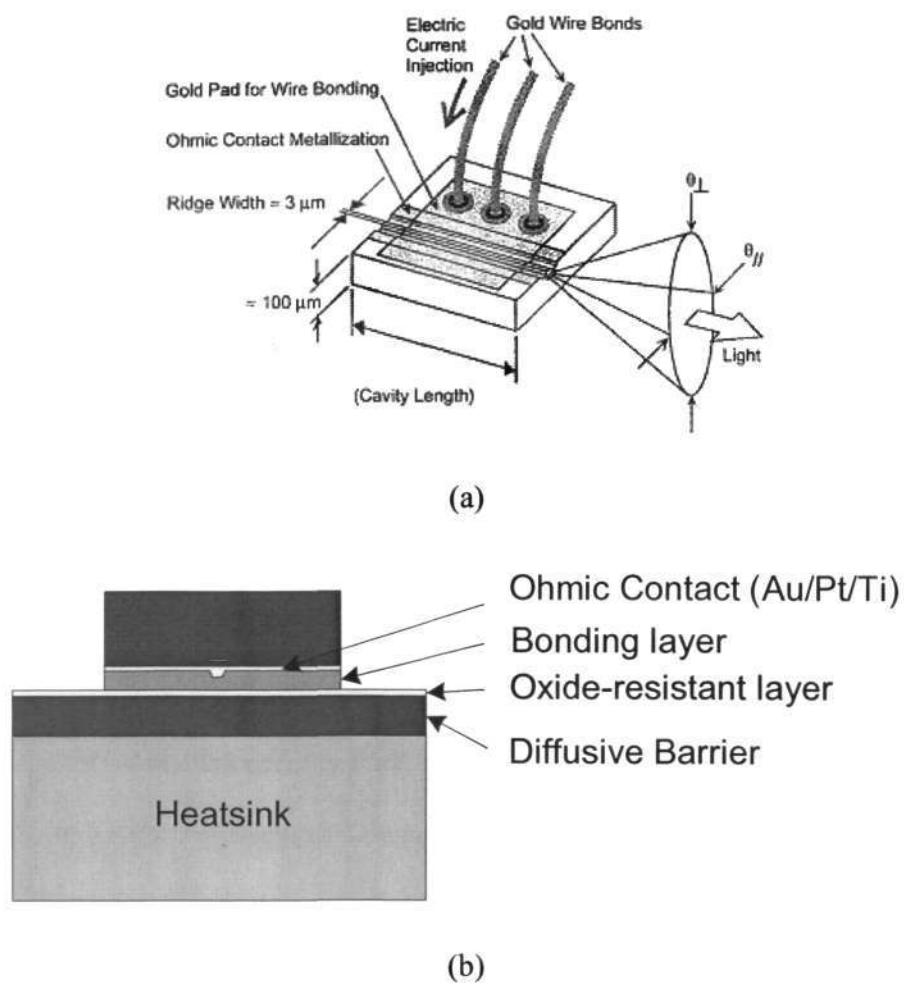


Figure 2-12 (a) Schematic diagram of ridge-waveguide LD and its diverging output beam profile; (b) Typical cross-sectional view of multi-layer metallization in packaged LD.

Other than the environmental considerations, the requisites for packaging of laser chips involve: (1) compatibility of high temperature solders with metallization on the heatsink & epitaxial chip side, (2) material of the package heatsink, (3) minimizing thermal expansion mismatch and (4) connection of the chip pads to the package leads. For attachment of the laser chip to the package heatsink, the metallization must satisfy the following requirements:

- Sufficient adhesion of LD [75]
- Low material strain for maintaining mechanical durability [103]
- Thermal stability at device operated temperature [104-106]
- Process manufacturability

- Low electrical contact resistance for low loss and high performance [107]
- Low thermal impedance for effective dissipation of internally generated heat [108], [109]

Table 3. Properties of materials used in optoelectronic packaging [110, 111].

Requirement	Mounting Components		Adhesive & Diffusive Barrier			Bonding layers			
	GaAs	Cu	Cr	Ti	Ni	In	Sn-37Pb	Sn-3.8Ag-0.7Cu	Au-20Sn
Density [g cm ⁻³]	5.31	8.92	7.14	4.50 7	8.90 8	7.31	8.36	7.5	14.7
Melting Pt [°C]	1238	1084	1907	1668	1455	156. 6	183	21 7	278
Young Modulus [GPa]	82.68	130	279	116	200	11	31.0 3	-	68
Electrical Resistance [μΩ.cm]	-	1.7	12.7	40	7	8	0.14 6	13	-
Thermal Conductivity [W/cm/°C]	0.44	3.98	0.94	0.22	0.91	0.82	0.50 9	-	0.58
CTE [K ⁻¹ X 10 ⁶]	5.8- 6.4	16.5	4.9	8.6	13.4	32.1	25	-	16
Shear Strength [MPa]	-	-	-	-	-	-	23	27	50
Poisson Ratio	0.31	0.34	0.21	0.32	0.31	0.44 5	0.4	-	0.40 5

However, all the above-mentioned requirements cannot be satisfied by a single metal layer and hence the necessity for multi-layer metallization at the bonding interface as shown in Figure 2-12(b). Table 3 provides some useful information on the selection of each layer.

2.4 Classification of Material

2.4.1 Heatsink [112-116]

Copper (Cu) is by far the most common heatsink material for power modules due to its high thermal conductivity, easy mechanical handling, galvanic plating, amenability and moderate pricing. The high thermal conductivity can lead to longer lifetime and reduced linewidth of LD. However, the coefficient of thermal expansion (CTE) mismatch between the heatsink and LD is the primary disadvantage in using copper. This mismatch generates a significant amount of thermal stress and mechanical strain on the bonding layer. Consequently, the interface between the LD and the heatsink is one of the primary failure sources of a power module. At present, substitution of the Cu heatsink is significantly more expensive. Thus, in a cost-driven market, it is unlikely that expensive heatsink materials would readily replace conventional low-cost Cu plate. Consequently, in this research, Cu is selected as the heatsink material.

2.4.2 Bonding Layer (Solder)

Table 4. Comparison of various solder materials used in photonics packaging applications and their physical properties [117].

Solder	Physical Properties				
	Melting Point (°C)	Tensile Strength (MPa)	Creep Resistance	Thermal conductivity (W/m/°C)	Electrical Resistivity (μΩ.cm)
Hermetic Sealing: Eutectic die attach – fiber location – fluxless soldering					
Au88Ge12	356E	185	Excellent	44	-
Au80Sn20	280E	276	Excellent	57	16
Opto-package assembly step soldering – non amenable to fluxless soldering					
Sn63Pb37	183E	32	Moderate	50	15
96SnAgCu	215-225	~40	High	-	Na
Fiber ferrule joining					
Indium	156	2.5	Poor	80	8.8

In97Ag3	146E	5.5	Poor	73	7.5
In52Sn48	118E	11.9	Low	34	15
Component Anchoring					
Bi58Sn42	138E	55	Moderate	19	35
Bi40Sn60	138-170	-	Moderate	21	38

In a typical LD butterfly package, different solders are used at various assembly processes such as die attachment, assembly step-soldering, fiber-ferrule joining, component anchoring, and hermetic packaging. The table below shows some of the solder materials used in the photonics packaging applications and their physical properties. For die attachment of LDs, Au80Sn20 and indium solders are frequently utilized in the photonics industries.

Solder is used for the purposes of electrical interconnect, mechanical support, and heat dissipating channel. Solders are usually categorized into 2 types, hard solder and soft solder. In general, hard Au80Sn20 solder is used for high temperature assemblies, while soft In solder is meant for lower temperature assemblies [118, 119], [119]. Hard solder [120] has very high yield strength, and thus incurs elastic rather than plastic deformation under stresses. Soft solder, on the other hand, has very low yield strength and incurs plastic deformation under stresses. The decision to use soft (In) or hard (Au80Sn20) solder is based on the optimization of a number of properties, including solder strength, solder migration, creep, fatigue, whisker formation, stress, thermal expansion, liquidus temperature, and thermal conductivity of each solder type.

In optoelectronic applications, semiconductor lasers exhibit low fracture strength and are easily damaged by stress [121-123]. Hence, soft solders, such as In and In-based alloys, are used widely in optoelectronics die attach applications such as LDs and photonic switches. It is quite ductile and can help release the stresses developed in a structure through plastic deformation. Their capability to deform plastically helps to relieve the

stress developed in the bonded structure and prevents device fracture. However, this makes soft solder subject to thermal fatigue and creep rupture, causing long-term reliability problems [124-126]. The deterioration of In solder is thermally enhanced by the reaction between In atoms and Au atoms. The diffusion of Au atoms into the In layer forms Au_3In , AuIn , or AuIn_2 intermetallics. They are also attributed to solder instabilities like whisker growth, void formation at the bonding part, and diffusion growth [127-131]. Growth of In whiskers may short the electrical connection and obstruct its optical beam. Furthermore, thermal and electrical resistances of In-bonded devices increase during storage and aging [132-134]. In optoelectronic applications, the LD modules are usually required to have long service lifetime. Hence, bonding of LDs using soft solder face impending reliability problems [124, 135, 136].

In applications where creep cannot be tolerated, eutectic $\text{Au}_{80}\text{Sn}_{20}$ alloy can be replaced to overcome such instabilities [52]. Accordingly, it has good thermal conductivity and is free from thermal fatigue and creep movement phenomena [137]. Unfortunately, hard solder does not help release the stresses developed because of low plastic deformation. To comprehend the bonding principle, the binary phase diagram and intermetallic compounds (IMCs) of Au-Sn are briefly reviewed. The binary Au-Sn equilibrium phase diagram [138] consists of four different stable IMCs as well as two eutectic and at least three peritectic reactions. The eutectic that forms at $217\text{ }^\circ\text{C}$ (93.7 wt% Sn) is known to be brittle with Sn and AuSn_4 domains. Intermetallic compounds like AuSn_2 and AuSn_4 have negative influence on the fatigue life. On the contrary, the melting point of Au-rich eutectic $\text{Au}_{80}\text{Sn}_{20}$ is $280\text{ }^\circ\text{C}$. This eutectic point has a reaction $L \leftrightarrow [\delta + \zeta]$, and is of great interest as a soldering material. The phases of interest for $\text{Au}_{80}\text{Sn}_{20}$ eutectic solder are ζ' (Au_5Sn), ζ , and δ (AuSn), which will be described in more detail.

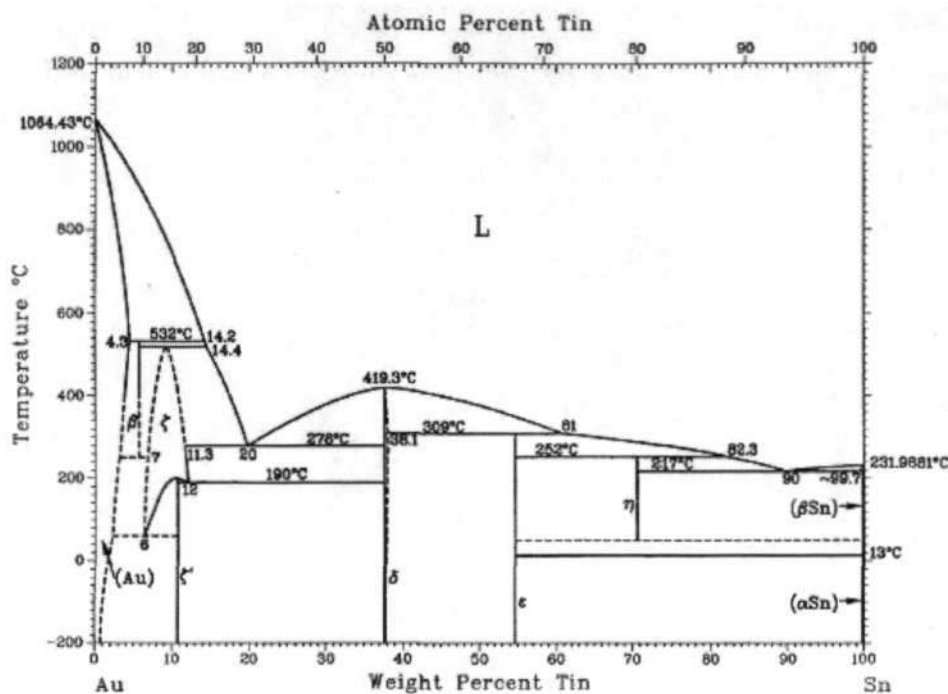


Figure 2-13 Gold-Tin binary phase diagram [139].

The δ phase, which has an hexagonal cubic packing (hcp) crystal structure, exists from the peritectic $\beta + L \leftrightarrow \zeta$ from 9.1 at.% Sn at 521 °C to 17.6 at.% Sn at 280 °C, and 13.9 at.% Sn at 190 °C [140]. It has good mechanical properties, increased thermal conductivity and excellent reliability. The ζ (Au₅Sn) phase has a composition of 16.7 at.% Sn, and exists up to 190 °C. At temperatures lower than 190 °C, the ζ phase is transformed to ζ' phase, an extension of the ζ phase at low temperature [141]. On the other hand, the δ phase or AuSn is a hexagonal IMC with a melting temperature of 419.3 °C. It is a non-stoichiometric compound with a homogeneity range between 50.0 and 50.5 at.% Sn and can be designated as $Au_{(1-x)}Sn_{(0.00 \leq x \leq 0.02)}$.

Au80Sn20 soldered devices have been successfully tested without measurable degradation after 10,000 power cycles of 40 °C to 140 °C [97]. LDs bonded using Au80Sn20 solder also observed good aging characteristics [132].

2.4.3 Diffusion Barrier [142]

In a solder joint, the major concern is the formation of IMCs caused by diffusion of copper atoms from the substrate to the joint. The growth of intermetallics makes the solder joint less ductile and less capable of releasing stresses through plastic strain. As a result, the chip may crack under thermal or mechanical cyclic loading conditions. Prevention of copper diffusion is needed in applications as they proved detrimental to the function of solder connection. This undesirable diffusion growth is of particular technological concern since it is always ongoing and may cause cracks and delaminations especially in the presence of residual stress. It continues to grow, though much more slowly, during storage and service. Consequently, the composition, microstructure and physical properties of the joint change within the device life. The formation of such IMCs can be avoided by coating the surface of the heatsink with a diffusion barrier. This will eliminate the formation of IMCs by its physical presence and lower its degradation rate. This blocking function can suppress the growth of intermetallics such as CuIn and Cu_9In_4 in the case of In solder, and Cu_6Sn_5 and Cu_3Sn for Au80Sn20 solder.

In industrial applications, nickel (Ni) is plated over Cu in numerous applications due to its low cost and process manufacturability. Ni has superior thermal and electrical conductivities [143] as compared to other potential barrier metals such as Chromium (Cr) and Platinum (Pt). Ni is also found to have limited mutual solubility rate of Ni in Au at temperature below 350 °C, as well as a low solubility rate of Ni in Sn-based solders [144], [145]. After these considerations, Ni plating over the Cu heatsink is adopted.

2.5 Conclusion of LD Packaging Technique

Based on the stringent requirements in optoelectronics packaging, the cost in the development of LD packaging is significantly elevated. As such, there is not much comparative study for packaging of LDs [6, 7]. To create cost-effective packaging studies, diced Si/GaAs wafers are utilized in place of LDs to simulate the LD packaging process [76-78, 146]. Integrity of the solder joint has been reported with metallurgical and mechanical investigations. These studies emphasized the microstructure evolution and intermetallics growth, affecting the bonding integrity under accelerated reliability testing conditions [88, 147-149]. In addition, these investigations are based on different bonding material, different bonding processes, and different bonding parameters [79, 81, 82, 88, 90, 147-150]. Thermosonic, ultrasonic and thermo-compression bonding have been introduced. With different bonding materials used, the bonding temperature ranges from 160 °C to 370 °C, bonding pressure ranges from 39.2 kPa – 1 MPa, and bonding duration ranges from a few seconds to several minutes.

In general, there is a lack of systematic study of the bonding process, performance, and reliability. A practical approach must be adopted with metallurgical and mechanical investigations of the bonding interface and electrical-optical-spectral evaluation of the LD performance. In order to obtain a highly reliable solder joint, the bonding process has to be optimized because the joint is strongly dependent on the initial microstructure. Optimization of the bonding process also helps to facilitate possible industrial volume production. The processing parameters and conditions (reflow environment) need to be tailored to minimize the void content and/or microscopic irregularities in the bonding layer, and to increase the homogeneity of the bonding layer for maximum heat transfer. Furthermore, comprehensive comparison of different bonding techniques is also required

to identify the optimal bonding technique. Since the performance of a semiconductor laser is largely dependent on its thermal management, theoretical analyses on key LD performances are also required to understand the intrinsic properties of the LD. Numerical modeling of packaged LD is needed to understand the thermal behavior of bonded LDs better. These theoretical understandings can validate the experimental findings in terms of the LD performances.

Based on the literature review, development of an optimized bonding technique need to be introduced to alleviate current packaging challenges in optoelectronics applications. Destructive metallurgical and mechanical examinations of the package should be carried out to observe structural integrity at the solder joint. Although metallurgical and mechanical studies of the solder joint are mandatory to achieve good bonding integrity, parametric evaluations of the packaged LDs are also essential to ensure performance optimization. The intrinsic behaviors should be uncovered to improve the electro-optical properties of LDs. The functionality of bonded LDs should also be discussed. Device functionality and performance optimization could be obtained from these investigations. Long-term reliability testing of bonded LDs should also be carried out to observe long operational service life of the packaged LDs. Since the LD performance depends largely on the heat generation and means of dissipating it, the thermal behavior of LDs as well as temperature distribution of the package should also be comprehended. A multi-scale simulation exercise should be used to explore and identify the physics of heat generation and heat transfer of bonded LDs.

CHAPTER 3

EXPERIMENTAL TECHNIQUE

3.1 Preparation of Cu Heatsink

Diced Cu plates of 5 mm by 5 mm by 3 mm were treated with electroless nickel (Ni) and gold (Au) plating. Electroless plating is a selective autocatalytic metal deposition process based purely on chemical reaction. Its efficient and simplicity benefits lead to substantial cost reduction in the overall metallization process. A sequence of electroless chemical treatments have been established [151] as shown in Figure 3-1.

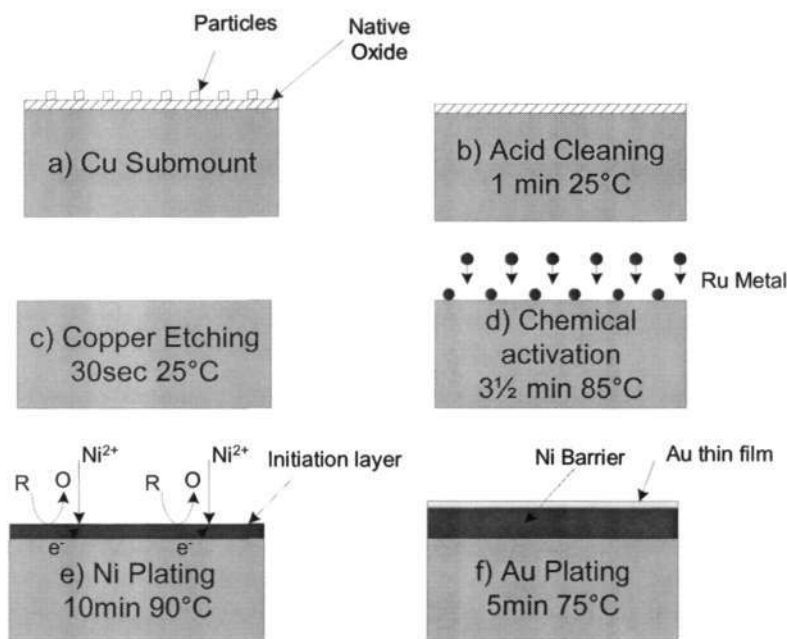


Figure 3-1 Development of an electroless plating technique. a) After surface polishing, residues and oxide remains on the surface of the copper; b) An acid solution removes the residues from the surface; c) Native oxide is etched off with a micro-etchant; d) Deposition of Ru metal behaves as a chemical activation for Ni plating; e) Ni is strongly absorbed on the Ru thin film accompanied by dissolution of Ru by simple immersion; f) Ion exchange between Ni and Au ion in the solution.

Gross surface preparation of Cu heatsinks promoted better adhesion and reduced particles/contaminants. KSN-Z2 Acid Cleaner, an acid cleaning process, is designed to remove dust and organic residues from Cu as a first stage surface preparation because adhesion and homogeneity of electroless metal deposits suffer if the surface is not sufficiently clean. The next step, namely deoxidizing, is crucial, because if the native oxide is not removed completely from the Cu surface, a subsequent deposit becomes non-uniform. A simple wet chemical etching technique such as KSN-SE Chemical Polish/Microetch fitted easily into the process line. This micro-etchant was aggressive enough to penetrate through the tenacious oxide barrier even at room temperature. It produced a leveled surface of uniform texture providing an ideal surface for Ni/Au plating. Prior to electroless Ni plating, chemical activation of Ruthenium (Ru) is necessary since Cu is not catalytic to chemicals. The Cu heatsinks were immersed into Planar Pre-initiator XL. Planar Pre-initiator XL is a metallic immersion coating that ensures complete coverage of Cu areas. The areas with Ru deposit would be sensitized and Ni can then be deposited.

Electroless Ni deposit not only sealed the Cu surface as a diffusion barrier layer, it also provided hardness, mechanical strength and solderability to the bonding pad. Essentially, Ni was deposited initially by ion exchange or displacement reaction aided by the reducing agent. Once initiated, the process autocatalyzed itself to continue Ni deposition at a rate depending on the temperature and pH of the solution. This Ni plating solution produced a phosphorous (P) content of ~10wt% in the plated region. The immersion Au plating process using Super MEX #250 Make Up solution was specifically developed for plating onto electroless Ni. It provided pure Au deposit by ion exchange between the substrate

metal and Au ions in the solution. The Au layer provided oxidation resistance and improved its wettability for the underlying Ni during soldering.

3.2 Bonding Process

After the plating process, the laser diodes (LDs) were bonded onto Cu plated specimens. During bonding, the LDs were exposed to high temperature. To prevent thermal shock and device degradation, the bonding time should be restrained. When the solder was at its molten stage, its wettability improved and good joint integrity could be achieved within a short duration. In order to produce high bonding quality, the stage was encapsulated as shown in Figure 3-2. This encapsulation behaved as a cover gas since solder preforms were susceptible to oxidation prior to the bonding cycle. To ensure good wetting, the reflow step was usually carried out with the use of reduction gas or O₂ purge gas since the surrounding environment influenced the wetting process and solder joint quality [91, 152]. With the stage opening at the top, Argon (Ar) gas was utilized as purge gas. Ar gas would be retained in the stage while O₂ and N₂ would be purged because Ar is significantly denser. Accurate bonding alignment is also essential for optimal LD performance. Digital image correlation technique [153], [154] was used to align LD onto the edge of the Cu heatsink.

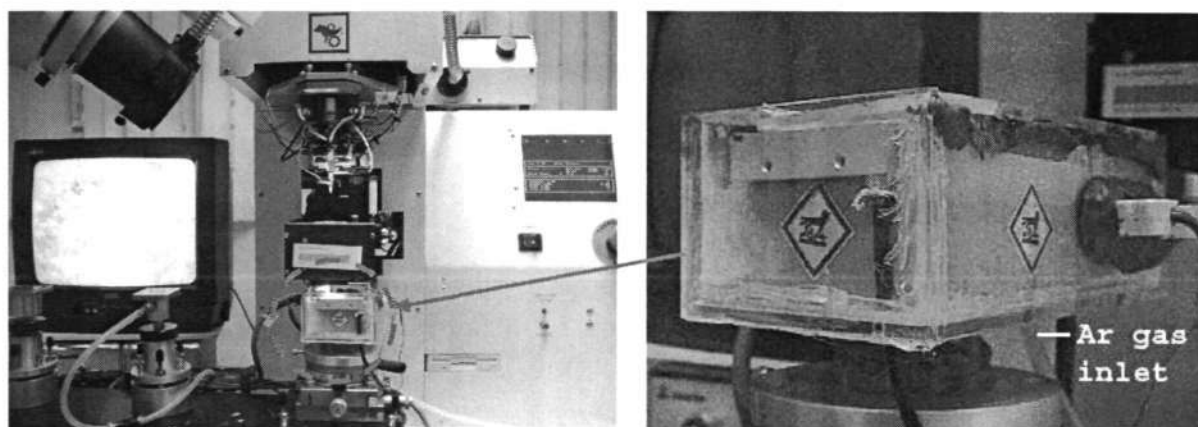


Figure 3-2 Die bonder with stage encapsulation. Ar gas is flushed into the stage to ensure good wettability.

The modified bonding process was conducted using semi-automatic die-bonding equipment (Semiconductor Equipment Corp. Model 860). The LD was picked up by a vacuum tool, positioned and pressed against the heatsink that is fixed by vacuum on the bonding stage. For soldering, the LD and heatsink were heated separately by the tool and the bonding stage.

The modified bonding process can be summarized as follows:

- 1) The bonding stage is filled with Argon (Ar) gas to reduce oxidation.
- 2) The laser chip is picked up from a waffle pack by a vacuum pickup collet. The heatsink is held onto the bonding platform via vacuum.
- 3) The collet is heated to a considerable temperature (~ 60 °C) while the stage is fixed at the processing temperature. The heating rate approximates 18.8-20.0 °C/sec. This processing temperature must be higher than the melting temperature of the solder, but sufficient to achieve good wettability and avoid premature failure.
- 4) A eutectic Au80Sn20 solder preform is picked, aligned and placed onto the edge of the heatsink.

- 5) The chip is then aligned to the edge of the heatsink using a digital image correlation technique.
- 6) The chip is pressed gently against the molten solder. Administration of bonding pressure is applied to create sufficient contact at the bonding interface.
- 7) Upon contact, the collet is heated further to ~ 100 °C to reduce thermal shock impact onto the device. The progressive heating at the LD helps to prevent device degradation. The duration of solder reflow is determined by the diffusivity of the bonding material.
- 8) The pickup collet releases the chip and the bonded sample is gradually cooled to 100°C before extraction from the Argon-filled stage.

3.3 Characterization of Semiconductor Lasers

After bonding, the short-term and long-term performance stability of the LDs were examined. Since the quality of the bonding area is critical to the operation and reliability of LDs, electrical and optical performances of bonded LDs should also be observed. Electrical performance was studied to analyze the contact metallization and integrity of the heterostructures while the optical performance was studied to observe the maximum capability. Hence, a LD characterization system was developed with a TEC controller, a peltier-controlled LD holder, a LD driver, an Optical detector and a Power meter as depicted in Figure 3-3. A classification test using a ILX lightwave laser diode parametric analyzer LPA-9084 was programmed to screen LDs for functional quality and failure analysis. During testing, a computer was used to automate the instrument control and data acquisition process. The thermoelectric Controller (TEC) was used to regulate the heatsink temperature with 0.1 °C accuracy. Upon temperature stabilization, the LD Driver provided a continuous wave (CW) current sweep of 1mA step size at 1msec interval. The

Integrating Sphere accepted direct optical input from the laser and provided accurate light power measurement without being sensitive to polarization mode or beam profile at the end of the fiber. The Photodiode Power Meter measured the current flow at the back facet of the Photodetector, combined with the Integrating Sphere to directly measure optical power.

To attain accurate results, the LD holder used a low resistivity contact pin and peltier-controlled temperature module. Good temperature control is required to minimize the temperature fluctuation during long hours of testing. The thermistor was calibrated with temperature accuracy of $\pm 0.1^{\circ}\text{C}$. This is crucial since the properties of the LDs are dependent on the operating temperature.

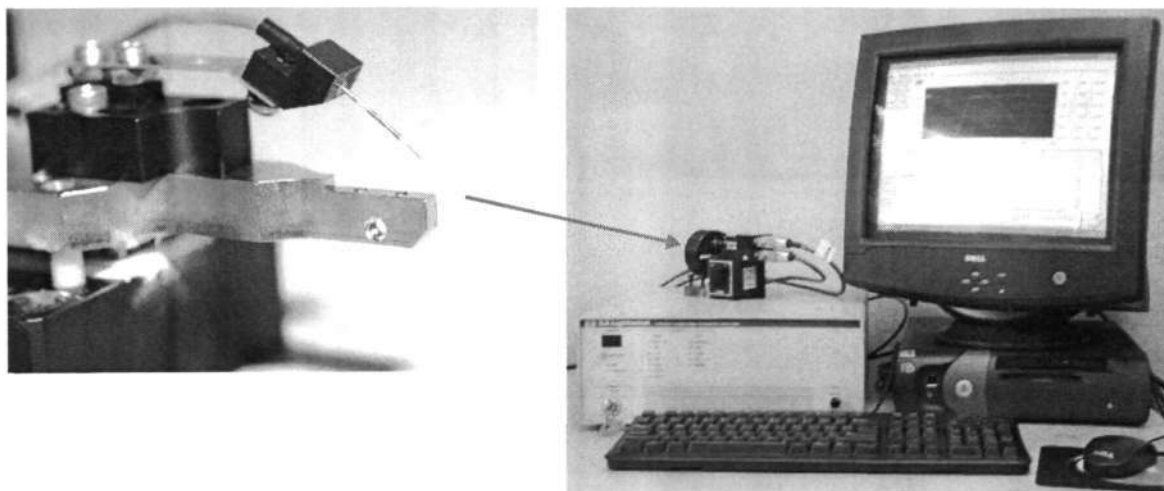


Figure 3-3 Schematic diagram of LD holder in LD characterization system. The LD holder provides good electrical contact & stable temperature control.

3.4 Microstructural Preparation

Metallurgical examination of the package is also a basic necessity to inspect the bonding quality. Although Scanning Acoustic Microscope (SAM) could provide a quick and

nondestructive evaluation of the bond quality, it falls short in resolution ($\geq 20 \mu\text{m}$) where failure analysis is concerned. Optical observation of the bonding interface gave good indications to the reliability of the joint, by studying various possible failure modes of the assembly, which include brittle fracture of the die, delamination, and thermal fatigue of the solder joints. The standard procedures of metallographic preparation were sample mounting, grinding and polishing, chemical etching, microscope examination and measurements. The bonded samples were cold-mounted with epoxy for 8 hrs and polished (KEMET Inc.). The mold was ground using silicon carbide (SiC) papers of grit 600 to expose the interface. SiC paper of grit 1200 was then used to further grind the materials until the cross-section of the sample was visible as seen in Figure 3-4(a).

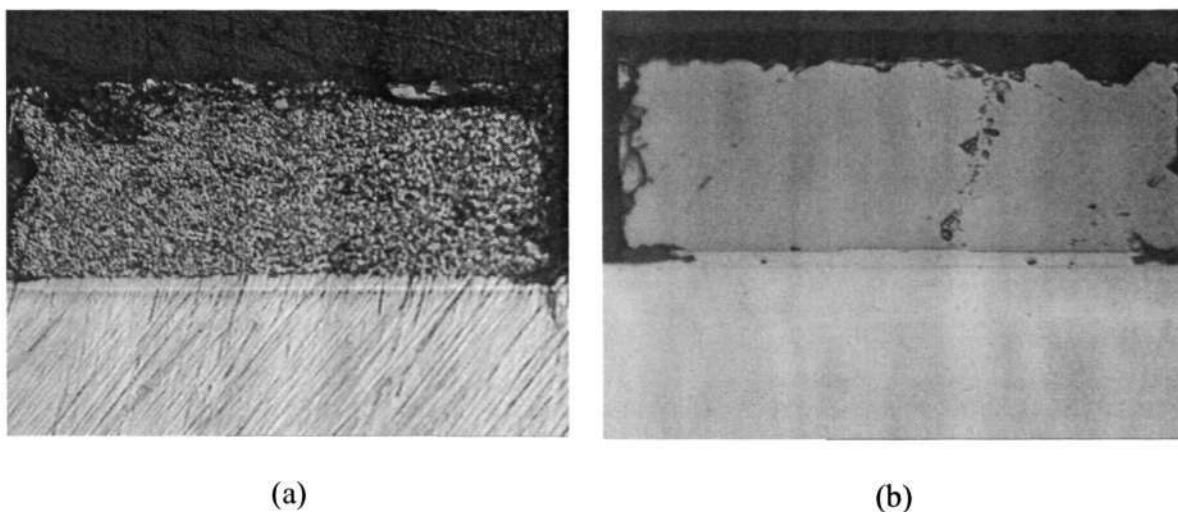


Figure 3-4 Cross-sectional view of (a) grinded and (b) polished samples.

Next, the sectioned area was polished with Type K alumina suspension (liquid diamond) of $3 \mu\text{m}$, $1 \mu\text{m}$, and $0.5 \mu\text{m}$ sequentially until the interface and internal microstructure of the solder joint can be seen clearly under an optical microscope. A final touchup using polishing suspensions (COL-K) allowed better surface finishing for microstructural analysis as shown in Figure 3-4(b). The samples were then examined with a combination of optical microscope and SEM/EDX. The composition of each phase was determined

using the JOEL JSM-6360A SEM, operating at 20 ekV. For every data point, at least 5 measurements were made.

3.5 Mechanical Testing

To study the mechanical strength of the bond, shear testing according to MIL-STD-883C (Method 2019) [155] was performed till complete fracture of the joint. Shear Test Analysis STA-3100 (Keller Technology Corps.), with a 1 kg transducer, was used to perform die shear tests. Figure 3-5 shows the submount being held onto a 5 kg vacuum stage and the shear tool position relative to the die (to prevent scraping of the submount's surface). As the mechanical properties of the solder joint were sensitive to temperature and strain rate, the American Society for Testing Materials (ASTM) shearing speed of 0.25 mm/sec to 6 mm/sec was recommended to avoid creep deformation behaviors. The shear rate was selected to be 3 mm/sec. In cases where there was evidence of less than 50% adhesion of the die attach medium (failure criteria 3.2b) [155], or no evidence of adhesion (failure criteria 3.2c) [155], the shear strengths were < 300 g (1.25X) or < 400 g (2.0X) respectively for joint size smaller than 0.32258 mm². The soldering pad for these LDs is 0.18 mm². Residues attached in discrete areas of the die attach media shall be considered as evidence of good adhesion.

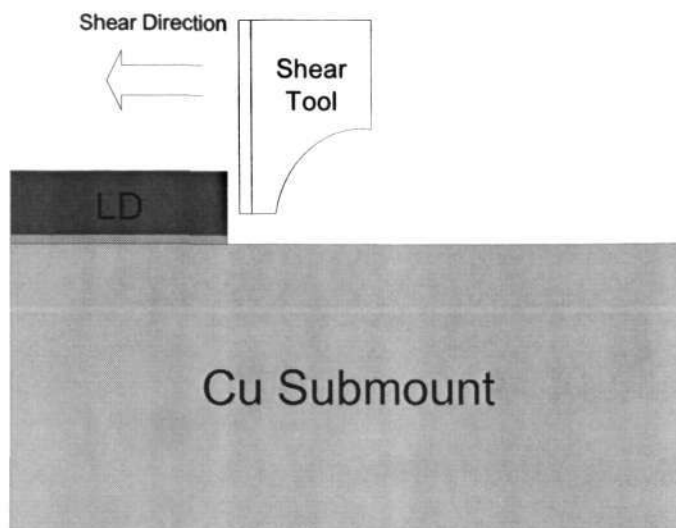


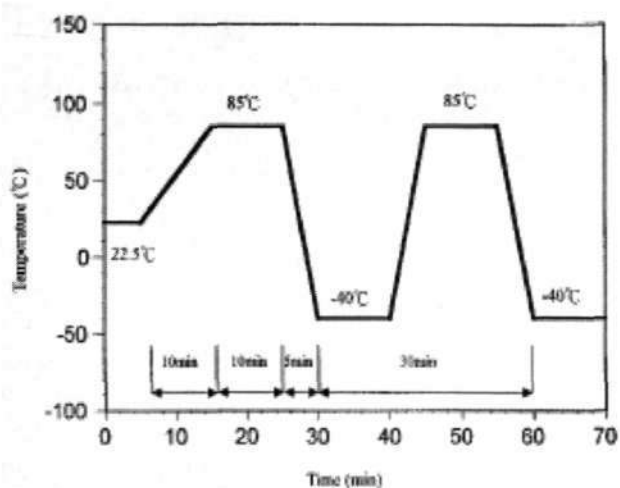
Figure 3-5 Shear Test. The shear tool was elevated from the surface to ensure consistent shearing measurement.

3.6 Reliability Testing

The packaged device must withstand temperature cycling, resulting in coefficient of thermal expansion (CTE) mismatch induced stress on component interconnections. The submounts were placed into a furnace that repeats thermal cycling conditions specified by the Bellcore Reliability Assurance Practices of TA-TSY-000983 [156] as shown in Figure 3-6. During temperature cycling test, the temperature was changed from $-40\text{ }^{\circ}\text{C}$ to $85\text{ }^{\circ}\text{C}$ within 40 min per cycle. The ramp rate was $12.7\text{ }^{\circ}\text{C}/\text{min}$ and the dwell time was greater than 10 min for a total of 500 cycles. This temperature change allows sufficient screening at the intended temperature extremes. During temperature ramping, elastic-plastic deformation was performed followed by creep deformation at the dwell duration. The mean temperature was $22.5\text{ }^{\circ}\text{C}$ and the cyclic frequency was 36 cycles/day.



(a)



(b)

Figure 3-6 (a) Thermal cycling chamber; (b) Temperature profile using Bellcore Reliability Practice - Thermal cycling Test [156].

All the submounts were tested before the start of thermal cycling, at scheduled intermediate checkpoints, and at the end. Intermediate monitoring of the electrical, mechanical, and material characterizations identified the failure mechanism in the package. Electro-optical characterizations were monitored as indications of defects and to supplement information for future failure analysis. The effect of temperature cycling on the joint strength was also investigated. Metallurgical studies on the interfacial intermetallic growth, and coarsening of intermetallics, and orientation evolution of intermetallics were also explored. These studies provide useful design guidance for understanding and evaluating the solder joint strength under temperature cycling tests for LD packaging applications.

CHAPTER 4

DEVELOPMENT OF MODIFIED FACE-DOWN BONDING PROCESS FOR PACKAGING OF RIDGE-WAVEGUIDE LASERS

4.1 Introduction

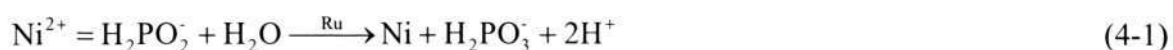
Reliable, reproducible, high yield packaging technologies are essential to meet the cost, performance, and service objectives in optoelectronic system. From the literature survey, face-down bonding approach is recommended for effective heat transfer. A modified face-down bonding technique for single-mode ridge-waveguide LDs is introduced and the effect of bonding parameters on the bonding integrity of the solder joint and the LD performance are analyzed.

4.2 Electroless Ni/Au Plating

Attachment of LDs onto a heatsink required the two surfaces to be flat and smooth in order to provide good thermal and mechanical contact. However, all surfaces have microscopic roughness as well as macroscopic non-planarity. Hence, the uniformity across the heatsink is vital in achieving proper contact during the bonding process. Irregular stress can incur on the LD due to oblique bonding. To acquire good bonding contact, the height accuracy of the heatsink was selected to be $\pm 2.5 \mu\text{m}$.

Based on the plating guidelines from MacDermid [157], the Cu submounts were cleansed with KSN-Z2 Acid Cleaner for 1½ min and etched with KSN-SE Chemical Polish/Microetch solution for 30 s before plating. The Cu submounts were then dipped into Planar Pre-initiator XL, Ni plating solution and Super MEX #250 Make Up solution

sequentially. The plating duration was 3½ mins, 9 mins, and 5 mins respectively. The chemical interaction of the electroless Ni/Au plating process was first investigated. Chemical deposition of nickel metal with hypophosphite solution meets the Reduction-Oxidation potential criteria without changing the mass of the substrate:



Since electroless nickel deposition was accompanied by hydrogen evolution, hypophosphite-based electroless nickel solution would not represent the true electroless plating reaction. As shown in Figure 4-1, a small amount of phosphorous content was found within the nickel layer. This Ni/P solution produced a phosphorous (P) content of ~10wt% in the plated layer.

To facilitate proper plating control, the thickness and surface texture of the plating process were analyzed. Cross-sectional Scanning Electron Microscopy (SEM) observation of the plating process was conducted to identify the plating thickness to the underlying Cu layer. An approximate 2-3 µm thick of Ni/P was deposited onto the Cu heatsink. This layer behaved both as adhesion layer to the copper substrate and diffusive barrier for the solder alloy from interacting with the base metal (Cu). Immediate coating of 0.1µm gold layer prevented oxidation and improved solderability. Neither visible (gross) voiding nor a broad Au reaction layer [158] could be observed from the plating process. The uniformity and quality of the plating deposition were also important to the development of the packaging process. Further surface characterizations using SEM and

optical interferometer were carried out to ensure that the plating process improved the surface texture and surface irregularities for ease of packaging.

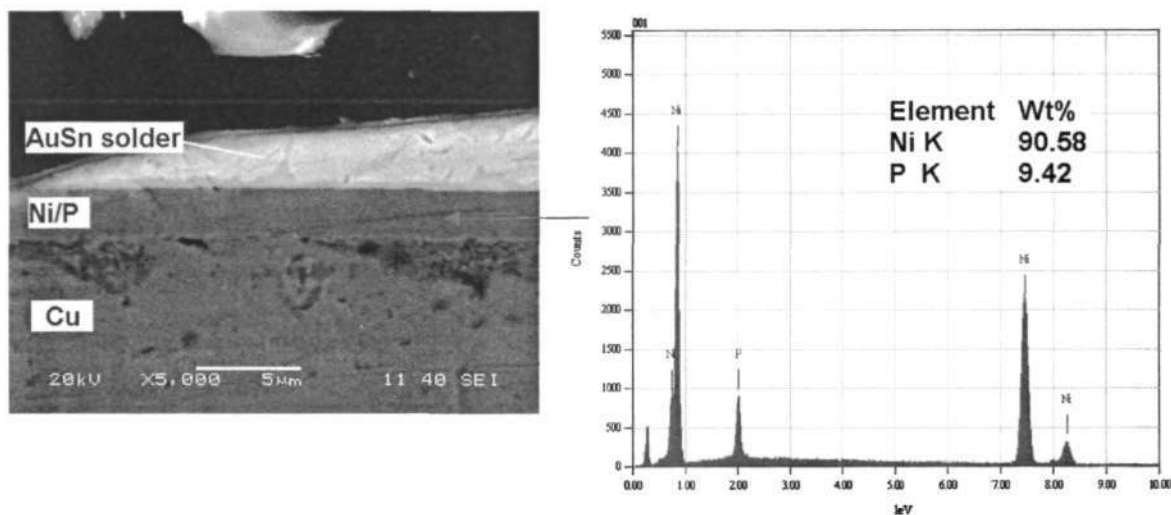


Figure 4-1 Typical cross-sectional view of Ni/P layer, sandwiched between Au/Sn solder and Cu heatsink. EDX analysis showed ~10wt.% of P content in the Ni layer.

The surface texture at each plating stage was first studied. As shown in Figure 4-2, the surface texture after the plating process improved significantly and created a conducive surface for solder reflow. Polishing striations and random pores could be observed on the Cu surface. The tiny pores were cavities embedded within the Cu plate as shown in Figure 4-2(a). As the Cu was not catalytic to chemicals, Ru was utilized as a chemical activation source for subsequent Ni plating [159]. A thin layer of Ru covered the entire Cu surface. Random distribution of the Ru deposit could be observed on the Cu surface. Thereafter, Ni plating replicated the underlying features of the Cu surface, with random nucleations shown in Figure 4-2(c). The nucleation was caused by sensitization with the Ru deposit. During Ni plating, the Ni ions from the solution were deposited initially by displacement reaction with the Ru deposit, followed by autocatalytic deposition. The striations were observed to reduce significantly as the plating thickened and the cavities were completely covered by the Ni layer. The texture of the immersion Au was almost

exactly similar to that of the underlying Ni surface except that the amount of nucleations was visibly reduced. This is important as wettability is dependent on to the surface texture.

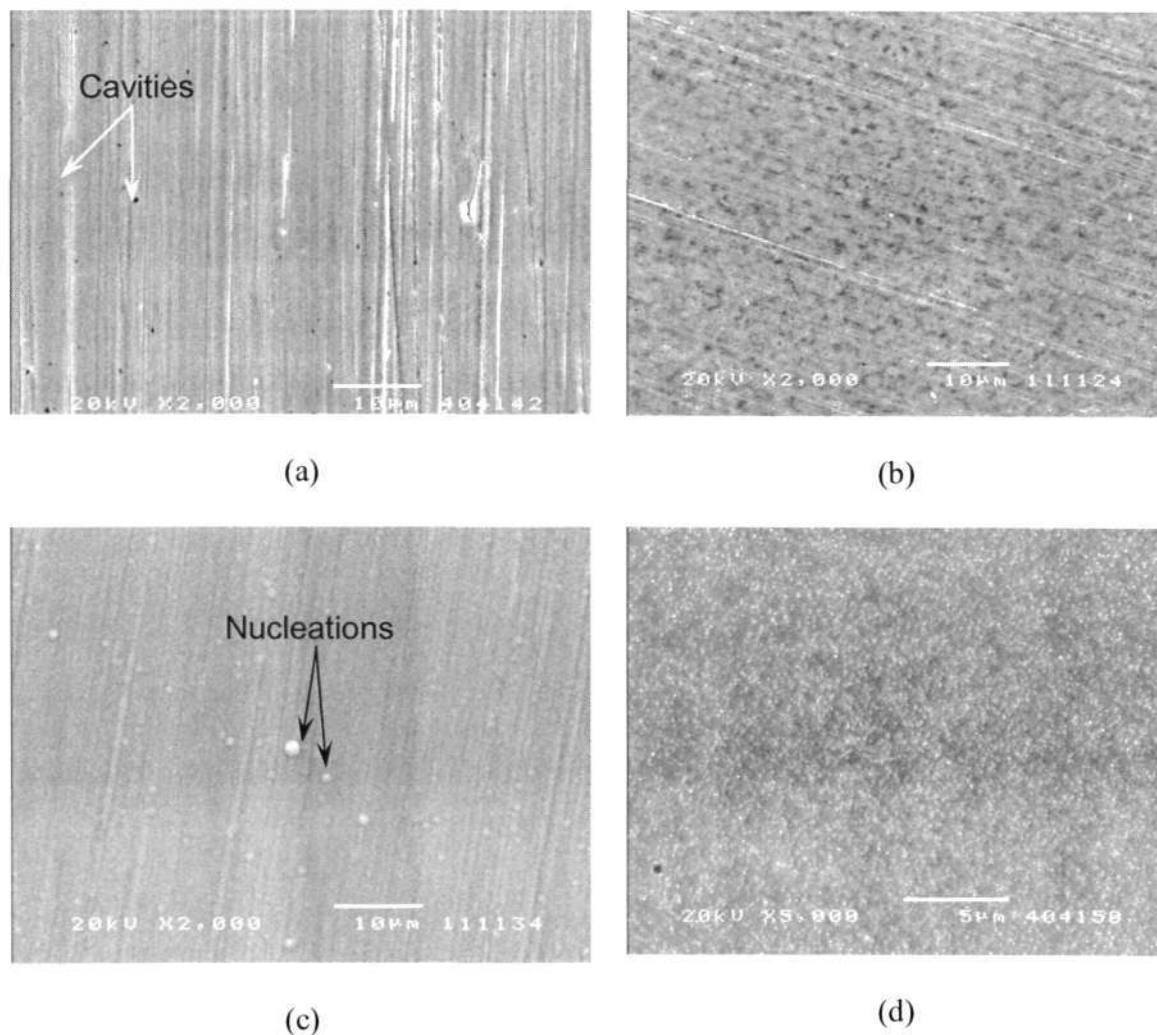


Figure 4-2 Surface morphology at different stages of the plating process. (a) Grinding scratches on the Cu surface; (b) Activation of Ru atoms onto the Cu surface; (c) Complete deposition of Ni layer with isolated Ni atoms on the surface; and (d) Good Au surface texture overlapping the Ni surface area.

Topographical measurement of the plated surface was then compared. Surface topography of the plated surface was frequently characterized with a surface probing system such as Atomic Force Microscopy (AFM) and surface profilometer. However, the

techniques of a probing system involved contact and tapping modes, which might deform/remove surface features on the soft plated material. Vital features such as nucleations might be distorted, leading to misinterpreted information. Its area of focus was also relatively small to suggest any curvature and uniformity over the entire bonding area. An optical interferometer (WYKO NT2000) measured surface heights from 0.1 nm to several millimeters with a roughness measurement resolution better than 1 Angstrom (See Figure 4-3). Its non-contact feature under high magnification permitted accurate topology measurement without damaging the surface. Hence, optical interferometer was preferred over probing systems due to its high roughness measurement resolution without physical contact.

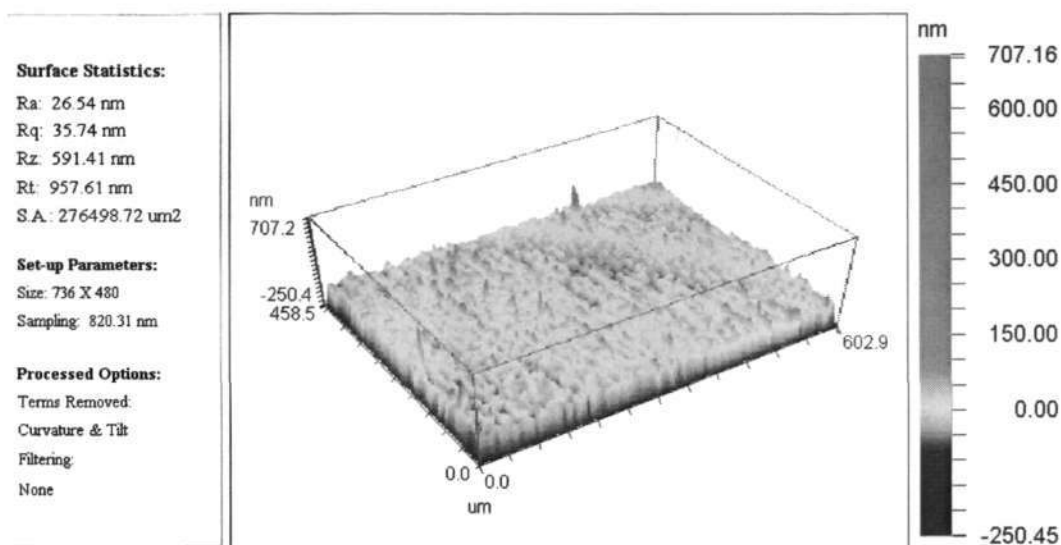


Figure 4-3 Typical surface roughness measured during the plating process. Striations of peaks (red) and valleys (blue) could be observed from the surface.

Topographical measurement at different stages of the plating process was studied to determine the robustness of the bonding area. In the activation process, random nucleation associated with Ru activation decreased the overall uniformity due to uneven grain size scatter. As shown in Figure 4-4, the surface roughness increased after Ru

activation. Nevertheless, electroless deposition of Ni and Au onto the Cu heatsink was observed to improve the surface finishing [160]. Initial surface roughness of 40-50 nm can be improved to 26-35 nm after the plating process. Striations of polishing lines were concealed by the deposited metallization. Since the surface roughness improved, the wettability of the of the plated surface also improved [161]. The plating process on the Cu heatsink was deemed sufficient for bonding of LDs.

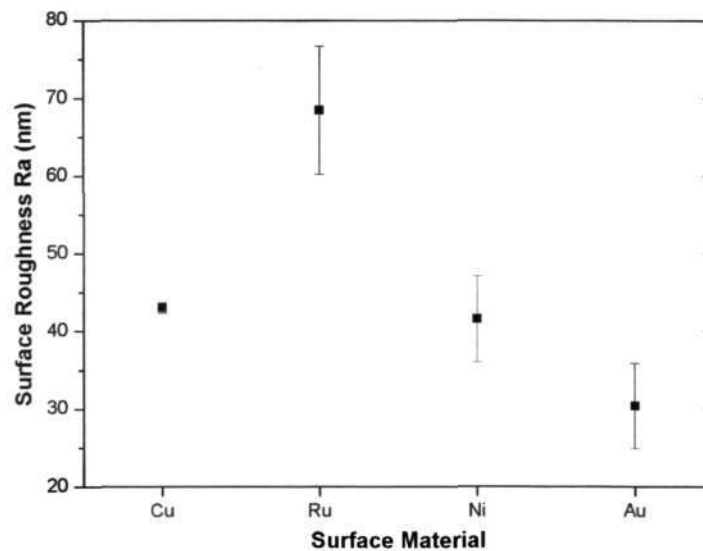


Figure 4-4 Comparison of surface roughness at different stages of the plating process.

Improved surface roughness could be obtained from the plating process.

4.3 Bonding Process

Figure 4-5 shows a schematic diagram of a face-down bonded LD. The LD has a width and a cavity length of 250 μm by 600 μm , respectively. The ridge, which is created over a series of masking and etching processes, has an approximate width of 3 μm and a height of 1.59 μm . The active region, which is the heat source, is less than 2 μm from the ridge and about 100 μm from the substrate. Due to the proximity of the active region to the epitaxial metallization, the solder may bridge onto the facet easily in a face-down bonding

approach. A metal opening at the ridge over the SiN passivation layer restricts the electrical current flow within the ridge. Ti/Pt/Au metallization was then deposited onto the LD to provide electrical connection. Finally, an annealing process improved the adhesion property of Ti/Pt/Au metallization onto the substrate. Understanding the peripheral and the epitaxial layers of these LDs pose significant advantages in the packaging development.

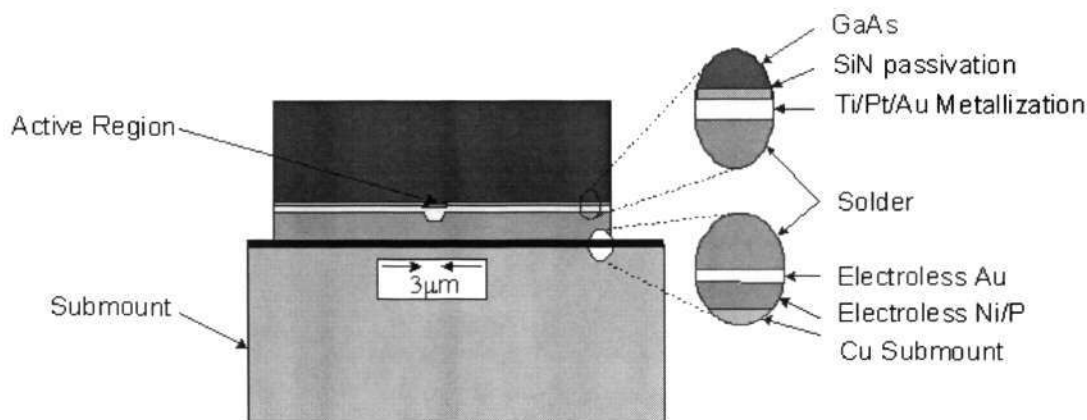


Figure 4-5 Simplified cross-sectional view of ridge-waveguide edge emitting LDs.

In a thermo-compression bonding process, three key bonding parameters are required to create chemical bonding – temperature, applied pressure, duration. While a bonding pressure assist in creating physical contact of two bonding surfaces, reflow temperature and duration are applied to create chemical bonding. From the viewpoint of interconnection, physical bonding offers the contact between the LD and heatsink, while chemical bonding is through the formation of intermetallic compound (IMC) at the interfaces. The reflow duration is defined as the duration above the liquidus state of the solder. In general, the reflow duration is usually kept as small as possible but long enough to form chemical bonding. Long reflow duration would readily reduce the integrity of the solder joint with thicker IMC formation and increased void content. To understand the

thermodynamic stability of the interconnect, the phase diagrams of Au-Ni, Au-Sn and Ni-Sn systems were discussed.

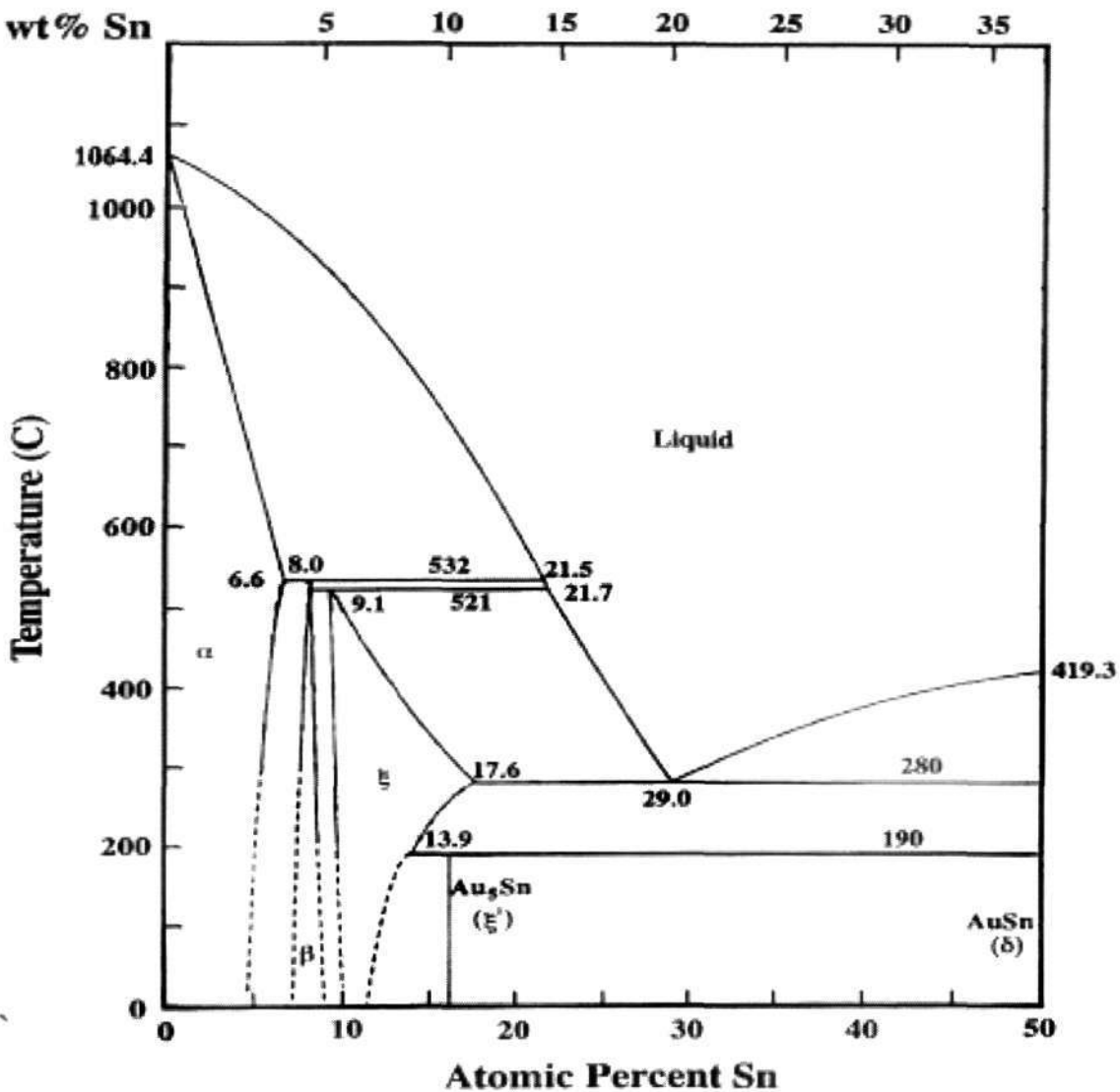


Figure 4-6 Binary phase diagram of Au-AuSn system.

For Au-rich 80Au/20Sn eutectic, the solder consists of two Au/Sn phase compounds; Au_5Sn and AuSn . From the phase diagram as shown in Figure 4-6, the reflow temperature must acquire a minimum of 280 °C for reflow soldering. Below 280 °C, the chemical interaction is slow and requires a long duration to achieve chemical bonding. During reflow soldering, any increase in Au and Ni elemental additive might increased the liquidus temperature of the solder. When additional Au diffused into the solder during

reflow, it increased the Au composition of the solder. Due to the thin solder layer of 5-8 μm , a small increase of Au content could result in a significant increase in the overall Au composition of the solder. According to the Au-AuSn phase diagram, a 1 at% increase of Au from the 80Au/20Sn eutectic would increase the liquidus temperature by 30 $^{\circ}\text{C}$. Similarly, during reflow, Ni from the heatsink diffused into the solder to form intermetallics. Reaction of Ni with Sn at the interfaces reduced the Sn activities in the bulk solder and increased the overall Au composition in the solder joint, which in turns, increase the liquidus temperature of the solder. Hence, bonding at 280 $^{\circ}\text{C}$ may result chemical instability due to the increased liquidus temperature.

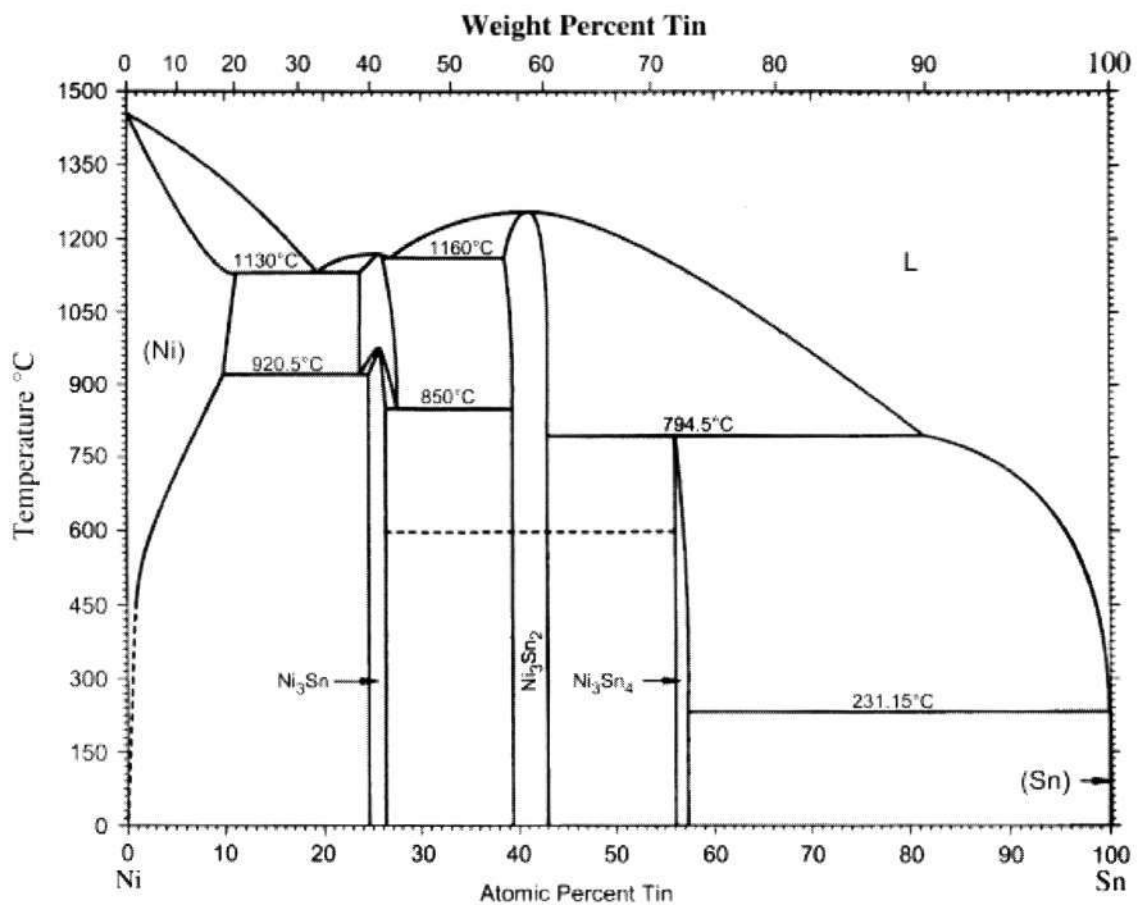


Figure 4-7 Binary phase diagram of Ni-Sn alloy system.

When Sn-bearing solder reacts with Ni, it forms Ni-Sn intermetallics at the interfaces. As shown in Figure 4-7, only Ni₃Sn₄ IMCs can be formed at reflow temperatures of 280 °C to 320 °C. According to the phase diagram, the atomic percent of Sn at 320 °C is less than 1 at%. The low solubility of Sn into Ni at the reflow temperature range of 280 °C to 320 °C could result in improved interfacial stability to the solder joint.

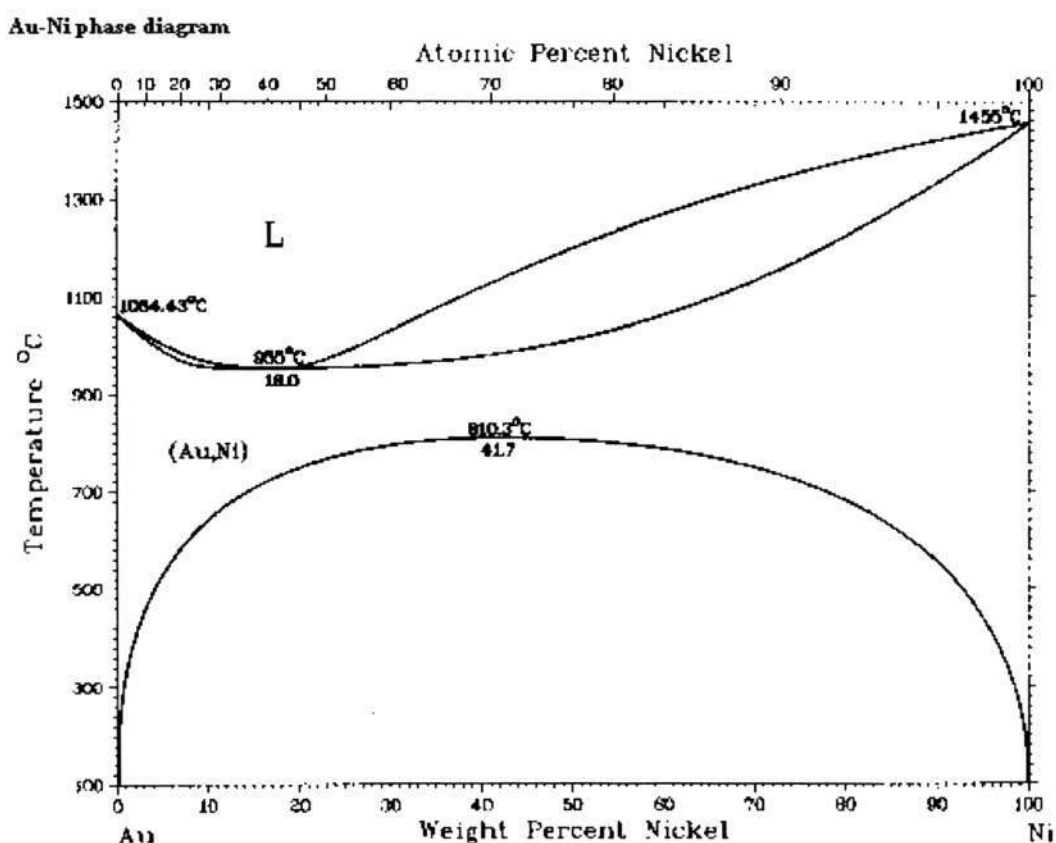


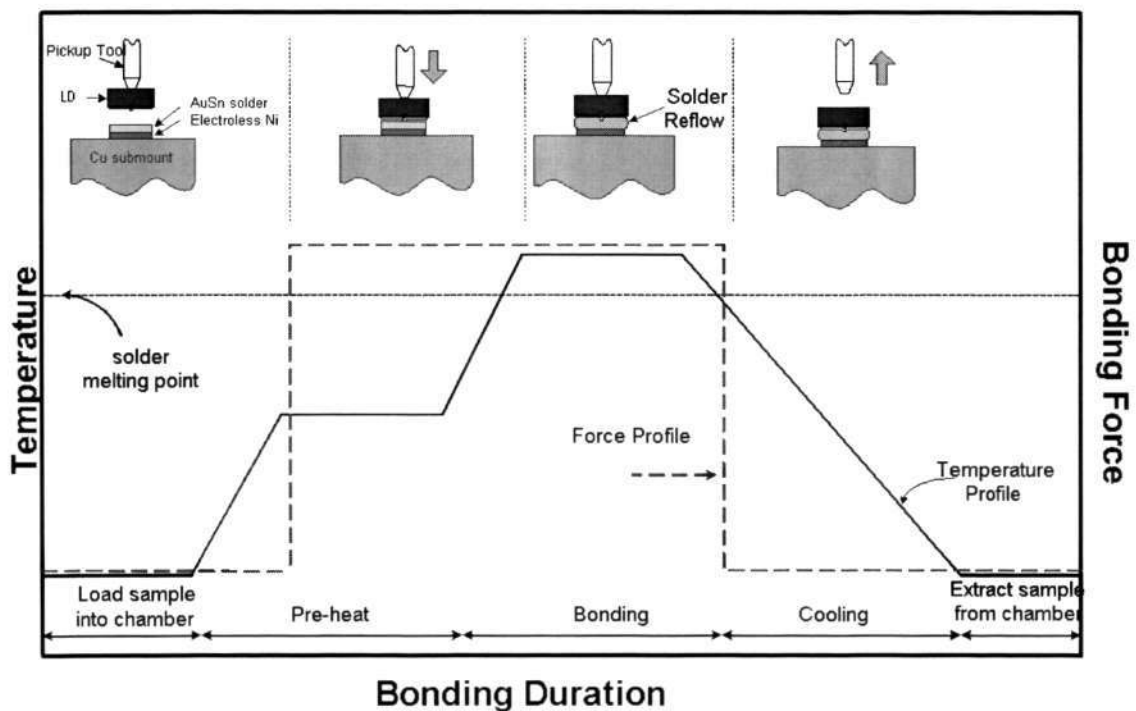
Figure 4-8 Binary phase diagram of Au-Ni system.

From the Au-Ni phase diagram, it can be observed that Au and Ni limited mutual solubility. As shown in Figure 4-8, Au and Ni react at high temperature of 800 °C and above. At low temperatures of 280 °C to 320 °C, there was limited Au-Ni chemical interaction. Hence, in electronics packaging, Ni is frequently used as a diffusion barrier while Au is used as a surface protective layer to the underlying Ni metallization.

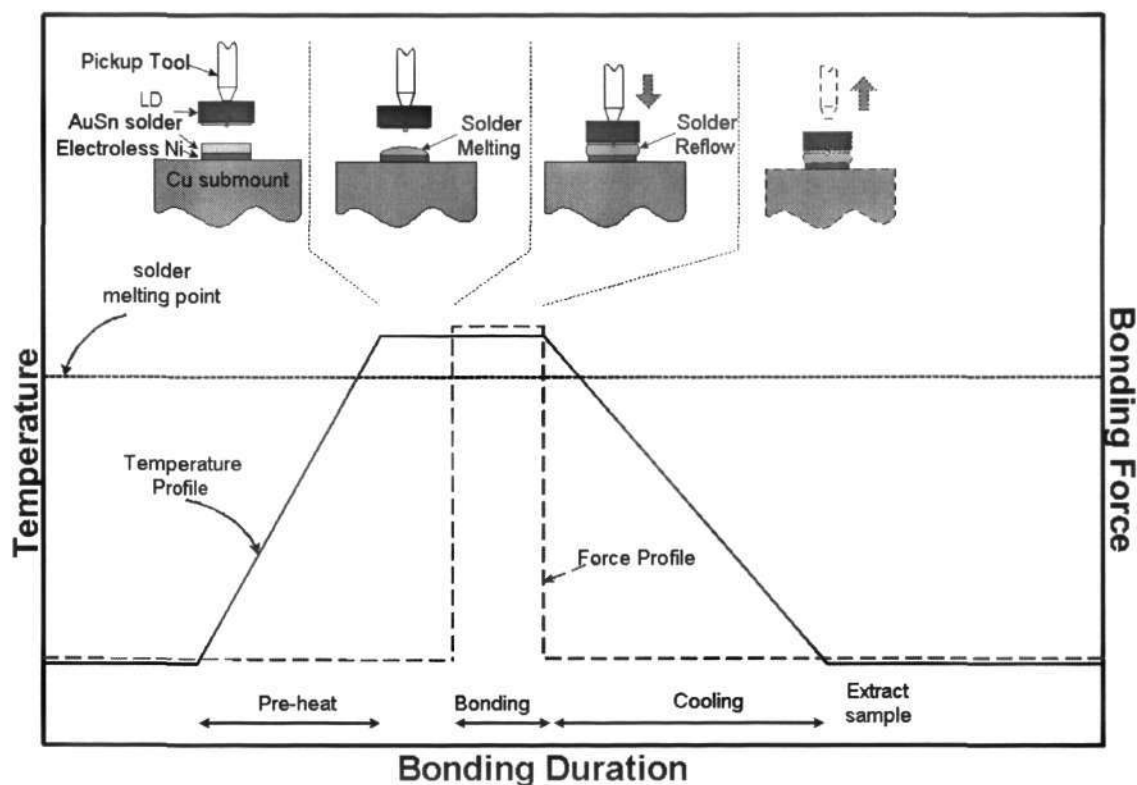
For bonding of LDs, the integrity of the bonding interface is strongly dependent on the bonding parameters i.e. pressure, temperature, and duration. In normal practices, the LD was loaded into the bonding stage during preheating as shown in Figure 4-9(a). Bonding pressure was then applied against the heatsink before solder was reflowed [6, 53, 82, 90, 162]. Due to the ridge-waveguide structure, the bonding pressure must provide sufficient contact in order to achieve good bonding integrity during the bonding process. On the other hand, this built up large residual stress on the laser ridge when using hard solder. When a mechanical load was applied onto the laser ridge, compressive stress was concentrated at the laser ridge. Since the active region (lasing source) is directly beneath the ridge and only a few microns away, the induced mechanical stress may cause structural distortion to the device.

To improve the wettability of the solder, the bonding temperature must be sufficiently high. The bonding duration must also be sufficient to permit formation of IMC at the LD/solder and solder/heatsink interfaces. However, long bonding duration, large bonding pressure and high bonding temperature would readily degrade the performance and reliability of the LDs. To minimize the bonding stress induced, a modified bonding process, with low bonding pressure, short bonding duration and low bonding temperature, should be introduced. This can be achieved when the bonding stage was heated above the melting point of the solder before application of a mechanical load. As shown in Figure 4-9(b), the bonding stage was heated above the melting point of the solder material and then the LDs were loaded into the bonding stage. This could significantly reduce the thermal shock impact as the LDs were exposed to shorter bonding duration at high bonding temperature. The bonding duration could also be reduced since the wettability of the solder improved when it was in its molten state. The bonding pressure could also be reduced since the molten solder readily conformed to the bonding surfaces.

This modified bonding process exploited two contact methods with different metallurgies: thermo-compression bonding and eutectic soldering. The metallurgy of contacts formed by thermo-compression bonding showed high stability without remarkable interdiffusion given the short reflow. The molten solder, which cushioned the bonding pressure, compensated alignment tolerances and stress maxima [163]. Coincidentally, this combination of short bonding duration and low bonding pressure could also reduced thermal shock impact and residual stress induced onto the LD. Hence, eutectic soldering and thermo-compression bonding could improve the reliability of the LD package.



(a)



(b)

Figure 4-9 Comparison of different bonding profile at the bonding stage. Short bonding cycle, together with low bonding pressure, could be attained in this (b) modified bonding process compared to (a) conventional approach.

For face-up bonding of LDs, mechanical loading was usually applied onto the LDs before solder reflow. The LDs were pressed against the solder preform and then the temperature at the bonding stage was raised above the melting point of the solder to create interdiffusion at the bonding interface. However, for the face-down approach, the bonding process must be modified since residual stress and bonding quality had been a major concern in the packaging technology. This bonding process often resulted in high bonding stress induced and/or structural damage to the laser ridge. To prevent damages to the ridge of the LD, bonding stress must be significantly moderated when using hard Au80Sn20 solder. In order to cushion the bonding load, Au80Sn20 solder was heated above its melting temperature before a mechanical load was applied. Good interfacial contact could be obtained since the molten solder would readily conform to surface irregularities.

Based on this modified face-down bonding technique introduced, a test program was constructed with temperature ranging from 280 to 320 °C, bonding pressure ranging from 0.981 to 9.81 N, and at a bonding duration of 5 to 15 s. The temperature range was selected between the melting point of Au80Sn20 solder, which is 280 °C, and the typical bonding temperature for LD packaging when using Au80Sn20 solder, 320 °C. Higher bonding temperature was avoided as it might degrade the LD performances. As depicted in Table 1 (see Section 2.2.2), the bonding pressure falls between 0.276-0.375 MPa. However, the bonding pressure was extended from less than 0.196 MPa to more than 0.523 MPa to observe the limiting effects of different bonding loads. In optoelectronics packaging, a short bonding duration was preferred to avoid thermal shock impact onto the LDs. Hence, the bonding duration was confined to within 15 s.

Firstly, LDs were bonded at 300 °C for 5, 10 and 15 s. All the LDs were well-adhered onto the heatsink with sufficient formation of IMC at the LD/solder and solder/heatsink interfaces. To meet the requirement of good bonding formation and without degrading performance/reliability, the bonding duration was restricted to 5 s. At least 3 samples were used for each combination of bonding parameters in the test program shown in Table 5.

Table 5. Test program for face-down bonding of LDs using Au80Sn20 solder.

Dwell Time (5 s)		Bonding Pressure (MPa)							
		<0.196	0.196	0.262	0.327	0.392	0.458	0.523	>0.523
Temperature (°C)	320								
	310								
	300								
	290								
	280								

From the experimental matrix, the effect of various bonding parameters on the joint integrity and the LD optical performance was summarized as shown in Table 6. Mechanical shear testing was conducted to evaluate the integrity of the solder joint and parametric investigation was conducted to study the LD optical improvement after bonding. From the shear test, two types of fractures were observed; solder joint and die rupture. The different fracture behavior was perceived by the quality of the solder joint. Voids, cracks and delamination in the solder joint were perceived to degrade the mechanical integrity of the solder. The optical performance of the LDs improved after bonding due to heat transfer from the LD onto the heatsink. This optical improvement depends largely on the bonding integrity of the solder joint and will be elaborated in the following sections.

Table 6. Experimental results of bonded LDs at various bonding parameters.

Dwell Time (5 s)			Bonding Pressure (MPa)				
			<0.196	0.196-0.262	0.327-0.392	0.458-0.523	>0.523
Temperature (°C)	320	Optical Improvement	1.99-2.43	1.84-2.49	2.98	2.42-2.66	2.89
		Yield	4/6	3/8	1/6	2/5	1/4
		Shear Test	Solder Joint	Die Rupture	Die Rupture	Die Rupture	Die Rupture
	310	Optical Improvement	1.71-2.53	2.25-2.55	2.34-3.01	2.26-2.39	2.69
		Yield	5/7	4/6	2/7	3/8	1/3
		Shear Test	Solder Joint	Die Rupture	Die Rupture	Die Rupture	Die Rupture
	300	Optical Improvement	1.99-2.22	2.53-2.64	2.28-2.96	2.1-2.45	2.16-2.45
		Yield	2/3	4/4	4/5	4/5	2/3
		Shear Test	Solder Joint	Die Rupture	Die Rupture	Die Rupture	Die Rupture
	290	Optical Improvement	1.31-1.66	1.88-2.71	1.87-2.13	2.07-2.65	1.5-2.81
		Yield	3/3	5/6	6/6	5/6	3/3
		Shear Test	Solder Joint	Solder/Die Rupture	Die Rupture	Die Rupture	Die Rupture
280	Optical Improvement	0.91-1.19	1.09-1.15	1.06-1.43	1.14-2.08	1.68-1.91	
	Yield	3/3	3/3	3/3	3/3	2/3	
	Shear Test	Solder Joint	Solder Joint	Solder Joint	Solder Joint	Solder Joint	

From the mechanical shear testing, failure site occurring in the solder joint is demonstrated to be a poor bond due to the formation of voids, cracks and delamination. Due to the high mechanical strength of AuSn solder, failure site occurring within the LD die shows that good bonding integrity was observed. From this mechanical integrity perceptive, the bonding integrity for bonding temperatures of 280 °C and bonding pressure of <0.196 MPa was deemed insufficient to create good bonding behavior. Based

on this experimentation, the solder joint was divided into two zones of good and bad bonding integrity as shown in Table 7.

Table 7 . Mechanical integrity of bonded LDs.

Dwell Time (5 s)		Bonding Pressure (MPa)				
		<0.196	0.196-0.262	0.327-0.392	0.458-0.523	>0.523
Temperature (°C)	320	Good bonding integrity				
	310					
	300					
	290	Poor bonding integrity				
	280					

From Table 8, it was observed that at high bonding temperature, the bond yield was significantly reduced. Out of 36 bonded LDs, only 11 LDs was functioning. Further to the mechanical testing, the optical performance of the LDs was also studied to understand the effect of different bonding parameters as shown in Figure 4-10. The optical improvement for 280 °C bonding temperature was lesser as compared to the higher bonding temperatures. And for each bonding temperature, the optical performance was lower for applied pressure of <0.196 MPa. The lower optical improvement was attributed by the poor bonding integrity in the solder joint. When the bonding integrity was poor, heat transfer from the LDs to the heatsink was limited.

Table 8. Effect of bonding parameters on the bonding yield.

Dwell Time (5 s)		Bonding Pressure (MPa)				
		<0.196	0.196-0.262	0.327-0.392	0.458-0.523	>0.523
Temperature (°C)	320	High probability of solder bridging onto facets				
	310					
	300	High probability of electrical functionality				
	290					
	280					

As the optical performance of the LDs are strongly dependent on the bonding parameters, the optical performance of the LDs were observed at various bonding temperatures and bonding pressures. In general, the optical performances increased with higher bonding temperature and higher bonding pressure. As shown in Figure 4-10, the optical performance for 280 °C bonding temperature was observed to increase with bonding pressure. With increased bonding pressure, the molten solder conformed better to the bonding surfaces, thereby creating a better physical contact with the LD. Likewise, as the bonding temperature increased, the wetting characteristics of the solder improved. As shown in Figure 4-10, for a bonding pressure of 0.327-0.392 MPa, the optical output of the LDs increased with temperature.

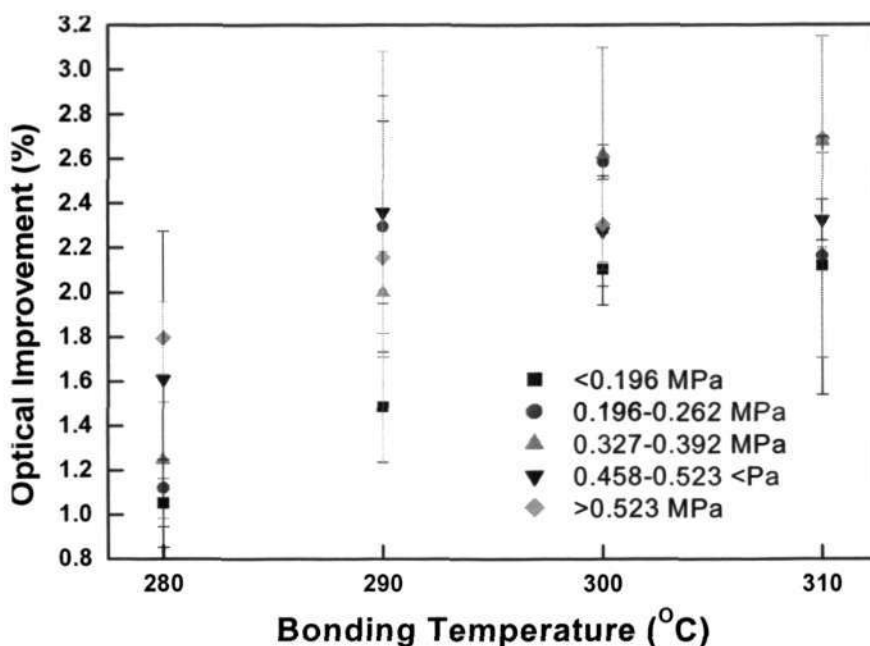


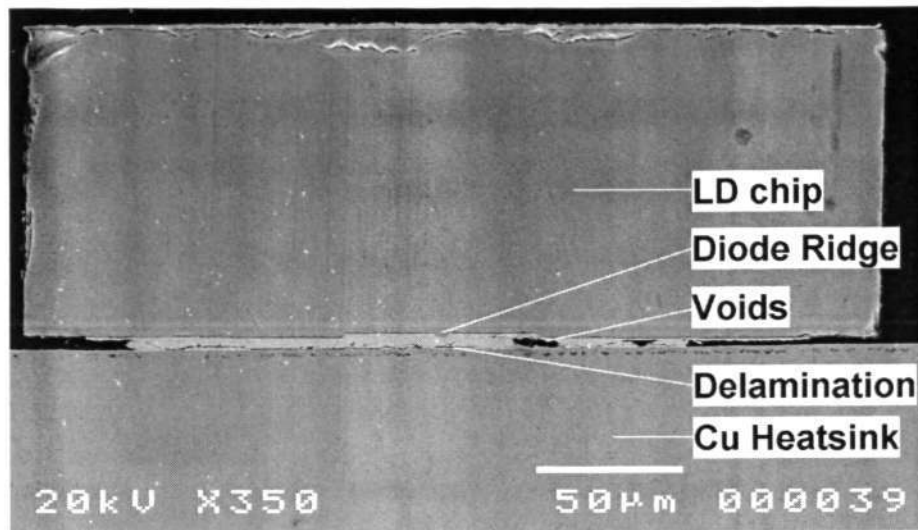
Figure 4-10. Effects of bonding parameters on the optical performance of the LDs.

4.3.1 Effects of Bonding Temperature

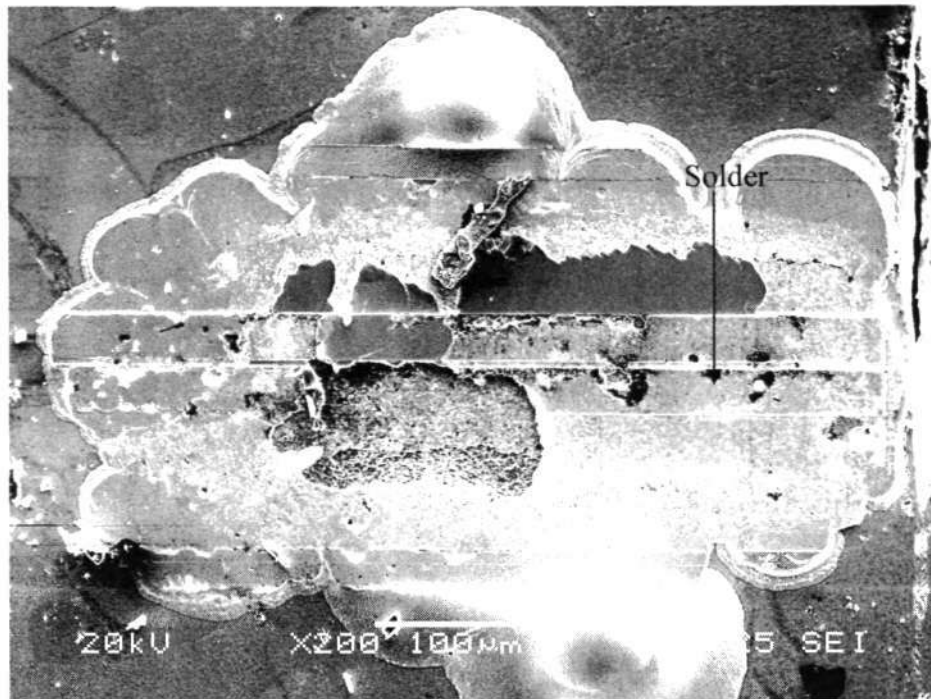
Insufficient Wetting at Low Temperature

During reflow, the temperature must be high enough to ensure complete melting of the solder as well as sufficient wetting of solder to the base material. In general, as the bonding temperature increased, the wetting characteristics of the solder increased while the reaction between the solder and the substrate metallization also increased. While high bonding temperature improves the soldering process, it forms thicker interfacial IMC and degrade the integrity of the solder joint. At 280 °C solder reflow, the wettability of the solder preform was insufficient to form good bonding as shown in Figure 4-11(a). As the bonding temperature fluctuated about the melting point of the Au80Sn20 solder, incomplete melting caused interfacial void formation and delaminations, which could act as a source of crack initiation during reliability testing. Partial bonding between the LD and the heatsink resulted in poor solder interconnect, compromising the mechanical

integrity of the solder joint. This often resulted in solder failure when subjected to shear test. As shown in Figure 4-11(b), Au80Sn20 solder was detected from the fracture surface.



(a)



(b)

Figure 4-11 (a) Typical cross-sectional view of as-bonded LDs with insufficient wetting at the solder layer. (b) Au80Sn20 solder was detected from the fracture surface after shear test.

When LDs were poorly bonded at 280 °C and/or lesser than 0.196 MPa (also see Figure 4-15), heat transfer through the solder joint was ineffective. In LD packaging, the purpose

of bonding the device to the heatsink via solder is to create mechanical support as well as to assure good heat transfer. Thermal management through this solder material is crucial in such applications. Any voids formations and/or delamination in the solder joint caused the thermal resistance between the LD and the package to increase significantly at that point due to hot spots. LDs bonded in this region had an average optical output of 80-120 mW as shown in Figure 4-12. With the increased thermal resistance in the solder joint due to void formation, the heat dissipation was not effective and the optical output could only reached a manageable 1.2-1.5 times increment from its original value.

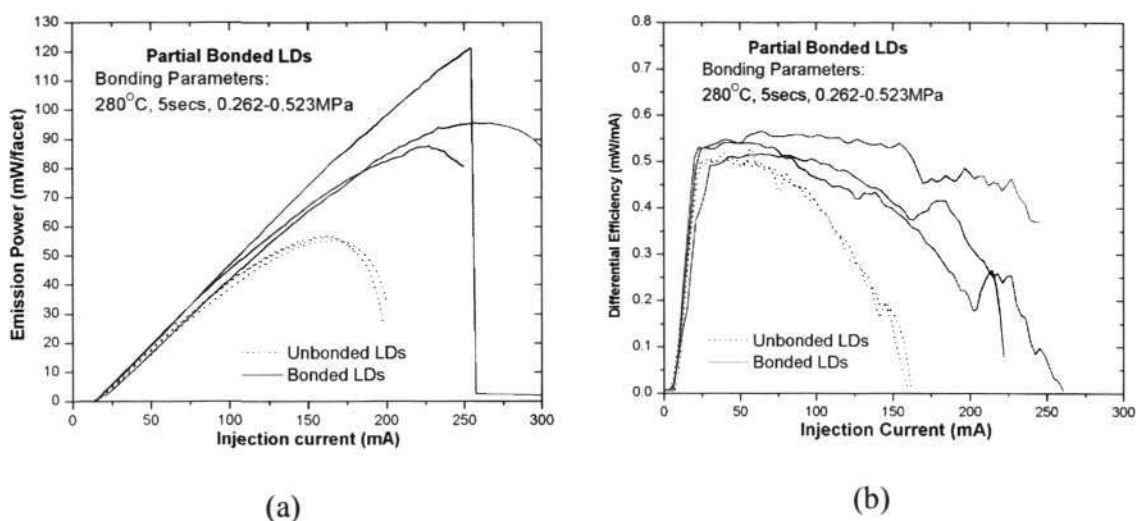


Figure 4-12 Optical performance of partially bonded LDs. Marginal optical output of 80-120 mW could be achieved, depending on the degree of bonding integrity. The differential quantum efficiency was observed to improve slightly after bonding.

Low Yield at High Temperature

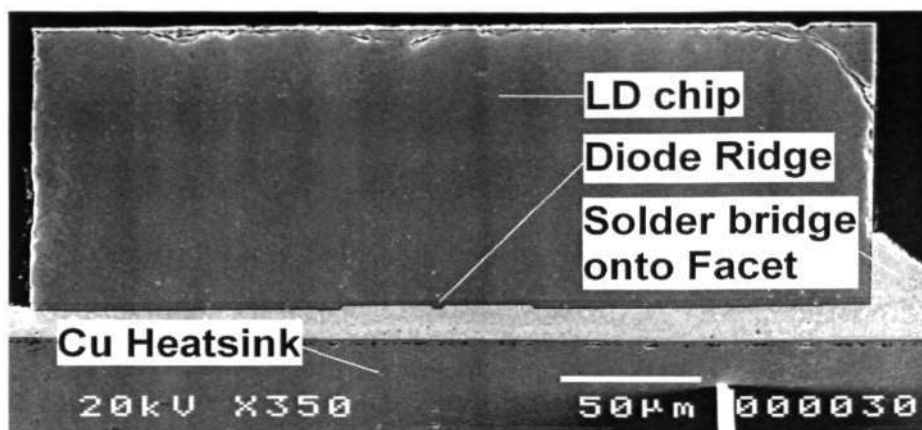


Figure 4-13 Typical cross-sectional view of solder bridging onto facet of LDs.

On the other hand, yield was significantly reduced when the bonding temperature increased to 320 °C. Out of the 36 samples bonded, only 11 samples were functioning. The most of the samples were short-circuited due to solder bridging along the cavity length of the LD as shown in Figure 4-13. The optical beam could also be obscured when the solder overflow onto the emitting facets as shown in Figure 4-14. High bonding temperature might also degrade these LDs. LDs bonded in this region would not be feasible for industrial production.

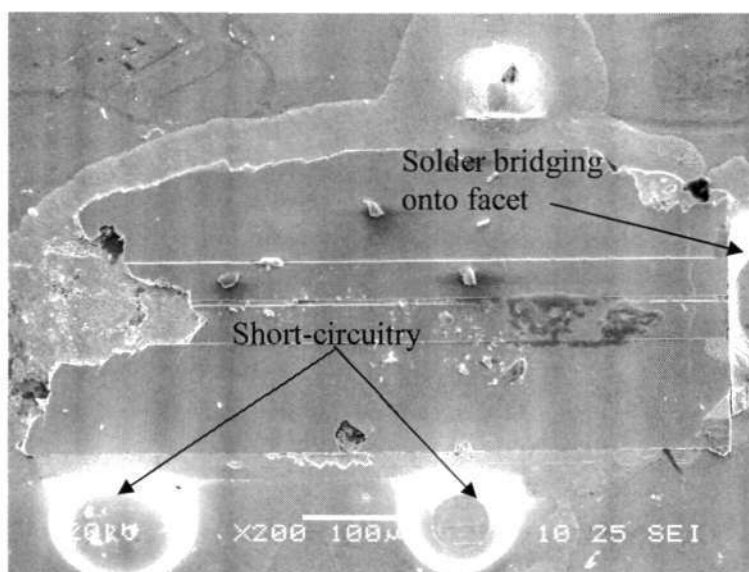


Figure 4-14 Fracture analysis of sheared LD package in face-down bonding configuration. Solder was observed to obscure the emitting facet and short-circuitry along the length of the LD was observed.

4.3.2 Effects of Bonding Pressure

Poor Bonding Integrity resulted from Small Bonding Pressure

In die bonding, a contact force is applied during the bonding process to spread out the interface material to achieve a void-free solder joint as well as to minimize the solder thickness. For different packages, the applied force varies depending on the material's compressibility, surface flatness, surface furnish, and area of contact. In face-down LD bonding approach, where the surface topology is non-uniform, the application of pressure has a large factor in reducing the thermal resistance of a joint. In general, the thermal resistance can be reduced by applying a pressure while reducing the material thickness. The thermal resistance created by the material itself (assuming void-free case) for a given thickness is constant as a function of pressure; however, the contact resistance at the interfaces is extremely dependent on pressure. Typically, there is a minimum contact force that should be applied to the package for contacting and forces beyond that value would decrease the thermal resistance until the assembly can withstand. To reduce the contact resistance, the solder material should be void free and the interfacial resistance be minimized.

However, bonding pressure was frequently traded between mechanical integrity/void formations and residual stress induced. Poor bonding integrity was observed when the bonding pressure was smaller than 0.196 MPa. Due to the irregular ridge LD structure,

voids were evidently found around the ridge region. The pressure is insufficient to spread out the solder material. Weak adhesion strength, with voids and delaminations, was observed in the solder joint as depicted in Figure 4-15.

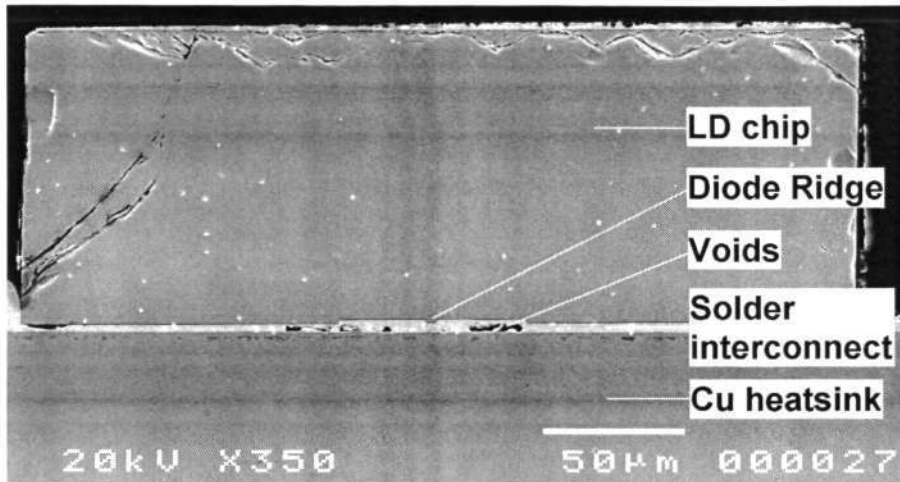


Figure 4-15 Typical cross-sectional view of insufficient bonding contact at the solder interface.

For LDs bonded at 280 °C and/or less than 0.196 MPa, weak adhesion strength could be observed in these partially bonded LDs. Figure 4-16 shows a typical fracture behavior of partially-bonded LDs. Due to the void formations, delaminations and non-wetting characteristics at the interfaces, fracture occurred in the solder joint with an average shear strength of 90 g (4.9 MPa).

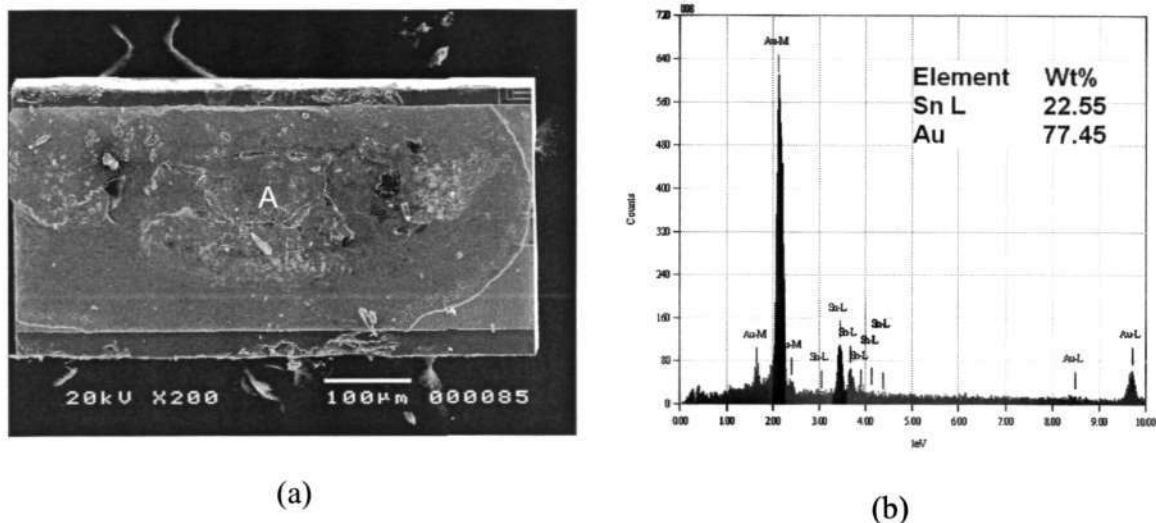


Figure 4-16 (a) Typical sheared surface of partially bonded LDs; (b) SEM/EDX analysis at region A of the fracture surface.

Good Bonding Integrity

As the bonding pressure increased to 0.196 MPa and the bonding temperature increased between 290 °C to 310 °C, good bonding integrity could be observed (see Figure 4-17). The wettability of the solder improved and the Au layer from the LD and heatsink were observed to diffuse completely into the solder. When the applied pressure increased beyond 0.196 MPa, good bonding integrity could be observed. The applied pressure permitted the solder to spread evenly across the bonding area during the reflow process and a void-free solder joint was observed. Except for the bonding condition of 290 °C and 0.196 MPa, all the LDs bonded above 280 °C and more than 0.196 MPa exhibited good mechanical integrity, with brittle fracture occurring within the device. Distinct cleavage fractures were observed to initiate on many parallel cleavage planes, which was referred as wallner lines, at the GaAs material. In the process of shear testing, the strain in the joint would increase and microvoids would nucleate at regions of localized strain discontinuity. These microvoids grew, coalesced, and eventually formed a continuous fracture surface. The wallner lines were resulted from the interaction of a simultaneously

propagating crack front and an elastic shock wave in the material. The average shear strength for these well-bonded LDs was 450 g (24.5 MPa) and this exceeded the shear strength criterion benchmarked by MIL-STD-883C.

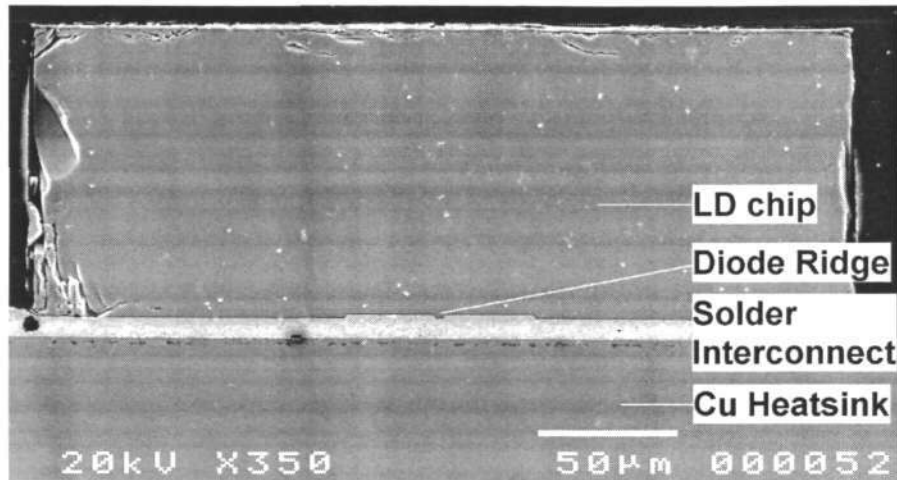


Figure 4-17 Typical cross-sectional view of well-bonded LDs in the bonding process window.

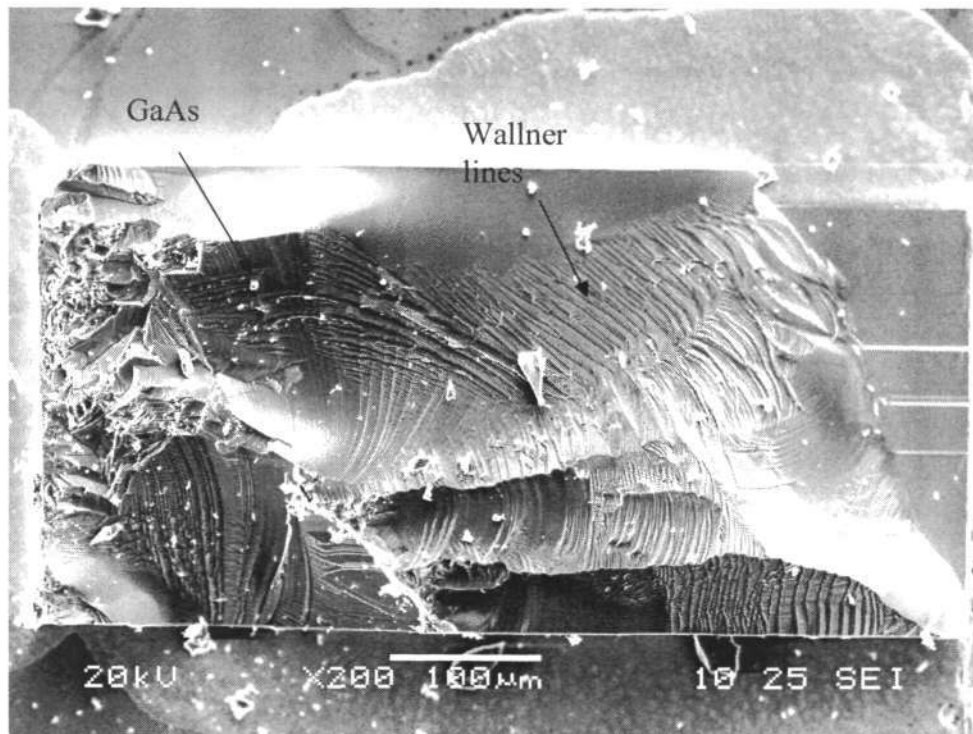


Figure 4-18 Fracture analysis of well-bonded LDs after shear test. LD residues was found on the fracture surface after shear test.

The maximum optical output achieved depended on the quality of the bonding interface. Table 9 shows the output power variation with different bonding area through visual observation. A partial bonding area of 60-75% had an optical improvement of 2.14 ± 0.14 and a $0.06-0.072 \text{ mW/mA}$ increased in the slope efficiency. Devices with above 80% bonding area further improved the optical performance by 2.57 ± 0.27 and the slope efficiency demonstrated an increment of $0.088-0.146 \text{ mW/mA}$.

Table 9. Optical performance comparison with different bonding area.

Bonding Quality (%)	Emission Power per facet (mW)			Differential efficiency (mW/mA)		
	Before	After	Relative	Before	After	Relative
100	58.144	139	2.391	0.353	0.418	0.065
90	59.528	150.612	2.53	0.371	0.478	0.107
60	61.295	131.546	2.146	0.328	0.418	0.09
65	56.927	129.608	2.277	0.332	0.404	0.072
100	52.395	140.938	2.69	0.318	0.461	0.143
70	52.036	112.538	2.16	0.313	0.373	0.06
90	51.18	125.183	2.446	0.309	0.418	0.109
75	57.148	119.377	2.089	0.329	0.35	0.021
65	58.723	118.004	2.01	0.355	0.443	0.088
80	51.291	133.751	2.068	0.341	0.414	0.073

Nevertheless, when LDs were bonded at higher than $280 \text{ }^\circ\text{C}$ and at 0.196 MPa and above, good bonding could be observed. The LDs demonstrated optical improvement to 150-160

mW, limited by Catastrophic Optical Damage (COD) of the facet. The COD facets were caused by accumulation of defects at high injection current. The differential quantum efficiency of these LDs was observed to be constant up to $10I_{th}$ without any thermal influence or disturbance to the characteristic (see Figure 4-19). Due to the effective heat-dissipating channel, from the active region (heat source) to the heatsink, the temperature in the active region was lowered. Hence, the LDs could be driven to higher injection current, leading to higher emission power. A high bonding yield of 74.4% was also achieved in this region. Out of the 39 samples bonded, 30 samples exhibit optical performances. 7 bonded samples were either short-circuited or the optical beam were obstructed by solder overflowing to the emitting facets while another 2 samples exhibited marginal optical output.

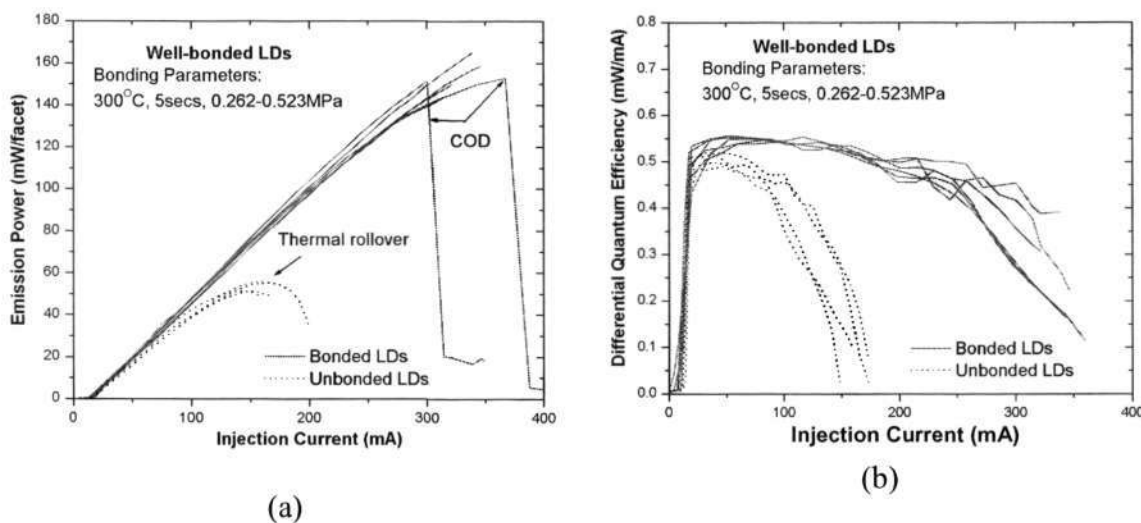


Figure 4-19 Optical performance of well-bonded LDs. Optimal optical performance, with more than 150 mW optical output can be achieved. The differential quantum efficiency showed good stability at high injection current.

High Stress induced due to Large Bonding Pressure

Although large bonding pressure may reduce the thermal resistance of the solder joint, it may degrade the performance of active devices such as LDs. During a bonding process, the LD would experience stresses; mechanical stress from the bonding pressure applied and thermal stress due to the coefficient of thermal expansion (CTE) mismatch between the LD and the Cu heatsink. Since the active region is near ($< 2\mu\text{m}$) and directly beneath the ridge of the LD, the mechanical stress induced was assumed to be the applied bonding pressure. When the applied pressure increased beyond 0.523 MPa, the pressure induced large mechanical stresses onto the package, damaging the active layers of the LD. However, for thermal stress, the stress was estimated using numerical modeling. As shown in Figure 4-20, compressive stress would be imposed for face-down bonded LDs and tensile stress for face-up bonded LDs. During the cooling stage of the bonding process, the bonded LDs would induce stresses due to different CTE and different material properties. Because of the CTE mismatch, different elongation and contractions would take place in the LD assembly. The LD would experience relative motions during which shear and bending stresses were induced in the LD assembly. As the CTE value of LD material was significantly lower than the Cu heatsink, compressive stress would be induced on the LD and its respective active region if it was face-down bonded while tensile stress would be imposed on the LD if it was face-up bonded.

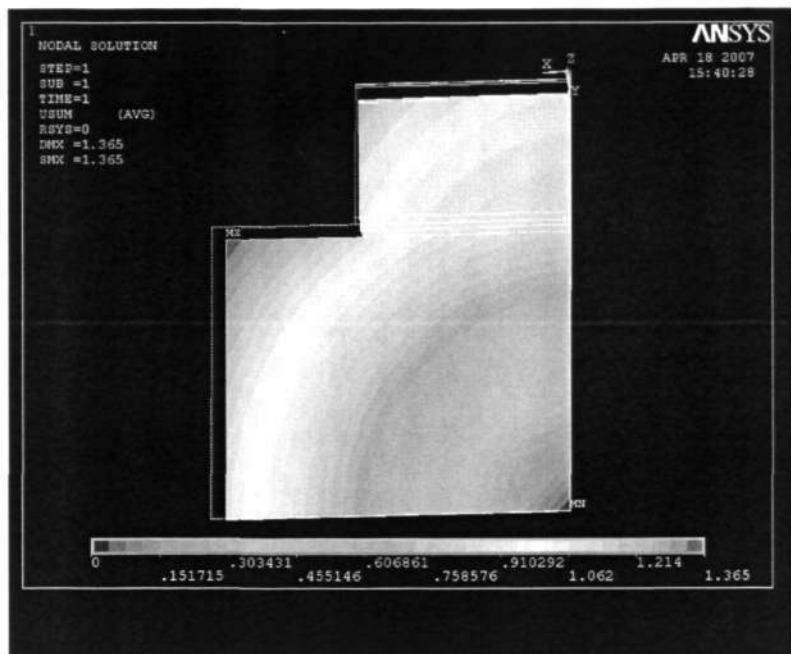
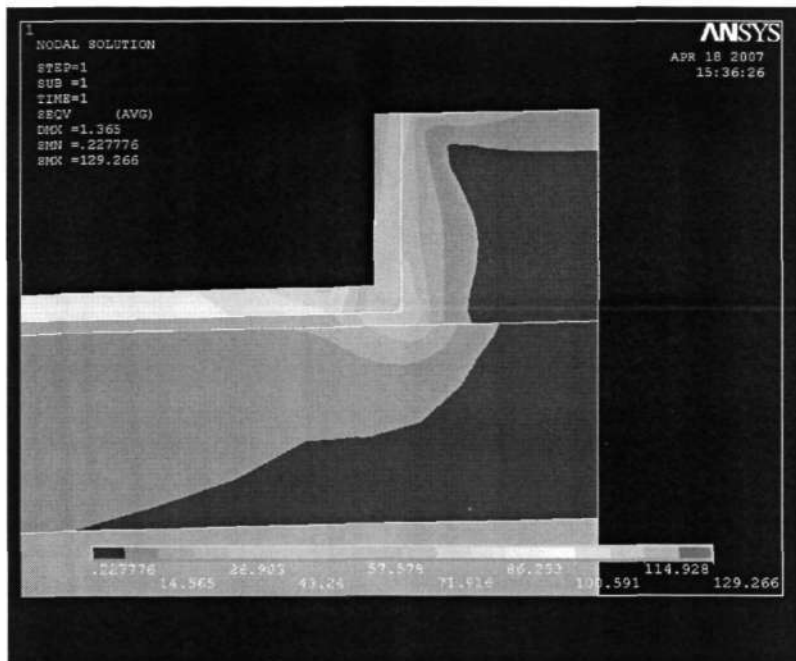
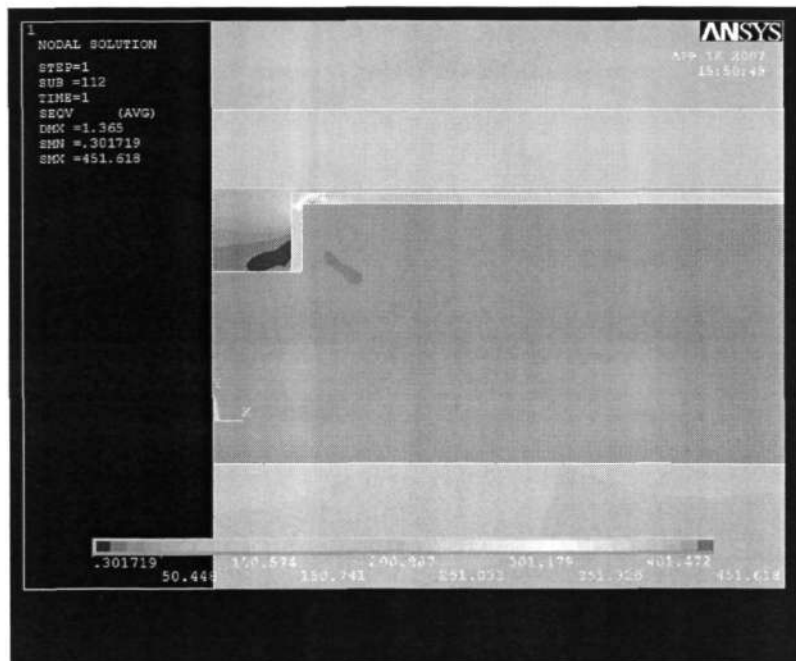


Figure 4-20. Deformation contour of LD package after bonding process from 280 °C to 25 °C. Compressive stress would occur on the LD if face-down bonded while tensile stress would be imposed if it is face-up bonded.

In addition, the stress induced at the active region for a face-down bonding configuration was significantly larger than face-up bonded LDs as shown in Figure 4-21. Further external loading applied onto the LDs, i.e. applied pressure, could further cause the LD material to induce stress and cause a degradation to the intrinsic behavior of the LD structure. The higher stress state might cause the electronic bandgap at the active region of the LDs to change. The bandgap modification at the active region might alter the lasing behavior of the LDs and increased the intrinsic optical losses. The increased optical losses might, in turn, increase the threshold current value and lower the optical power. This will be elaborated in the following paragraphs.



(a)



(b)

Figure 4-21. Von mises stress induced after the bonding process. (a) face-up bonded LDs and (b) face-down bonded LDs.

However, when the bonding pressure increased beyond 0.523 MPa, the intrinsic LD properties deteriorated. From the I-V and dV/dI characteristics in Figure 4-22, a slight deterioration was observed. This suggests that the junction experienced some structure modifications.

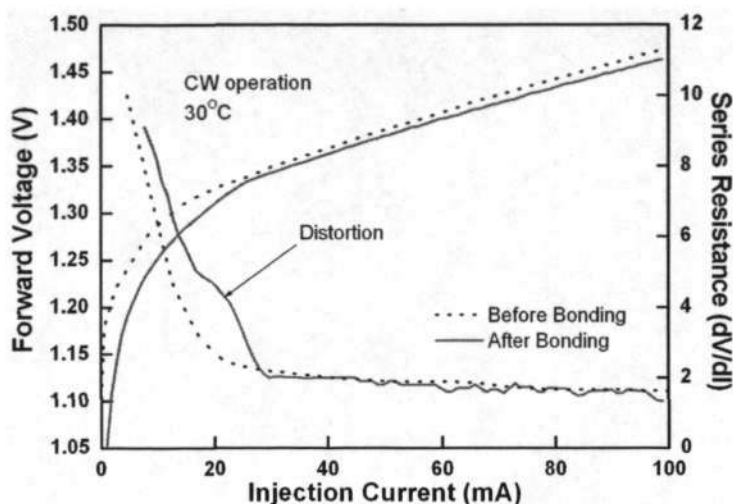


Figure 4-22 Electrical derivative measurements of I-V characteristic of LDs. Heterojunction distortion can be observed for large bonding load.

Large bonding pressure might also cause the threshold current to degrade. These AlGaAs/GaAs LDs had a typical threshold current of 16-18 mA. The threshold current, which is often a measure of LD degradation, increased to as much as 28 mA after bonding as shown in Figure 4-23. It is essential to ensure that the bonding process did not deteriorate the intrinsic properties of the LD. The changes to the heterojunctions might reduce the sensitivity of the device with temperature, increasing the non-radiative processes in the quantum wells.

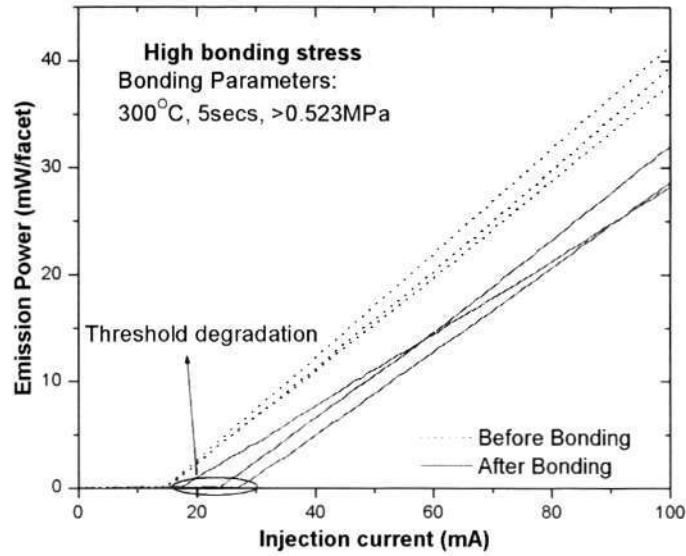


Figure 4-23 Threshold current degradation due to large residual stress experienced.

To understand the effect of large bonding pressure on the intrinsic changes of the LDs, the threshold current was measured under pulsed condition of 0.1 μ sec at 0.1% duty cycle. Short pulse width and low duty cycle ensured that the measurements were influenced by the bonding process, rather than induced by carrier density or temperature.

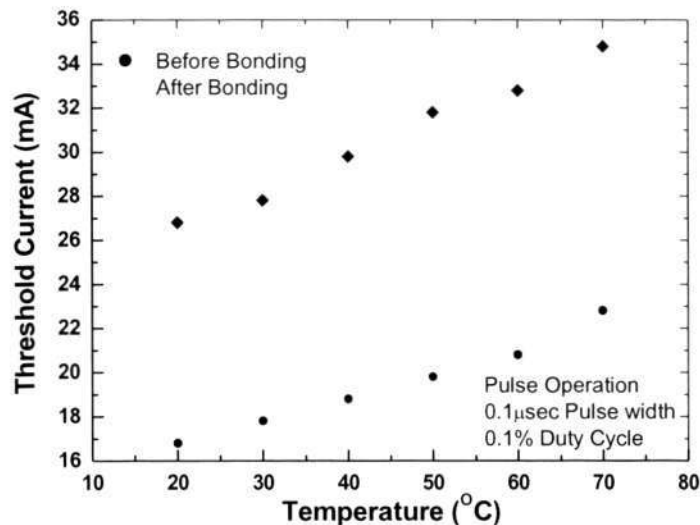


Figure 4-24 Temperature dependence of threshold current I_{th} in these LDs. The I_{th} deteriorated at elevated temperature due to increased non-radiative processes at high operating temperature.

As observed in Figure 4-24, the threshold current I_{th} increased significantly when subjected to large bonding pressure. This might be induced by the modifications to the heterojunctions, resulting in ineffective radiative recombination of carriers in the active region and increased loss mechanisms such as leakage current. Due to the high bonding stress induced, the active region experienced compressive stress. Compressive stress applied perpendicular to the active region increased the threshold current due to modification to the band structure caused by deformation [164].

Differential quantum efficiency was also plotted under a short pulse width and low duty cycle condition as shown in Figure 4-25. Firstly, the differential quantum efficiency η_D was observed to deteriorate above 50°C. The decrease of η_D suggested an increased of non-radiative recombination at elevated temperatures and that the intrinsic quantum efficiency η_i deteriorates at high injection current. Secondly, the abrupt change of η_D after bonding showed that the structural distortion caused further increased conversion of excitation energy into non-radiative recombination processes.

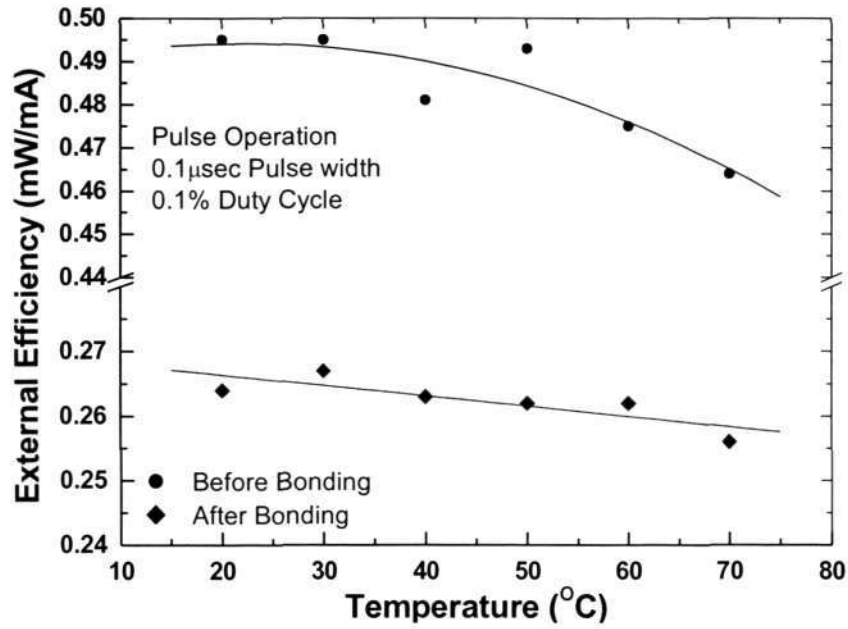


Figure 4-25 Temperature dependence of differential quantum efficiency η_D in these LDs. The η_D deteriorated at elevated temperature due to increased non-radiative processes at high operating temperature.

Wavelength stability is also an important parameter for high-power optical pump applications because a reduced wavelength shift with increasing temperature would allow a relaxed temperature control. Electroluminescence measurement was conducted to observe the emission wavelength after bonding. As shown in Figure 4-26, the emission wavelength shifted due to bandgap renormalization in the active region. This further substantiated that large bonding load induced structural distortion of the junction found in the electrical-optical characterization.

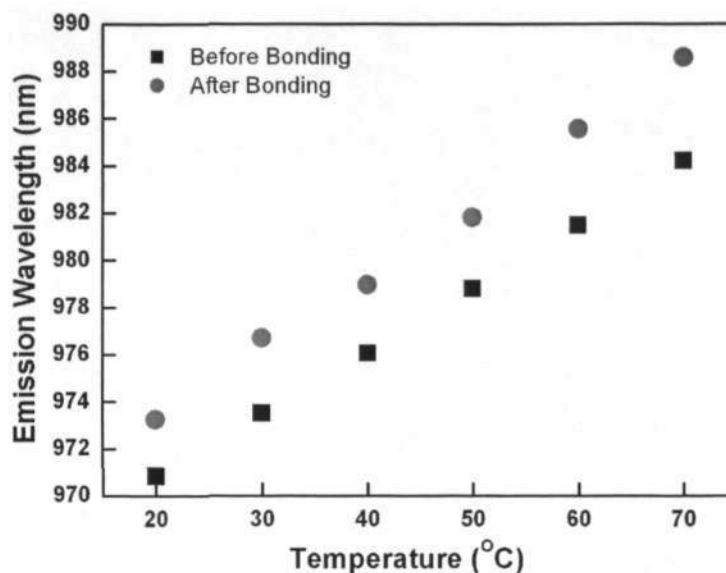


Figure 4-26 Effects of emission wavelength at different heatsink temperatures. Linear dependence of wavelength shift on operating temperature could be observed.

Due to the large bonding pressure, the active region experienced stress and the performance deteriorated due to a change in its band structure properties [165, 166]. Compressive stress applied perpendicular to the junction plane of the LD increased threshold current due to the energy splitting and mixing between the valence-band wave functions caused by deformation [164]. Briefly, uniaxial strains break the cubic crystal symmetry and cause the heavy hole, light hole, and split-off bands to shift in energy relative to one another, lifting the degeneracy of the heavy hole and light hole band and split-off band.

4.3.3 Optimal Bonding Window


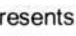
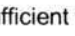
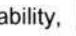

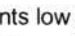
Based on these observations, mixtures of bad bonding mechanisms could also be observed. A combination of low bonding temperature and small bonding pressure were found to be insufficient in achieving good mechanical integrity between 280-290 °C with less than 0.262 MPa. Low bonding temperature reduced the wettability of the Au₈₀Sn₂₀

solder and low bonding pressure induced partial bonding due to insufficient contact with the solder.

Hence, the LD performance was influenced not only by the thermal management of the packaging design, but also attributed by the bonding stress induced. Interfacial investigation of the bonding interface was used to explain the performance of the LDs and can be summarized in the table below.

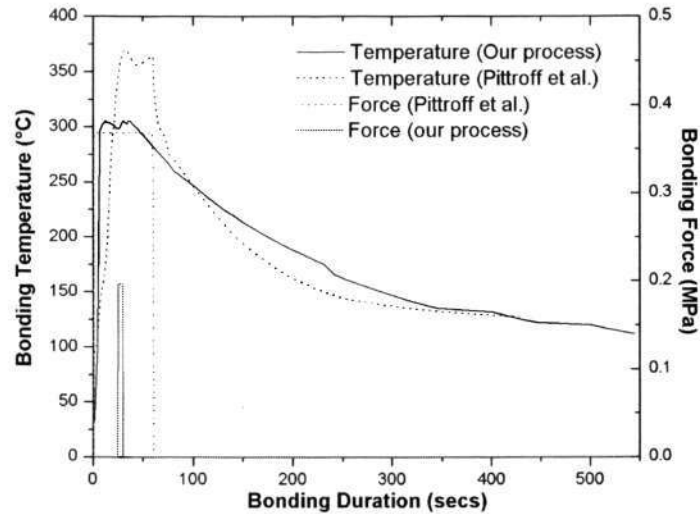
Table 10. Experimental matrix for face-down bonding of 3 μm ridge-waveguide LDs using Au80Sn20 solder. The bonding window is derived from both interfacial and parametric evaluations.

Dwell Time (5 secs)		Bonding Force (MPa)							
		<0.196	0.196	0.262	0.327	0.392	0.458	0.523	>0.523
Temperature (°C)	320	insufficient wettability	low yield	low yield	low yield	low yield	low yield	device degradation	device degradation
	310	poor bonding integrity			low yield	low yield	low yield	low yield	device degradation
	300	poor bonding integrity							device degradation
	290	poor bonding integrity							device degradation
	280	poor bonding integrity							device degradation

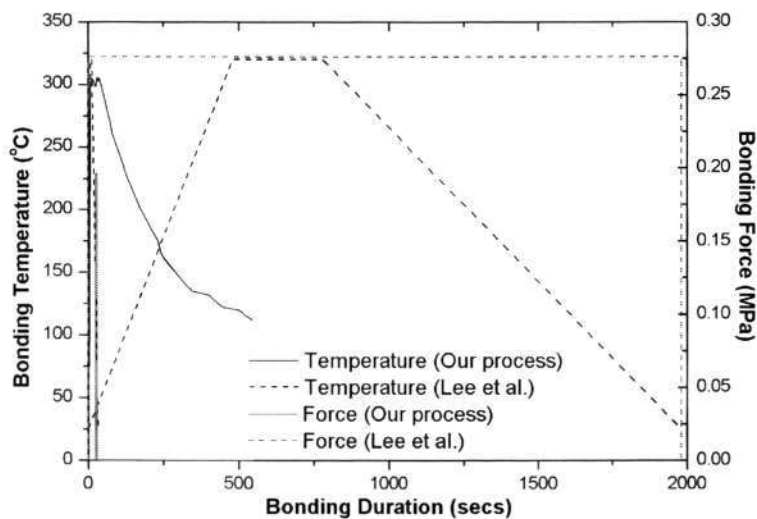
where  represents insufficient wettability,  represents low yield,  represents device degradation,  represents poor bonding integrity, and  represents a mixture of bad bonding effects, and  represents the bonding window.

With the optimized bonding process window, its reflow profile was then compared with existing bonding techniques as shown in Figure 4-27. With reference to Lee et al.'s approach [78], the bonding temperature was reduced from 320 °C to 290 °C. The bonding duration was significantly reduced from 13 mins to 5 s. Although Pittroff et al.'s method [6] offered similar bonding duration, the bonding temperature was significantly higher at

370 °C. The bonding pressure required to achieve good bonding integrity was also reduced to 0.196 MPa as compared to the above-mentioned methods.



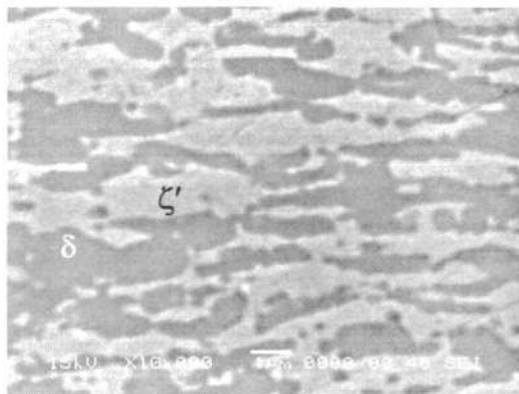
(a)



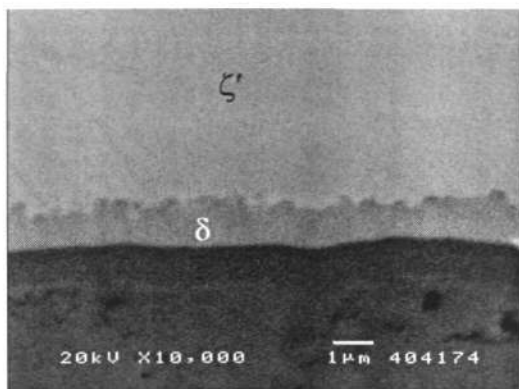
(b)

Figure 4-27 Comparison of different bonding profiles for Au80Sn20 solder joint. Bonding pressure, temperature and time were three key bonding parameters used. (a) The heating and cooling rate of the Pittroff et al. method were measured using Semiconductor Equipment Corp. Model 860 die bonder; (b) The heating and cooling rate of the Lee et al. bonding process were assumed to be linear.

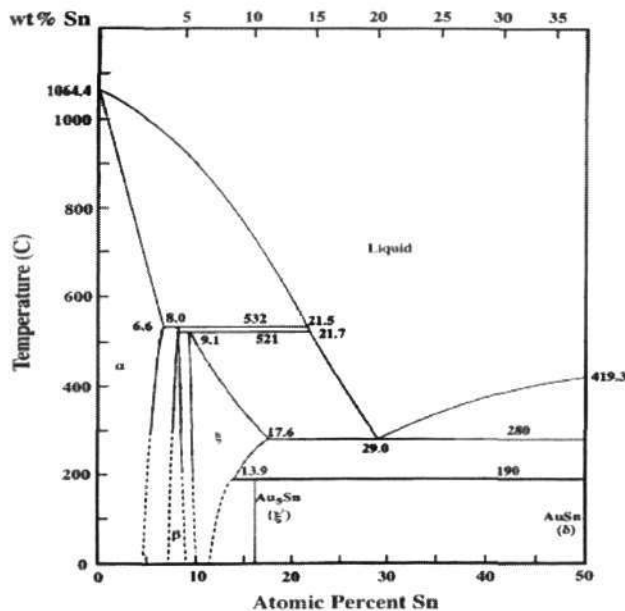
4.4 Microstructure of Solder Interconnect



(a) Before reflow



(b) After reflow



(c) Au-Sn phase diagram [139]

Figure 4-28 Microstructure evolution of Au80Sn20 solder (a) before and (b) after solder reflow with Au/Ni metallization. (c) Phase diagram of binary Au-Sn system.

The Au80Sn20 solder preform has an initial coarse random distribution of dark and light domains as shown in Figure 4-28(a)-(b). EDX analysis showed a high tin content of 35-40 wt% in the dark domain while the light domain has a smaller tin content of 8-12 wt%. The dark and light domains can be confirmed to be δ and ζ' phases with the phase diagram as shown in Figure 4-28(c). When the temperature lowers below the eutectic melting point of 280 °C, δ and ζ phases will solidify simultaneously in the solder interconnect as follows [139]:



At temperature lower than 190 °C, ζ phase is transformed to ζ' (Au_5Sn) phase, an extension of ζ phase at low temperature.

In a reflow process, material transportation of diffusing species occurs by atomic motion. This chemical reaction is called diffusion and the factors that influence the chemical reaction is the diffusing species and temperature. The rate of atomic diffusion depends on the magnitude of the diffusing species as well as the temperature at which it is run. As the temperature increases, the atoms, which have higher kinetic energy, move faster and therefore collide more frequently. In this atomic transportation, the atoms must overcome the activation energy for chemical reaction to occur. The relationship between the temperature and the rate of a reaction typically depends on the temperature at which the reaction is run and an Arrhenius equation can be used to determine the activation energy for a reaction,

$$D = D_0 \exp\left(-\frac{Q_d}{RT}\right) \quad (4-3)$$

where k is the rate constant for the reaction, Z is a proportionality constant that varies from one reaction to another, E_a is the activation energy for the reaction, R is the ideal gas constant in joules per mole kelvin, and T is the temperature in kelvin.

The diffusion coefficient can be identified by studying the intermetallic growth at various reflow durations. By taking the natural logarithms of equation 4-3, the activation energy can be found.

$$\ln D = \ln D_0 - \frac{Q_d}{R} \left(\frac{1}{T}\right) \quad (4-4)$$

Before discussion on the intermetallics formed during the reflow process, the possible intermetallics formed in the Au-Ni, Ni-Sn and Au-AuSn binary systems were discussed. As shown in Figure 4-6, two phase compounds were formed in the Au-rich eutectic 80Au/20Sn solder; AuSn and Au₅Sn. The AuSn phase compound has lower surface tension as compared to Au₅Sn during molten state. The lower surface tension of AuSn phase compound could result in higher affinity to the interface rather than in the bulk solder. During solder, Sn from the solder could react with Ni to form IMCs at the interface. From the Ni-Sn phase diagram, several intermetallics could be formed; Ni₃Sn₄, Ni₃Sn₂ and Ni₃Sn. Ni₃Sn₄ is likely to be formed in high Sn content bearing solders such as Sn-Pb and Sn-Ag-Cu solders while Ni₃Sn₂ and Ni₃Sn is likely be formed in low Sn content bearing solder such as 80Au/20Sn solder. Depending on the bonding condition, different IMCs could be formed. In the Au-Ni system, the mutual solubility is limited at low reflow temperature of 320 °C. The limited interaction between Au and Ni caused the Ni and Sn to be the dominant chemical interaction during reflow. To further understand the intermetallics formed at the interface, the ternary Au-Ni-Sn phase diagram was discussed. When Au-rich 80Au/20Sn solder reacts with Ni, the AuSn and the Au₅Sn phases could react with Ni to form IMCs. In the AuSn phase compound, three possible intermetallics could be formed; Ni₃Sn₄(Au), Ni₃Sn₂(Au) and AuSn(Ni). The concentration of Ni can vary from 75 to 90 at%, depending of the types of IMCs formed. In the Au₅Sn phase compound, the concentration of Ni can varies from 17 to 70 at% and Au₅Sn(Ni), Ni₃Sn₂(Au) and AuSn(Ni) IMCs could be formed.. During reflow, Ni diffused into the solder to form IMCs at the interfaces. Due to the low Sn concentration in the 80Au/20Sn solder, the chemical interaction between Ni and Sn were limited and the formation of Ni₃Sn₄(Au) IMC was not likely to be present. The diffusivity of Ni into the solder was further limited by the short reflow condition and the low bonding temperature. Hence, Ni₃Sn₂(Au) IMC was also not likely to be present in the solder joint. During

reflow, Ni diffusion into the Au_5Sn phase compound could form $\text{Au}_5\text{Sn}(\text{Au})$ IMC and Ni diffusion into the AuSn phase compound could form $\text{AuSn}(\text{Ni})$ IMC. As mentioned earlier, due to the lower surface tension in AuSn phase compound compared to Au_5Sn phase compound, the AuSn phase compound would coalesce to the interfaces while the Au_5Sn phase compound remained at the center of the solder joint. The higher affinity of AuSn phase compound to the interfaces forms $\text{AuSn}(\text{Ni})$ IMCs. Furthermore, in the Au-Ni-Sn chemical interaction, the primary chemical interaction in the diffusion process involved Ni and Sn. Due to the lower Sn concentration in the Au_5Sn phase compound (17.6 at%) as compared to AuSn phase compound (50 at%), diffusion of Ni into the Au_5Sn phase compound was slower and limited. Hence, Au_5Sn phase compound was not observed in the solder joint.

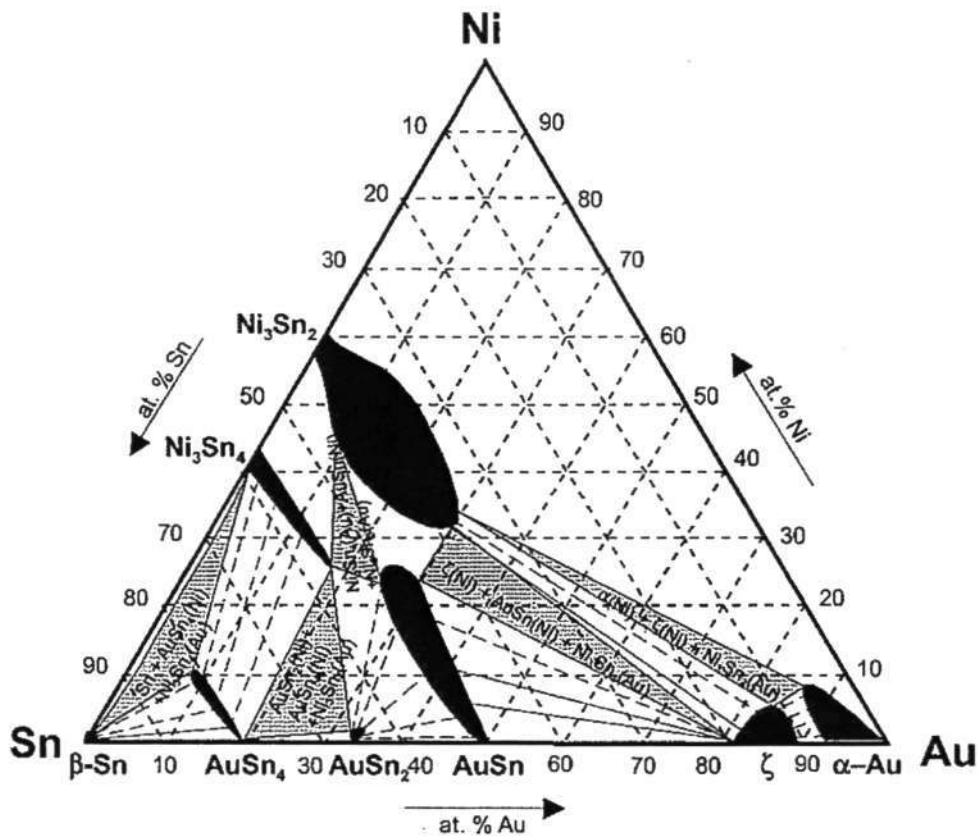


Figure 4-29 Ternary phase diagram of Au-Ni-Sn system.

Between 280 °C to 320 °C reflow temperature, chemical reaction between Au and Ni is unlikely to occur. Ni reacts largely with Au-Sn intermetallics to form Au-Ni-Sn IMCs. Due to the short reflow duration and low Sn content in the 80Au/20Sn solder, the rate of chemical reaction was limited. While it is necessary to form IMC at the interfaces for chemical bonding between the LD and the heatsink to occur, too thick an IMC layer can be a source of mechanical weakness in soldered joints due to its brittle cracking, or delamination. The thickness of the IMC layer can also be reduced by reducing the temperature and duration of the reflow process.

When Au₈₀Sn₂₀ solder was reflowed onto Au/Ni metallization, δ phase was observed to coalesce at the solder/heatsink interface as shown in Figure 4-28(b). The possibility of δ phase compound moving towards the interface and ζ' phase remaining at the center of the solder joint, could be postulated by the lower surface tension in δ phase than ζ' phase [167]. The δ phase had greater affinity to the Ni layer than the ζ' phase due to its higher wettability. Hence, δ phase compound coalesced toward the Ni layer while the ζ' phase compound remained at the center of the solder joint. Since the ζ' phase has good mechanical and thermal properties [168], the mechanical integrity of the solder joint and heat transfer may be improved. For partially bonded LDs (See Figure 4-30), the microstructure at bad bonding regions such as voids and delaminations showed random distribution of Sn-rich and Au-rich whereas the Sn-rich phase drifted towards the edges of the solder interconnect at good bonding regions. This signified that the Sn-rich phase had higher affinity with the interface. This interfacial interaction was further observed for well-bonded LDs.

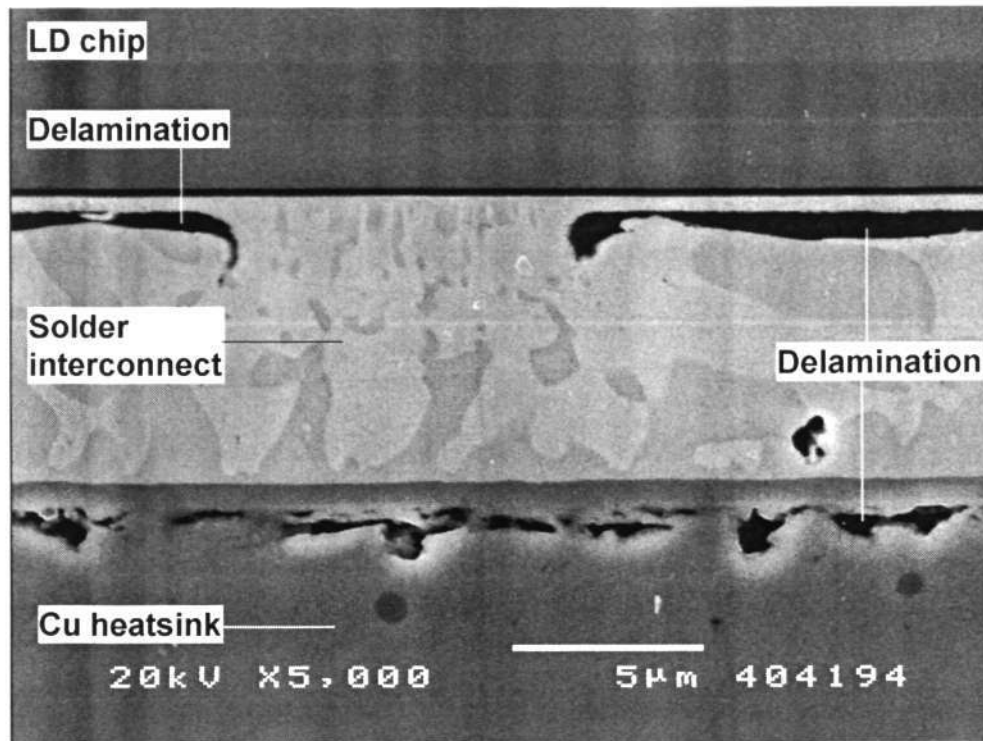


Figure 4-30 Delaminations observed in partially bonded LDs.

During soldering, complete dissolution of Au from the LD into the solder joint could be observed. As depicted in Figure 4-31, SEM/EDX analyses showed that the solder joint comprised of a layer of Sn-rich phase near the LD/solder and solder/heatsink interfaces, Au-rich phase at the center of the solder joint, and a layer of (Au,Ni)Sn IMC at the solder/heatsink interface. Metallurgical interaction between Sn and Pt form PtSn and PtSn₄ IMCs at the LD/solder interface. The intermetallic layers at the LD/solder interface have already been investigated elsewhere [144] and will not be elaborated here. Instead, the IMC at the solder/heatsink interface will be emphasized. Interfacial reaction between eutectic Au₈₀Sn₂₀ solder and the Au/Ni bonding pad was studied since the formation of IMC in the solder joint depended on the multi-layer metallization, solder alloy and application condition.

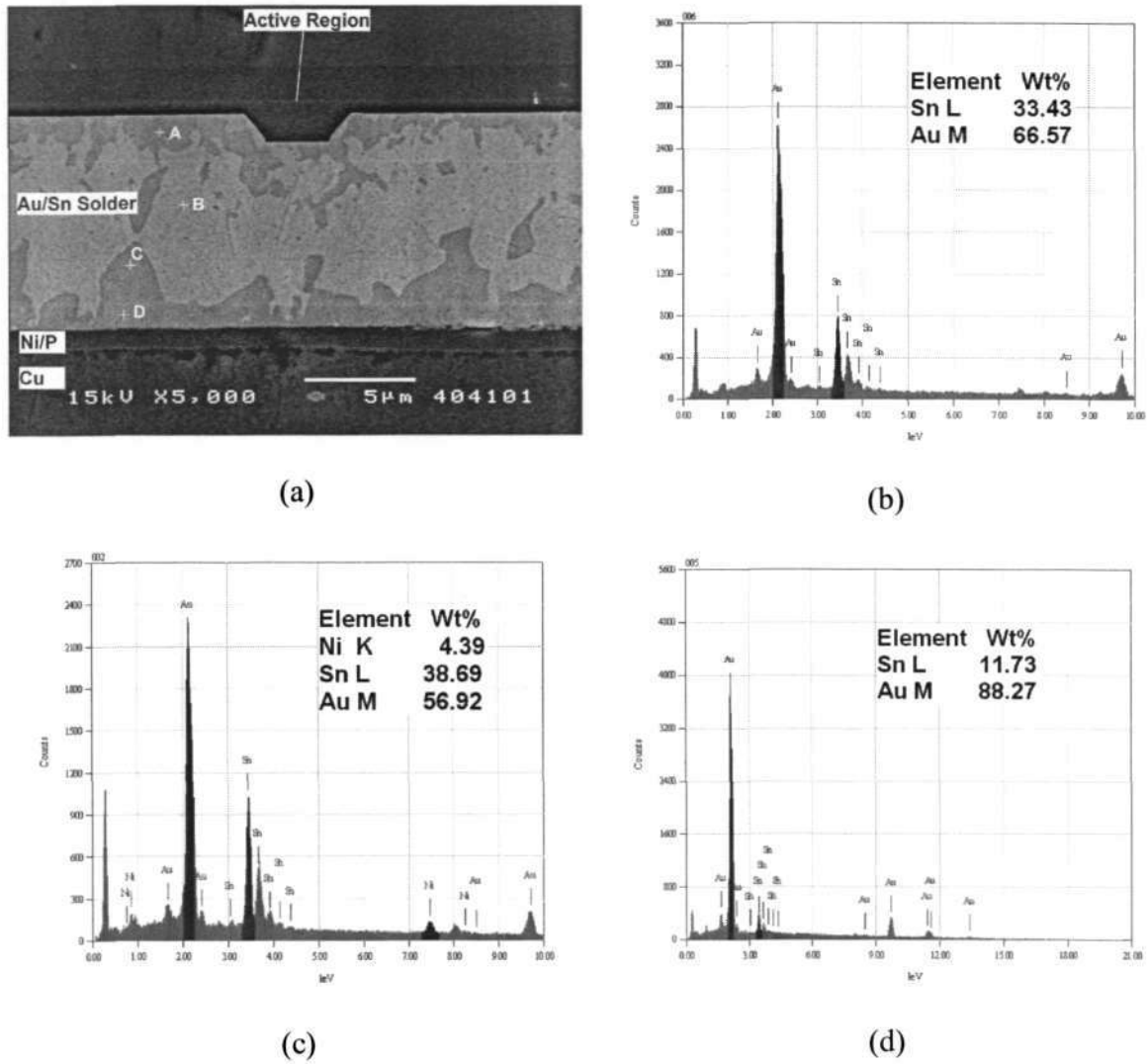
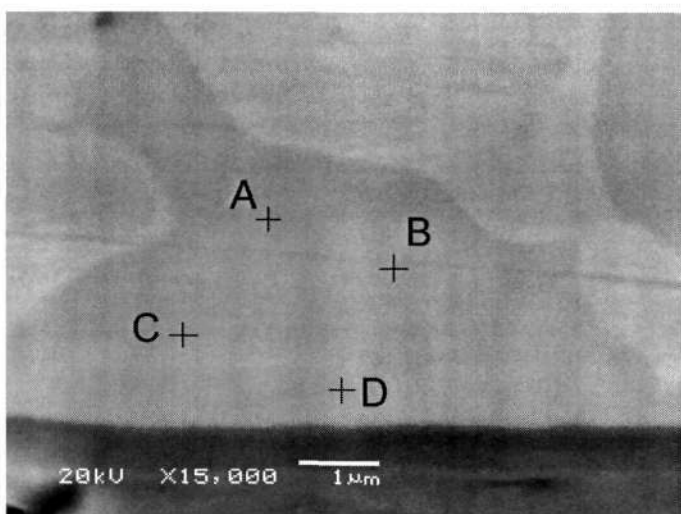


Figure 4-31 (a) Cross-sectional view of as-solidified LD bonding interface; (b) δ phase is identified at regions A and C; (c) (Au,Ni)Sn IMC at region D; and (d) ζ' phase at region B.

During the heating stage, quick dissolution of Au from the heatsink into the solder layer inevitably exposed the Ni layer, which also diffused into the solder. As shown in Figure 4-32(b), Ni could only be detected within 1-2 μm of the Sn-rich δ phase and the amount of Ni varied according to the location of the δ phases. For those δ phases further away from the interface as depicted at region B and C, the concentration of Ni was approximately 1 wt%. For those nearer the interface, the concentration of Ni could be as high as 3 wt%. The low concentration of Ni detected is due to the limited solubility of Ni

into solder [169]. As the concentration of Sn remained unchanged, substitution of Ni with Au was expected to form (Au,Ni)Sn IMC. (Au,Ni)Sn and (Au,Ni)₃Sn₂ were previously reported at the solder/heatsink interface after a long reflow duration of 75 s at a peak temperature of 315 °C, and the solder joints were aged at 200 °C for 365 days [170]. (Au,Ni)₃Sn₂ IMC layer was not detected here as this modified bonding process had a short reflow duration of 5 s.



Region	Sn(L)	Au(M)	Ni(K)
A	37.7	62.3	-
B	38.14	60.66	1.21
C	38.08	60.48	1.44
D	38.46	58.00	3.54

(b)

(a)

Figure 4-32 (a) Cross-sectional view of solder/heatsink interface; (b) SEM/EDX analyses of Ni concentration at different locations of δ phase at the solder/heatsink interface.

EDX mapping of the solder joint was also conducted as shown in Figure 4-33. Random distribution of Sn-rich and Au-rich phases was observed in the solder joint. Further analysis of the 80Au/20Sn intermetallics in the solder joint was carried out using EBSD technique to identify the phase transformation. Reasonable matching of standard diffraction patterns from the database of indices for Au-Sn intermetallics was performed. At the Sn-rich region, a hexagonal δ phase crystal structure was detected. However, at the Au-rich region, two different crystal structures were observed; a trigonal ζ' phase and a hexagonal β phase. Although ζ' and β phases have very similar chemistry, their

crystallographical patterns are obviously different as depicted in Figure 4-34. Based on this crystallographical diffraction patterns, the solder joint actually consist of three phases; δ , ζ' and β phases. Based on the EDX and EBSD analysis, mapping of the solder joint was carried out as shown in Figure 4-34,

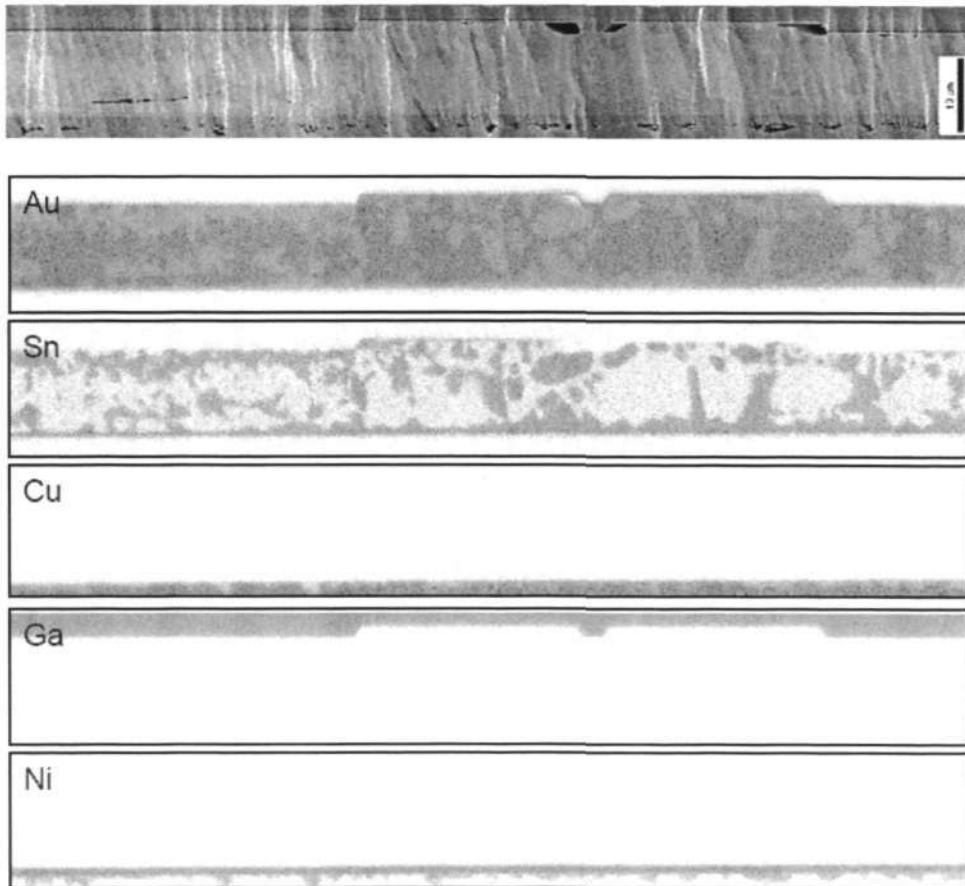
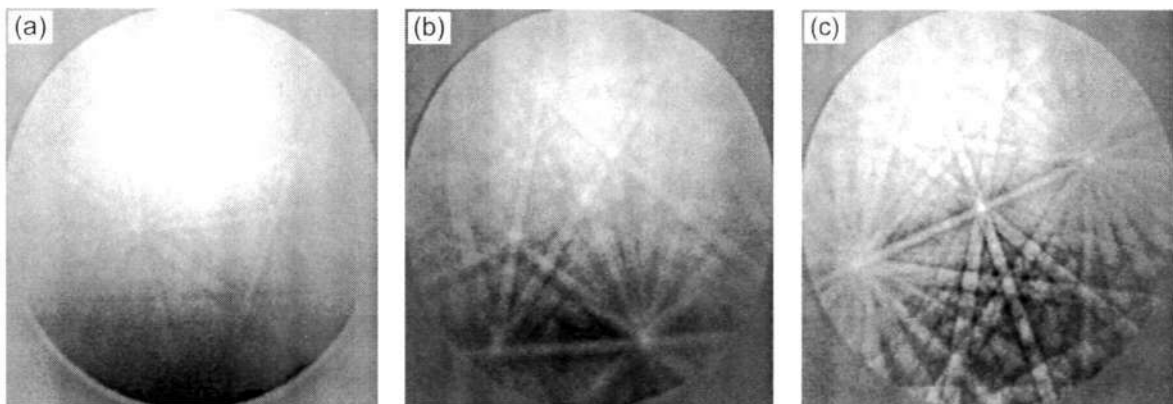


Figure 4-33 Typical SEM micrograph Au80Sn20 solder joint and its corresponding EDX mapping results.

The formation of this β phase shows that the Au layer from the LD electrode and Cu heatsink diffused not only into the δ phases to form ζ' phases, but also into the ζ' phases to form β phases during reflow. However, the diffusivity rate of Au into the δ and ζ' phases is unknown and requires further investigations. During reflow, Sn and Ni interdiffused to form IMCs. However, due to the low Sn content in these ζ' and β phases, diffusion of Sn to the interfaces were limited, resulting in slow IMC kinetic growth

during aging [86, 170]. The Au-rich β and ζ' phases acted as a form of diffusion barrier to the formation of interfacial IMCs. Song et al. [170] have demonstrated that the IMC thickness was only 6 μm after 200 °C thermal aging for 365 days. The metallurgical stability of the solder joint is an important aspect in optoelectronics packaging as these LDs are expected to have a service lifetime of 10^5 hrs [32, 171, 172]. Furthermore, the mechanical properties of a solder joint is governed by the microstructure and interfacial IMCs formed.



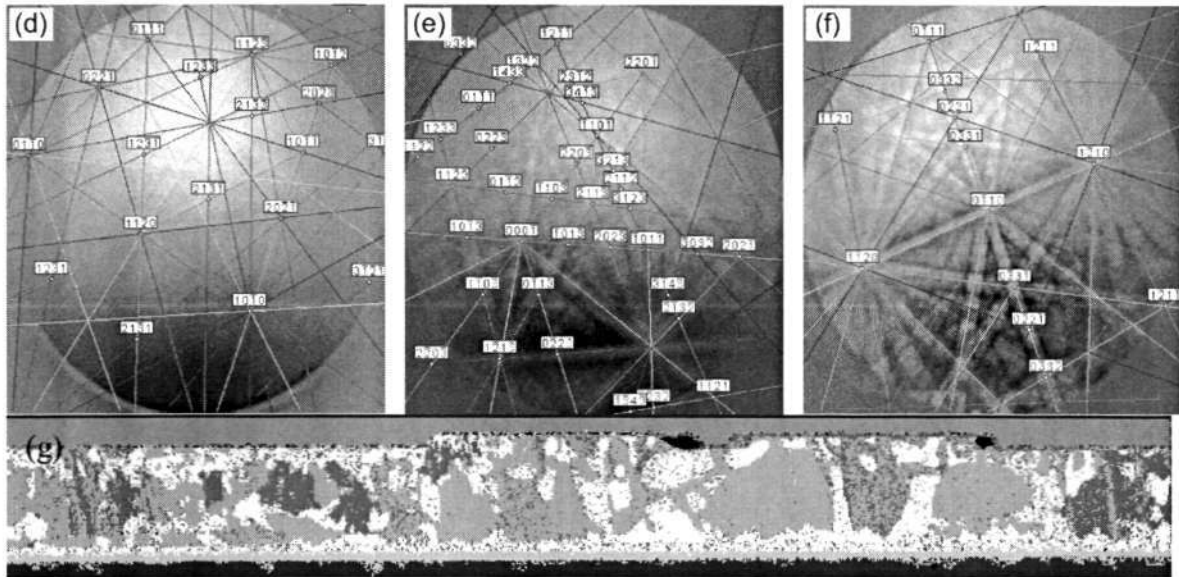
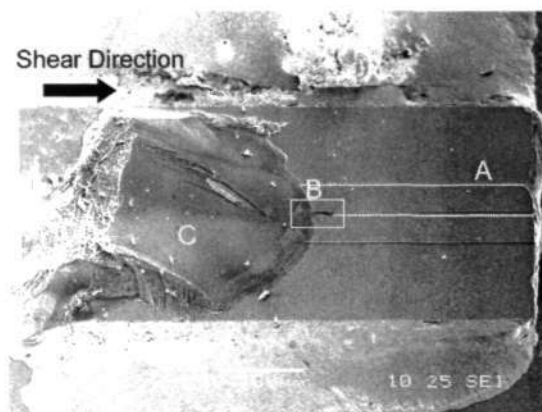


Figure 4-34 EBSD diffraction patterns of intermetallics formed in the solder joint. (a) Diffraction pattern found from the Sn-rich region and (b)-(c) diffraction patterns found from the Au-rich phases. Kikuchi bands and poles of (d) δ , (e) ζ' and (f) β phases was indexed according to the lattice orientations on the specimen surface. (g) EBSD mapping of the solder joint.

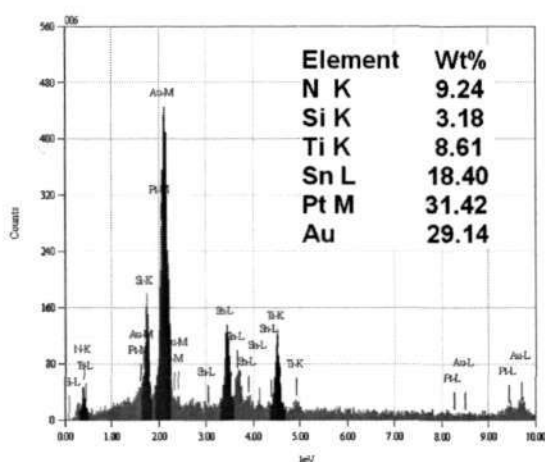
4.5 Mechanical Strength and Failure Mode



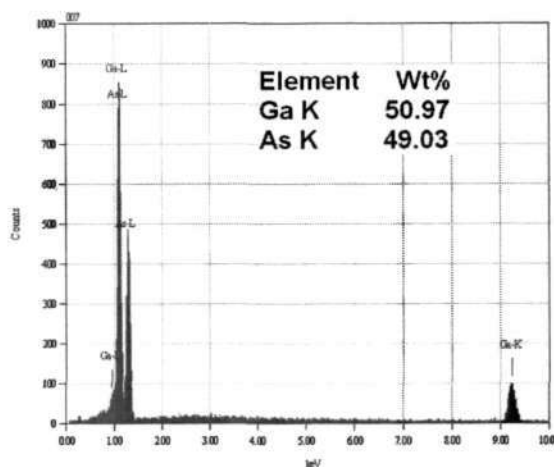
(a)



(b)



(c)



(d)

Figure 4-35 (a) Typical planar-view of well-bonded LDs after shear test; (b) Magnified view of sheared LD at region B; (c) SEM/EDX analysis of fracture mode at region A; (d) SEM/EDX analysis of fracture initiation at region C.

To study the mechanical strength of the bond, die shear testing was performed until complete fracture of the joint. Identification of the material brittleness/ductility and fracture behavior of the solder joint were then determined with metallurgical investigation. The micrographs in Figure 4-35 show a typical well-bonded sample with LD residues remaining on the heatsink after shear test. At region C, GaAs was detected while Si, N, and Ti/Pt/Au metallization were detected at region A. This showed that the fracture initiated at the GaAs substrate and propagated towards the SiN layer. Brittle fracture occurring within the LD and Ti/Pt/Au metallization layers remaining on the

heatsink, unequivocally demonstrated that the solder joint yield good mechanical properties. These results showed that the Ti/Pt/Au metallization provide strong adhesion and mechanical stability for the SiN layer [173].

As depicted in Figure 4-35(b), the fracture mode appeared to occur at an interface. To further verify the fracture mechanism, depth profiling was conducted at region A of the fracture surface. Secondary Ion Mass Spectroscopy (SIMS) was used to analyze the distribution and concentration of the elements of interest on the fracture surface as shown in Figure 4-36. Firstly, Ga and Si were detected simultaneously off the surface, followed by Ti. This further substantiated that the fracture location was between the GaAs and the SiN passivation layer. Thereafter, Au was detected to diffuse completely into the joint. Due to the large sampling rate and thin Pt barrier layer, Pt was not detected.

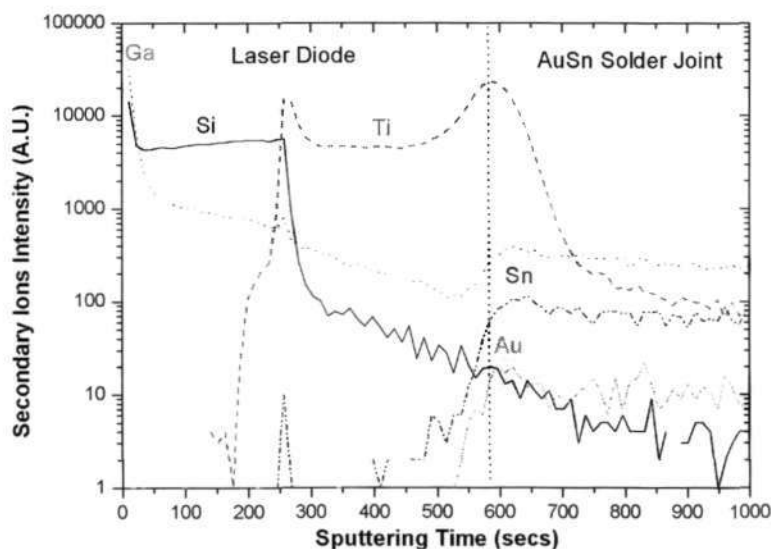


Figure 4-36 SIMS depth profile at region A of the fracture surface. Ga and Si were detected off the fracture surface.

However, a separate depth profiling was conducted on the epitaxial metallization of the LD. Analysis showed the presence of a thin Pt layer in Figure 4-37.

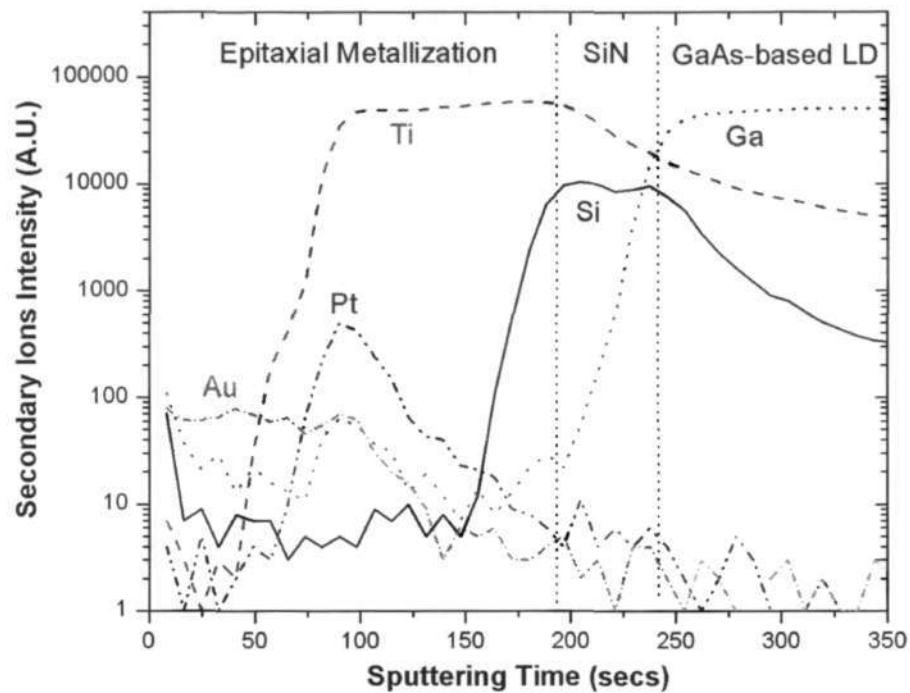


Figure 4-37 SIMS depth profile on the LD epitaxial metallization.

4.6 Summary

A modified fluxless face-down bonding of LDs using Au80Sn20 solder has been introduced. This modified bonding process offered to resolve the issues of ridge damage and misalignment. For long-term reliability, hard Au80Sn20 solder was used to enhance fatigue and creep resistance. The microstructural evolution of the solder joint was investigated. The interconnect comprised of a layer of Sn-rich δ phase near the LD/solder and solder/heatsink interfaces, Au-rich β and ζ' phases at the center of solder joint, and a layer of (Au,Ni)Sn IMC at the solder/heatsink interface. Au diffused into δ phase to form ζ' phase and into ζ' phases to form β phase. Ni diffused into the δ phase to form (Au,Ni)Sn IMC at the solder/heatsink interface. The δ phase was postulated to coalesce at the interfaces due to lower surface tension. The solder joint also possessed excellent mechanical properties. Mechanical testing showed that the fracture mode occurred within

the LD, at the GaAs/SiN interface. As such, the underlying integrity of the die attach was achieved using this modified bonding methodology.

In electronic packaging, bonding integrity in the solder joint is the primary concern. Unlike electronic packaging, packaging of optoelectronic components requires further attention to the electrical and optical properties of the LDs. Both destructive and non-destructive testing methodologies were explored to generate a comprehensive understanding on the integrity of the solder joint and functionality of the LD. The effect of bonding parameters on the bonding integrity and the performance of the LD was established. The integrity of the bonding interface was found to be strongly dependent on the bonding time, bonding temperature and bonding pressure. The bonding time should be sufficient to permit formation of IMC at the LD/solder and solder/heatsink interfaces. The bonding pressure should provide sufficient contact during bonding. The bonding temperature should also be sufficiently high to improve the wettability of the solder. Electro-optical characterization showed that the LD performance was largely dependent on the bonding process. Weak adhesion properties in the solder joint resulted in marginal optical output of 80-120 mW. Optimal optical output of >150 mW was achieved when good bonding integrity was achieved. However, large bonding pressure damaged the LD heterostructure and caused threshold current to deteriorate due to bandgap deformation. Hence, it is important not only to improve the LD performance with good bonding integrity but also to develop an assembly technology that can reduce strain in order to realize high output power and high reliability.

From the test program, a robust bonding process window using AuSn solder was established. The primary advantages of this bonding window are its short bonding cycle, low bonding pressure incurred, lower bonding temperature, and reproducible reliable

solder joint. This modified bonding process demonstrated a significant reduction in bonding time to merely 5 s at 290 °C. The bonding pressure was also moderated to less than 0.2 MPa. Based on the optimized bonding profile, a comprehensive investigation of different bonding techniques should be conducted to identify the optimal bonding technique.

CHAPTER 5

PERFORMANCE VERIFICATION OF BOND LASER DIODE WITH NUMERICAL SIMULATION

5.1 Introduction

Thermal properties are one of the important factors in semiconductor laser characterization because it is associated with the threshold current, output power, emission wavelength, as well as the device reliability. To successfully implement a packaging concept, fundamental knowledge of the thermal capabilities of the packaging design will facilitate prominent advantages to the development of the packaging technology. Hence, it is mandatory to acquire theoretical understanding of the thermal behavior of a laser diode (LD) since its performance depends largely on the heat generation and dissipation it.

In this chapter, the thermal behavior of packaged laser diodes will be studied using FE modeling. FE modeling will be used to study the temperature gradient across the packaged LD. Subsequently, the thermal behavior of the packaged LD will be correlated to understand the physics of heat dissipation with different packaging designs. This thermal simulation exercise will also serve to verify the performance capability for each bonding configuration.

5.2 Thermal Behavior of Semiconductor Lasers

5.2.1 Thermal Analysis using Electronic Bandgap Calculations

It is well known that the emission wavelength of semiconductor laser is a sensitive indicator of temperature. Hence, determination of temperature change in a semiconductor laser is usually deduced from its emission properties. Before further discussion, it is important to highlight the temperature-dependent characteristics of semiconductor lasers.

These semiconductor materials have temperature-dependent quantities, with functional form often fitted to the empirical Varshni form [174],

$$E_g(T) = E_g(0) - \frac{\alpha T^2}{T + \beta} \quad (5-1a)$$

where α and β are adjustable (Varshni) parameters. The temperature-dependence bandgap for GaAs [175, 176] is

$$E_g(GaAs) = 1.519 - \frac{5.405 \times 10^{-4} T^2}{T + 204} \text{ in eV} \quad (5-1b)$$

and the temperature-dependence bandgap of InAs [177] is

$$E_g(InAs) = 0.42 - \frac{2.5 \times 10^{-4} T^2}{T + 75} \text{ in eV} \quad (5-1c)$$

The emission wavelength has the same temperature dependence as the bandgap energy [178]:

$$\lambda(T) = \frac{1.24}{E_g(T)} \text{ in nm} \quad (5-2)$$

The lasing wavelength increased in proportion to the temperature rise in the active region because of the bandgap shrinkage effect [7]. When the temperature in the active region

rise, the center wavelength shifted to a larger wavelength as shown in Figure 5-1. Deabsorption of spontaneous and simulated emission and non-radiative recombination at higher temperature resulted in the shift of laser emission. With an increase of temperature, the carrier distribution broadened due to carrier scattering. As a consequence, more carriers must be injected into the active region to achieve the same magnitude of peak modal gain. With more carriers, wavelength shift due to bandgap renormalization and band filling increased. These led to a reduction of the fundamental bandgap of the material.

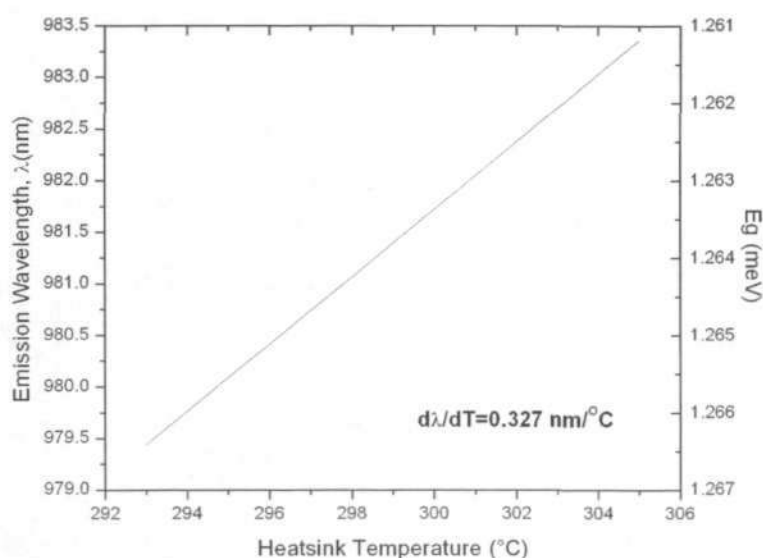


Figure 5-1 Calculated emission wavelength as a function of heatsink temperatures using electronic band structure theory.

These semiconductor lasers were calculated to have a wavelength tuning coefficient of 0.327 nm/°C from Varshni empirical equations [28]. This temperature-dependent emission wavelength property was calculated based on the electronic band structure theory. Utilizing this emission wavelength as a temperature sensitive parameter, the estimated temperature rise in the active region can be compared with the experimental measurements.

5.2.2 Transient and Steady-State Analysis

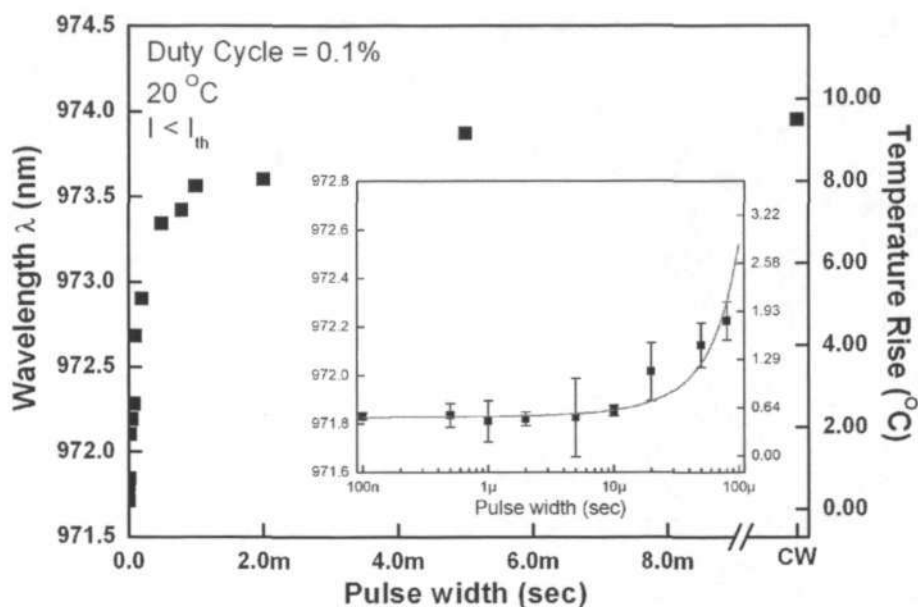


Figure 5-2 Transient temperature of the active region is derived from the calibrated emission properties. Temperature was observed to rise within micro-seconds and saturate in milli-seconds.

To understand the heat flow in the diode, it is important to study the transient behavior of the LDs. Pulse measurement of varying pulse widths showed that the temperature in the active region did not increase during the first 1 μ sec of operation. As the pulse width increased, transient heating could be observed as depicted in Figure 5-2. The emission wavelength (temperature rise) rose abruptly and saturated within several milliseconds. Localized heating was confined to the active region. The thermal heat capacity of the LD prevented the heat generated at the junction from diffusing far from it since the thermal conductance of the passivation layer and the GaAs substrate was much lower than the metal electrode. From the analogy of heat conduction, the heat generated in the active region spread to its adjacent layers after 1 μ sec. The time for the excess heat energy to be transported to the GaAs substrate and reached thermal equilibrium depends

on the device and its surrounding medium. Likewise, the temperature in the active region was also observed to vary with duty cycle as shown in Figure 5-3. When the frequency of the pulse repetition rate increased above 10%, the temperature distribution across the LD was non-uniform and the temperature in the active region increased exponentially till cw operation. At high pulse repetition rate, the temperature rise in the active region might lead to performance deterioration.

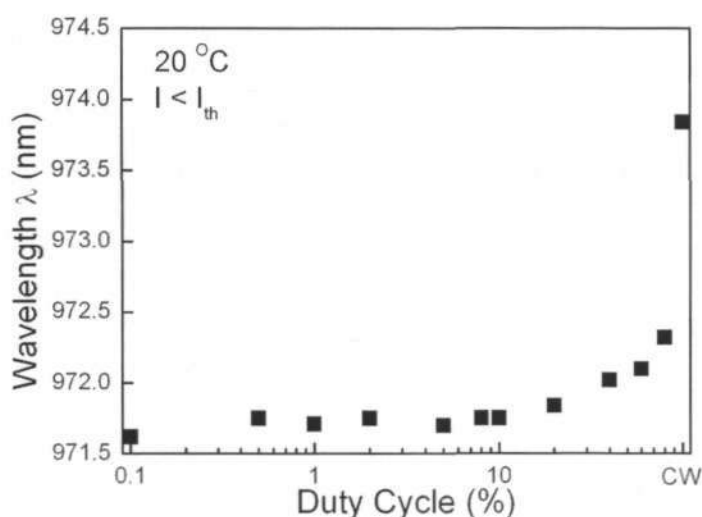


Figure 5-3 Influence of pulse repetition rate on the temperature characteristics of the LDs.

To effectively study the temperature-dependent behavior of these LDs, spectral shift of spontaneous emission peak in a 0.1 μ sec pulsed operation with a duty cycle of 0.1% was conducted at different heatsink temperatures. These LDs demonstrated a wavelength tuning coefficient of 0.312 nm/ $^{\circ}$ C and the spectral shift was approximately the same as that of bulk GaAs, 0.3 nm/ $^{\circ}$ C [179]. The temperature rise and its associated thermal resistance were deduced from the comparison of emission wavelength peak in cw and pulsed operation of the laser, since the diode was essentially at the heatsink temperature at short pulses and low duty factor.

Principle of Null Measurement

For these AlGaAs/GaAs LDs, the threshold current density runs in the order of 1-10 kAcm⁻². This represents a large input power of approximately 1.5-15 Wcm⁻², depending on the voltage drop at the junction. This input power is sufficient to elevate the temperature in the active region and produce profound effects on its emission. Hence, the performance of the semiconductor lasers fluctuates with different conditions.

In semiconductor lasers, the temperature rise in the active region is dependent on the ambient temperature and operating condition. Notably, the ambient temperature represents the temperature in the active region at idle condition, and the heat generated in the active region corresponds to the operating condition. Consequently, the temperature rise for CW operation can be determined provided that the wavelength shift is nullified. In the present work, a calibration of $\partial\lambda/\partial T$ was done by measuring the peak wavelength at different ambient conditions. This null measurement utilized a pulsed measurement at various heatsink temperatures.

Firstly, it took approximately 400 ns for the heat to diffuse after the LD was switched on [25], and heat accumulated in the active region was transferred to the heatsink within several micro-s. For pulse lengths shorter than this, therefore, the heat conduction might be ignored and the temperature rise could be calculated from the heat capacity only. The thermal heat capacity of the LD prevented the heat generated at the junction from diffusing far from it. Thus far, it had been assumed that the diode was operated in a manner such that at the start of the pulse, the temperature of the LD was equal to the base temperature. This is true for a single pulse, but for this assumption to be valid for repeated pulses, sufficient time must be elapsed between the application of individual pulses such

that the heat generated within the LD must be conducted away and dissipated. If the pulse repetition rate is too fast, this assumption is not valid. The temperature across the LD would no longer be constant and equal to the base temperature, but would be dependent on this rate. The influence of pulse repetition rate on the active region mean temperature [26] had shown that longer pulses corresponded to a decrease in thermal conductivity, which in turn caused larger temperature rise.

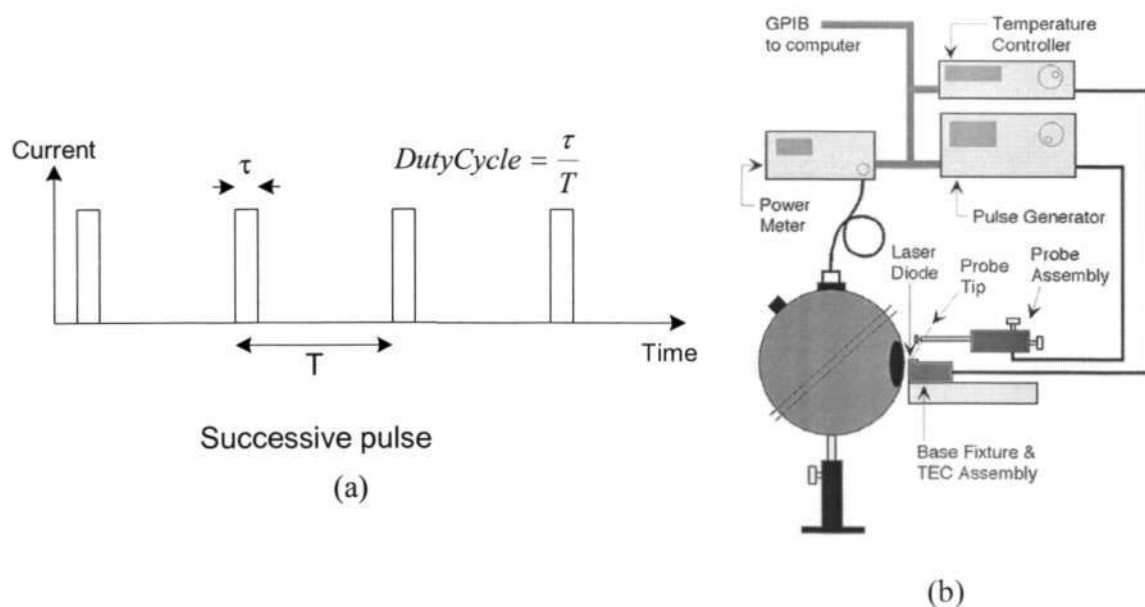


Figure 5-4 Schematic diagram of pulsed LD characterization system. Short pulse width and low duty cycle was performed to prevent parasitic heating in the LD.

Hence, a solution is possible if the off time is sufficiently long so that the temperature distribution across the LD is relatively uniform at the time the next pulse is applied. This solution depended critically on the ability of the structure to conduct the heat from the diode. The thickness and nature of the solder layer, together with the quality of their contact to the LD, were also important. A pulse condition with a very low duty cycle of 0.1% was usually utilized [25]. A precision pulsed current source (ILXlightwave LDP-3811) is capable of producing repetitive pulse with less than 5% overshoot as shown in

Figure 5-3. A short pulses width of 100 ns prevented heat accumulation in the active region and low duty cycle of 0.1% limited parasitic heating due to successive pulses.

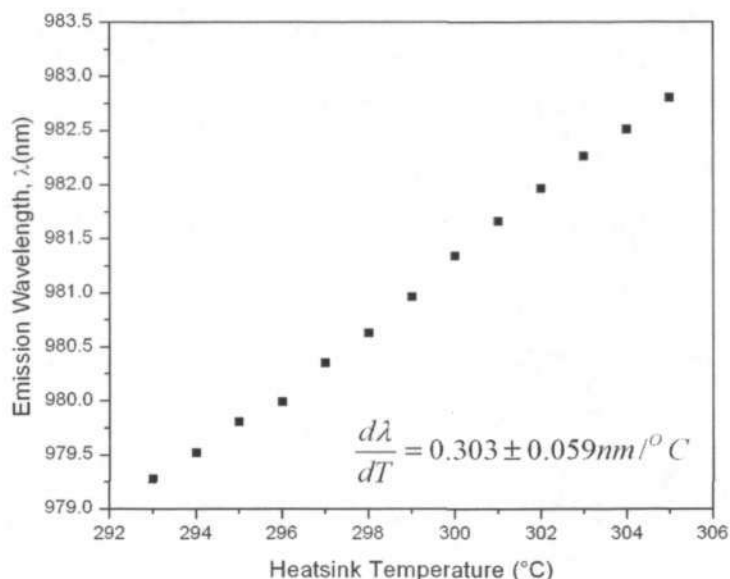


Figure 5-5 Experimental measurement of emission wavelength as a function of various heatsink temperatures.

Despite the mode-hopping phenomenon, a linear wavelength increment of 0.303 ± 0.059 nm/°C could be observed for these LDs as shown in Figure 5-5. This experimental measurements showed close approximation to the calculated value and can be used to measure the thermal behavior of the LDs. M. Voss et al. [30] and W. Engeler et al. [25] also showed similar behavior for these AlGaAs/GaAs LDs. Using this calibration technique, the results were further compared with the simulation results to understand the temperature distribution across the LD.

5.2.3 Radiative Energy Transfer

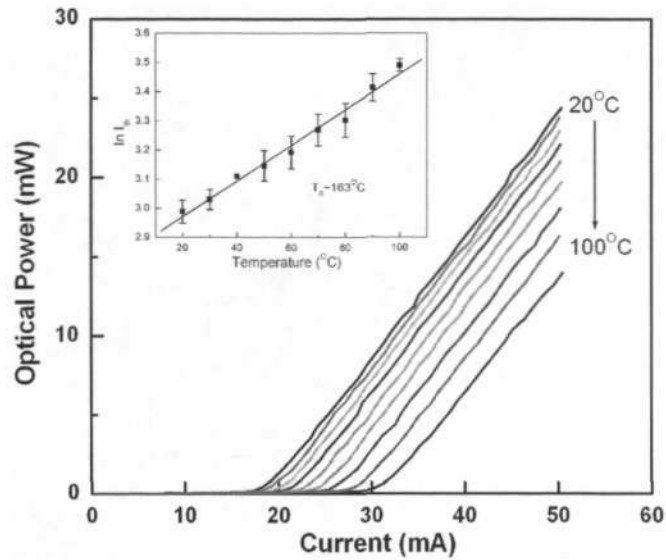
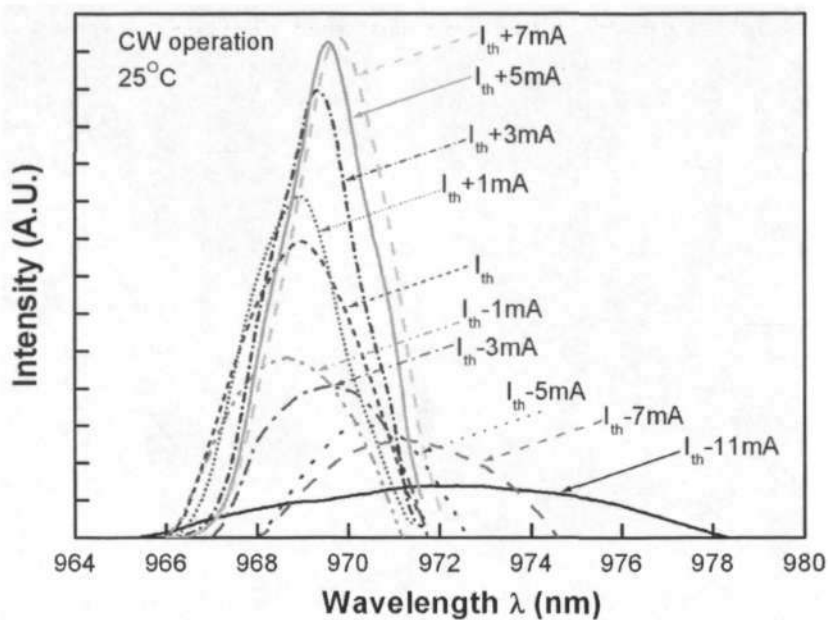
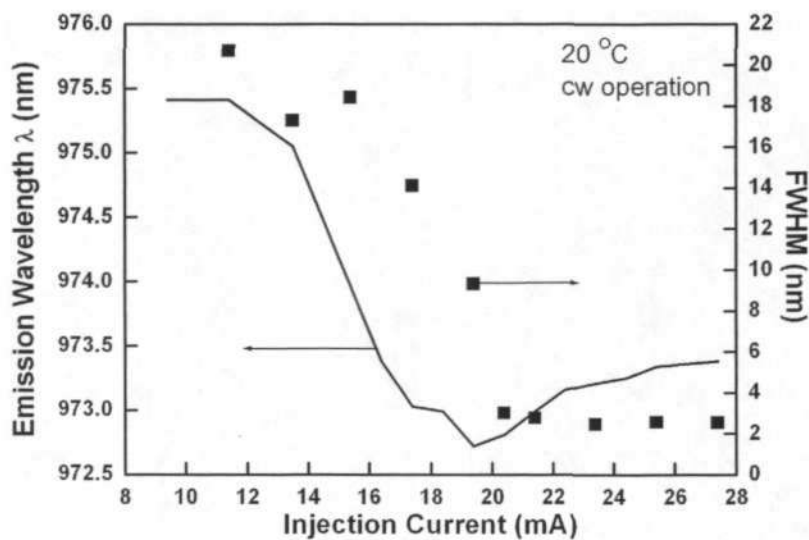


Figure 5-6 Typical light output power versus injection current at a function of heatsink temperature for these LDs under cw operation.

Figure 5-6 shows a typical light output versus current characteristic of these InGaAs/GaAs LDs at heatsink temperatures of 20-100 °C. The characteristic temperature T_0 was estimated to be around 163°C experimentally. Research studies had demonstrated that the characteristic temperature was controlled by intrinsic mechanisms such as temperature-dependence of optical gain and loss and carrier recombination [180-182]. As the temperature increased, higher operating carrier density was required due to the increase of non-stimulated recombination current.



(a)

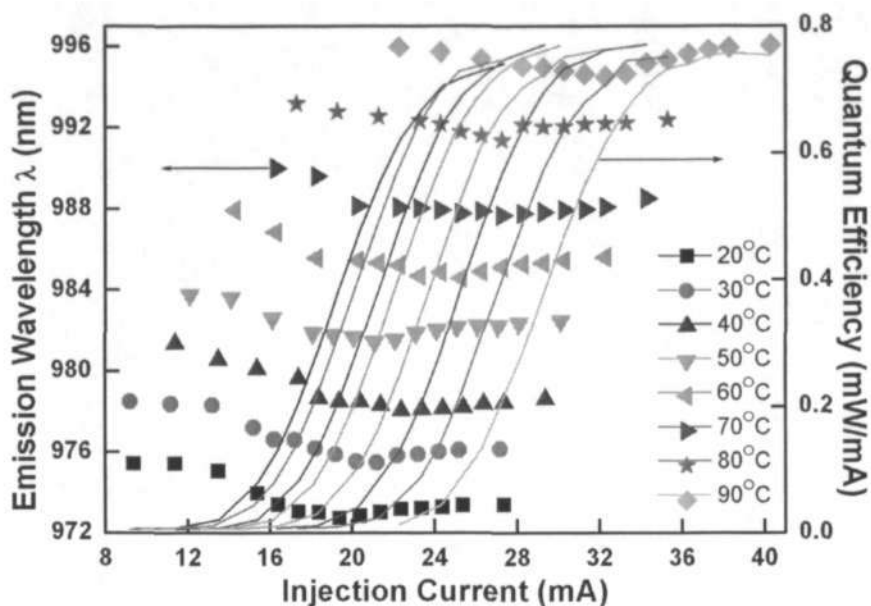


(b)

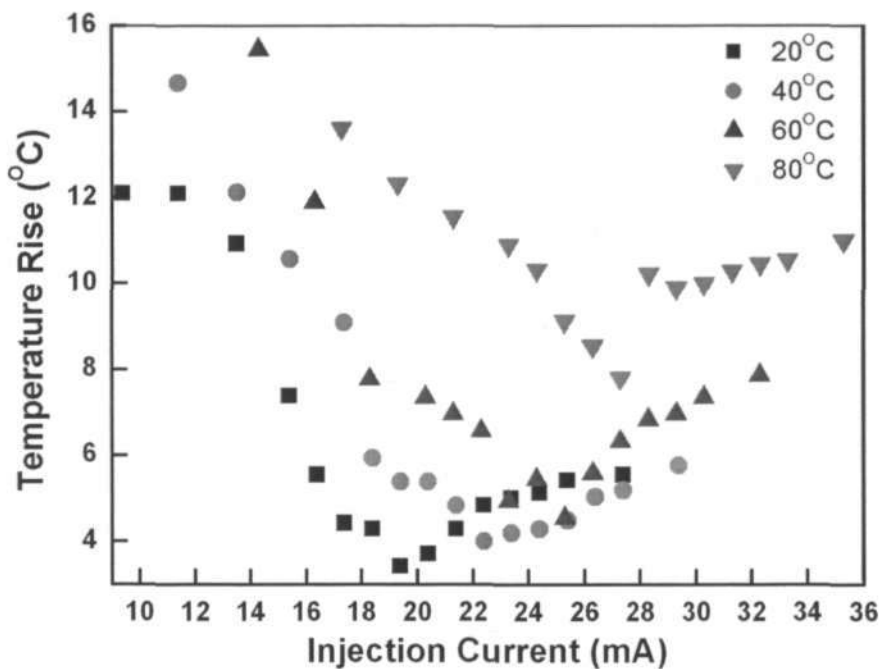
Figure 5-7 (a) Typical emission spectra at different injection currents. (b) Change of emission wavelength and FWHM w around the lasing threshold.

The temperature-dependence of I_{th} , which is usually indicated by T_0 , was further analyzed with emission measurements. By observing the Full-Width Half-Maximum (FWHM) of the emission spectra, together with the shift of the emission wavelength, the lasing threshold can be verified with the measurements obtained from the LI curves. Figure 5-7(a) represents a typical behavior of the emission spectra at different injection currents at

20 °C. From the FWHM measurements (see Figure 5-7(b)), the gain was observed to saturate beyond the lasing threshold. Above the lasing threshold, the carrier density was usually fixed. Hakki and Paoli also reported that the gain at a fixed wavelength increased linearly with current up to the lasing threshold and saturated beyond the lasing threshold [183, 184]. Furthermore, two distinct behaviors were observed. Below the lasing threshold, the emission wavelength was observed to shift towards shorter wavelength whereas a longer shift of emission wavelength occurred beyond the lasing threshold. The shift of emission wavelength was often associated with changes in the refractive index. The change of the refractive index was resulted from the thermal band gap shift and from the change of carrier density in the active region. The effect of band gap shift and injection current will be discussed in the following sections.



(a)



(b)

Figure 5-8 (a) Current dependence of spectral emission peak and differential quantum efficiency. The differential quantum efficiency is given by the solid curve while the dotted points show the spectral measurements at different injection current. (b) Current dependence of temperature rise at the active region for different heatsink temperatures. The temperature in the active region dropped to a minimum at its lasing threshold.

In order to optimize the performance of LDs below and above the lasing threshold, the dependence of current and temperature on the associated thermal resistance must be known. Figure 5-8(a) shows the dependence of injection current on the differential quantum efficiency and peak emission wavelength at different heatsink temperatures. At low injection current, the quantum efficiency was invariably small and a strong shift of emission spectra was observed. Light absorption, which may initially occur at a depleted area of the active region close to the facet and/or due to bandgap narrowing, led to the generation of electron-hole pairs. These electron-hole pairs raised the temperature near the facet due to non-radiative recombination by ways of surface states located at the facet [47]. Non-radiative recombination and absorption were restricted to the vicinity of the active region. The input power was mostly dissipated near the active region, generating a significant increase of localized heating at the emitting facet. As the injection current increased towards its lasing threshold, the efficiency of converting the electrical input into photons improved. This can be observed in Figure 5-8(a) whereby the differential quantum efficiency exhibited improved photon output rate near its lasing threshold. In contrast, the emission wavelength reduced abruptly and dropped to a minimum at its lasing threshold. Since the differential quantum efficiency was independent of temperature for these LDs (see Figure 5-8(a)), the change of emission wavelength was proportional to the change of spontaneous emission and non-radiative recombination of free carriers into stimulated emission. Beyond I_{th} , photon absorption and Joule heating due to the series resistance were the dominant causes for the raised temperature in the active region. When the current increased above I_{th} , the emission spectra shifted to longer wavelength. Coherent radiation which was not extracted from the LD was absorbed and converted into heat since these LDs had an external efficiency of ~ 0.8 .

From the calibrated temperature-dependent emission wavelength, the temperature rise in the active region can be obtained. As shown in Figure 5-8(b), the temperature in the active region was observed to change around the lasing threshold. Surprisingly, the temperature at below the lasing threshold was observed to be higher than that above the lasing threshold, up to 36 mA. This was expected as the optical losses due to non-radiative recombination and absorption at below the lasing threshold was significantly larger than those beyond I_{th} . This behavior was also observed for elevated temperatures. As the heatsink temperature increased, the emitted power at a given current dropped owing to an increase in the lasing threshold. Hence, the temperature difference between the active region and the heatsink become larger due to the heating effect. These findings show that it is essential to have (1) low I_{th} to reduce self-heating and (2) a low temperature sensitivity of I_{th} as the operating lifetime of the LD decreases exponentially with temperature.

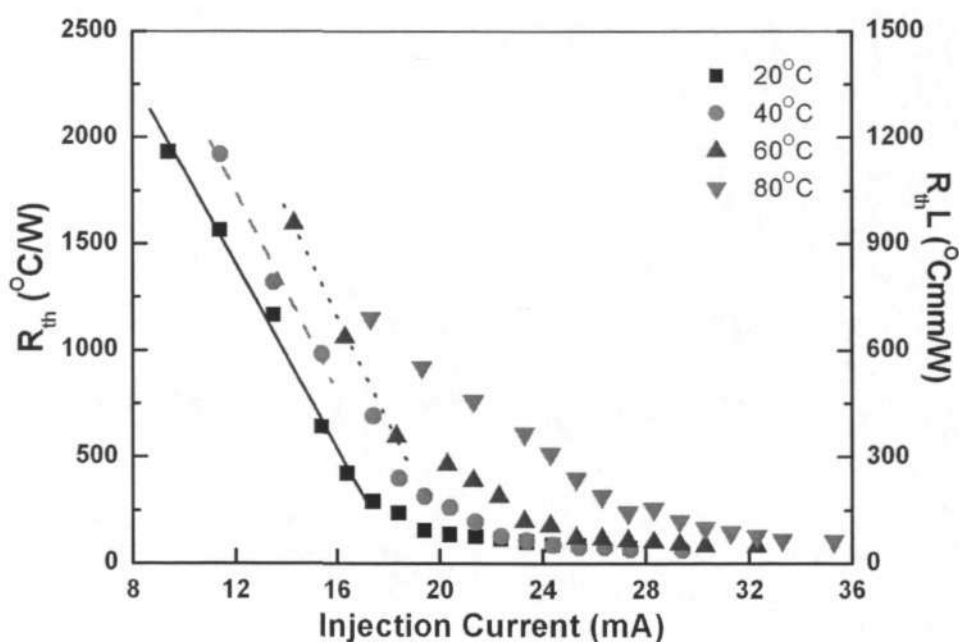


Figure 5-9 Thermal resistance of LD at a function of current. The effective thermal resistance of the diode varies with current.

The thermal behavior of LDs could also be expressed in terms of thermal resistance R_{th} . The thermal resistance of the LD can be defined as the ratio of the temperature rise in the active region to the input power

$$R_{LD} = \frac{\Delta T}{\Delta P} \quad (5-3)$$

where ΔT is the average temperature rise in the active region for a given injected power ΔP .

This calculation is valid for heat generated below the threshold current since most of the electrical input is converted into heat energy. As the current increases close to its lasing threshold, photon emission becomes more apparent. The electrical incremental input is now converted into both heat energy and optical power. Hence, the emitted optical power must be corrected to obtain the heat generation rate. Consideration of the heat generated in the active region alone is insufficient to deduce the R_{LD} at high operating conditions. Other sources of heating element may also surface; radiative absorption of free carriers and series resistance of the diode. Firstly, the rate of photon absorption may change with current densities i.e. at high injection current, thermal rollover exists with an increased of photon absorption. The heat generated in the active region is significantly large and the effective heat generation rate for ΔP is therefore

$$\Delta P = P - \eta \cdot P = (1 - \eta)P \quad (5-4)$$

where η is the external differential efficiency of the diode and can be extracted from the LI curve. Following Eq. (3) & (4), to account for the optical absorption, the thermal resistance is change to

$$R_{LD} = \frac{\Delta T}{(1 - \eta)P} \quad (5-5)$$

In addition to the heat generated at the junction, Joules heating due to the series resistance R may also be present. At low injection current, R can be neglected as $IV \gg I^2R$. However, as the injection current increases i.e. $IV \ll I^2R$, Joules heating becomes apparent as it increases to the square of current. While the effect of R is included in this calculation, they are important only at high current levels.

$$R_{LD} = \frac{\Delta T}{(1 - \eta)P + I^2R} \quad (5-6)$$

During cw operation, the heat generated in the active region is assumed to be uniform along the cavity length. Heat loss from the top and sides of the diode to the ambient is also assumed to be negligible. Since R_{th} varies inversely with diode length, the product $R_{th}L$ will be used for effective comparison of thermal behavior. As shown in Figure 5-9, the associated thermal resistance of the LD differs at below and above the lasing threshold. A large $R_{th}L$ of as much as 1400 °Cmm/W could be observed below the threshold current and it dropped abruptly to 60-80 °Cmm/W as it approached towards its lasing threshold value. Below the lasing threshold, the thermal resistance followed a linear regression of 130-150 °Cmm/W at a function of injection current for all heatsink temperatures, and it remained relatively constant thereafter. This constant reading was considered as the effective thermal resistance of the device. The change of thermal resistance was induced by the transfer of non-radiative energy (non-stimulated emission) into radiative emission of free carriers as discussed earlier. This shows that the dominant cause for the temperature rise, at low injection current, is dominated by the efficiency of radiative recombination.

5.2.4 Joules Heating due to Series Resistance

The dependence of current on the thermal behavior of LDs may further lead to reliability deterioration in terms of lifetime at higher injection current. To study the effect of Joules heating, high pulsed and cw operations were applied to the LDs. In short-pulsed condition, the temperature rise was less than 10 °C at 300 mA. Joules heating was minimized as the short pulse width and low duty factor reduced parasitic heating.

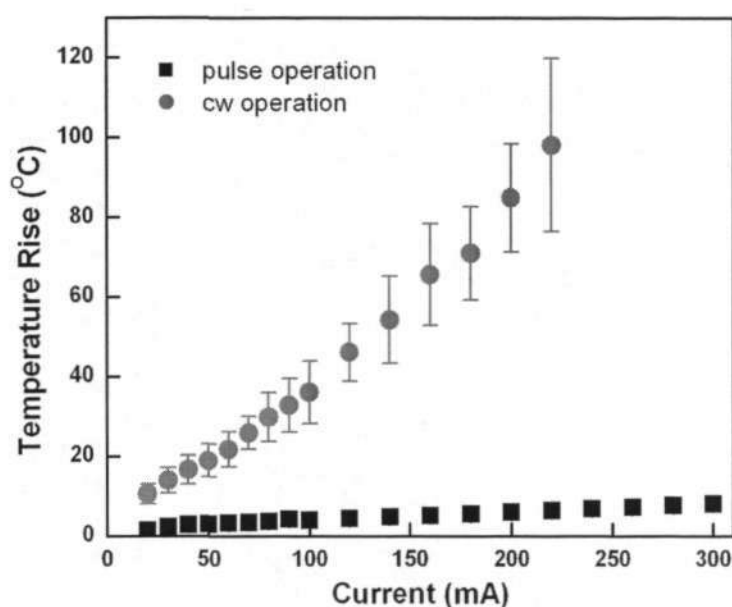


Figure 5-10 Temperature rise at high pulsed and cw injection currents. Joules heating due to the series resistance increased facet heating significantly.

In cw operation, the heat accumulated in the active region increased steadily with increasing current as shown in Figure 5-10. Facet heating of as much as 120 °C was observed at 240 mA and the LDs failed thereafter. The emitting facets experienced optical damages and the devices did not functioned as a LD. Beyond I_{th} , the heat generated in the active region due to non-stimulated current was fairly proportional to the injection current as the differential quantum efficiency was relatively constant. However, Joules heating attributed by the series resistance was significant as it increased to the square of current.

The mechanism for the heat generation at high injection current includes non-radiative recombination in the active region, Joules heating throughout the structure and absorption of spontaneous emission [31, 185, 186]. As a result, thermal runaway process usually occurred in cw operation and caused catastrophic damage at the facet.

5.3 Influence of Bonding on the heating response

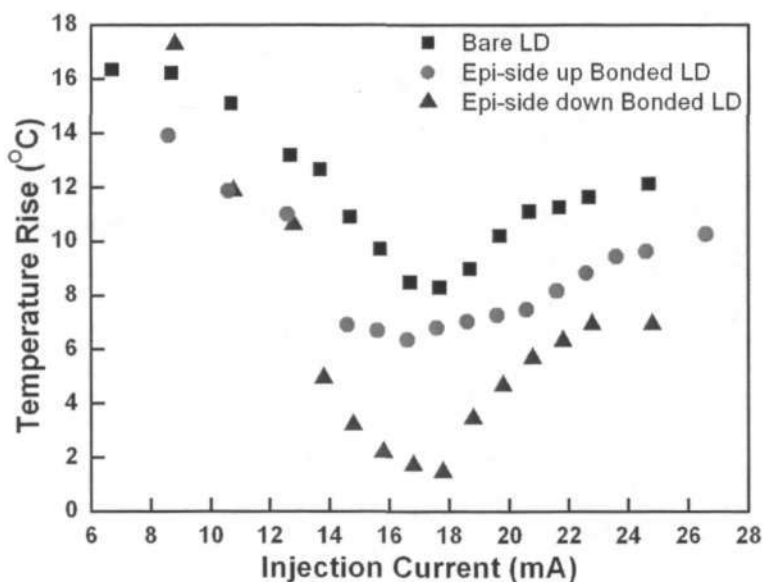


Figure 5-11 Comparison of bonding configuration on the thermal behavior of LD. The temperature in the active region reduced after bonding, with improved thermal management in face- down bonding approach.

The heating response due to the radiative energy transfer was also observed for face-up and face-down bonded samples as shown in Figure 5-11. The temperature in the active region was reduced by $\sim 30\%$ and $\sim 50\%$ after face-up and face-down bonding, respectively. Although the temperature characteristics of the LDs improved in face-up bonding approach, the poor thermal conductivity of the GaAs substrate limited the heat flow to the heatsink. The heat generated in the active region spread laterally across the laser as it transported towards the heatsink, leading to a two-dimensional heat flow

[13,17]. In face-down bonding approach, the heat transfer from the LD to the heatsink depended on the thermal conductivity of the heatsink material. Owing to the proximity of the active region to the heatsink and the good thermal conductivity of the heatsink material, the heat produced in the active region could be rapidly distributed to the entire heatsink. Hence, the temperature in the active region was significantly reduced for face-down bonded LDs compared to face-up approach and unbonded LDs.

In an optoelectronic assembly, LDs are usually bonded onto heatsink as a means of heat dissipation as well as electrical interconnect. Solders are usually used as interconnect in photonic packaging due to its relatively good electrical, thermal and mechanical properties. The thermal resistance of the assembly comprises of

$$R_{th} = R_{LD} + R_{solder} + R_{hs} \quad (5-7)$$

where R_{LD} is the thermal resistance of the LD, R_{solder} is the thermal resistance of the solder and R_{hs} is the thermal resistance of the heatsink.

The usual measure of how well the heat generated in a material is dissipated is the thermal resistance. The thermal resistance of a material can be expressed as,

$$R_{th} = \frac{T_c - T_{hs}}{Q} \quad \text{or} \quad R_{th} = \frac{L}{kA} \quad (5-8)$$

where T_c is the device case temperature, T_{hs} is the heatsink temperature, Q is the rate of conductive heat transfer, L is the interface thickness, k is the thermal conductivity of the material, and A is the area of heat transfer. For a homogeneous material, the heat flow is unidirectional and the thermal resistance of the solder and the Cu heatsink can be represented as

$$R = \frac{t}{l \cdot w \cdot k} \quad (5-9)$$

where t , l , w , and k are the thickness, length, width, and thermal conductivity of the material, respectively. The total thermal resistance of the LD assembly becomes

$$R_{th} = \frac{\Delta T}{(1-\eta)P + I^2 R} + \frac{t_{Solder}}{l_{Solder} \cdot w_{Solder} \cdot k_{Solder}} + \frac{t_{heat\ sink}}{l_{heat\ sink} \cdot w_{heat\ sink} \cdot k_{heat\ sink}} \quad (5-10)$$

The thermal resistance of the LD can be extracted by subtracting the solder and heatsink value from the total thermal resistance. The thermal behavior of these LDs was also investigated at high injection currents of up to 300 mA.

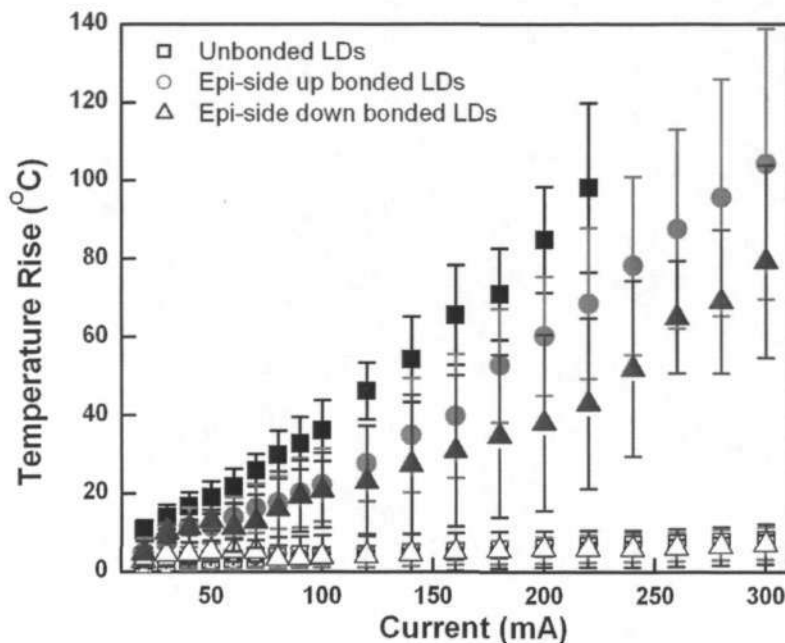


Figure 5-12 Heating response of unbonded and bonded LDs at high pulse and cw operation. Joules heating could be observed at high cw injection current.

Figure 5-12 shows the effects of different bonding configuration on the temperature rise in the active region under high pulse and cw operating conditions. In pulse operation, the temperature in the active region did not increase significantly even at a high injection current of 300 mA. A linear increment of 0.2 °C/mA was observed. The thermal behavior

of the LDs also did not vary significantly before and after bonding. This suggested that, at pulse operation, the heatsink did not have an influence on the thermal behavior of the LD and that the heat generated was localized within the LD. At short pulse operation, the thermal heat capacity of the LD prevented the heat generated at the junction from diffusing far from it since the thermal conductance of the passivation layer and the GaAs substrate was much lower than the metal electrode. Since the pulsed measurement minimized the current (Joule) heating effects, the heat generated in the LD was perceived to be caused by rate of photon absorption.

In cw operation, Joule heating was evidently shown (see Figure 5-12). For the unbonded samples, measurements were conducted until 220 mA before catastrophic damage occurred at its emitting facets. A large temperature rise of more than 100 °C could be observed in the LD. For face-up and face-down bonding, the heat removal means from the LD to the heatsink reduced the temperature in the active region at 220 mA to an average of ~ 70 °C and ~ 40 °C, respectively. Hence, higher measurements were permissible for face-up and face-down bonding approach. Two other important characteristics were observed. Firstly, at low injection current, the temperature rise for face-up bonded LDs and unbonded LDs were higher than face-down bonded LDs. The heat generated in the active region could not be removed effectively in unbonded and face-up bonded samples and, hence the temperature in the active region was larger than the face-down bonded LDs. Secondly, as the injection current increased, an exponential increment of device heating could be observed. At high injection current, additional heating source due to the series resistance of the LD was apparent. This behavior suggested that Joules heating was the dominant heating mechanism at high cw operating conditions, frequently resulting in the irreversible COD effect in GaAs-based lasers.

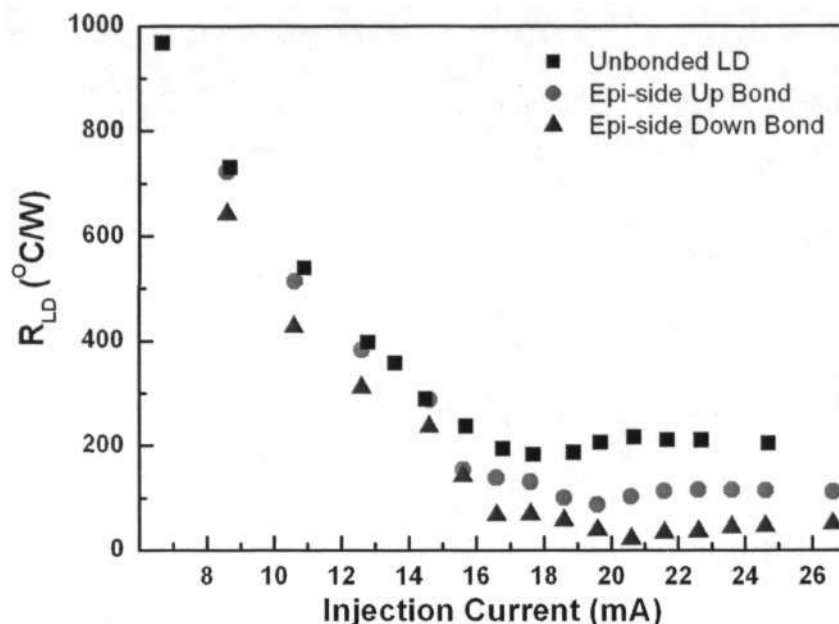


Figure 5-13 Comparison of bonding configuration on the thermal resistance of LD. The associated thermal resistance of the LDs reduced after bonding.

As shown in Figure 5-13, the thermal resistance is reduced after bonding, with lower R_{LD} achieved in face-down approach. The reduction of the thermal resistance might lead to improved LD performance. To study the dependence of the thermal resistance on the injection currents, the electrical-optical characteristics of the LDs were compared before and after bonding. These InGaAs/GaAs LDs had an average threshold current of 17.8-19.7 mA and exhibited thermal rollover of ~ 200 mW at 320 mA. The characteristic temperature T_0 , which was the inverse slope of the semi-logarithmic threshold current versus temperature plot, was estimated to be 414 K for these LDs. As shown in Figure 5-14, the LD performance improved after bonding, with higher optical power achieved and lowered threshold current variation. The typical power achieved for face-up bonded LDs was 260 mW and the T_0 was approximately 458 K whereas in face-down bonding approach, the optical power and T_0 further improved to 300 mW and 460 K, respectively. Face-down bonding can significantly reduce the device heating and its associated thermal

resistance and, hence higher instantaneous optical power levels can be achieved compared to face-up and unbonded samples.

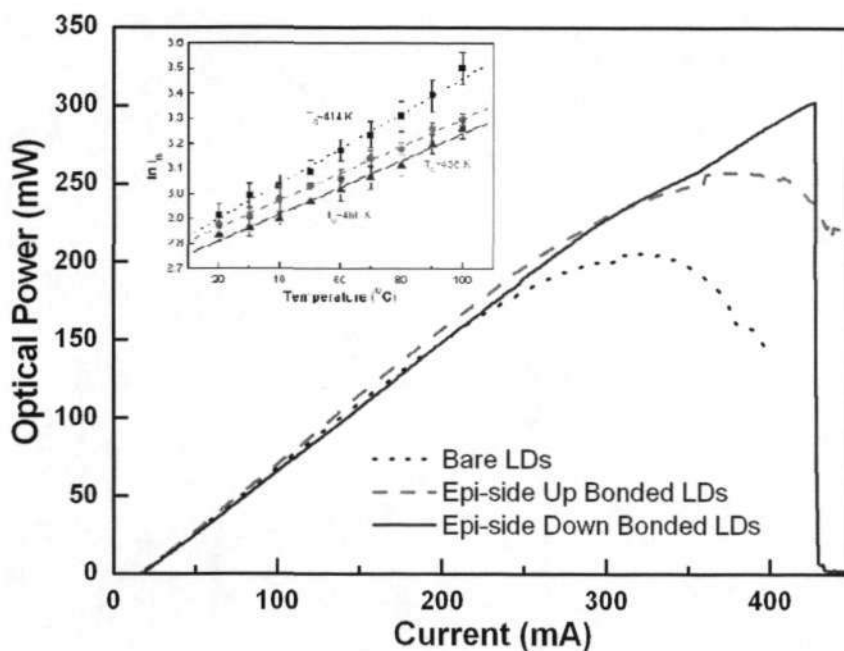


Figure 5-14 Influence of bonding on the electrical-optical characteristics of LDs. Inset: Characteristic temperature T_0 improved after bonding due to better heat dissipation means through the solder joint.

In most applications, the ability of the LD to perform well at elevated temperatures is of great interest. This is especially of concern in the case of high-power LDs where the amount of heat generated causes the device temperature to rise significantly. As a result, it is of utmost importance for the semiconductor laser to be robust enough so as not to degrade due to device operation at high temperatures. The characteristic temperature of the LD, which is commonly referred to as T_0 , is a measure of the device sensitivity to temperature. Higher values of T_0 imply that the threshold current and differential quantum efficiency of the LD increase less rapidly with increasing temperatures. This translates into the laser being more thermally stable. This can further be comprehended with Pankove's empirical equation [178],

$$\begin{aligned}
 I_{th1} &= I_o \exp \left[\frac{T_1}{T_o} \right] \\
 I_{th2} &= I_o \exp \left[\frac{T_2}{T_o} \right] \\
 \ln(I_{th1}) - \ln(I_{th2}) &= \frac{T_1 - T_2}{T_o} \\
 \Delta \ln(I_{th}) &= \frac{\Delta T}{T_o} \\
 T_o &= \frac{\Delta T}{\Delta \ln(I_{th})}
 \end{aligned}
 \tag{5-11}$$

With these findings, the thermal behavior of LDs could then be analyzed by comparing their emission wavelengths between pulsed and CW measurements.

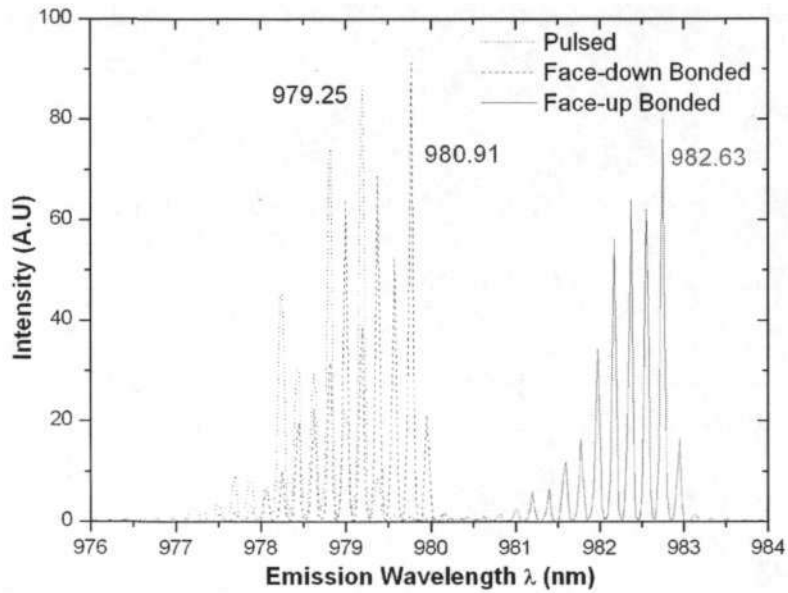


Figure 5-15 Comparison of typical emission wavelength under different bonding configurations.

From the calibrated $\partial\lambda/\partial T$, the temperature rise in the LD for face-up and face-down bonding configurations could be observed with the shift of emission wavelength between pulse and CW operation. As shown in Figure 5-15, the emission wavelength shifted from 979.25 nm (pulse operation) to 982.63 nm and 980.91 nm for face-up and face-down bonded LDs respectively under CW operation. From the wavelength shift, the

temperature rise was estimated to be 7-8 °C for face-up bonded LDs and 2-3 °C for face-down bonded LDs respectively. This is due to the effective heat dissipating channel and further explains the higher optical performance attainable for the face-down configuration compared to the face-up design. This correlation technique was further compared with FE simulation.

5.4 Numerical Simulation of Packaged LDs

ABAQUS/Standard capability for uncoupled heat transfer analysis is intended to model solid body heat conduction with thermal properties, internal energy (including latent heat effects), and general convection and radiation boundary conditions. This section will describe the basic energy balance, boundary conditions and finite element discretization in the thermal analysis.

In a three-dimensional isotropic one-bodied system, the governing equation is given by,

$$\rho \bullet C_p \frac{\partial T}{\partial t} = \kappa \left(\frac{\partial^2 T}{\partial x^2} + \frac{\partial^2 T}{\partial y^2} + \frac{\partial^2 T}{\partial z^2} \right) + Q \quad (5-12)$$

where κ is the thermal conductivity, ρ is the density, Q describes the distribution of heat source density, and C_p is the specific heat.

The heat flow along the solid body can be expressed as,

$$\frac{dQ}{dt} = -\kappa_x A \frac{dT}{dx} \quad (5-13a)$$

$$\frac{dQ}{dt} = -\kappa_y A \frac{dT}{dy} \quad (5-13b)$$

$$\frac{dQ}{dt} = -\kappa_z A \frac{dT}{dz} \quad (5-13c)$$

where dT/dx is the temperature distribution along the x-direction; A is the cross-sectional area of the sample perpendicular to the heat transfer direction; dQ/dt is the thermal power.

Initial and Steady-State Conditions

In this LD assembly, several conditions were specified in the thermal analysis. During operation, the first condition applies to the active region (temperature source), which has a constant heat generation. The TE Controller fixed the base temperature of the Cu heatsink to its prescribed operating temperature as an initial condition. The initial temperature condition of the LD package was also prescribed. Convection must also be considered to mimic the environmental behavior. Atmospheric air was adopted as the field condition.

- 1) Heatsink temperature can be prescribed as boundary conditions at a boundary $y=0$

$$\theta = \theta_{Cu}(y, t) \Big|_{y=0}$$

- 2) Prescribed heat flux q acting over the active region as a heat source

$$q = q_{\text{active region}}(x, y, t)$$

- 3) Specified convection surfaces acting around the periphery of the LD assembly.

$$\begin{aligned} q &= h_{LD}(\theta - \theta^o) \\ &= h_{\text{solder}}(\theta - \theta^o) \\ &= h_{\text{heat sink}}(\theta - \theta^o) \end{aligned}$$

where $h = h(x, y, t)$ is the film coefficient and $\theta^o = \theta^o(x, y, t)$ is the sink temperature

The other necessary conditions are $T=T_B$ at $x=y=0$ for all times, and that $T=T_B$ at all x and y for $t=0$. That is to say that the junction and entire cross-sectional LD design were

initially at the base temperature (25 °C) while the bottom of the heatsink is maintained at this temperature as shown in Figure 5-16.

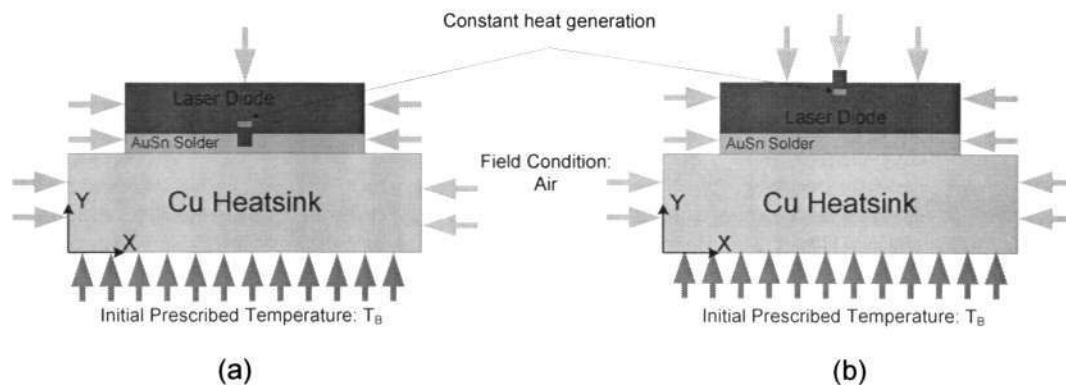


Figure 5-16 Thermal boundary conditions for (a) face-up and (b) face-down bonding configurations.

Two-dimensional Steady-State Model

Measurement of temperature distribution had been studied along the cavity length of the LD [21, 22]. In practice, there will be temperature gradients along the LD during continuous-wave operation. A sharp increase in temperature of as much as 120 K at the emitting facets could be observed. The heat generated at the active region was accumulated within 5-10 μm of the emitting facets while the cavity body of the LD remained relatively close to the operating condition. Since the temperature rise at the emitting facets was the highest along the laser cavity and the temperature gradient occurs near the emitting facets, the area of interest should be at the emitting facets. For simplicity, only a two-dimensional model of the cross-sectional laser structure needed to be created in order to understand the thermal behavior of LDs under different bonding configurations. These gradients were critical in the thermal analysis of continuous wave operation. Thus, only steady-state would be analyzed in this modeling.

This model was segmented with higher element nodes near the active region (heat source) and lesser nodes towards the Cu heatsink peripheral. Global meshing was adopted and the total number of node elements was more than 10,000 for both bonding configurations. All these effects are adopted in a global Cartesian coordinate system as shown in Figure 5-17.

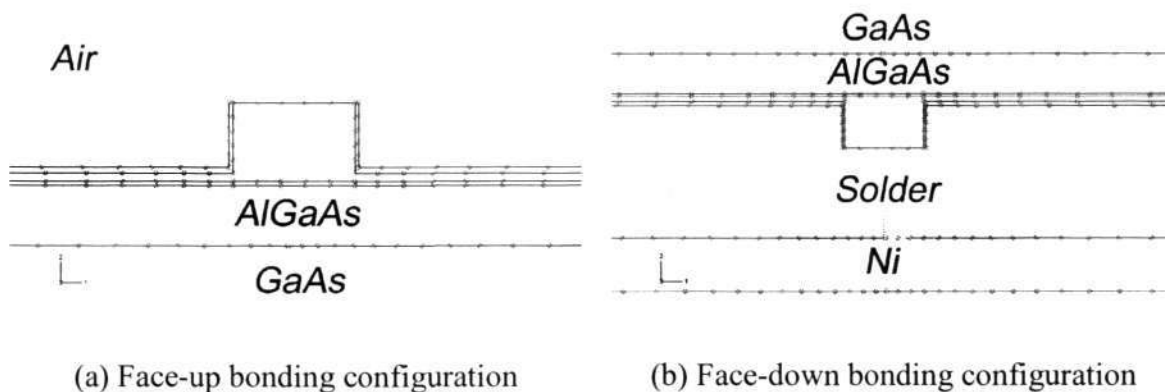
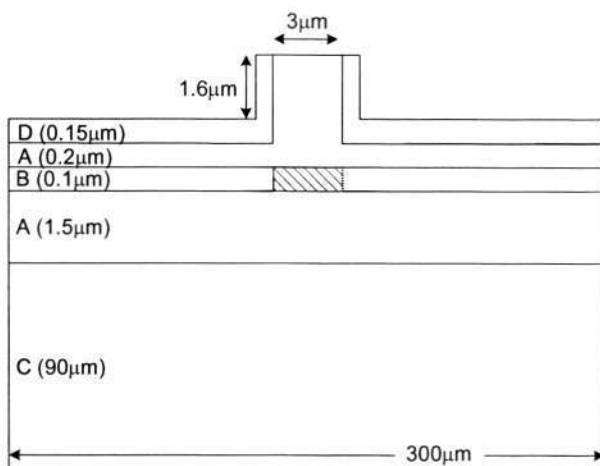


Figure 5-17 Global element meshing was conducted on both packaged LDs with higher concentration at the active region. Instances were constructed such that the ridge region and the heat source have higher biased node elements compared to the periphery of the bonding designs.

To reduce calculation time, the LD structure was simplified into a 5-layer stripe-geometry heterostructure as shown in Figure 5-18(a). The InGaAs active region, which was assumed to be 100 nm, was bounded with AlGaAs cladding layers. The effect of electrical confinement within the ridge region was also included with a SiN passivation layer beside the ridge. The LDs were face-up and face-down bonded onto Cu heatsink using Au80Sn20 solder of 5 μm thickness. The thickness of the Ni barrier layer was chosen to be 2 μm in the analysis. To account for environmental losses, the packaging design was bounded by ambient conditions (air). The architecture of the LD structure and its physical parameters can be found in Figure 5-18. The values of thermal conductivity

for the GaAs-based LD were from Adachi [187]. The thermal conductivity values for the remaining materials were found in [111, 112, 188].



(a)

Layer	Material	Thermal conductivity (W/μm.°C)	Density (g/um ³)	Specific Heat Capacity (J/g.°C)
A	AlGaAs	12.11e ⁻⁶	4.852e ⁻¹²	0.336
B	InGaAs	8.325e ⁻⁶	5.62e ⁻¹²	(0.33)
C	GaAs	44e ⁻⁶	5.32e ⁻¹²	0.33
D	SiN	18.5e ⁻⁶	3.1e ⁻¹²	0.234
	AuSn solder	58e ⁻⁶	14.7e ⁻¹²	(0.12874)
	Ni	91e ⁻⁶	8.9e ⁻¹²	0.444
	Cu heatsink	385e ⁻⁶	8.96e ⁻¹²	0.385
	Air	0.0256e ⁻⁶	0.00109e ⁻¹²	0.716

(b)

Figure 5-18 (a) Schematic structure of InGaAs/GaAs/AlGaAs ridge-waveguide LD; (b) the thermal properties of each layer are represented. The thermal conductivity κ and heat capacity C_p are assumed to be constant over the temperature rise.

Heat generation Source

In microelectronics applications, the devices converted their power into heat energy during operation. Joule heating arised when the energy dissipated by an electrical current

flowing through a conductor was converted into thermal energy. The internal heat generated in the thermal problem is a function of electrical current.

The flow of electrical current is described by Ohm's law:

$$J = \sigma^E . E \quad (5-14)$$

where σ^E is the electrical conductivity matrix.

Joule's law describes the rate of electrical energy, P_{ec} , dissipated by current flowing through a conductor as

$$P_{ec} = E . J \quad (5-15)$$

where J is the electrical current density.

The electric field in a conducting material is governed by Maxwell's equation of conservation of charge. Assuming steady-state direct current, the equation can be expressed as,

$$\int_S J . n dS = \int_V r_c dV \quad (5-16)$$

where V is any control volume whose surface is S, n is the outward normal to S, and r_c is the internal volumetric current source per unit volume.

Unlike microelectronic devices, semiconductor lasers comprised an integral of thermal, electrical, and optical performances. In semiconductor lasers, the current flowing through the diode caused heating in three distinct ways. First, heat was generated at the junction due to the inefficiencies of the light production process. Only a fraction of the current was converted to light, while the rest of the injected current was converted to Joule heating. In

addition to the heat generated at the junction, heating induced by the bulk series resistance of the LD and contact resistance were also included.

To study the thermal behavior of LDs, the characteristics of LDs were compared between pulse and CW operations. In CW mode operation, the heat generated in the confinement layers due to carrier recombination significantly raised the temperature in the active region. This heating effect became more pronounced when the injection current increased. As shown in Figure 5-12, when the LD was operated above its threshold current, the characteristics of LDs might not follow a direct relationship to the physics of heat generation in the LD [189]. The carrier population in the confinement layers increased steeply [18] as temperature increased. A sufficiently high heatsink temperature might give rise to a run-away thermal process [17]. In this simulation exercise, the heat generation rate was chosen to be at the lasing threshold (~ 17 mA) of the LDs so that the thermal comparison reflects purely on the bonding comparison. At the threshold current, the LD's optical losses (and its associated heat generation) were at its minimum. A heat generation rate of 3.63×10^{-5} W/ μm^2 was obtained for these LDs.

Influence of the Cu Heatsink Periphery

Before further discussion, it is important to understand other contributing factors that may influence the thermal behavior of the LD assembly. To study the influence of the peripheral heatsinking, the dimension of Cu heatsinks were studied with different widths and thicknesses. In these analyses, the face-down approach was utilized as the heat source had close contact to the heatsink material.

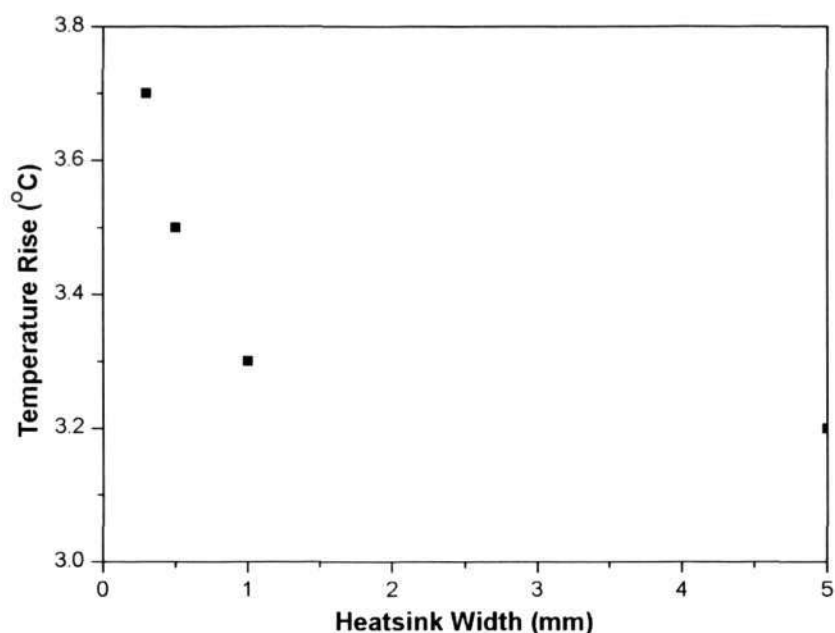


Figure 5-19 Study of temperature rise in the active region at various heatsinking widths.

Firstly, the influence of different heatsink widths was studied from 300 μm to 5 mm. As shown in Figure 5-19, the width of the Cu heatsink did not influence the temperature rise in the active region significantly, with temperature fluctuating merely between 3.2 $^{\circ}\text{C}$ - 3.8 $^{\circ}\text{C}$. However, for effective lateral spreading of heat fluxes, at least 1 mm of heatsink width was required. Secondly, the thickness was also varied from 100 μm to 3 mm. The thickness of the Cu heatsink had an immediate impact on the temperature distribution of the design. The temperature rise in the active region was observed to increase readily when the heatsink thickness was reduced. The temperature rise was more significant when the heatsink thickness reduced to lesser than 1 mm as shown in Figure 5-20. To reduce the geometrical influence of the heatsinking material in the thermal analysis, the heatsink width and thickness should be chosen such that the subsequent parametric investigations of the LDs reflect on the bonding configurations. The heatsink width and thickness were chosen at 3 mm and 5 mm respectively, much larger than the simulation results to reduce the effect of heatsinking periphery.

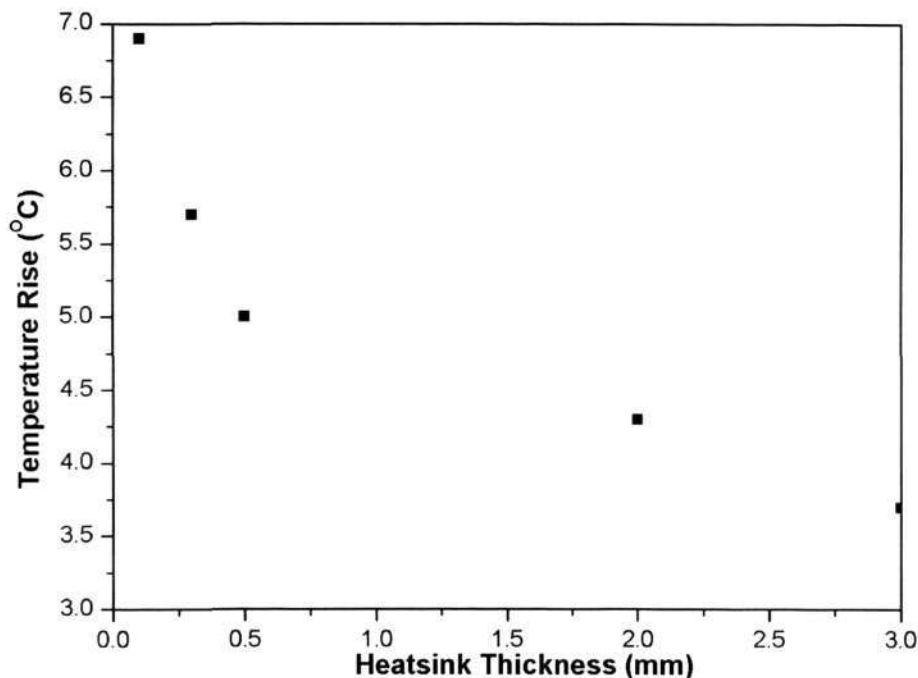
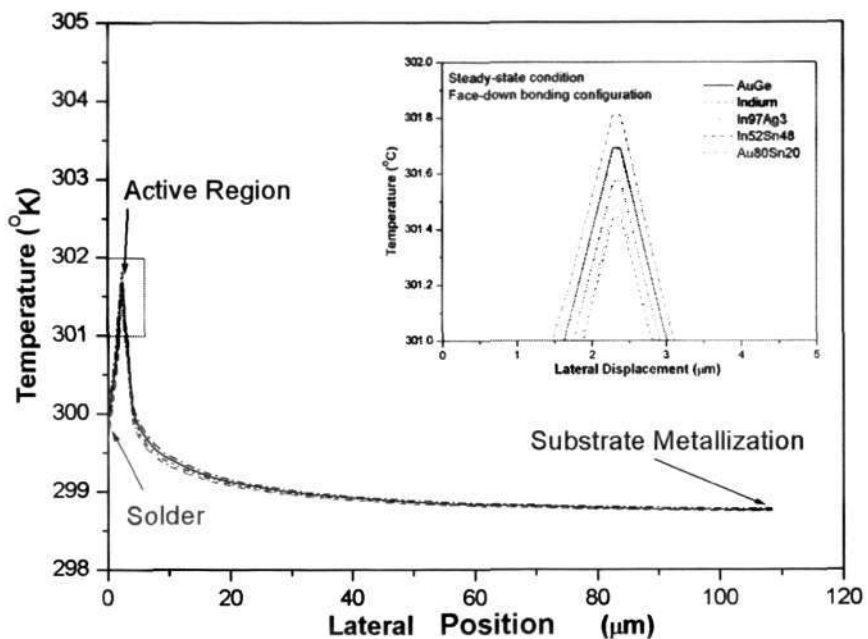


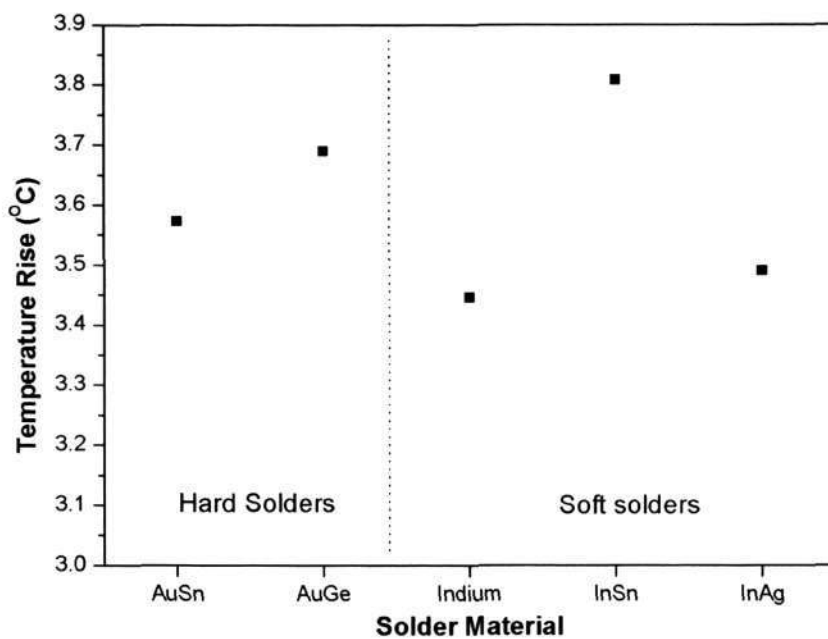
Figure 5-20 Study of heat distribution at various heatsink thicknesses.

Influence of Solder Materials

Solders were used frequently in photonics die attach processing. Generally, hard solders were utilized for high temperature assemblies while soft solders were utilized for low temperature assemblies. Hence, it is mandatory to study the influence of different solder materials affecting the thermal capability of the packaging design. For bonding of LDs, it was recommended to adopt a fluxless process to avoid contaminations/residues to the emitting facets of the LDs. Hence, solders that were amendable to fluxless assembly should be studied. The thermal parameters of the solder materials can be extracted from Table 4 and Cookson Electronics Assembly Materials [117].



(a)



(b)

Figure 5-21 Study of heat distribution using different solder materials; (a) Comparison of temperature profiles across the LD to the solder layer. Insert: the device heating in the active region depends on the thermal conductivity of the solder material; (b) Comparison of temperature rises in the active region.

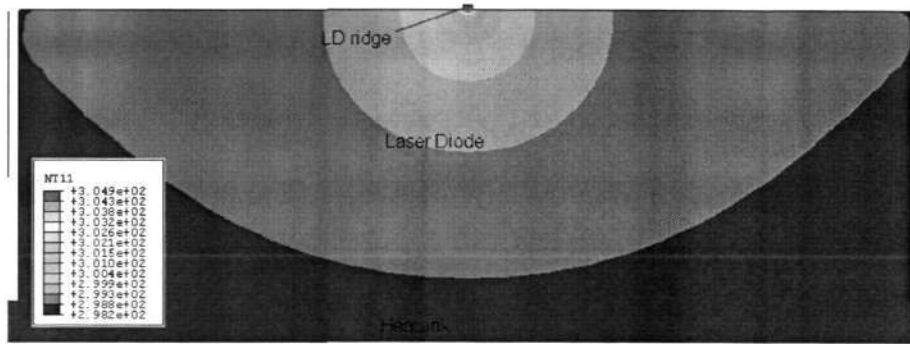
As shown in Figure 5-21, the temperature rise in the active region and temperature distribution across the LD were compared using different solder materials. The temperature distribution across the laser structure was not affected significantly by the solder materials. However, the temperature rise in the packaged LD was observed to be affected by the thermal conductivity of the solder material. As the thermal conductivity of the solder material improved, the temperature rise at the active region reduced. This was due to the improved efficiency in extracting heat fluxes from the heat generation source. Among all the solders analyzed, In and In97Ag3 solders offered the best solution to the heat transfer solution, followed by Au80Sn20 and Au88Ge12 solders. As discussed in CHAPTER 2, the low creep resistance in soft solders such as In and In97Ag3 caused long-term reliability concerns whereas hard Au80Sn20 and Au88Ge12 solders offered better mechanical and reliability behaviors. Hence, hard Au80Sn20 and Au88Ge12 solders were preferred over soft In and In97Ag3 solders. Between the two hard solders, Au80Sn20 solder demonstrated a slight advantage in thermal dissipation compared to Au88Ge12 solder. In addition, the melting point for Au80Sn20 solder was also significantly lower than Au88Ge12 solder. This enforced the adoption of Au80Sn20 solder for the LD die attach process and continued assessment of different bonding configurations using Au80Sn20 solder.

5.4.1 Face-up Bonding Configuration

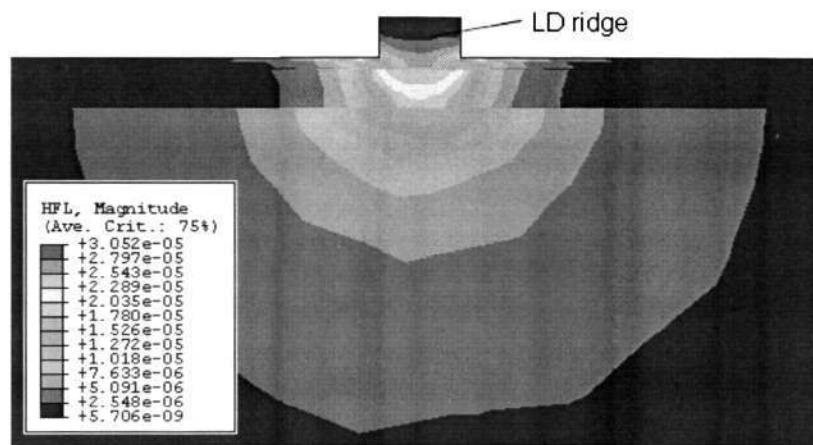
A typical two-dimensional facet temperature distribution across the LD could be observed in Figure 5-22. Localized heating at the active region could be observed with an approximate temperature rise of 7 °C. The SiN passivation layer restricted the electrical (heat) flow within the ridge area. This had an adverse thermal disadvantage as the bulk of the heat generation was confined within the active region. Due to the low thermal

conductivity of ternary cladding layers and multiple heterostructures, the thermal heat capacity of the diode further prevented the heat generated at the junction from diffusing far from it. The solder layer, which was also several diffusion lengths away from the junction area, was incapable of removing the heat generated in the active region.

The heat fluxes, which are the amount of heat that is transferred across a surface area over time, could also be obtained by fitting a two-dimensional model of heat diffusion to the LD structure, $\delta = \kappa / C_p$. As shown in Figure 5-22(b), the heat fluxes, which are heat diffusion vectors, were observed to concentrate at the active region. Due to the low thermal conductivity of air, the heat fluxes directed towards the ridge could not be extracted to the environment. Hence, most of the heat fluxes were observed to accumulate at the SiN layer near the heating source and this influenced the heat accumulation at the ridge area significantly. The proper solution to the heat flow problem is to solve simultaneously the heat flow equations for conduction in both directions.



(a)

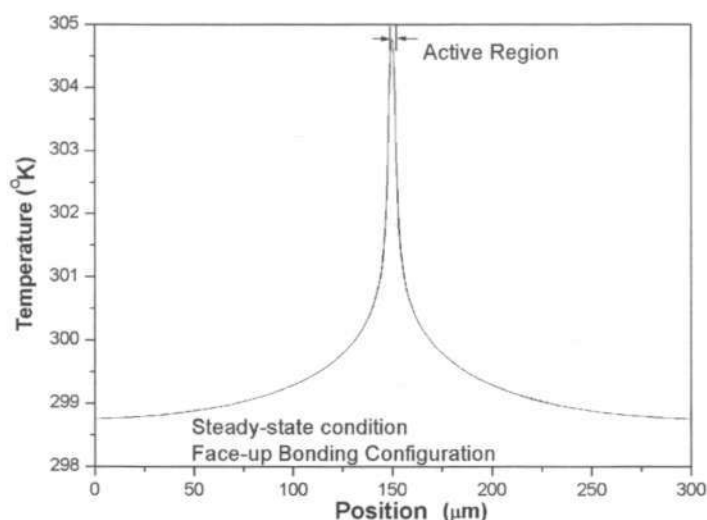


(b)

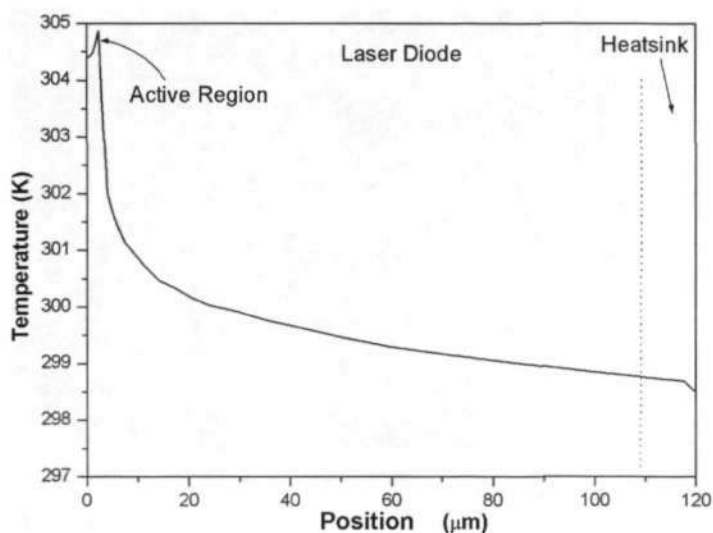
Figure 5-22 (a) Typical temperature contour at the facet of the LD for face-up bonded LDs; (b) Typical heat flux distribution across the cross-sectional laser structure for face-up bonding configuration. The bulk of the heat flux was observed to accumulate within the active region under the ridge.

The temperature profile across the active region was also analyzed vertically and laterally. The heat flux not only accumulated beneath the ridge width, but also spread along the active region as shown in Figure 5-23(a). The heat generated in the active region spread laterally over the entire width of the LD as it flowed to the heatsink, leading to a two-dimensional flow in the LD, whereas in the heatsink, the flow was vertical and extended over the whole width of the cross-section. This two-dimensional heat flow in the LD accounted for the logarithmic dependence of thermal resistance for the face-up

approach as reported by O.J.F. Martin et al. [29]. As shown in Figure 5-23(b), the temperature generated at the active region was gradually dissipated across the LD structure. The heat diffused from the junction region, a portion diffusing up through the p-type material and a portion through the n-type material. The heatsink did not extract much heat from the heat source due to the low thermal conductivity of the GaAs substrate. The temperature at the LD surface and its proximity were also observed to elevate significantly. Due to the electrical confinement beneath the ridge and its ineffective means of heat dissipation, the temperature on the LD surface increased. The proximity of the active region to the environment (air) would affect the temperature distribution in the active region considerably since the thermal conductivity of air is very low. In this bonding approach, the heat flow demonstrated an ineffective two-dimensional heat accumulation near the active region.



(a)

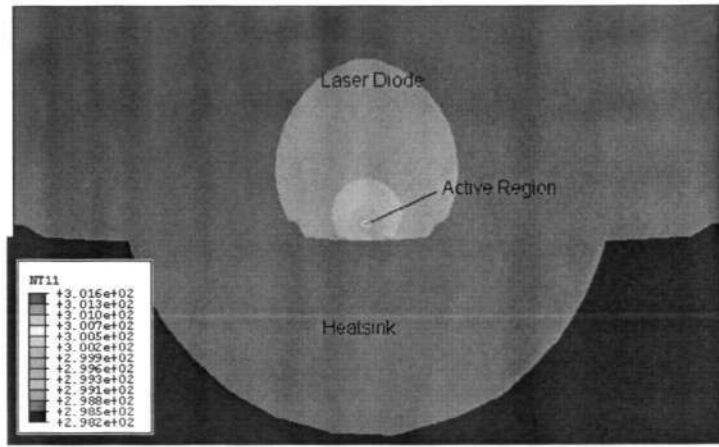


(b)

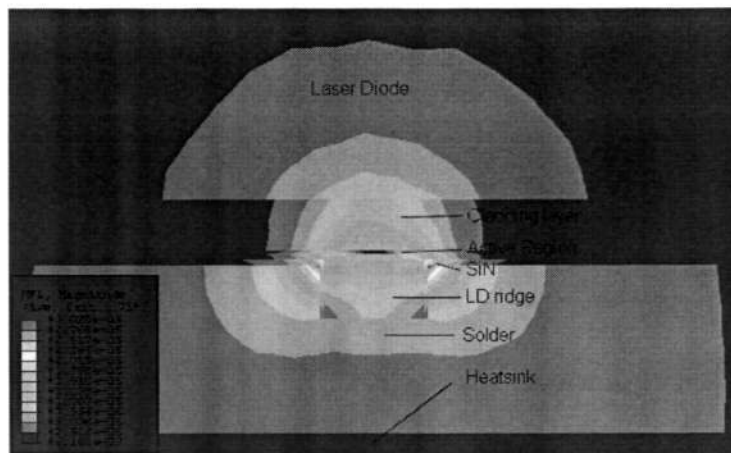
Figure 5-23 Temperature profile of face-up bonded LD on Cu heatsink; (a) lateral profile along the active region of the LD; (b) vertical profile across from the LD to the base of the heatsink material.

5.4.2 Face-down Bonding Configuration

The temperature distribution for face-down bonded LDs can be found in Figure 5-24. Heat generated could be observed in the active region. However, improved thermal management could also be observed with lower temperature rise in the active region. The temperature rise was lowered to 3 °C in this face-down approach. The majority of the heat flow was shown to shift towards the heatsink material due to the proximity of the heat source to the high thermal conductive Cu heatsink. The heat flux demonstrated direct heat flow across the heatsink, through the solder material. With effective heat transfer from the heat source, the source temperature (active region) did not elevate significantly.



(a)

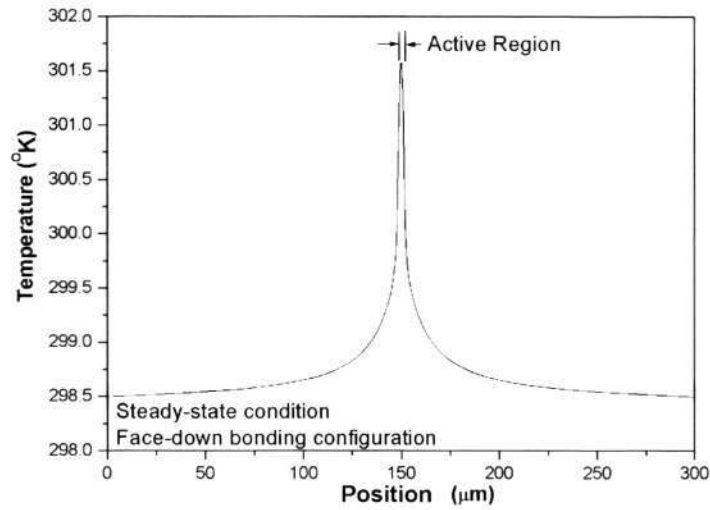


(b)

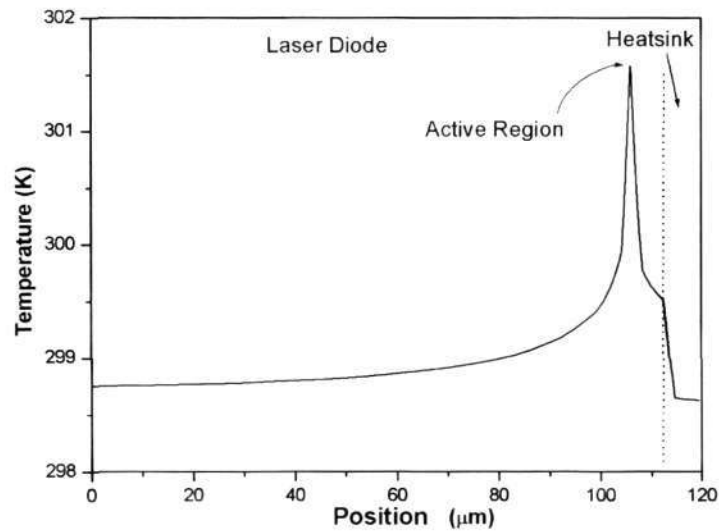
Figure 5-24 (a) Typical temperature contour at the facet of the LD for face-down bonded LDs; (b) Typical heat flux distribution across the cross-sectional laser structure for face-down bonding configuration. The bulk of the heat flux was observed to flow towards the heatsink effectively.

The temperature profile across the active region was also observed laterally and vertically as shown in Figure 5-25. The heat generated in the active region did not spread laterally over the entire width of the LD as demonstrated in the face-up bonding configuration. The temperature at the LD substrate also did not elevate as most of the heat generated was dissipated effectively onto the heatsink material. Owing to the good conductivity of the heatsink material and the proximity of the active region to the top of the heatsink, the heat

produced in the active region was rapidly distributed over the whole heatsink width. This led to a one-dimensional vertical heat flow and the expansion of the heat flow in the upper part of the heatsink depended on the heatsinking material. This shows that the heat generated for face-down bonded LDs exhibited a direct heat removal channel towards the Cu heatsink.



(a)



(b)

Figure 5-25 Temperature profile of face-down bonded LD onto Cu heatsink; (a) lateral profile along the active region of the LD; (b) vertical profile across from the LD to the base of the heatsink material.

Based on these simulation results, face-down bonded LDs clearly exhibited improved thermal management as compared to the face-up bonding approach. Not only was the temperature rise in the active region lowered, the temperature distribution across the LD also exhibited more heat flux vectors moving towards the heatsink.

5.5 Discussion

The dynamic thermal behavior of semiconductor lasers was studied with different operating conditions. Transient and steady-state heating response of InGaAs/GaAs LDs below and above the lasing threshold was reported. The effect of temperature and carrier density on the emission wavelength had been discussed with the gain-induced refractive index and emission/absorption processes. As current flow through the LD, three distinct characteristics can be observed. Below I_{th} , large optical losses due to non-radiative recombination and spontaneous emission caused an increase of temperature in the active region, leading to a large R_{th} across the device. At I_{th} , efficient radiative energy transfer resulted in reduced device heating and its associated R_{th} dropped to a minimum. Beyond I_{th} , the optical gain saturated and phonon absorption and Joule heating becomes important. At high injection current, the heat generated by the series resistance R_S was much larger than the heat generated at the junction. Joules heating occurred in high cw injection current since Ohmic heating increased with the square of current. Understanding the carrier-induced heating response in semiconductor lasers is essential to improve the device performance and reliability in the fabrication and packaging design. The maximum optical power output of LDs is usually limited by either the catastrophic optical damage (COD) of the facet or output power saturation, known as thermal rollover, due to heating

of the active region. Knowledge of the temperature distribution can give information about the facet heating mechanism and quality of the bond between LD and heatsink.

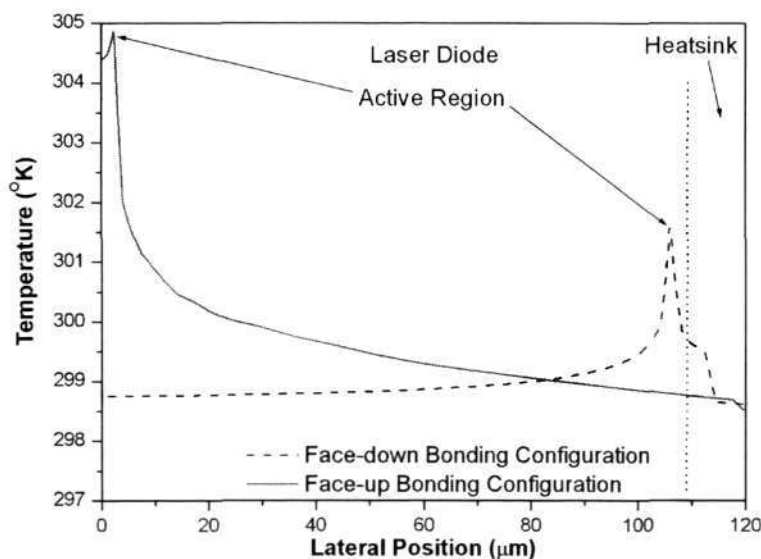


Figure 5-26 Comparison of temperature profile across the LD to the base of the Cu heatsink. Face-down bonding approach demonstrates an effective heat dissipating channel compared to face-up bonding.

The thermal behaviors of different bonding configurations were numerically modeled and comprehended. Close numerical fitting of heat generation in the active region between band structure theory and experimental measurement could be observed. Face-down bonded LDs demonstrated improved thermal management, with lower temperature rise in face-down bonded LDs than face-up bonded LDs. From the simulation results, the temperature rise for both face-up and face-down bonded LDs were ~ 7 °C and ~ 3 °C respectively. Although the temperature difference between the face-up and face-down approach is negligibly small at the lasing threshold, the temperature difference were significantly large at higher injection current. Due to the effective heat transfer for face-down bonded LDs, direct heat flow towards the heatsink could be observed whereas face-up bonded LDs exhibited two-dimensional heat accumulation in the active region. Since

the temperature was lowered by reducing the device heating in a face-down bonding approach, the optical performance could increase further.

Hence, face-down bonding approach was recommended to improve the overall LD performances. With this simulation exercise, a face-down bonding technique is recommended for single-mode ridge-waveguide LDs. It should also be noted that although this simulation designs dealt with InGaAs/GaAs junction LDs, its method of solution is applicable to laser junctions of other semiconducting materials.

CHAPTER 6

ASSESSMENT OF LONG-TERM RELIABILITY OF MODIFIED FACE-DOWN BONDING PROCESS

6.1 Introduction

Reliability in optoelectronics packaging is also a great concern to packaging design engineers. The major concern is the structural integrity of packaging design when subjected to thermal cycling and isothermal loading conditions. This chapter helps to develop better understanding of the reliability problems faced by the optoelectronic packaging industry.

Characterization of laser diode (LD) and solder joint only offers short-term reliability analysis of the bonding quality. As these LDs are required to have long operational lifetime, reliability testing must also be carried out to exhibit their long-term capability. To ensure that these bonded devices exhibit good long-term stability, the bonded devices underwent reliability testing to provide useful design guidance for fabricating reliable LD packages. Thermal cycling and accelerated aging are two commonly used long-term reliability testing approaches to assess the stability of the module.

6.2 Effect of Thermal Cycling Loading on Reliability of Bonded LDs

Thermal cycling tests have been used in the semiconductor industry to assess the reliability of solder joints in laser module packages. Although other acceleration stresses, such as vibration, mechanical and thermal shocks may lead to solder joint failure, the failure is mainly caused by thermal stresses during temperature cycling tests. Hence,

detailed knowledge of solder joints in LD packaging under temperature cycling test is important for the practical design and fabrication of reliable optoelectronic packaging. Evaluation of the solder joint strength under temperature cycling conditions for LD packaging applications have been conducted by others [190]. Thermal-elasticity-plasticity model were employed numerically to predict the integrity and residual stress distribution in the assembly. In addition, fiber alignment shifts [191] during temperature cycling tests have also been conducted to understand possible fiber alignment shifts. Although alignment shift in optoelectronic packaging were small, in the micron range, up to 50% loss in coupled power was incurred, and resulted in performance degradation of the packaged lasers. Their experimental observations were made for 500 cycles, however, they did not discuss the LD performance and microstructure analysis after thermal cycling aging [190].

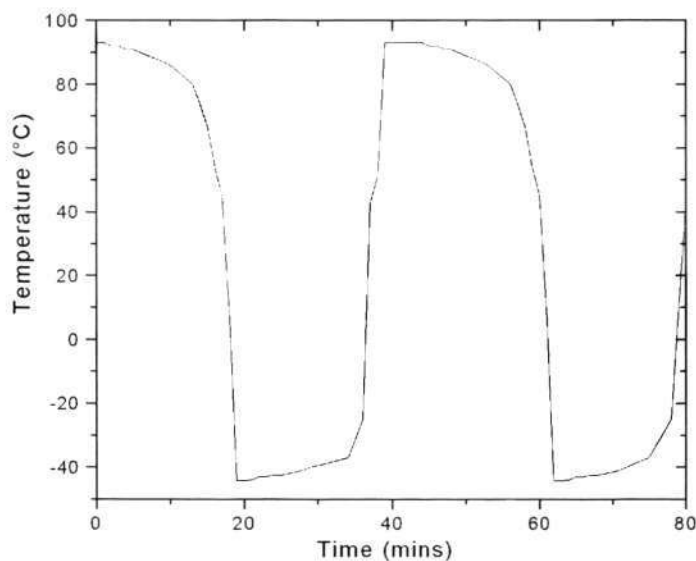
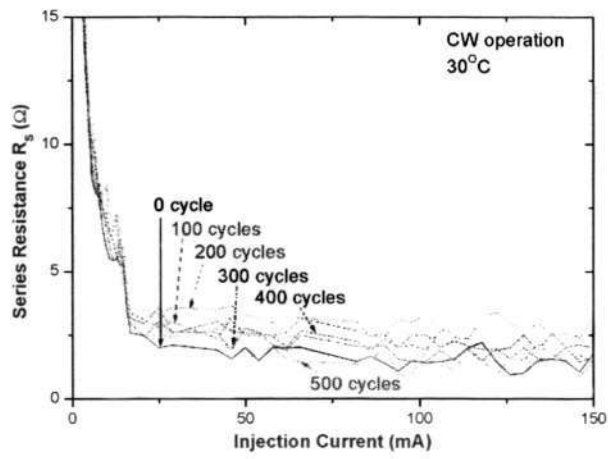
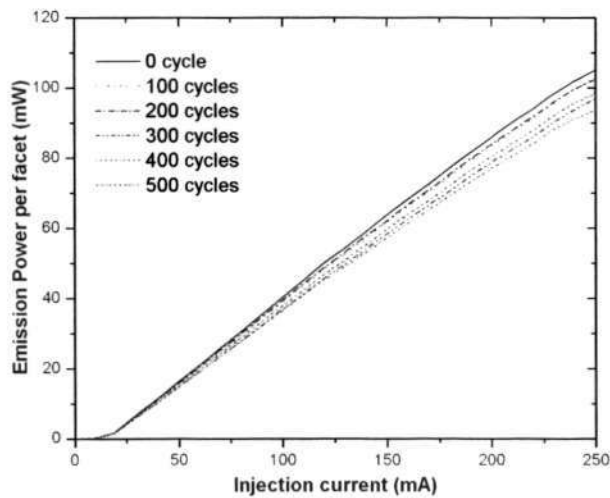


Figure 6-1 Typical temperature profile of thermal cycling conditions of -40 °C to +85 °C.

To investigate its long-term reliability, five well-bonded samples underwent 500 thermal cycle testing. The real temperature profile of the chamber was shown in Figure 6-1. Every 100 cycles, the bonded lasers were characterized using a ILXlightwave LPA-9084. The main electrical and optical parameters of LDs were measured to obtain supplementary information for future failure analysis. After 500 thermal cycles, the LDs were cross-sectioned to observe the microstructural evolution in the solder joint.



(a)



(b)

Figure 6-2 Electrical and optical characteristic of LDs before and after each interim cycles. (a) Comparison of series resistance before and after every 100 cycles; (b) Comparison of optical performance before and after every 100 cycles.

The series resistance, R_S , did not increase significantly after 500 thermal cycles aging as shown in Figure 6-2(a). No measurable deterioration of the epitaxial heterojunctions and bonding quality was observed. The threshold current, which is often a measure of the device degradation and lifetime [192], also did not increase after 500 cycles. This shows that the thermal aging process did not damage the LDs or their intrinsic properties significantly. However, slight optical degradation could be observed at high injection current after 500 thermal cycles as shown in Figure 6-2(b). The optical degradation may be attributed by the microstructural evolution, such as the growth of an IMC layer in the solder joint.

Hence, microstructural studies of the solder joint after aging were also studied since exposure to thermal cycling condition readily caused the intermetallic layer to grow by solid state diffusion. However, no significant microstructural changes or IMC growth were observed after aging as shown in Figure 6-3. This might be due to the short reflow duration and limited mutual interdiffusion between Ni and Au80Sn20 solder [169]. The LD and solder joint still maintained their good thermal behavior with this modified bonding process. Hence, good bonding integrity was achieved after 500 temperature cycles tests.

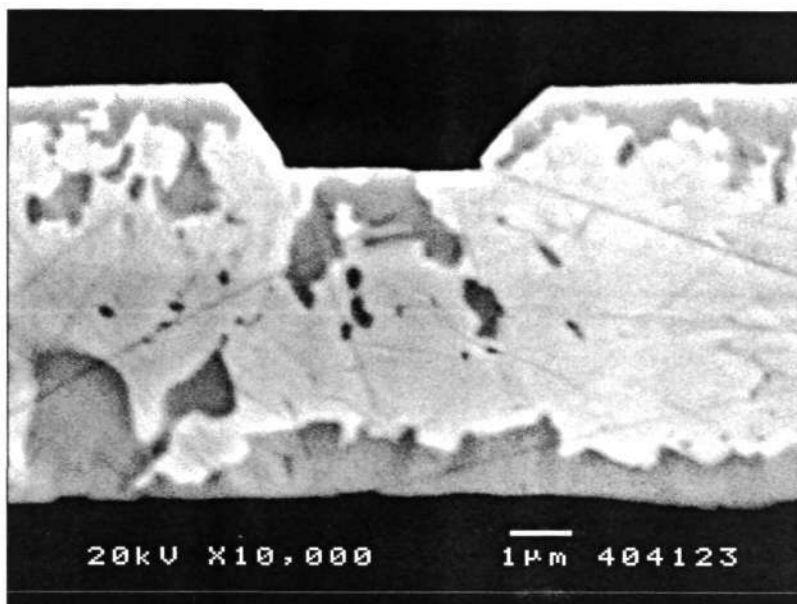


Figure 6-3 Typical cross-sectional view of bonded LD after 500 thermal cycles. No significant microstructure changes in the solder joint.

6.3 Effect of Thermal Aging Loading on Reliability of Bonded LDs

As these LDs were expected to have long service lifetimes, accelerated aging was also conducted to understand the reliability of the bonded sample. Accelerated aging at high stress levels i.e. high injection current and high operating temperature were employed to understand the mechanisms involved in the degradation process. Typically, these LDs were biased at 1.2-1.5 times the initial threshold current, and the operating condition for these uncooled LDs was 25°C. The LDs were burned-in under high constant current aging of 90 mA at 85 °C.

Long-term storage at ambient temperature can also lead to changes in the laser characteristics due to various thermally activated processes. Such effects can be largely pre-empted by an artificial aging process. The LD characterization system assembled in Figure 3-3. was used to screen devices, burn in devices to stabilize their characteristics, or estimate the lifetime of the package. The bonded lasers were subjected to an initial purge

test to weed out lasers with weak failure mechanisms. This strenuous test involved a high operating current of 90 mA at an elevated temperature of 85 °C. The lifetime of the LDs can be estimated from an Arrhenius relationship [193, 194],

$$Lifetime = t_o \exp \left\{ -\frac{E_a}{k} \left[\frac{1}{T_0} - \frac{1}{T} \right] \right\} \quad (8-1)$$

where t_o is the lifetime at normal working condition, T is the aging temperature, E_a is the activation energy and k is the Boltzmann constant.

However, this relationship only accounted for experimental setup at low injection current, typically at 1.2 -1.5 times its threshold current. When the injection current increased significantly, the stress level increased due to Joule heating should also be accounted for.

$$Lifetime = t_o \left(\frac{I}{I_o} \right)^{-n} \exp \left\{ -\frac{E_a}{k} \left[\frac{1}{T_0} - \frac{1}{T} \right] \right\} \quad (8-2)$$

where I_o is the operating current, I is the accelerated stress current, and n for GaAs LDs is typically 1-1.3.

6.3.1 Analysis of LD Degradation

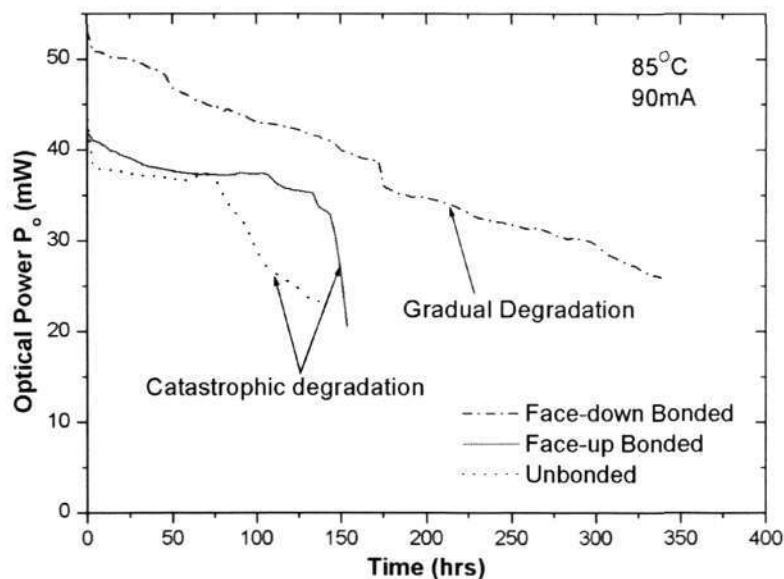
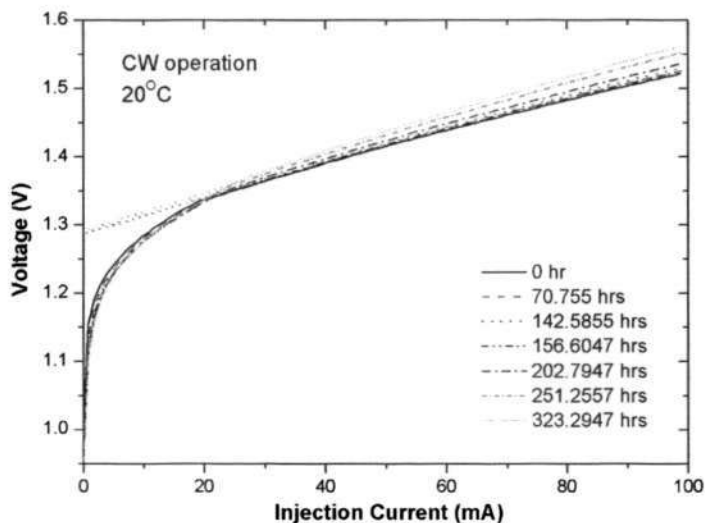


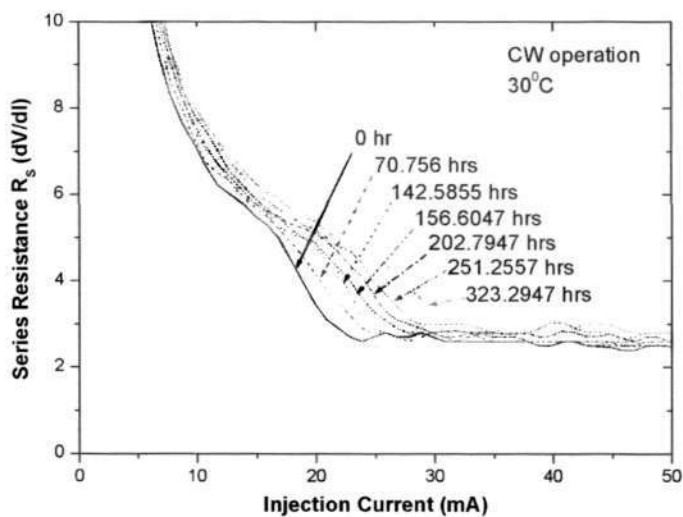
Figure 6-4 Characterization of optical performance during the aging process. Rapid degradation process can be observed for unbonded LDs while face-down bonded LDs exhibit gradual degradation.

During the aging process, in-situ optical measurement showed the degradation characteristic. The initial optical power for unbonded and face-up bonded LDs were ~ 40 mW/facet while modified face-down bonded LDs exhibited higher optical performance at ~ 50 mW/facet. The higher optical performance in face-down bonded LDs was attributed to the effectiveness of heat dissipation for the bonded LDs. Catastrophic degradation, detected by a very fast decrease in output power, could be observed for both unbonded and face-up bonded LDs while face-down bonded LDs exhibited gradual degradation characteristic as shown in Figure 6-4. The time dependence of the optical performance indicated that the optical power decrease was caused by diffusion of some kinds of defects. The degradation failure for these unbonded LDs was estimated to be 75 hrs. A kink was also observed at 157 hrs in the face down approach. The LD was halted at ~ 157 hrs to study the electrical and optical performance degradation. After bonding, the failure

for face-up and face-down bonded LDs improved to 140 hrs and 350 hrs respectively. Again, the improved lifetime was due to the improved thermal management after bonding. Nevertheless, the electro-optical characteristics of the bonded samples were also investigated to estimate any degradation of the LD performance.



(a)



(b)

Figure 6-5 Electrical characterization of LD as a function of time; (a) Forward voltage drops while (b) series resistance increases due to changes to the junction properties.

The forward voltage and series resistance were observed during the aging process. The forward voltage decreased while a slight increase in series resistance could be observed

in Figure 6-5. The drop in forward voltage indicated a change in the junction characteristics and this distortion could be better interpreted in the $\frac{dV}{dI}$ plot. As shown in Figure 6-5(b), the junction was observed to distort with aging. During aging, heating in the LD occurred easily through the non-radiative processes of the photo-induced carriers. The heat generation enlarged the thickness of the region having a high absorption coefficient by bandgap reduction. The energy emitted through the non-radiative recombination process in this region enhanced defect diffusion. Therefore, some kinds of defects were gradually introduced from the interface during aging. These defects increased the temperature at the interface through the increased rate of non-radiative recombination. This additional temperature rise might also induce a positive feedback towards COD.

6.3.2 Catastrophic Optical Damage

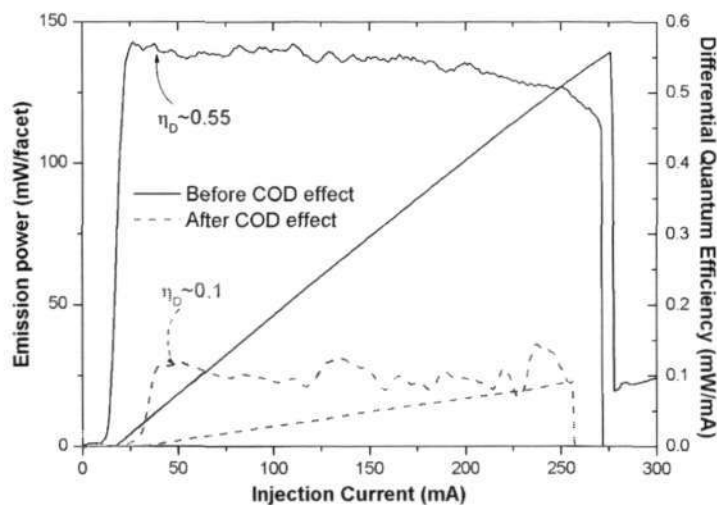


Figure 6-6 Effect of COD degradation on the optical performance. Threshold current and differential quantum efficiency deteriorated significantly.

Unlike thermal rollover, COD effect resulted in irreversible damage to the active region and its operation. Large loss in laser output power was resulted from the facet melting.

The characteristics of the LD were damaged as the specified optical output could no longer be achieved as shown in Figure 6-6. The threshold current also increased significantly. The adverse effects of lattice disorder on carrier confinement to the quantum well might also be responsible for the degraded performance.

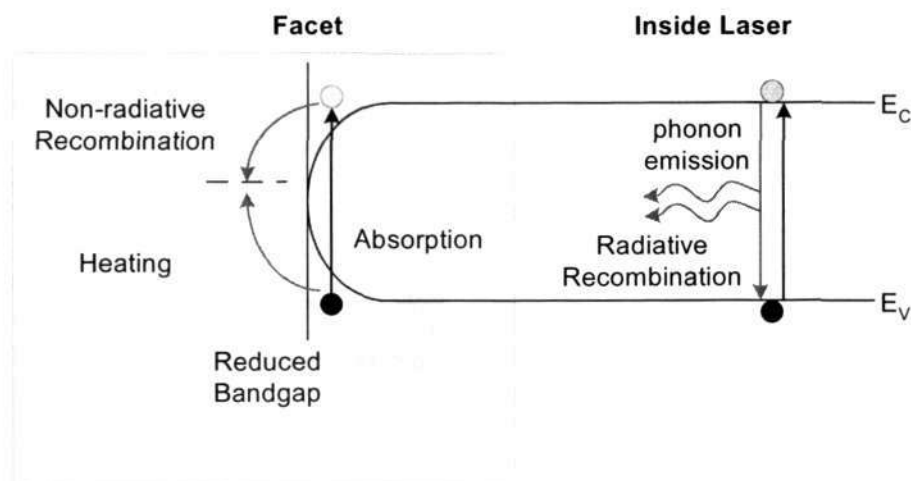
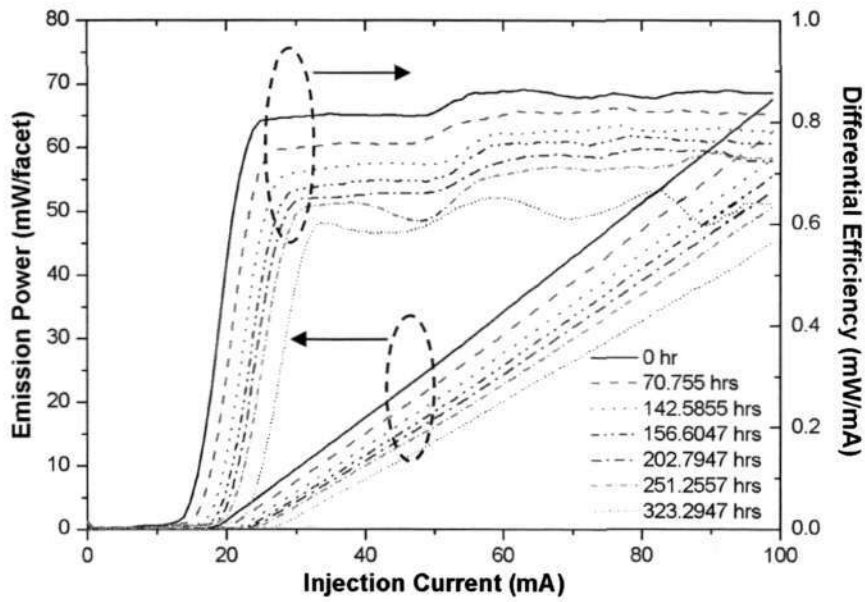
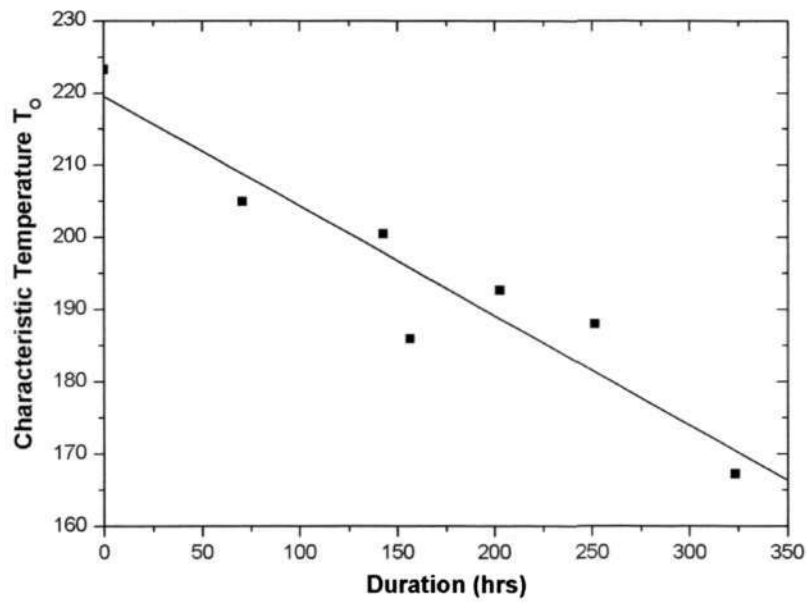


Figure 6-7 Schematic diagram of non-radiative recombination near the facet end. Carrier absorption towards the facet resulted in higher heat generated along the cavity length.

Surface recombination at the facets and the associated depletion of charge carriers caused the active region near the facet to become absorbing at the lasing wavelength. Due to the high surface recombination rate at the facet-air interface, the temperature at the facets increased during operation. The raised temperature reduced the bandgap energy in the region, causing further heating at the facet. Higher heat flux generated at the facet drained more current in order to compensate uniform optical gain along the active region. This resulted in higher temperature at the facet than at the bulk material, eventually reaching a critical temperature, thermal runaway and then COD. The absorption of energy eventually increased the temperature at the facet to the melting point of the material (>1000 °C) and the laser degraded sufficiently until non-radiative recombination was obtained [34]. The failure mechanism is better elucidated with Figure 6-7.



(a)



(b)

Figure 6-8 Evaluation of parametric behavior during the aging process; (a) Threshold current increases significantly as shown by the emission power measurements while differential quantum efficiency decreases gradually in the aging process; (b) The characteristic temperature T_0 decreases gradually with time.

To substantiate the findings, I_{th} , η_D , and T_0 were further characterized during the aging process as shown in Figure 6-8. During accelerated aging, degradation manifested itself by an increasing threshold from 18 mA to 28 mA and a slight decrease in η_D from 0.8 mW/mA to 0.6 mW/mA. A summary of the degradation characteristic was depicted in Table 8. The increased threshold current might be due to a decrease of η_i via an increased conversion of excitation energy into non-radiative recombination processes [39]. From equation 2-9, the decrease of η_i induced a deterioration of η_D . The characteristic temperature T_0 was observed to deteriorate in the aging process (See Figure 6-8(b)). Due to the generation of accumulated defects in the active region, the radiative recombination process in the active region reduced and the LD could not function as robust as the initial condition. The non-radiative recombination processes at the diffused defects disrupted the basic waveguide working mechanism as discussed in CHAPTER 2.

Table 11. Comparison of packaged LD before and after accelerated aging.

Parameters	Before aging	After Aging
I_{th}	19.8mA	29.8mA
η_D	0.815	0.595
P_O	52.58mW	25.95mW
T_0	223.214°C	167.224°C

A generic degradation mechanism for 980 nm $In_xGa_{1-x}As/GaAs$ QW structure has been reported with In out diffusion from the InGaAs well into the adjacent GaAs barriers, driven by compositional discontinuity at the interfaces [44]. Hence, surface morphology at the facet ends were observed under SEM before and after aging. As shown in Figure 6-9(a)-(b), the cleaved facet on the top and side view showed no abnormalities before aging. However, after high current aging, the ridge at the facet end deformed and the active region seemed to melt under the ridge (see Figure 6-9(c)-(d)). The most plausible cause for this is that, at COD, material close to the facet melt and pushed through to the

surrounding area. As shown in Figure 6-9(d), a dark region was generated at the interface and then grew towards the inner region and also affected the surrounding areas. Dark Line Defect (DLD) was generated from the interface towards the inner region.

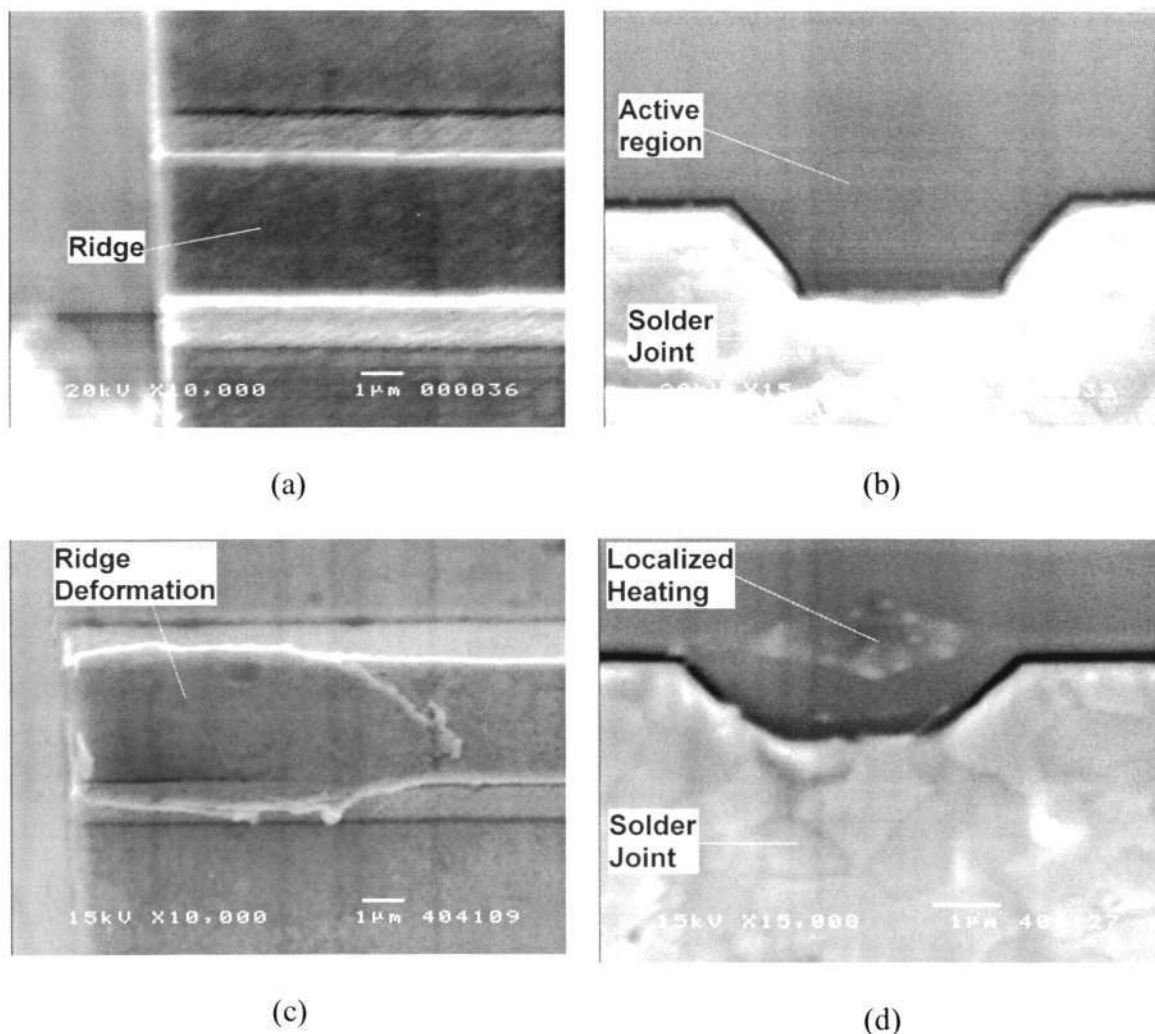


Figure 6-9 Facet observation (a)-(b) before and (c)-(d) after aging. Evidence for this catastrophic failure can be seen from scanning electron microscope (SEM) images of post-COD laser facets. Protrusion can be observed from the outline of the laser ridge. Material at the active region has melted and pushed through the facet before resolidifying. The damage occurred at the center where optical field intensity is at maximum.

The catastrophic damage resulting from propagation of a melted zone confined to the active region can be explained by Figure 6-10. Propagation of the molten zone confined to the active layer from the cleaved facet to deep within the crystal might be due to the dark line associated with catastrophic damage. The local melting might be initiated at defects or at defect-free cleaved surfaces [195], [34]. Progressive accumulation of defects at the facets acted as non-radiative recombination centers under long-term aging. This progressive defect accumulation might provide a simple means of optical degradation during the aging process. As defects were formed near the facets, the rate of non-radiative recombination and facet heating increased. The increased temperature enhanced the defects generation rate further in the vicinity of the interface and non-radiative recombination rates increased accordingly. As mentioned, the bandgap began to narrow, leading to self-absorption at the band edges. These processes formed a time-dependent positive feedback cycle and the loop could be added in parallel to non-radiative recombination and heating [43]. Hence, the damage did not occur just at the cleaved surface, but extended inwards from the facet. This rate of defective degradation depended on the capacity of heat dissipation from the active region (heat source).

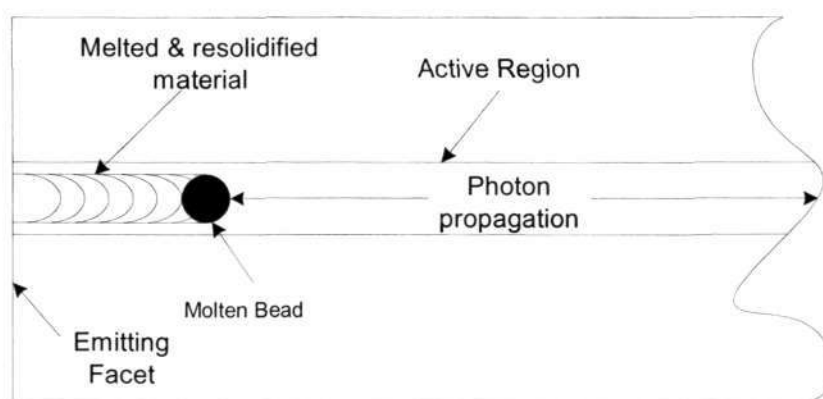


Figure 6-10 Facet deformation at the active region resulted from the localized melting. Progressive propagation of molten zone along the active region resulted in malfunction of the device.

As the LD aged, the liquid-solid interface moved inwards. The molten region was maintained by absorption of energy from the laser beam while the back facet formed an optical cavity and lasing continued. The re-solidified material, which consisted of intermixed elements from the InGaAs active region as well as the adjacent AlGaAs cladding layers, was highly defective. Movement of the solid-liquid interface continued until the laser degraded sufficiently such that there was insufficient optical energy within the laser cavity to sustain the molten region [196]. These hypotheses are in good agreement with our micrographs.

6.4 Summary

In this chapter, thermal cycling and thermal aging reliability testing was conducted. In both tests, good solder joint reliability could be identified.

In thermal cycling testing, no significant microstructure evolution could be observed in the solder joint after 500 aging cycles. The series resistance also did not increase significantly after aging. No measureable deterioration of the epitaxial heterojunctions or bonding quality was observed. This demonstrated that the packaged LDs are capable of withstanding 500 thermal cycles.

In thermal aging, face-down bonded LDs exhibited improved lifetime over unbonded and face-up bonded LDs. During the aging process, parametric measurements of the packaged LDs demonstrated that the degradation occurred within the device. Progressive accumulation of defects at the facets acted as non-radiative recombination centers during long-term aging. This defect accumulation resulted in facet heating and optical degradation.

CHAPTER 7

CONCLUSIONS

7.1 Conclusion

In emerging photonics/optoelectronics applications, development of LD packaging is essential to a new cutting-edge class of high-power photonics devices. In this thesis, a modified fluxless face-down bonding process for single-mode ridge-waveguide LDs was introduced to resolve complicating packaging issues such as ridge damage and misalignment. For long-term reliability, hard Au80Sn20 solder was used to enhance fatigue and creep resistance. Good bonding integrity can be achieved at a low bonding pressure of 0.196 MPa and short bonding duration of 5 s during 290 °C reflow. Microstructural evolution of the solder joint showed that the solder joint possessed good stability with low growth rate of IMC formation at the interfaces due to the short reflow time. Mechanical testing showed that the fracture mode occurred within the LD and that the bonding strength exceeded MIL-STD-883C Method 2019 conditions.

Based on this modified bonding technique, a robust bonding process window was established. Extensive investigation on the bonding integrity and LD performance were studied during the creation of the bonding process window. The bonded LDs demonstrated improved electro-optical properties with excellent bonding integrity of the solder joint. The optical performance improved ~ 3 times without deteriorating its electrical and spectral characteristics of LDs. Furthermore, comparison of different bonding techniques demonstrated that the packaging technique influenced the LD performance considerably. Three different bonding approaches were considered; face-up bonding, existing face-down bonding and modified face-down bonding. For the face-up

bonding technique, heat transfer was insufficient to optimize the LD performance. Using an existing face-down approach, the single-mode ridge-waveguide LDs experienced performance degradation caused by the bonding process. No performance degradation was observed with the modified face-down bonding process. Electrical, optical, spectral, and thermal characterization of LDs were also shown to be improved over various bonding methods. Since the performances of these LDs were temperature dependent, the electrical-optical-spectral-thermal properties were considered in the comparison analysis, together with the mechanical integrity of the bonding interface. The modified face-down bonding technique yielded better performance and reliability.

A multi-scale thermal simulation exercise, experimental elucidation accompanied with theoretical analyses, was necessary to understand and verify heat generation and temperature distribution in the packaging design. A null technique of emission wavelength was conducted to estimate the temperature rise in the package. With relation to the band structure theory, close numerical fitting of bandgap energy calculations with experimental emission wavelength was further achieved. The calculated temperature rise corresponds well to the experimental measurements. FE simulation using ABAQUS 6.4.1 was then conducted to evaluate the optimal bonding configuration. The temperature distribution of different bonding configurations was analyzed. Numerical modeling demonstrated improved thermal management in the face-down approach. The improved LD performances with superior thermal management were verified for the face-down bonding approach.

Basic reliability testing also showed good bonding integrity in the solder joint after thermal cycling and accelerated thermal aging. No significant microstructural changes could be observed in the solder joint after either thermal cycling or thermal aging tests.

Parametric studies demonstrated that the degradation occurred within the LD. The degradation characteristic and failure mechanism in the packaging design was further comprehended.

The single-mode ridge-waveguide LD was used in this project because it is one of the promising laser devices used in telecommunications applications and it faces imminent packaging issues due to its narrow ridge width of less than 4 μm . Although only single-mode ridge-waveguide LDs were used in this thesis, this modified bonding process is also expected to be applicable to a plurality of semiconductor devices. Hence, this fluxless process might be attractive to many applications involving LDs, Laser Arrays (LDAs), Light Emitting Devices (LEDs), LED arrays, Multiple Quantum-Wells (MQWs) structures, and optoelectronics and photonics integrated circuits. These devices are frequently utilized in photonics switches, pump lasers, and solid-state lasers. This bonding process is also applicable to electronics components such as Metal-Semiconductor-Field-Effect-Transistor (MESFET) devices and circuits, and Pseudo High Electron Mobility Transistors (PHEMTs). These devices can be used in high-frequency, high-power applications such as RF communications modules, power amplifier, and electronics integrated circuits as well.

7.2 Recommendations

In this work, basic reliability testing methodologies were carried out to study the bonding integrity at the solder joint. However, to create a comprehensive investigation of the solder joint reliability, long-term reliability testing must be conducted to realize practical reliability prediction over long service hours. Based on the process optimization, long-term reliability investigations of these LDs and solder joint at different environmental and

service conditions must be adequately addressed. LD degradation is the result of the interaction between different intrinsic (material properties, crystal defects, quality of the interfaces etc) and external factors (packaging, bonding, temperature, injection current, facet coating etc), which introduce profound changes in the materials forming the active parts of the devices, with the result of a decrease in the quantum efficiency. While the influence of physical degradation is strongly affected by the device characteristics themselves, the packaging design may also contribute to the long-term stability of the entire module. The many inputs that contribute to the degradation render difficult a full understanding of the physical processes governing the failure mechanism. Hence, fundamental understanding of the degradation modes is the basis to long-term reliability of the package. However, this is not performed in this thesis work as it is an expensive experimental methodology study. These LDs are expected to have a typical lifetime of 10^6 hrs and equipment required for such a reliability study is also costly.

In addition, thermal resistance of the bonding layer should be kept minimal to facilitate proper heat transfer to the heatsink. Hence, Au80Sn20 solder is used in this project. However, the thermal resistance of the solder joint can be further improved by adding a high thermal conductivity composite material into the solder joint. Recently, carbon nanotubes (CNTs) were found to have excellent thermal conductivity and mechanical strength. Formulating CNTs additives into solders have already shown tremendous mechanical and thermal advantages over existing solder alloys. However, integrating such composite material into optoelectronics packaging remains a technological challenge as there are material and design oriented problems to be resolved.

List of Publications

Journals:

1. J.W.R. Tew, X.Q. Shi and S. Yuan, "*Au/Sn Solder for Face-Down Bonding of AlGaAs/GaAs Ridge Waveguide Laser Diodes*," *Materials Lett.*, 58, 2695-2699 (2004).
2. C.Y. Liu, S.F. Yoon, W.J. Fan, J.W.R. Tew and S. Yuan, "*Low threshold current density and high characteristic temperature narrow-stripe native oxide-confined 1.3- μ m InGaAsN triple quantum well lasers*," *Opt. Express*, 13, 9045-9051 (2005).
3. J.W.R. Tew, G.Y. Li, M.S. Ling, Z.F. Wang and X.Q. Shi, "*Parametric Investigation of Laser Diode Bonding using Eutectic AuSn solder*," *Thin Solid Films*, in press (2006).
4. J.W.R. Tew, X.Q. Shi, S. Yuan, G.Y. Li and Z.F. Wang, "*Modified Face-Down Bonding of Ridge-Waveguide Lasers Using Hard Solder*," *IEEE Trans. Electron. Packag. Manufactur.*, (Accepted for publication).
5. J.W.R. Tew, G.Y. Li, M.S. Ling, Z.F. Wang and X.Q. Shi, "*Influence of Bonding Temperature and Applied Load on the Bonding Integrity and Optical Performance of Face-Down Bonded Ridge-Waveguide Lasers*," *J. Electron. Mater.*, (Accepted for publication).
6. J.W.R. Tew, F.L. Ng, L.S.K. Goi, Y.F. Sun, Z.F. Wang, X.Q. Shi, J. Wei, and G.Y. Li, "*Microstructure of Eutectic 80Au/20Sn solder joint in Laser Diode Package*," *J. Electron. Mater.*, (Accepted for publication).

7. J.W.R. Tew, L.S.K. Goi, L.H. Xiao, W.C. Lim, Z.F. Wang and G.Y. Li, "*Dependence of Injection Current on Facet Heating and Thermal resistance in Semiconductor Lasers*," Optical Express, (submitted for publication).

8. J.W.R. Tew, L.S.K. Goi, W.C. Lim, X.H. Li, Z.F. Wang and G.Y. Li, "*Influence of Radiative Energy Transfer on the Thermal Behavior of Bonded InGaAs/GaAs Lasers*," IEEE Quant. Electron., (modification for publication).

Conferences:

1. J.W.R. Tew, Z.F. Wang, X.Q. Shi and G.Y. Li, "*An Optimized Face-Down Bonding Process for Laser Diode Packages*," Proceedings of IEEE 6th EPTC, 2004, pp. 390-395.

2. C.Y. Liu, S.F. Yoon, W.J. Fan, Z.Z. Sun and R.J.W. Tew, "*Ridge Width Effect on the Characteristic Temperature of GaInNAs Triple Quantum Well Ridge Waveguide Lasers*," Proceedings of CLEO 2005, 2005.

3. S.F. Yoon, C.Y. Liu, W.J. Fan, R.J.W. Tew and Z.Z. Sun, "*Comparison of Characteristic Temperature from Triple quantum Well and Single Quantum Well GaInNAs Ridge Waveguide Lasers*," Proceedings of CLEO, 2005, pp. 859-860.

4. C.Y. Liu, J.W.R. Tew, S. Yuan, S.Z. Wang and S.F. Yoon, "*InGaAsN/GaAs lasers fabricated with pulsed anodic oxides*," In Proc. CLEO, 2002.

References

1. W. Hunziker, "Low-cost packaging of semiconductor laser arrays," IEEE Circuit and Devices Magazine, 13 19-25 (Jan 1997).
2. A. Larsson, S. Forouhar, J. Cody and R.J. Lang, "High-power operation of highly reliable narrow stripe pseudomorphic single quantum well lasers emitting at 980nm," IEEE Photon. Technol. Lett., 2 307-309 (May 1990).
3. J. Zhao, L. Li, W.M. Wang and Y.C. Lu, "High-power and low-divergence 980-nm InGaAs-GaAsP-AlGaAs strain-compensated quantum-well diode laser grown by MOCVD," IEEE Photon. Technol. Lett., 15 1507-1509 (Nov 2003).
4. G.W. Yang, R.J. Hwu, Z.T. Xu and X.Y. Ma, "High-performance 980-nm quantum-well lasers using a hybrid material system of an Al-free InGaAs-InGaAsP active region and AlGaAs cladding layers grown by metal-organic chemical vapor deposition," IEEE J. Quant. Electron., 35 1535-1541 (1999).
5. Y. Qu, S. Yuan, C.Y. Liu, B.X. Bo, G.J. Liu and H.L. Jiang, "High-power InAlGaAs/GaAs and AlGaAs/GaAs Semiconductor laser arrays emitting at 808nm," IEEE Photon. Technol. Lett., 16 389-391 (Feb 2004).
6. W. Pittroff, G. Erbert, G. Beister, F. Bugge, A. Klein, A. Knauer, J. Maege, P. Ressel, J. Sebastian, R. Staske, and G. Traenkle, "Mounting of high power laser diodes on Boron Nitride heat sinks using an optimized Au/Sn metallurgy," IEEE Trans. Adv. Packag., 24 434-441 (Nov 2001).
7. K. Shigihara, Y. Nagai, S. Karakida, M. Aiga, M. Otsubo and K. Ikeda, "Estimation of strain arising from the assembling process and influence of assembling materials on performance of laser diodes," J. Appl. Phys., 78 1419-1423 (1995).

8. H. Asonen, A. Ovtchinnikov, G. Zhang, J. Nappi, P. Savolainen and M. Pessa, "Aluminum-free 980-nm GaInAs/GaInAsP/GaInP pump lasers," *IEEE J. Quant. Electron.*, 30 415-423 (Feb. 1994).
9. N. Chand, S.N.G. Chu, N.K. Dutta, J. Lopata, M. Geva, A.V. Syrbu, A.Z. Mereutza, and V.P. Yakovlev, "Growth and fabrication of high-performance 980-nm strained InGaAs quantum-well lasers for erbium-doped fiber amplifiers," *IEEE J. Quant. Electron.*, 30 424-440 (1994).
10. J.H. Lee, W.J. Lee and N. Park, "Comparative study of temperature dependent multichannel gain and noise figure distortion for 1.48- and 0.98-um pumped EDFAs," *IEEE Photon. Technol. Lett.*, 10 1721-1723 (1998).
11. R.I. Laming, M.C. Farries, P.R. Morkel, L. Reekie and D.N. Payne, "Efficient pump wavelengths of erbium-doped fiber optical amplifier," *IEEE Electron. Lett.*, 25 12-14 (1989).
12. E. Desurvire, "Spectral noise figure of Er³⁺-doped fiber amplifiers," *IEEE Photon. Technol. Lett.*, 2 208-210 (Mar 1990).
13. B. Pederson, B.A. Thompson, S. Zemon, W.J. Miniscalco and T. Wei, "Power requirements for erbium-doped fiber amplifiers pumped in the 800, 980, 1480nm bands," *IEEE Photon. Technol. Lett.*, 4 46-49 (1992).
14. K.I. Shigihara, K. Kawasaki, Y. Yoshida, S. Yamamura, T. Yagi and E. Omura, "High-power 980-nm ridge waveguide laser diodes including an asymmetrically expanded optical field normal to the active layer," *IEEE J. Quant. Electron.*, 38 1081 - 1088 (Aug. 2002).
15. J.A.V. Veichten and T.K. Bergstresser, "Electronic Structures of Semiconductor Alloys," *Phys. Rev. B*, 1 3351-3358 (1970).
16. I. Vurgaftman and J.R. Meyer, "Band parameters for III-V compound semiconductors and their alloys," *J. Appl. Phys.*, 89 5815-5875 (Jun 2001).

17. G.H.B. Thompson, "*Physics of Semiconductor Laser Devices*," Bath, UK: John Wiley & Sons; 1980.
18. G. Zhang and A. Ovtchinnikov, "*Temperature sensitivity of strained-layer InGaAs/Ga(In)As(P)/GaInP separate-confinement-heterostructure quantum well lasers ($\lambda \sim 980$ nm)*," J. Appl. Phys., 73 3599-3602 (1993).
19. E.S. Yang, "*Microelectronic Devices*," New York: McGraw-Hill; 1988.
20. H. Kressel, H. Nelson and F.Z. Hawrylo, "*Control of Optical Losses in p-n Junction Lasers by Use of a Heterojunction: Theory and Experiment*," J. Appl. Phys., 41 2019-2031 (Apr 1970).
21. F.P. Dabkowschi, A.K. Chin, P. Gavrilovic, S. Alie and D.M. Beyea, "*Temperature profile along the cavity axis of high power quantum well lasers during operation*," Appl. Phys. Lett., 64 13-15 (Jan 1994).
22. T. Hayakawa, "*Facet Temperature distribution in broad stripe high power laser diodes*," Appl. Phys. Lett., 75 3204-3206 (Nov 1999).
23. S.J. Sweeney, L.J. Lyons, A.R. Adams and D.A. Lock, "*Direct measurement of facet temperature up to melting point and COD in high-power 980-nm semiconductor diode lasers*," IEEE J. Select. Topics Quant. Electron., 9 1325-1331 (2003).
24. C.H. Gooch, "*The thermal properties of gallium arsenide laser structures*," IEEE J. Quant. Electron., 4 140-143 (1968).
25. W. Engeler and M. Garfinkel, "*Thermal characteristics of GaAs laser junctions under high power pulsed conditions*," Solid-State Electron., 8 585-604 (1965).
26. V. Spagnolo, M. Troccoli and G. Scamarcio, "*Thermal resistance and temperature characteristics of GaAs/Al_{0.33}Ga_{0.67}As quantum-cascade lasers*," Appl. Phys. Lett., 78 1177-1179 (Feb 2001).

27. T. Makino, J.D. Evans and G. Mak, "*Maximum output power and maximum operating temperature of quantum well lasers*," Appl. Phys. Lett., 71 2871-2873 (Nov 1997).
28. T.L. Paoli, "*A new technique for measuring the thermal impedance of junction lasers*," IEEE J. Quant. Electron., 11 498-503 (Jul 1975).
29. O.J.F. Martin, G.-L. Bona and P. Wolf, "*Thermal behaviour of visible AlGaInP-GaInP ridge laser diodes*," IEEE J. Quant. Electron., 28 2582-2588 (Nov 1992).
30. M. Voss, C. Lier, U. Menzel, A. Barwolff and T. Elsaesser, "*Time-resolved emission studies of GaAs/AlGaAs laser diode arrays on different heat sinks*," J. Appl. Phys., 79 1170-1172 (Jan 1996).
31. J.S. Manning, "*Thermal impedance of diode lasers: Comparison of experimental methods and a theoretical model*," J. Appl. Phys., 52 3179-3184 (May 1981).
32. A.R. Hartman and R.W. Dixon, "*Reliability of DH GaAs lasers at elevated temperatures*," Appl. Phys. Lett., 26 239-242 (1975).
33. J.G. Endriz, M. Vakili, G.S. Browder, M. DeVito, J.M. Haden, G.L. Harnagel, W.E. Plano, M. Sakamoto, D.F. Welch, S. Willing, D.P. Worland, and H.C. Yao, "*High power diode laser arrays*," IEEE J. Quant. Electron., 28 952-965 (1992).
34. C.H. Henry, P.M. Petroff, R.A. Logan and F.R. Merritt, "*Catastrophic damage of $Al_xGa_{1-x}As$ double-heterostructure laser material*," J. Appl. Phys., 50 3721-3732 (May 1979).
35. G. Oliveti, A. Piccirillo and P.E. Bagnoli, "*Analysis of laser diode thermal properties with spatial resolution by means of the TRAIT method*," Microelectronics Journal, 28 293-300 (1997).
36. D.H. Newman, D.J. Bond and J. Stefani, "*Thermal-resistance models for proton-isolated double-heterostructure lasers*," Solid State Electron. Devices, 2 41-46 (1978).

37. K. Takeshi and F. Yoshitaka, "*Temperature Distribution in the GaAs-AlGaAs Double-Heterostructure Laser below and above the Threshold Current*," Japan. J. Appl. Phys., 14 1981-1986 (Dec 1975).
38. S.W. Feng, X.S. Xie, C.Z. Lu and G.D. Shen, "*The thermal characterization of packaged semiconductor device*," Proceedings of 16th IEEE SEMI-THERM Symposium, 2000, pp. 220-226.
39. E.W. Kreutz, N. Wiedmann, J. Jandeleit, D. Hoffmann, P. Loosen and R. Poprawe, "*Reliability and degradation mechanisms of InGa(Al)As/GaAs DQW high-power diode lasers*," J. Crystal Growth, 210 313-317 (2000).
40. J. Jimenez, "*Laser diode reliability: crystal defects and degradation modes*," Comptes Rendus Physique, 4 663-673 (2003).
41. J.W. Tomm, A. Bärwolff, A. Jaeger, T. Elsaesser, J. Bollmann and W.T. Masselink, "*Deep level spectroscopy of high-power laser diode arrays*," J. Appl. Phys., 84 1325-1332 (Aug 1998).
42. A. Moser, "*Thermodynamics of facet damage in cleaved AlGaAs lasers*," Appl. Phys. Lett., 59 (Jul. 1991).
43. F.A. Baiocchi, D.L. Neiman, W.C. Tang and H.J. Rosen, "*Chemical changes accompanying facet degradation of AlGaAs quantum well lasers*," J. Appl. Phys., 72 3884-3896 (Nov 1992).
44. S.N.G. Chu, N. Chand and W.B. Joyce, "*Generic degradation mechanism for 980nm In_xGa_{1-x}As/GaAs strained quantum-well lasers*," Appl. Phys. Lett., 78 3166-3168 (2001).
45. M. Fukuda, "*Reliability and Degradation of semiconductor lasers and LED*," Norwood: Artech House; 1991.
46. C.H. Henry and D.V. Lang, "*Nonradiative capture and recombination by multiphonon emission in GaAs and GaP*," Phys. Rev. B, 15 989-1016 (1977).

47. M. Fukuda, M. Okayasu, J. Temmyo and J.-I. Nakano, "*Degradation behavior of 0.98 μ m strained quantum well InGaAs/AlGaAs lasers under high-power operation*," IEEE J. Quant. Electron., 30 471-476 (Feb 1994).
48. S.A. Merritt, K. Mobarhan, R. Whaley, S. Fox and M. Dagenais, "Semiconductor Laser and Optical Amplifier Packaging," in *Optoelectronic Packaging*, A.R. Mickelson, N.R. Basavanhally and Y.C. Lee, Editors. John Wiley & Sons: New York. 1997, pp. 59-78.
49. D.S. Ellis and J.M. Xu, "*Electro-Opto-Thermal Modeling of Threshold Current Dependence on Temperature*," IEEE J. Select. Topics Quant. Electron., 3 640-648 (Apr 1997).
50. D.A. Ackerman, P.A. Morton, R.F. Kazarinov, T. Tanbun-Ek and R.A. Logan, "*Analysis of T_o in 1.3 μ m multi-quantum well and bulk active lasers*," Indium Phosphide and related materials, Santa Barbara CA 466-468 (1994).
51. R.L. Hartman and A.R. Hartman, "*Strain-induced degradation of GaAs injection lasers*," Appl. Phys. Lett., 23 147-149 (1973).
52. K. Fujiwara, *Method of mounting a semiconductor laser device*, in U.S. Patent. Nov 30, 1982.
53. A. Yamauchi and Y. Arai, "*Analysis and measures against heat-expansion for sub-micron LD assembly by passive alignment*," Proceedings of 51st Electronic Components and Technology Conference, 2001, pp. 242 - 246.
54. G. Chen, "*Thermal conductivity and ballistic-phonon transport in the cross-plane direction of superlattices*," Phys. Rev. B, 57 14958-14973 (1998).
55. W.S. Capinski, H.G. Maris, T. Ruf, M. Cardona, K. Ploog and D.S. Katzer, "*Thermal-conductivity measurements of GaAs/AlAs superlattices using a picosecond optical pump-and-probe technique*," Phys. Rev. B, 59 8105-8113 (1999).

56. R. Boudreau, M. Tabasky, C. Armiento, A. Bellows, V. Cataldo, R. Morrison, M. Urban, R. Sargent, A. Negri, and P. Haugsjaa, "Fluxless die bonding for optoelectronics," Proceedings of 43rd Electronic Components and Technology Conference, 1993, pp. 485 - 490.
57. J.H. Lau, "Flip Chip Technologies," New York: McGraw-Hill; 1995.
58. Y.C. Lee and N. Basavanahally, "Overview - solder engineering for optoelectronic packaging," J. Minerals, Metals Material, 46 46 (Jun 1994).
59. T. Hayashi, "An innovative bonding technique for optical chips using solder bumps that eliminate chip positioning adjustments," IEEE Trans. Comp., Hybrids, & Manufact. Technol., 15 225 (Apr. 1992).
60. K. Katsura, T. Hayashi, F. Ohira, S. Hata and K. Iwashita, "A novel flip-chip interconnection technique using solder bumps for high-speed photoreceivers," J. Lightwave Technol., 8 1323-1327 (Sept 1990).
61. F. Delpiano, R. Paoletti, P. Audagnotto and M. Puleo, "High frequency modeling and characterization of high performance DFB laser modules," IEEE Trans Comp., packag., & Manufact. Technol. B, 17 412-417 (Aug. 1994).
62. C.C. Lee and D.H. Chien, "Thermal and package design of high power laser diodes," Proceedings of 9th IEEE SEMI-THERM Symposium, 1993, pp. 75-80.
63. M. Ito and T. Kimura, "Stationary and Transient Thermal Properties of Semiconductor Laser Diodes," IEEE J. Quant. Electron., 17 787-795 (May 1981).
64. P. Martin, J.P. Landesman, R. Bisaro, E. Martin, A. Fily and J.P. Hirtz, "Packaging-induced stress distribution in high-power AlGaAs laser diodes by photoluminescence mapping," Mater. Sci. Eng. B, 80 188-192 (2001).
65. A. Gerhardt, J.W. Tomm, R. Muller, A. Barwolff, D. Lorenzen and J. Donecker, "Measurement of mounting-induced strain and defects in high-power laser diodes

- using *Fourier-transform photocurrent spectroscopy*," Mater. Sci. Eng. B, 91-92 476-480 (2002).
66. A. Barwolff, J.W. Tomm, R. Muller, S. WeiB, M. Hutter, H. Oppermann, and H. Reichl, "*Spectroscopic Measurement of Mounting-induced strain in optoelectronic devices*," IEEE Trans. Adv. Packag., 23 170-175 (May 2000).
67. U. Zeimer, J. Grenzer, T. Baumbach, D. Lubbert, A. Mazuelas and G. Erbert, "*Strain and temperature distribution in broad-area high-power laser diodes under operation determined by high resolution X-ray diffraction and topography*," Materials Science & Engineering, B80 87-90 (2001).
68. V. Swaminathan, W.R. Wagner, P.J. Anthony, G. Henein and L.A. Koszi, "*Bonding pad induced stresses in (Al,Ga)As double heterostructure lasers*," J. Appl. Phys., 54 3763-3768 (Jul 1983).
69. C.S. Adams and D.T. Cassidy, "*Effects of stress on threshold, wavelength, and polarization of the output of InGaAsP semiconductor diode lasers*," J. Appl. Phys., 64 6631-6638 (Dec 1988).
70. N.B. Patel, J.E. Ripper and P. Brosson, "*Behaviour of threshold current and polarization of stimulated emission of GaAs injection lasers under uniaxial stress*," IEEE J. Quant. Electron., QE-9 338-341 (Feb 1973).
71. T. Hayakawa, N. Miyauchi, S. Yamamoto, H. Hayashi, S. Yano and T. Hijikata, "*Improved lifetimes of (GaAl)As visible (740nm) lasers by reducing bonding stress*," Appl. Phys. Lett., 42 23-24 (Jan 1983).
72. M.J. Robertson, B. Wakefield and P. Hutchinson, "*Strain-related degradation phenomena in long-lived GaAlAs stripe lasers*," J. Appl. Phys., 52 4462-4466 (Jul 1981).

73. A. Yamauchi, "Submicron flip-chip bonding technology for opto-electronic devices," Proceedings of 50th Electronic Components & Technology Conference, 2000, pp. 1743-1746.
74. M. Wale and M. Goodwin, *Flip-chip bonding optimizes Opto-ICs*, in *IEEE Circuit & Devices Magazine*. Nov 1992. p. 25-31.
75. W.D. Bascom and J.L. Bitner, "Void reduction in large area bonding of IC components," *Microelectron. Reliability*, 15 37-39 (1976).
76. K. Mizuishi and M. Tokuda, "Fluxless and virtually voidless soldering for semiconductor chips," *IEEE Trans. Comp., Hybrids, & Manufact. Technol.*, 11 447-451 (1988).
77. C.C. Lee and C.Y. Wang, "A low temperature bonding process using deposited gold-tin composites," *Thin Solid Films*, 208 202-209 (1992).
78. C.C. Lee, C.Y. Wang and G.S. Matijasevic, "A new bonding technology using gold and tin multilayer composite structures," *IEEE Trans. Comp., Hybrids, & Manufact. Technol.*, 14 407-412 (Jun 1991).
79. M. Nishiguchi, "Highly reliable Au-Sn eutectic bonding with background GaAs LSI chips," *IEEE Trans. Comp., Hybrids, & Manufact. Technol.*, 14 523-528 (Sept 1991).
80. G.R. Dohle, J.J. Callahan, K.P. Martin and T.J. Drabik, "A new bonding technique for microwave devices," *IEEE Trans. Comp., Packag., & Manufact. Technol. B*, 19 57-63 (Feb 1996).
81. G.R. Dohle, T.J. Drabik, J.J. Callahan and K.P. Martin, "Low temperature bonding of epitaxial lift off devices with AuSn," *IEEE Trans. Comp., Packag., & Manufact. Technol. B*, 19 575-580 (1996).
82. W. Pittroff, G. Erbert, A. Klein, R. Staske, B. Sumpf and G. Traenkle, "Mounting of laser bars on copper heat sinks using Au/Sn solder and CuW submounts,"

- Proceedings of 52nd *Electronic Components and Technology Conference*, 2002, pp. 276-281.
83. S.A. Merritt, P.J.S. Heim, S.H. Cho and M. Dagenais, "*Controlled solder interdiffusion for high power semiconductor laser diode die bonding*," IEEE Trans. Comp., Packag., & Manufact. Technol. B, 20 141-145 (May 1997).
84. W.S. Wong, A.B. Wengrow, Y. Cho, A. Salleo, N.J. Quitoriano, N.W. Cheung, and T. Sands, "*Integration of GaN Thin Films with dissimilar substrate materials by Pd-In Metal Bonding and Laser Lift-off*," J. Electron. Material, 28 1409-1413 (1999).
85. M. Buda, H.H. Tan, L. Fu, L. Josyula and C. Jagadish, "*Improvement of kink-free operation in InGaAs/GaAs/AlGaAs high power, ridge waveguide laser diodes*," Proceedings of *Optoelectronic and Microelectronic Materials Conference*, Dec. 2002, pp. 25 - 28.
86. M.T. Sheen, Y.H. Ho, C.L. Wang, K.C. Hsieh and W.H. Cheng, "*The Joint Strength and Microstructure of Fluxless Au/Sn Solders in InP-Based Laser Diode Packages*," J. Electron. Mater., 34 1318-1323 (2005).
87. H. Hatanaka, "*Packaging processes using flip chip bonder and future directions of technology development*," Proceedings of *4th Electronics Packaging Technology Conference*, Dec. 2002, pp. 434-439.
88. H.L.J. Pang, K.H. Tan, X.Q. Shi and Z.P. Wang, "*Microstructure and intermetallics growth effects on shear and fatigue strength of solder joints subjected to thermal cycling aging*," Materials Science & Engineering, A307 42-50 (2001).
89. J.S. Kim, "*Thermal and Adhesive properties of Cu interconnect deposited by electroless plating*," Proceedings of *Int'l Symposium on electronic materials and packaging*, 2001, pp. 182-184.

90. W.W. So and C.C. Chin, "*Fluxless process of fabricating In-Au joints on copper substrates*," IEEE Trans. Comp. and Packag. Technol., 23 377-382 (Jun 2000).
91. J.F. Kuhmann, A. Preuss, B. Adolphi, K. Maly, T. Wirth, W. Oesterle, W. Pittroff, G. Weyer, and M. Fanciulli, "*Oxidation and reduction kinetics of eutectic SnPb, InSn, and AuSn: A knowledge base for fluxless solder bonding applications*," IEEE Trans. Comp., Packag., & Manufact. Technol. C, 21 134-141 (Apr 1998).
92. D.P. Yao and J.K. Shang, "*Effect of cooling rate on interfacial fatigue-crack growth in Sn-Pb solder joints*," IEEE Trans Comp., Hybrids, & Manufact. Technol. B, 19 154-165 (1996).
93. M.A. Fritz and D.T. Cassidy, "*Cooling rate in diode laser bonding*," IEEE Trans. Comp. and Packag. Technol., 27 147-154 (Mar 2004).
94. B. Chandran, W.F. Schmidt and M.H. Gordon, "*A novel bonding technique to bond CTE mismatched devices*," Proceedings of *Electronic Components and Technology Conference*, 1996.
95. S. Radeck, D. Kellenberger and C. Luechinger, "*Soft solder die bonding of multiple die devices*," IEEE Trans. Comp., Packag., & Manufact. Technol, 23 646-656 (Dec 2000).
96. T.P.L. Li, E.L. Zigler and D.E. Hillyer, "*AES/ESCA/SEM/EDX studies of die bond materials and interfaces*," Proceedings of 22nd *IEEE Int. Reliability Physics Symp.*, 1984, pp. 169-174.
97. D.R. Olsen and H.M. Berg, "*Properties of die bond alloys relating to thermal fatigue*," IEEE Trans. Comp., Hybrids, & Manufact. Technol., 2 257-263 (Jun 1979).
98. G.S. Selvaduray, "*Die bond materials and bonding mechanisms in microelectronics packaging*," Thin Solid Films, 153 431-455 (1987).

99. R.K. Shukla and N.P. Mincinger, "A critical review of VLSI die attachment in high reliability application," *Solid-State Technology*, 28 67-74 (Jul 1985).
100. P.T. Vianco and F.G. Yost, *A ban on use of lead-bearing solders: implications for electronic industry*. Apr 1992, Sandia National Labs: Albuquerque.
101. D.F. Bernier, "The nature of white residue on printed circuit assemblies," *Des Plaines: Kester Solder*; Oct 1998.
102. T.S. Perry, *Cleaning up*, in *IEEE Spectrum*. Feb 1993. p. 20-26.
103. H.L.J. Pang, T.I. Tan, G.Y. Lim and C.L. Wong, "Thermal stress analysis of direct chip attach electronic packaging assembly," *Proceedings of 1st IEEE/CPT Electronic Packaging Technology Conference*, 1997, pp. 170-176.
104. M. Mahalingam, M. Nagarkar, L. Lofgran, J. Andrews, D.R. Olsen and H.M. Berg, "Thermal effects of die bond voids on metal, ceramic, and plastic packages," *Proceedings of IEEE Electronic Components Conference*, 1984, pp. 469-477.
105. A.J. Yerman, J.F. Bergess, R.O. Carlson and C.A. Neugebauer, "Hot spots caused by voids and cracks in the chip mountdown medium in power semiconductor packaging," *IEEE Trans. Comp., Hybrids, & Manufact. Technol.*, 6 473-479 (Dec 1983).
106. S. Haque, *Processing & characterization of deice solder interconnection and module attachment for power electronics modules*. Dec 1999, Virginia Polytechnique Institute and State University. p. Chapt. 4.
107. M. Aoki, M. Komori, T. Tsuchiya, H. Sato, K. Nakahara and K. Uomi, "InP-Based Reversed-Mesa Ridge-Waveguide Structure for High-Performance Long-Wavelength Laser Diodes," *IEEE J. Select. Topics Quant. Electron.*, 3 672-683 (Apr 1997).

108. M. Early, S. Lee and M. Pello, "*Thermal performance of interface material in microelectronics packaging applications*," Proceedings of IEPS Conference, 1995, pp. 534-544.
109. S. Haque, *Processing and Characterization of Device Solder Interconnection and Module Attachment for Power Electronics Modules*, in *Materials Engineering & Science*. 1999, Virginia Polytechnic Institute and State University.
110. A. Nayar, *The Metals Databook*, Escorts Research Centre: Faridabad.
111. H.E. Boyer and T.L. Gall, "*Metals Handbook: Desk Edition*," Metals Park, Ohio: American Society for metals; 1992.
112. H.H. Glascock and H.F. Webster, "*Structured Copper: A pliable high conductance material for bonding to silicon power devices*," IEEE Trans. Comp., Hybrids, & Manufact. Technol., 6 460-466 (1983).
113. M. Harris, "*An overview of the DOD needs for power electronics and power electronics packaging*," Advancing Microelectronics, 24 (Feb 1997).
114. P.e.a. McCluskey, "*Packaging of Power Electronics for High Temperature Applications*," Advancing Microelectronics, 25 (Feb 1998).
115. N.B. Nguyen, "*Packaging Trends of Power Electronics Modules*," Advancing Microelectronics, 24 (Feb 1997).
116. D. White, S.D. Keck and T.G. Nakanishi, "*New SiC/Al base plates for high performance power modules*," Proceedings of 29th Int. PCIM (Europe) Conference, 1996, pp. 341-346.
117. *In, Au/Sn and Sn/Pb Solders for Photonic Packaging*, Cookson Electronics Assembly Materials.
118. D.P. Bour, N.A. Dinkel, D.B. Gilbert, K.B. Fabian and M.G. Harvey, "*980nm diode laser for pumping Er³⁺-doped fiber amplifiers*," IEEE Photon. Technol. Lett., 2 153-155 (Mar 1990).

119. W.J. Fritz, "*Analysis of rapid degradation in high-power (AlGa)As laser diodes,*" IEEE J. Quant. Electron., 26 68-74 (Jan 1990).
120. C.Y. Wang, Y.C. Chen and C.C. Lee, "*Directly deposited fluxless Lead-Indium-Gold composite solder,*" IEEE Trans. Comp., Hybrids, & Manufact. Technol., 16 789-793 (Dec 1993).
121. C. Wang, *A new bonding technology using gold-tin multilayer composites for microelectronics and photonics,* in *Department of Electrical and Computing Engineering.* 1992, University of California: Irvine.
122. J.L. Freer and J.W. Morris, "*Microstructure and creep of eutectic Indium/Tin on copper and nickel substrates,*" J. Electron. Mater., 21 647-652 (1992).
123. S.P. Sim, A. Christou and B.A. Unger, "*A review of the reliability of III-V optoelectronic components,*" Kluwer: Norwell; 1990.
124. S. Knecht and R.R. Fox, "*Constitutive relation and creep-fatigue life model of eutectic tin-lead solder,*" IEEE Trans. Comp., Hybrids, & Manufact. Technol., 13 424-433 (Jun 1990).
125. J.H. Lau and D.W. Rice, "*Solder joint fatigue in surface mount technology: State of the art,*" Microelectron. Reliability, 26 1189 (Oct 1985).
126. H.D. Solomon, "*Fatigue of 60/40 Solder,*" IEEE Trans. Comp., Hybrids, & Manufact. Technol., 9 423-432 (1986).
127. N.A.J. Sabbag and H.J. McQuen, "*Metal Finishing,*" (Mar 1975).
128. K. Mizuishi, "*Some aspects of bonding-solder deterioration observed in long-lived semiconductor lasers: Solder migration and whisker growth,*" J. Appl. Phys., 55 289-295 (1984).
129. M. Fukuda, O. Fujita and G. Iwane, "*Failure modes in InGaAsP/InP lasers due to adhesives,*" IEEE Trans. Comp., Hybrids, & Manufact. Technol., 7 202-206 (1984).

130. S.M. Arnold, "*Repressing the growth of tin whiskers*," *Plating*, 96 (Jan 1966).
131. K. Mizuishi, M. Sawai, S. Todoroki, S. Tsuiji, S. Hirao and M. Nakamura, "*Reliability of InGaAsP/InP Buried Heterostructure 1.3um lasers*," *IEEE J. Quantum Electronic*, QE-19 1294-1301 (1983).
132. K. Fujiwara, T. Fujiwara, K. Hori and M. Takusagawa, "*Aging characteristics of Ga_{1-x}Al_x as double-heterostructure lasers bonded with gold eutectic alloy solder*," *Appl. Phys. Lett.*, 34 668-670 (1979).
133. K. Fujiwara, H. Imai, T. Fujiwara, K. Hori and M. Takusagawa, "*Analysis of deterioration in In solder for GaAlAs DH lasers*," *Appl. Phys. Lett.*, 35 861-863 (1979).
134. H. Kressel, ed. "*Thermal resistance increase in In solder*," *Characterization of Epitaxial and Semiconductor Films*. 1976, Elsevier: Amsterdam.
135. X.Q. Shi, Z.P. Wang, W. Zhou, H.L.J. Pang and Q.J. Yang, "*A new creep constitutive model for eutectic solder alloy*," *ASME J. Electron. Packag.*, 124 85-90 (Jun 2002).
136. X.Q. Shi, H.L.J. Pang, J.Z. W. and Z.P. Wang, "*Low cycle fatigue analysis of temperature and frequency effects in eutectic solder alloy*," *Int. J. of Fatigue*, 22 217-228 (2000).
137. G.S. Matijasevic, C.C. Lee and C.Y. Wang, "*Au-Sn alloy phase diagram and properties related to its use as a bonding medium*," *Thin Solid Films*, 223 276-287 (1993).
138. E. Zakei and H. Reichl, eds. "*Flip chip assembly using the gold, gold-tin and nickel-gold metallurgy*," ed. J. Lau. May 1995, McGraw-Hill: New York.
139. H. Okamoto and T.B. Massalski, "*Binary Alloy Phase Diagrams*," Metal Park: ASM International; 1990.

140. J. Doesburg and D.G. Ivey, "*Microstructure and preferred orientation of Au-Sn alloy plated deposits*," Mater. Sci. Eng. B, 78 44-52 (2000).
141. L. Buene, H. Falkenberg-Arell, J. Gjønnnes and J. Taftø, "*A study of evaporated gold-tin films using transmission electron microscopy*," Thin Solid Films, 65 247-257 (1980).
142. W.W. So, S. Choe, R. Chuang and C.C. Lee, "*An effective diffusion barrier metallization process on copper*," Thin Solid Films, 376 164-169 (2000).
143. N.G. Koopman, T.C. Reiley and P.A. Totta, "*Microelectronics packaging Handbook*," ed. R.R. Tummala and E.J. Rymaszewski New York: Van Nostrand Reinhold; 1989. 395.
144. C.H. Lee, Y.M. Wong, C.J. Doherty, K.L. Tai, K.L. Katz, E. Lane, D.D. Bacon, and F.A. Baiocchi, "*Study of Ni as a barrier metal in AuSn soldering application for laser chip/submount assembly*," J. Appl. Phys., 72 3808-3815 (1992).
145. R.A. Roy, R. Petkie and A. Boulding, "*Properties and microstructure of tungsten films deposited by ion-assisted evaporation*," J. Mater. Res., 6 80-91 (1991).
146. C.C. Lee and R.W. Chuang, "*Fluxless Non-Eutectic Joints Fabricated Using Gold-Tin Multilayer Composite*," IEEE Trans. Comp. & Packag. Technol., 26 416-422 (Jun 2003).
147. X.Q. Shi, H.F. Kwan, S.M.L. Nai and G.H. Lim, "*Kinetics of interface reaction and intermetallics growth of Sn-3.5Ag-0.7Cu/Au/Ni/Cu system under isothermal aging*," J. Materials Sci. Lett., 39 1095-1099 (2004).
148. J.H.L. Pang, K.H. Prakash and T.H. Low, "*Isothermal and thermal cycling aging on IMC growth rate in Pb-free and Pb-based solder interfaces*," Proceedings of 9th Conference on Thermal and Thermomechanical Phenomena in Electronic Systems, pp. 109-115.

149. G.H. Lim, H.F. Kwan and X.Q. Shi, "*Intermetallic growth study on lead-free solder joint under thermal cycling and isothermal aging*," Proceedings of *5th Electronics Packaging Technology Conference*, Dec. 2003, pp. 578-583.
150. C.C. Lee and W.W. So, "*High temperature silver-indium joints manufactured at low temperature*," *Thin Solid Films*, 366 196-201 (2000).
151. D.W. Baudrand, "Surface Engineering," in *ASM handbook*, M.E. Browning, Editor. ASM International. 1986.
152. G. Schoulen, "*Benefits of inert gas soldering in reducing soldering defects*," Proceedings of *NEPCON*, Feb. 1991, pp. 1728-1734.
153. H. Kergel and B. Monno, "*Ultra-fine Placement Soldering and Bonding Workstations for all purpose High-leadcount Assembly and Rework*," Proceedings of *ITAP Symposium*, 1996, pp. 105-112.
154. R. Sawada, H. Nakada and F. Ohira, "*Highly accurate and quick bonding for planar lightwave circuit and laser-diode chip*," Proceedings of *2nd IEMT/IMC Symposium*, Apr. 1998, pp. 133-137.
155. *Test Methods and procedures for microelectronics*, in *MIL-STD 883C, Method 2019*. Aug 1983.
156. *Bellcore Reliability Assurance practices for Optoelectronic Devices in Loop Applications in Loop applications*, in *Standard TA-TSY-000983*. Jan 1990.
157. "Surface Engineering," in *ASM handbook*. ASM International: Materials Park, OH. 1986.
158. Y. Tomita, Q. Wu, A. Maeda, S. Baba and N. Ueda, "*Advanced surface plating on the organic FC-BGA package*," Proceedings of *Electronic Components & Technology*, 2000, pp. 861-867.
159. D.W. Baudrand, "Plating and Electrolessplating," in *ASM Handbook*, M.E. Browning, Editor.

160. M. Datta, S.A. Merritt and M. Dagenais, "*Electroless metallization of aluminum bond pads on CMOS driver chip for flip-chip attachment to vertical cavity surface emitting lasers (VCSEL's)*," IEEE Trans. Comp. and Packag. Technol., 22 299-306 (Jun 1999).
161. J.-K. Kim, M. Lebbaj, J.H. Liu, J.H. Kim and M.M.F. Yuen, "*Interface adhesion between copper lead frame and epoxy moulding compound: effects of surface finish, oxidation and dimples*," Proceedings of 50th EPTC, May 2000, pp. 601 - 608.
162. S. WeiB, E. Zakel and H. Reichl, "*Mounting of high power laser diodes on diamond heatsinks*," IEEE Trans. Comp., Hybrids, & Manufact. Technol., A19 46-53 (Mar 1996).
163. E. Zakel, "*Reliable Au-Sn solder bump process for TAB inner lead bonding with reduced bonding pressure*," Proceedings of Proc. Japan IEMT, 1991, pp. 85.
164. C.S. Adams and D.T. Cassidy, "*Effects of stress on threshold, wavelength, and polarization of the output of InGaAsP semiconductor diode lasers*," J. Appl. Phys., 64 6631-6638 (Dec 1988).
165. P.D. Colbourne and D.T. Cassidy, "*Bonding stress measurements from the degree of polarization of facet emission of AlGaAs superluminescent diodes*," IEEE J. Quant. Electron., 27 914-920 (Apr 1991).
166. N.K. Dutta and D.C. Craft, "*Effect of stress on the polarization of stimulated emission from injection lasers*," J. Appl. Phys., 56 65-70 (Jul 1984).
167. S.W. Yoon, W.K. Choi and H.M. Lee, "*Calculation of surface tension and wetting properties of Sn-based solder alloys*," Scripta Materialia, 40 297-302 (1999).
168. X.Q. Shi, H.F. Kwan, S.M.L. Nai and G.H. Lim, "J. Materials Sci. Lett., (to be published).

169. T.B. Massalski, H. Okamoto, P.R. Subramanian and L. Kacprzak, "*Binary alloy phase diagrams.*" vol. 1. ASM International, Materials Park, Ohio 44073; Aug 1992. 433.
170. H.G. Song, J.P. Ahn and J. J.W. Morris, "*The microstructure of Eutectic Au-Sn solder Bumps on Cu/Electroless Ni/Au,*" J. Electron. Materials, 30 1083-1087 (2001).
171. M. A, "*Thermodynamics of facet damage in cleaved AlGaAs lasers,*" Appl. Phys. Lett., 59 522-524 (Jul 1991).
172. K. Mizuishi, M. Sawai, S. Todoroki, S. Tsuiji, M. Hirao and M. Nakamura, "*Reliability of InGaAsP/InP buried heterostructure 1.3um lasers,*" IEEE J. Quant. Electron., 19 1294-1301 (1983).
173. M. Buda, J. Hay, H.H. Tan, J. Wong-Leung and C. Jagadish, "*Low loss, thin p-clad 980-nm InGaAs semiconductor laser diodes with an asymmetric structure design,*" IEEE J. Quant. Electron., 39 625-633 (May 2003).
174. Y.P. Varshni, "*Temperature dependence of the energy gap in semiconductors,*" Physica, 34 149-154 (1967).
175. L. M.E. and S.L. Rumyantsev, "Handbook Series on Semiconductor Parameters," M. Shur, Editor. World Scientific: London. 1996, pp. 77-103.
176. A. Dargys and J. Kundrotas, "*Handbook on Physical Properties of Ge, Si, GaAs and InP,*" Vilnius: Science and Encyclopedia Publishers; 1994.
177. Z.M. Fang, K.Y. Ma, D.H. Jaw, R.M. Cohen and G.B. Stringfellow, "*Photoluminescence of InSb, InAs, and InAsSb grown by organometallic vapor phase epitaxy,*" J. Appl. Phys., 67 7034-7039 (1990).
178. J.I. Pankove, "*Temperature dependence of emission efficiency and lasing threshold in laser diodes,*" IEEE J. Quant. Electron., 4 119-122 (Apr 1968).

179. Landolt-Bornstein, ed. "Semiconductors," ed. O. Madelung. Vol. 17a. 1982, Springer: Berlin. 221.
180. T. Higashi, T. Yamamoto, S. Ogita and M. Kobayashi, "*Experimental Analysis of Characteristic Temperature in Quantum-Well Semiconductor Lasers*," IEEE J. Select. Topics Quant. Electron., 3 513-521 (1997).
181. R. Chin, N.H. Jr, B.A. Vojak, K. Hess, R.D. Dupuis and P.D. Dapkus, "*Temperature dependence of threshold current for quantum well AlGaAs-GaAs heterostructure laser diodes*," Appl. Phys. Lett., 36 19-21 (1980).
182. M. Asada, A.R. Adams, E. Stubkjaer, Y. Suematsu, Y. Itaya and S. Arai, "*The temperature dependence of the threshold current of GaInAsP/InP DH lasers*," IEEE J. Quant. Electron., 17 611-619 (1981).
183. B.W. Hakki and T.L. Paoli, "*Gain spectra in GaAs double-heterostructure injection lasers*," J. Appl. Phys., 46 1299-1306 (Mar 1975).
184. B.W. Hakki and T.L. Paoli, "*cw degradation at 300°K of GaAs double-heterostructure junction lasers. II. Electronic gain*," J. Appl. Phys., 44 4113-4119 (Sept 1973).
185. E. Duda, J.C. Carballes and J. Apruzzese, "*Thermal resistance and temperature distribution in double-heterostructure lasers: Calculations and experimental results*," IEEE J. Quant. Electron., 15 812-817 (1979).
186. W.B. Joyce and R.W. Dixon, "*Thermal resistance of heterostructure lasers*," J. Appl. Phys., 46 885-862 (Feb 1975).
187. S. Adachi, "*GaAs, AlAs, and Al_xGa_{1-x}As: Material parameters for use in research and device applications*," J. Appl. Phys., 58 R1-R29 (1985).
188. J. Strnad and A. Vengar, "*Stefan's measurement of the thermal conductivity of air*," Eur. J. Phys., 9-12 (1984).

189. W.C. Tang, H.J. Rosen, P. Vettiger and D.J. Webb, "*Comparison of the facet heating behavior between AlGaAs single quantum-well lasers and double-heterojunction lasers*," Appl Phys. Lett., 60 1043-1045 (Mar 1992).
190. J.H. Kuang, M.T. Sheen, C.F.H. Chang, C.C. Chen, G.L. Wang and W.H. Cheng, "*Effect of temperature cycling on joint strength of PbSn and AuSn solders in laser packages*," IEEE Trans. Adv. Packag., 24 563-568 (Nov 2001).
191. W.H. Cheng, M.T. Sheen, C.P. Chien, H.L. Chang and J.H. Kuang, "*Reduction of fiber alignment shifts in laser module packaging*," J. Lightwave Technol., 18 842-848 (2000).
192. S.L. Yellen, A.H. Shepard, R.J. Dalby, J.A. Baumann, H.B. Serreze, T.S. Guido, R. Soltz, K.J. Bystrom, C.M. Harding, and R.G. Waters, "*Reliability of GaAs-Based semiconductor diode lasers: 0.6-1.1um*," IEEE J. Quant. Electron., 29 2058-2067 (Jun 1993).
193. N. Hwang, S.-H. Lee, G.-C. Joo, M.-K. Song and K.-E. Pyun, "*Relationship between initial thermal characteristics and lifetime projection of semiconductor laser diodes*," Proceedings of 48th ECTC, 1998, pp. 1422-1423.
194. J.L. Spencer, "*Calculating Laser Diode Reliability*," Proceedings of Global Telecommunications Conference, 1988, pp. 63-69.
195. H. Yonezu, K. Endo, T. Kamejima, T. Torikai, T. Uasa and T. Furuse, "*Mirror degradation in AlGaAs double-heterostructure lasers*," J. Appl. Phys., 50 5150-5157 (1979).
196. A.K. Chin, Z.P. Wang, K.J. Luo, A. Nelson and Z.T. Xu, "*Failure-mode analysis of high-power single-mode 980-nm pump laser diodes*," Proceedings of Proceedings of the SPIE, 2003, pp. 84-90.